

Synthesis of CMR manganites and ordering phenomena in complex transition metal oxides

Von der Fakultät für Mathematik, Informatik und Naturwissenschaften
der Rheinisch-Westfälischen Technischen Hochschule Aachen zur
Erlangung des akademischen Grades eines Doktors der
Ingenieurwissenschaften genehmigte Dissertation

vorgelegt von

Master-Materials Science and Engineering

Haifeng Li

aus Shandong, China

Berichter: Universitätsprofessor Dr. Thomas Brückel
Universitätsprofessor Dr. Gernot Heger

Tag der mündlichen Prüfung: 30.01.2008

Diese Dissertation ist auf den Internetseiten der Hochschulbibliothek online verfügbar

No royal road to wisdom, no terminator of scientific research, only excelsior attitude of mind with the utmost fortitude.

Table of Contents

1	Introduction	1
2	Complex transition metal oxides (CTMO)	5
2.1	Novel phenomena and possible applications	5
2.1.1	High T_c superconductivity	5
2.1.2	Colossal magnetoresistance effect	7
2.1.3	Multiferroics	8
2.1.4	Metal-Insulator transition	9
2.1.5	Giant magnetostriction effect	10
2.2	Highly correlated electrons in perovskites	11
2.2.1	Electronic correlation and Hubbard model	11
2.2.2	Crystal structure	12
2.2.3	Jahn-Teller (JT) effect	13
2.2.4	Relative interactions	15
2.2.4.1	Orbital degeneracy versus crystal field	15
2.2.4.2	Double exchange	16
2.2.4.3	Superexchange	18
2.3	Complex ordering phenomena and electronic phase separation	19
2.3.1	Charge order	19
2.3.2	Orbital order	21
2.3.3	Spin order	23
2.3.4	Electronic phase separation	24
3	Experimental techniques	27
3.1	Elementary scattering theory: elastic scattering	27
3.1.1	Scattering geometry and scattering cross section	27
3.1.2	Scattered intensity	29
3.1.3	Pair correlation function	30
3.1.4	Form-factor	31
3.1.5	Bragg scattering from 3d periodic arrangements of atoms	32
3.2	Basics of x-ray and neutron scattering	33
3.2.1	Atomic form factor	33
3.2.2	Anomalous atomic scattering factor	35
3.2.3	Neutron scattering length	37
3.2.4	Magnetic neutron scattering	37
3.3	Powder diffraction and structure determination	39

3.4	Resonant soft x-ray scattering	44
4	Experimental instruments	47
4.1	Laboratory x-ray powder diffractometer	47
4.2	Neutron powder diffractometers	49
4.3	RSXS diffractometer	50
4.4	A new portable ultrahigh-vacuum goniometer for RSXS	51
5	Synthesis of perovskite manganites	55
5.1	Solid state reaction	55
5.2	Process optimization	58
5.2.1	Starting materials	58
5.2.2	Mixing and milling time	60
5.2.3	Reaction temperature and time	61
5.2.4	Binder effect	63
5.2.5	Other factors	64
5.3	Summary	65
6	Floating zone crystal growth of CTMO	69
6.1	Overview	69
6.2	Preparation of longer and stronger rods	70
6.3	Floating zone furnace and crystal growth	72
6.4	Necking technique	75
6.5	Characterizations	76
6.6	Summary	77
7	Crystal and magnetic properties of $\text{La}_{7/8}\text{Sr}_{1/8}\text{Mn}_{1\pm\gamma}\text{O}_{3+\delta}$ polycrystals	79
7.1	Introduction	79
7.2	Experimental details	82
7.3	Room-temperature structural and magnetic properties	83
7.3.1	Structural studies	83
7.3.2	Magnetic properties	89
7.3.3	Sources and accommodation of excess oxygen	91
7.3.4	Effect of Ar and O_2 annealings on T_c	92
7.3.5	Effect of Mn stoichiometry on T_c	93
7.3.6	Conclusions	96
7.4	Temperature dependent structural transition and magnetic order	97
7.4.1	Results	97
7.4.2	Discussion	106
7.4.3	Conclusions	109
8	Complex ordering phenomena in $\text{La}_{7/8}\text{Sr}_{1/8}\text{MnO}_3$ single crystals	111
8.1	Introduction	111
8.2	Lattice and magnetic order	114
8.2.1	Experimental details	114

8.2.2	Results	114
8.2.3	Discussion	124
8.2.4	Conclusions	128
8.3	Evidence of hole ordering from RSXS	129
8.3.1	Introduction	129
8.3.2	Results and discussion	129
8.3.3	Conclusions	133
9	Soft x-ray resonant scattering study of $\text{La}_1\text{Sr}_2\text{Mn}_2\text{O}_7$	135
9.1	Introduction	135
9.2	Double-layered $\text{La}_1\text{Sr}_2\text{Mn}_2\text{O}_7$	136
9.3	Diffraction data	138
9.4	Discussion	142
9.5	Conclusions	146
10	Summary and outlook	147
	Appendix	153
A	List of Abbreviations	153
B	An example of the PCR files for Rietveld refinement by Fullprof	155
C	Transformation of the orthorhombic $Pbnm$ and $Pnma$ symmetries	158
	Bibliography	159
	Acknowledgements	171
	Curriculum Vitae	173

Chapter 1

Introduction

The complicated enduring physical phenomena, e.g. high T_c superconductivity, colossal magnetoresistance (CMR) effect (i.e. a strong dependence of the electrical resistivity on the external magnetic field), multiferroics (e.g. simultaneous magnetic and ferroelectric long-range order), metal-insulator transition, etc, in complex transition metal oxides (CTMO) continue to be the focus of intense inquiry and debate in condensed matter science, since they are related to strong electronic correlations and cannot be explained within the ‘standard model’ of solid state physics. These novel functionalities make correlated electron systems prime candidates for applications, e.g. in information storage. A full understanding of the possible tuning of the physical properties of polycrystals, thin films and single crystals needs to be achieved before such applications become possible.

The materials synthesis is the first and critical step for any research in condensed matter physics. The interesting physical properties of CTMO are very sensitive to even very small changes in external parameters (e.g. temperature, pressure and chemical potential). For example, the perovskite $\text{La}_{1-x}\text{Sr}_x\text{MnO}_3$ system shows large differences in the structural and physical properties between samples prepared by different methods: (i) the structural evolutions versus temperature and Sr doping level, (ii) the Curie temperature T_c and (iii) the phase diagram including monotonic variations of the phase boundaries [1-11]. In addition, from the investigations of high T_c superconductivity, a crucial lesson has been learnt that materials synthesis is the sine qua non of progress [12]. A consensus on the importance of synthesizing materials and improving the crystal quality of already known materials has been reached [12, 13]. In this context, a large fraction of this thesis (chapters 5 and 6) is thus devoted to the materials syntheses, including the preparation of polycrystalline samples and the growth of large single crystals of fundamental interest to condensed matter physics.

Our present understanding of the properties and phenomena of condensed matter physics is based on atomic theories. The first question we pose when studying any condensed matter system is the question concerning the internal structure: what are the relevant building blocks and how are they arranged? The second question concerns the microscopic dynamics: how do these building blocks move and what are their internal degrees of freedom? These herculean tasks can be accomplished by modern scattering techniques: neutron and synchrotron x-ray scattering. Traditionally, solving complicated structures is the duty of powder diffraction (x-ray and neutron). Especially, neutron

scattering is a unique tool to solve magnetic structures and determine magnetic excitations and fluctuations [14].

The investigation of charge, spin and orbital degrees of freedom in CTMO has long been of interest to condensed matter scientists. Electrons in solids possess three attributes: charge (e^-), spin ($S = \pm 1/2$) and orbital symmetry. In many CTMO, the strong electron-electron and electron-lattice interactions usually lead to the emergence of novel quantum collective behaviours in multiple length and time scales, such as the charge and orbital ordering, which are normally accompanied by concomitant structural, magnetic and metal-to-insulator phase transitions [15]. The present understanding the physics of charge, spin and orbital ordering phenomena has been largely based on the classic ionic model. This ionic picture suggests that the involved electrons or holes would primarily reside on cation sites, while the oxygen $2p$ shells are fully filled. Therefore, the oxygen would play little role in determining the electronic structures and magnetic properties of CTMO. In this ionic scenario, the charge ordering (CO) is considered as the ordering of cations with different formal valencies, e.g. $\text{Mn}^{3+}/\text{Mn}^{4+}$ in mixed-valence manganites and $\text{Ni}^{2+}/\text{Ni}^{3+}$ in stripe-ordered phases of $\text{La}_{2-x}\text{Sr}_x\text{NiO}_4$. The orbital ordering (OO) is then regarded as the result of the unambiguous occupation of the degenerate $3d$ orbitals by fully localized electrons at cation sites. In addition, the magnetism relates to the localized magnetic moments possessed by transition metal (TM) ions only, e.g. Mn^{3+} ($S = 2$) and Mn^{4+} ($S = 3/2$). However, this rigid ionic model is being strongly challenged. For example, a model named Zener polaron [16], in which pairs of Mn^{3+} ions share a hole on a bridging O^- ion, was established in order to interpret the appearance of a superstructure for $\text{Pr}_{0.6}\text{Ca}_{0.4}\text{MnO}_3$, since the invalidation of the ionic $\text{Mn}^{3+}/\text{Mn}^{4+}$ CO picture. In fact, the importance of the hybridization between oxygen $2p$ and TM $3d$ bands and the prominent $2p$ character of involved electrons or holes have been demonstrated in earlier soft x-ray absorption experiments [17, 18]. Therefore, an alternative picture of the CO can be described as the ordering of the electronic holes on oxygen. The existence of such oxygen-hole ordered states was indeed suggested from an *ab-initio* calculation on $\text{La}_{0.5}\text{Ca}_{0.5}\text{MnO}_3$ [19]. Very recently, two studies on the spin-ladder compound $\text{Sr}_{14}\text{Cu}_{24}\text{O}_{41}$ [20] and the stripe-ordered phase of $\text{La}_{1.8}\text{Sr}_{0.2}\text{NiO}_4$ [21] with resonant soft x-ray scattering (RSXS) also strongly support this newly proposed oxygen-hole scenario. Therefore, the classic ionic model with integer valencies of TM ions is under suspicion. In order to reach a deeper understanding of the novel properties, the order and excitations of spin-, charge-, orbital- and lattice degrees of freedom have to be determined, which is a typical task for scattering methods. Especially, the emerging RSXS technique promises to be an ideal tool to fulfil this task due to its capability to obtain both spectroscopic and structural information and its tremendous sensitivity to the charge degrees of freedom of $3d$ electrons.

This thesis deals with: the instrumentation development; the optimization of the synthesis of polycrystalline materials; the single crystal growth of perovskite manganites; the determination of crystal and magnetic structures from x-ray powder diffraction (XRPD) and neutron powder diffraction (NPD) data of polycrystalline and powdered single-crystalline CMR $\text{La}_{1-x}\text{Sr}_x\text{MnO}_3$ manganites as well as its application in quantitatively correlating structural and magnetic properties; the application of the RSXS technique in the investigation of complex ordering phenomena in $\text{La}_{7/8}\text{Sr}_{1/8}\text{MnO}_3$ and $\text{La}_1\text{Sr}_2\text{Mn}_2\text{O}_7$ at the TM $L_{\text{II, III}}$ -edges and the rare earth $M_{\text{IV, V}}$ -edges, trying to obtain a qualitative understanding of the data.

The first part of chapter 2 introduces the enduringly interesting subjects in condensed

matter physics as well as their current research statuses and possible applications, followed by a description of the perovskite structures and a short introduction of the classical theories for strongly correlated electron systems, including the Hubbard model, orbital degeneracy, double exchange and superexchange. Finally, the charge, orbital and spin degrees of freedom and the electronic phase separation have been generally reviewed.

Chapters 3 and 4 refer to the experimental techniques and instruments. Apart from the basic theories for the powerful x-ray and neutron scattering techniques, chapter 3 is focused on the two main investigating methods utilized within this dissertation: powder diffraction and RSXS. The basic principles of the two methods as well as the fundamental aspects of structure refinement by the Rietveld method are introduced. Chapter 4 describes the details of the experimental setups. The emphasis of this chapter is on the development of two new devices: one is the rotating specimen holder for laboratory XRPD; another is the miniature goniometer for RSXS.

Chapters 5 and 6 show the scene of materials syntheses. The revival of syntheses in CTMO is likely to open new avenues to revisit the interesting physical behaviors and result in improved studies. With this motivation, chapter 5 describes the chemistry of the mostly used method for synthesizing perovskites, i.e. solid state reaction, and discusses the optimization process from the treatment of raw materials to the selection of reaction temperature and time taking $\text{La}_{7/8}\text{Sr}_{1/8}\text{MnO}_3$ as an example, trying to acquire a universal recipe for most of the perovskite syntheses. Despite the critical role of single crystal growth to the related researches and applications, to date there is a significant lack of growth theory describing its complex and delicate process. In this case, experience rather than physics is the mother of wisdom in chapter 6, where the aspects of single crystal growth from rod preparation, to mirror furnace and crystal growth procedure and to the subsequent preliminary characterizations and the in-depth studies are presented systematically.

Chapters 7 and 8 deal with the archetypal correlated electron system $\text{La}_{1-x}\text{Sr}_x\text{MnO}_3$. Due to the extreme sensitivity to external parameters, small changes in the stoichiometry of these compounds lead to huge effects in the physical parameters. This might be the reason for different structures, transition temperatures etc, reported in the literature. In chapter 7, three nominal $\text{La}_{1-x}\text{Sr}_x\text{MnO}_3$ ($x = 1/8$) polycrystals prepared under different conditions air, Ar and O_2 at 1 atm show huge differences in the Curie temperature T_c , e.g. the T_c for the Ar annealed sample is reduced by about 20% in contrast to that of other samples. A combined Rietveld refinement of the room-temperature x-ray and neutron powder diffraction data has been performed for these three samples. This study not only can determine the relative content of the various elements (especially the oxygen) with higher precision as compared to one probe alone, but also makes it possible to correlate the drastic change in T_c with the detailed structural parameters. In addition, the individual effect of the number of nearest magnetic neighbors on the structural and magnetic properties has been investigated in detail using a set of $\text{La}_{7/8}\text{Sr}_{1/8}\text{Mn}_y\text{O}_3$ samples with initial $y = 0.97, 1.00$ and 1.03 . Moreover, a systematic NPD study of the Ar annealed and air sintered $\text{La}_{7/8}\text{Sr}_{1/8}\text{Mn}_{1-\gamma}\text{O}_{3+\delta}$ samples between 10 and 900 K has been performed, where the structural and magnetic phases and their respective transitions for two samples are completely different. For the air sintered sample, a structural transition from rhombohedral to orthorhombic upon cooling from 180 to 65 K has been observed for the first time. From the refined parameters the cooperative JT distortion parameter Δ , the tolerance factor t based on the equilibrium La(Sr)-O and Mn-O bond lengths, and the

one-electron bandwidth W of the e_g -band have been determined. The first part of chapter 8 presents a NPD study on the crystal and magnetic structure of a powdered $\text{La}_{1-x}\text{Sr}_x\text{MnO}_3$ ($x \approx 1/8$) single crystal from 5 to 300 K. The structural information obtained from this study provides the basis for establishing the correct charge- and orbital- order model from single crystal anomalous x-ray scattering. Especially, the structural information in the JT regime has been established correctly for using for the first time. The measurements by a superconducting quantum interference device (SQUID) show very interesting magnetic properties, e.g. the existence of magnetic polarons. Based on the size of JT distortion and the Bond-valence sums (BVS's), the CO and OO phenomena are briefly discussed. The second part of chapter 8 reports the first direct observation of the hole ordering in a single-crystalline $\text{La}_{1-x}\text{Sr}_x\text{MnO}_3$ ($x \approx 1/8$) sample obtained via the RSXS technique, i.e. the strong resonances of the superstructural reflection $(0\ 0\ 1/2)$ in $Pbnm$ symmetry have been observed at the Mn L_{III} -edge and the oxygen K -edge but not at the Mn K -edge.

The ninth chapter presents the RSXS results of a double-layered $\text{La}_1\text{Sr}_2\text{Mn}_2\text{O}_7$. Two reflections were observed for $\text{La}_1\text{Sr}_2\text{Mn}_2\text{O}_7$, $(0\ 0\ 1)$ at the Mn $L_{\text{II, III}}$ -edges and $(0\ 0\ 2)$ at the La $M_{\text{IV, V}}$ -edges. The $(0\ 0\ 1)$ reflection can be clearly assigned to the A -type antiferromagnetism, whereas the unexpected dramatic enhancement of the Bragg $(0\ 0\ 2)$ reflection was observed for the first time and the possible driving forces are briefly discussed. In addition, the six obvious features displayed in the energy dependence of $(0\ 0\ 1)$ are confirmed to purely originate from the spin ordering. The temperature dependence of $(0\ 0\ 2)$ shows a strong interplay with that of the OO reflection.

Finally chapter 10 summarizes the main results of this thesis and presents some new perspectives which will undoubtedly be the subjects of further investigation.

Chapter 2

Complex transition metal oxides (CTMO)

As one particularly significant class of contemporary materials, CTMO, e.g. doped perovskite-type manganites, have attracted tremendous amounts of attention due to their remarkable structural, magnetic and electronic properties that are governed by the complicated (competitive or cooperative) interplay of lattice, charge, orbital and spin degrees of freedom. The high T_c superconductivity, CMR effect, multiferroic behaviour, metal-insulator transition, and giant magnetostriction effect are the main extraordinary properties. Although the structural, magnetic and electronic properties of polycrystals, single crystals and thin films of CTMO have been elaborately studied, complete and consistent understanding of the relevant interesting physics in CTMO has still not been achieved [22-32].

Both theoretical and experimental studies are being actively performed, not only because of the interesting fundamental properties, but also because of the potential technological applications, e.g. as cathode materials for solid fuel cells, new classes of memory devices, etc. A full understanding of the possible tuning of the physical properties of polycrystals, thin films and single crystals needs to be achieved before such applications become possible. There is a lot of work to be done.

In this chapter, I shall give an overview on the novel phenomena in CTMO as well as their possible applications in the first part, followed by an introduction to the relevant structures and interactions in the second part, and finally an overview of the complex ordering (charge, orbital and spin) phenomena and the electronic phase separation.

2.1 Novel phenomena and possible applications

2.1.1 High T_c superconductivity

High T_c superconductivity is one of the most brilliant discoveries in strongly correlated electron systems in the last century. Superconductivity is the unique ability of a certain material to conduct electricity without any consumption of energy, because the resistivity of the material is exactly zero below the critical superconducting transition temperature T_c (figure 2.1).

Since its primary discovery by Kamerlingh Onnes in mercury at 4.2 K in 1911 [33],

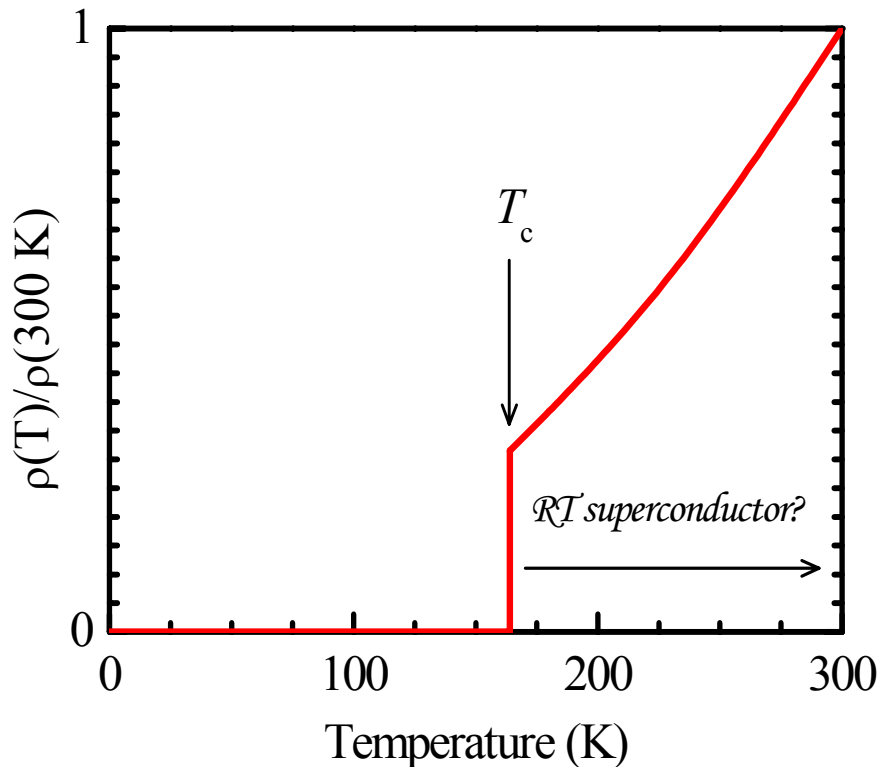


Figure 2.1: The electrical resistivity of a superconductor decreases to zero sharply at the Curie temperature T_c , entering into the superconducting state. The room-temperature (RT) superconductor has not been found yet.

a lot of experimental and theoretical work has been done in the ensuing ninety six years, especially after the experimental discovery [34] of the first high T_c superconducting system in 1986, which was recognized by the Nobel Prize in the following year. To date, the highest superconducting transition temperature reported is $T_c = 164 \text{ K}$, which was discovered in a cuprate-perovskite system of $\text{HgBa}_2\text{Ca}_{m-1}\text{Cu}_m\text{O}_{2m+2+\delta}$ ($m = 1, 2, \text{ and } 3$) under quasihydrostatic pressures [35]. These advances were motivated by not only the scientific interest in the anomalous behavior, but also the common goal of achieving a room-temperature superconductor.

The complete loss of electrical resistance in superconducting state underlies key technological applications. Current applications include superconducting quantum interference devices, electric power transmission, motors, magnetically levitated trains, and medical magnetic resonance imaging, etc [36]. In spite of the profitable commercial applications, high T_c superconductors show complex behaviors and the basic mechanism is not yet understood. A common fact in cuprates is that quasi-two-dimensional superconductivity occurs in the CuO_2 planes in the host materials [37]. One crucial lesson from the past years is that searching for new materials and improving the crystal quality of the ones already known are the sine qua non of progress. However, materials synthesis often has trouble attracting its fair share of glory and funding in a competitive environment [12].

2.1.2 Colossal magnetoresistance effect

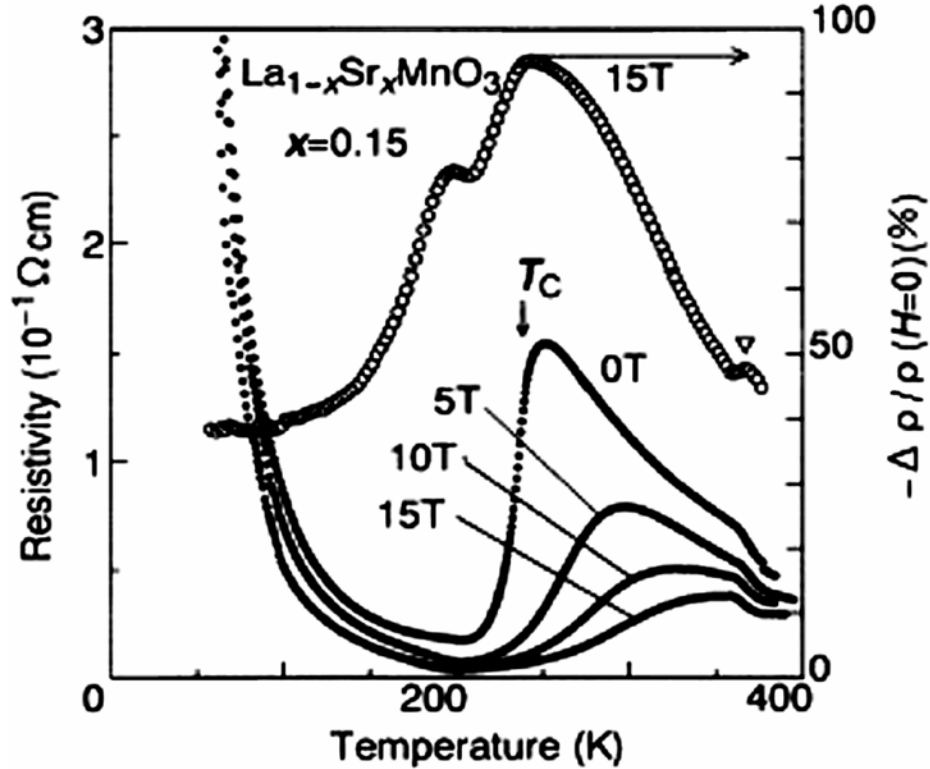


Figure 2.2: Temperature dependence of resistivity for $\text{La}_{1-x}\text{Sr}_x\text{MnO}_3$ ($x = 0.15$) under various magnetic fields. Open circles represent the magnitude of negative magnetoresistance $-\Delta\rho(T, H) = [\rho(T, H) - \rho(T, 0)]/\rho(T, 0)$ with a magnetic field of 15 T [38].

The CMR effect observed in manganites is one of the most exciting phenomena in CTMO. It describes that the application of a magnetic field leads to a gigantic decrease in resistivity of concerned manganites. The CMR value is usually defined as the ratio of:

$$\text{MR} = \Delta\rho/\rho_0 = [\rho(T, H) - \rho(T, 0)]/\rho(T, 0), \quad (2.1)$$

where ρ is the resistivity, T is temperature (Kelvin) and H is the applied magnetic field (Tesla). CMR occurs particularly close to the Curie temperature T_c in perovskites as a negative value, e.g. there is a sharp peak in the magnetoresistance of $\text{La}_{0.85}\text{Sr}_{0.15}\text{MnO}_3$ near $T_c = 240$ K and the calculated CMR value reaches about -95 percent at a field of $H = 15$ T as shown in figure 2.2 [38].

The large peak in the magnetoresistance was first observed in $\text{La}_{0.8}\text{Sr}_{0.2}\text{MnO}_3$ by Volger in 1954 [39]. Huge absolute CMR values as high as $\sim 1.27 \times 10^5$ percent near 77 K and $\sim 1.3 \times 10^3$ percent near room temperature were observed in thin oxide films of perovskite-like $\text{La}_{0.67}\text{Ca}_{0.33}\text{MnO}_x$ in 1994 [40]. Such an extreme enhancement could be useful for various magnetic and electric device applications if the observed effects of materials processing are optimized.

The CMR effect in manganites often occurs in an intermediate regime of the

transformations of charge (insulator, metal) order and spin (paramagnetic, ferromagnetic, antiferromagnetic) order. The double exchange interaction (chapter 2.2.4.2) can qualitatively explain the CMR effect based only on the charge and spin degrees of freedom, but fails to explain it quantitatively [41-43]. Other degrees of freedom also play an important role. The consensus reached at present is that the interplay of lattice, charge, orbital and spin degrees of freedom is essential to this effect.

The highly sensitive and electrically readable magnetic-field sensors have been in industrial demand for the read-head of the magnetic memory and it is anticipated that the CMR oxides may be one such candidate material [27].

2.1.3 Multiferroics

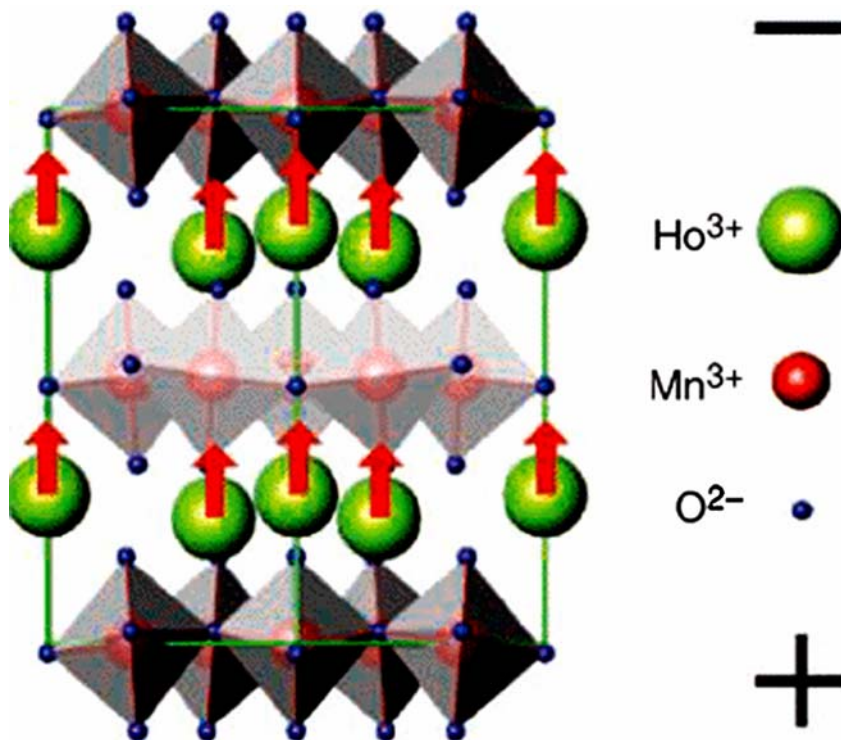


Figure 2.3: Hexagonal HoMnO₃ is ferroelectric, because the oxygen bipyramids surrounding each Mn³⁺ ion are tilted and shifted relative to the Ho³⁺ ions. It is also magnetic, with ferromagnetic alignment of the Ho³⁺ magnetic moments combined with antiferromagnetic Mn³⁺ ordering. Therefore, hexagonal HoMnO₃ is multiferroic [44].

One class of materials (e.g. Bi(Fe, Mn)O₃, REMnO₃ and RE = Y, Ho, Er, Tm, Yb, Lu, etc) in CTMO, exhibiting multiple functional properties, is called the multiferroics. One example HoMnO₃ [44] is shown in figure 2.3. Multiferroics are interesting materials because they simultaneously exhibit ferromagnetic (FM) and ferroelectric polarizations in the same phase and a coupling between them [13, 45].

Due to the nontrivial coupling between magnetic and ferroelectric domains (the

magneto-electric effect), the magnetic polarization can be switched by applying an electric field; likewise the ferroelectric polarization can be switched by applying a magnetic field. Multiferroics are thus likely to be used in a wide range of applications. First, the ability to couple to either the electric or the magnetic polarization allows an additional degree of freedom in device design. Other applications include multiple-state memory elements, in which data are stored both in the electric and magnetic polarizations, and novel memory media, which might allow the writing of a ferroelectric data bit and the reading of the magnetic data bit. Multiferroics have been used to realize a vast number of devices ranging from giant devices like electrical transformers to tiny devices like sensors, used in integrated circuits or as storage devices [13].

Synthesizing new compounds behaving as multiferroics and trying to understand the origin of multiferroism and the mechanism of coupling between ferroelectric and magnetic domains are challenging current subjects in scientific and industrial fields [13].

2.1.4 Metal-Insulator transition

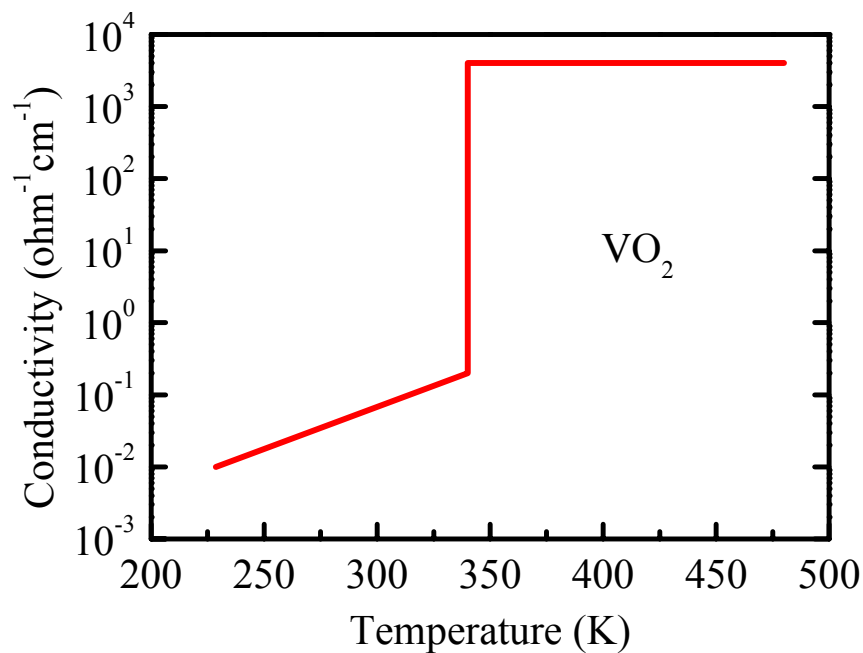


Figure 2.4: Temperature dependence of the conductivity of VO₂ [46].

In the noninteracting or weakly interacting electron theory, metals and insulators are described based on the filling of the electronic bands: for insulators the highest filled band is completely filled; for metals, it is partially filled. In other words, the Fermi level lies in a band gap in insulators while the level is inside a band for metals.

The Metal-insulator transition is a transition characterized by a sudden change in electrical transport properties (conductivity) due to a reversible change from localized to itinerant behavior of the electrons [47]. For example, the transition at 339 K in VO₂ [48,

49] is a first-order one with the conductivity jump of up to five orders in magnitude as shown in figure 2.4 [46], which is accompanied by a structural transition from high-temperature metallic tetragonal rutile to a low-temperature insulating distorted one with monoclinic symmetry [50]. With the absence of a strong first-order structural distortion, metal-insulator transition will hardly occur. However, a continuous second-order metal-insulator transition which is not accompanied by a structural change was observed only in the compound $\text{Ni}(\text{S}, \text{Se})_2$ at very low temperature by applying pressure [51].

Despite intense experimental and theoretical studies the detailed understanding of the microscopic origin is still far from complete [52]. Much more work needs to be done to unravel this puzzle. Fortunately, the revival in the synthesis and characterization of CTMO is likely to open new avenues to revisit the metal-insulator transition and result in improved studies. Furthermore, as we learn to control this physical phenomenon, practical applications of this effect will follow [53].

2.1.5 Giant magnetostriction effect

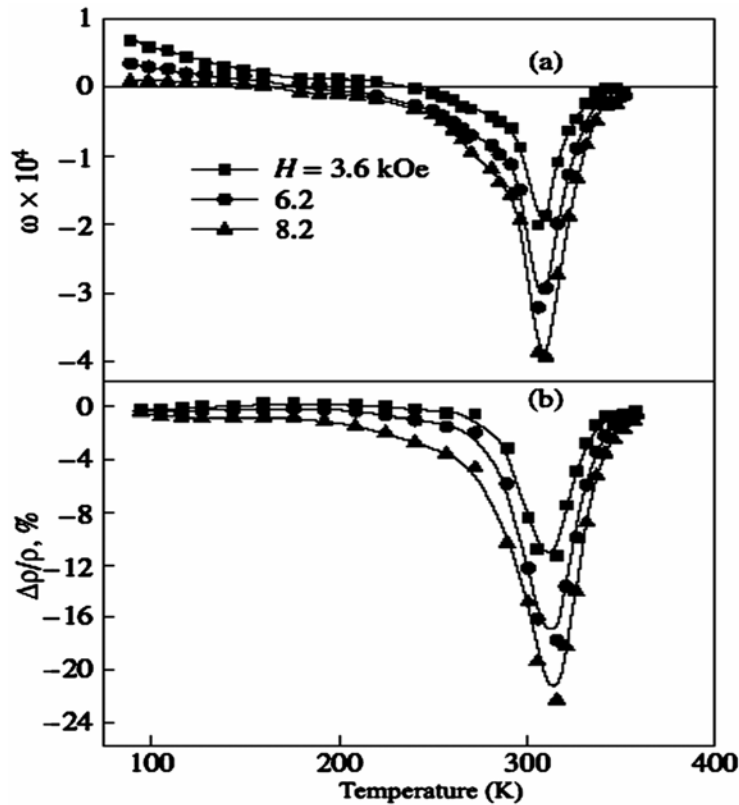


Figure 2.5: Temperature dependence of (a) volume magnetostriction $\omega(H)$ and (b) magneto-resistance measured in various magnetic fields for $\text{La}_{0.7}\text{Ba}_{0.3}\text{MnO}_3$ [54].

The giant magnetostriction (MS) effect observed in perovskite manganites, e.g. $\text{La}_{0.60}\text{Y}_{0.07}\text{Ca}_{0.33}\text{MnO}_3$ (spontaneous volume magnetic contribution $\sim 1 \times 10^{-3}$ at $T_c = (160 \pm 5)$ K) [55], $\text{R}_{1-x}\text{Sr}_x\text{MnO}_3$ ($\text{R} = \text{Sm}$, $x = 0.33, 0.40, 0.45$; $\text{R} = \text{Nd}$, $x = 0.33, 0.45$) [56], etc,

near the Curie temperature T_c is one of the most interesting phenomena from the theoretical as well as the practical point of view. This effect is an anomaly in the field dependence of the volume magnetostriction $\omega(H) = (\lambda_{\parallel} + 2\lambda_{\perp})$ (λ_{\parallel} and λ_{\perp} are the magnetostriction parallel and perpendicular to the applied magnetic field, respectively), which is due to the magnetic transition from paramagnetism to ferromagnetism.

Close to T_c , the $\text{La}_{1-x}\text{Sr}_x\text{MnO}_3$ system shows not only the CMR effect, but also the giant MS effect. Both effects exhibit a similar tendency, i.e. both $\omega(H)$ and $\Delta\rho/\rho_0$ (equation 2.1) are negative, their absolute values are maximum near the T_c and fall off with increasing x , and they do not saturate in the measuring field even up to 13 T. The MS effect observed in most perovskite systems occurs below room temperature, which curtails the application of these materials in magneto-mechanical devices [57, 58]. The first material reported having both CMR effect and MS effect at room temperature is the single-crystalline $\text{La}_{0.7}\text{Ba}_{0.3}\text{MnO}_3$ in which the absolute giant volume MS was observed to reach $\sim 2.54 \times 10^{-4}$ at room temperature and an even larger value of $\sim 4 \times 10^{-4}$ at $T_c = 310$ K at a magnetic field 0.82 T as shown in figure 2.5(a) [54]. At the same temperature and magnetic field, MS effect is complemented by a CMR value of ~ 15.2 and $\sim 22.7\%$ (figure 2.5(b)) [54], respectively.

The perovskites with a large MS effect could be generally used in devices that convert magnetic energy to mechanical energy [56]. Thus it is particularly interesting to search for the materials exhibiting a higher CMR value as well as a higher MS effect at room temperature in a lower magnetic field.

2.2 Highly correlated electrons in perovskites

2.2.1 Electronic correlation and Hubbard model

The investigations of solid state physics in a microscopic level have to face the many-body problem at a huge scale ($\sim 10^{23}$) and with extreme complexity. It is quite difficult to solve the possible correlations of such a huge number of constituents (ions, electrons, etc) analytically and quantitatively, although a variety of theoretical models were formed to challenge this Gordian knot. Among them, the intriguingly simple Hubbard model [59, 60] originally proposed to describe electronic interactions has been widely used and became a classical standard model in the investigation of strong electron correlation effects in condensed matter physics [61].

Consider a crystal of N_a lattice sites with a total of N itinerant electrons hopping between the neighboring lattice sites. Each site is capable of accommodating two electrons of opposite spin, with an interaction energy $U > 0$, which mimics a screened Coulomb repulsion among electrons. The Hubbard model [59, 62] is described by the Hamiltonian:

$$H = -t \sum_{\langle ij \rangle} \sum_{\sigma} (C_{i\sigma}^{\dagger} C_{j\sigma} + C_{i\sigma} C_{j\sigma}^{\dagger}) + U \sum_{i=1}^N n_{i\uparrow} n_{i\downarrow}, \quad (2.2)$$

where $C_{i\sigma}^{\dagger}$ and $C_{i\sigma}$ are, respectively, the creation and annihilation operators for an

electron of spin σ at the i th lattice site and $n_{i\sigma} = C_{i\sigma}^\dagger C_{i\sigma}$ is the occupation number operator. The summation $\langle ij \rangle$ is over nearest neighbors between which the hopping of electrons takes place. This form contains two energy terms: the first (t) is the kinetic energy allowing for hopping of electrons between lattice sites, leading to a bandwidth $W = 2zt$ (z is the number of nearest neighbors); the second (U) is the potential energy consisting of the intra-site Coulomb repulsion between electrons. Together, the two terms give rise to a competition between the electron hopping and the electron location. The electron hopping is controlled not only by the bandwidth, but also by bandfilling. Thus electron mobility becomes a function of the distance and angles between neighboring atoms and the hole or electron doping levels. The Hubbard model can therefore qualitatively explain and predict the metal-to-insulator transition in some perovskites when the hopping integral is reduced to the point where the onsite potential is dominant.

2.2.2 Crystal structure

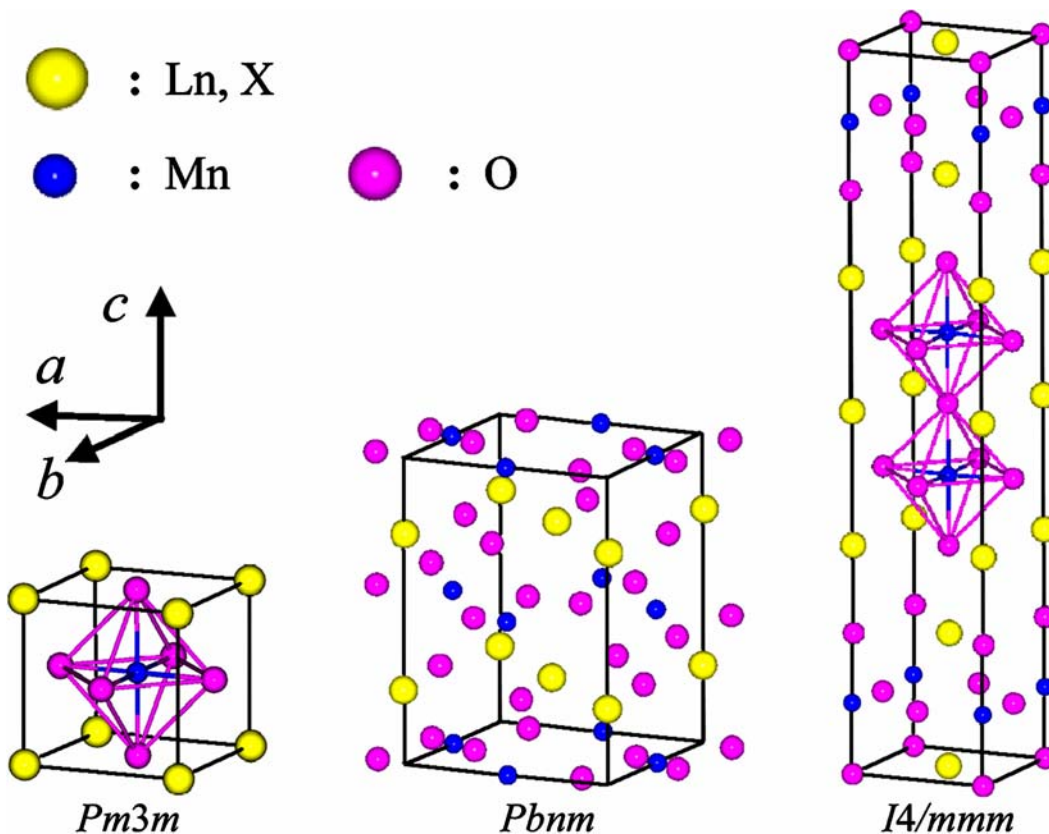


Figure 2.6: Unit cells of ideal cubic perovskite structure (left), distorted orthorhombic structure in most $(\text{Ln}_{1-x}\text{X}_x)\text{MnO}_3$ (middle) and distorted tetragonal structure in most $(\text{Ln}_{1-x}\text{X}_x)_3\text{Mn}_2\text{O}_7$ (right).

Most of the unusual phenomena occurring in manganites are tightly correlated with their versatile crystal structures. The ideal perovskite structure of LnMnO_3 is cubic as

illustrated in the left of figure 2.6, where the Mn ions are located in the center of O_6 octahedra which build up a three dimensional network in the way of sharing corners. The formula of the Ruddlesden-Popper series manganites derived from the perovskites is generally expressed as $(Ln_{1-x}X_x)_{n+1}Mn_nO_{3n+1}$, where Ln and X are trivalent rare-earth (La, Pr, Nd, Sm, Eu, Gd, Tb, Dy, Ho, Er, Y, Bi) and divalent alkaline-earth (Ca, Sr, Ba, Pb) ions, respectively. The Mn and O ions form a MnO_2 plane that is arranged in a variety of sequences with MnO_2 planes interleaved with (Ln, X)O planes as shown in the right of figure 2.6. The annotation of these compounds depends on the number of MnO_2 planes stacked between (Ln, X)O bilayers.

Substituting X for Ln with a homogeneous solid solution in manganites controls the mean valency and electronic doping of Mn ions. Simultaneously the interesting structures can thus be derived from the prototypical cubic one through modifying the tolerance factor $t = \langle Ln(X)-O \rangle / \sqrt{2} \langle Mn-O \rangle$ from unity [63]. The tolerance factor reflects the degree of mismatch between the equilibrium $Ln(X)-O$ and $Mn-O$ bond lengths, when the $Ln(X)$ ions are too small to fill the space between MnO_6 octahedra. We can also estimate the t value through the equation $t = (r_{Ln, X} + r_O) / \sqrt{2} (r_{Mn} + r_O)$ based on the mean ionic radii, but this kind of estimation is relatively rough in that doped perovskite-type manganites are not truly ionic compounds. In addition, the result depends on the values taken for the ionic radii. When $t = 1$, the compound has a perfect cubic structure with equal Mn-O bonds and straight (180°) Mn-O-Mn bond angles. When $t < 1$, the Mn-O and $Ln(X)-O$ bonds are subjected to compressive and tensile stresses, respectively. In order to relieve the internal chemical stress, MnO_6 octahedra will cooperatively rotate (normally leading to unequal Mn-O bonds) and/or tilt (making Mn-O-Mn bond angle $< 180^\circ$). This decreases the symmetry of the structure, thus resulting in the hexagonal, tetragonal (right of figure 2.6), orthorhombic (middle of figure 2.6), monoclinic and even triclinic structures, depending on the value of t . These distortions can be modified by temperature, magnetic field, annealing atmosphere and pressure, etc. They have a profound influence on the physical properties of manganites. The tunable magnitude of such distortions allows for systematic studies of the connections among structural, magnetic and electronic degrees of freedom.

2.2.3 Jahn-Teller (JT) effect

The Kramer's degeneracy theorem [64] states that the energy levels of systems with an odd number of spins, no matter what the crystal field is like, remain at least a residual degeneracy in the presence of purely electric fields (only magnetic field can lift it). Ions with an even number of electrons in the unfilled $3d$ -, $4d$ -, $5d$ - or $4f$ - shell are called the Kramer's ions. The JT effect happens only for the Kramer's ions. For manganites, if the symmetry of the crystal field is so high that the ground state of Mn^{3+} ions (Kramer's ions) is predicted to be orbitally degenerate, then it will be energetically favorable for the crystal to distort to lift the orbital degeneracy. This so-called JT effect is due to an electron-lattice interaction. The JT effect in manganites arises from an electronic instability inherent to the Mn^{3+} ions in asymmetric MnO_6 octahedra. Since neighboring octahedra share one oxygen ion, the JT distortion can be cooperative. The cooperative rotation of MnO_6 octahedra leads to a change in lattice symmetry. This is usually accompanied by the shortening and stretching of six Mn-O bonds. Consequently, the

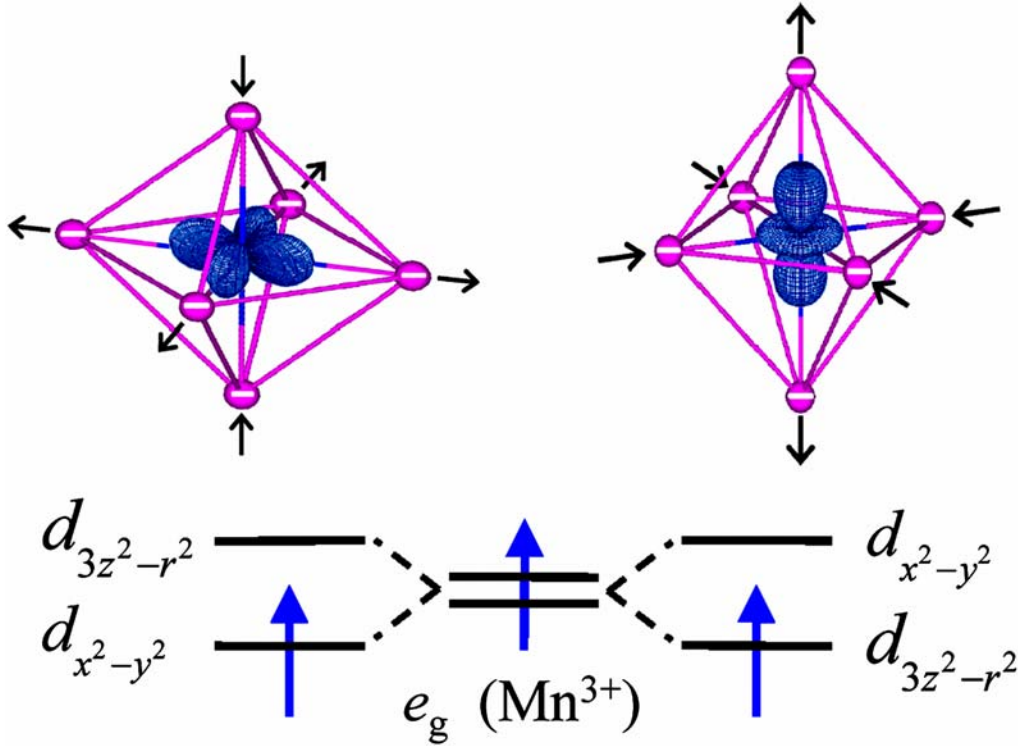


Figure 2.7: Effect of the JT distortion on the electronic structure of Mn^{3+} e_g states.

resulting various JT distortion modes lead to different electronic structures for the e_g states of Mn^{3+} ions as exemplified in figure 2.7. A quantitative measure of the magnitude of cooperative JT distortion is given by the octahedral distortion parameter Δ defined as:

$$\Delta = \left(\frac{1}{6} \right) \sum_{n=1,6} \left[\frac{(d_n - \langle d \rangle)^2}{\langle d \rangle} \right], \quad (2.3)$$

where $\langle d \rangle$ and d_n are the mean Mn-O bond length and the six Mn-O bond lengths along six different directions, respectively. The detailed bond lengths of a certain manganite can be obtained via a Rietveld structure determination by refining the high-resolution neutron and/or x-ray powder diffraction data.

Note that the Mn^{4+} ($3d^3$) ion (non-Kramer's ion) does not show the JT effect, since a net lowering of the electronic energy cannot be achieved with a preservation of the gravity center for all filled t_{2g} states in octahedral geometry. Therefore, a high concentration of Mn^{3+} ions tends to promote the distortions of MnO_6 octahedra, while the high concentration of Mn^{4+} will discourage such distortions. The $\text{Mn}^{3+}/\text{Mn}^{4+}$ ratio can be modified by different doping levels.

The JT effect naturally couples the magnetic, electron orbital and lattice degrees of freedom, thus playing significant roles in affecting the orbital degeneracy and governing the electronic properties of manganites, e.g. charge and orbital ordering, ferromagnetism, phase separation, the CMR effect, etc [65, 66].

2.2.4 Relative interactions

2.2.4.1 Orbital degeneracy versus crystal field

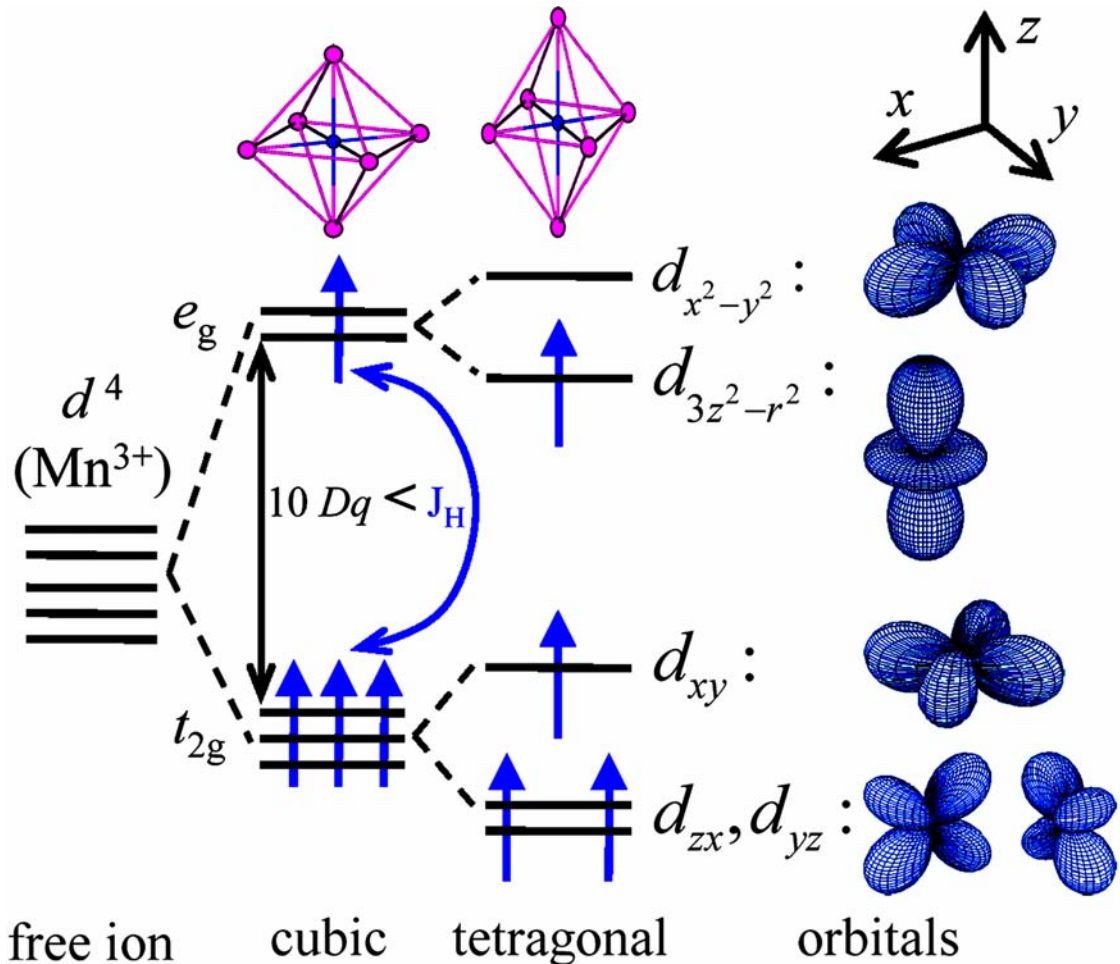


Figure 2.8: Crystal field splitting of fivefold degenerate d orbitals of $3d^4$ free ions (Mn^{3+}) in octahedral geometry as well as the corresponding approximate orbital shapes in real space. Since the crystal field splitting ($10 Dq \sim 1$ eV [67, 68]) is smaller than the Hund's coupling ($J_H \sim 2-3$ eV [69, 70]), the e_g spin is aligned to the t_{2g} spins, realizing a high-spin state.

The outer $3d^n$ shell of the TM ions in most cases is only partially filled ($n_{\max} = 2 \times (2l + 1) = 10$). The orbital degeneracy makes electronic structures more complicated and produces the orbital degrees of freedom whose importance has been realized in controlling the interesting properties of CTMO [71].

The possibilities of the degeneracy of d orbitals and the corresponding five wave functions, taking Mn^{3+} ions with four d -electrons ($e_g^1 t_{2g}^3$) in a high-spin state as one example, are illustrated in figure 2.8. The $3d$ states of free TM ions are fivefold degenerate. In perovskite manganites, the Mn ions are located in the centre of MnO_6 octahedra, surrounded by the six nearest-neighbor oxygen ions. The highly symmetric

ideal structure of cubic symmetry exhibits MnO_6 octahedra with six equal Mn-O bonds, generating a cubic crystal environment for Mn ions. In this case, the d -level splits in twofold degenerate e_g and threefold degenerate t_{2g} levels. In an octahedral environment, the e_g orbitals ($d_{x^2-y^2}$ and $d_{3z^2-r^2}$) occupy the higher energy states, while the t_{2g} orbitals (d_{xy} , d_{zx} and d_{yz}) occupy the lower energy state [72, 73]. The electron density distribution of the two e_g states points towards the negative charges of oxygen ions as shown in the top of figure 2.7 such that the single e_g electron of Mn^{3+} ions has a higher energy due to the Coulomb repulsion. As for the threefold t_{2g} states, they extend between negative charges, thus leading to a lower energy. As a consequence, the fivefold degeneracy is partly lifted in a cubic crystal environment. The two e_g orbitals have much larger overlap with the $2p$ orbitals of neighboring oxygen ions than the three t_{2g} orbitals; therefore, the e_g orbitals are σ -bonding and the t_{2g} orbitals are π -bonding. All electrons in d orbitals are subject to strong electronic repulsion effects so that they tend to be localized in stoichiometric LaMnO_3 , forming an insulating state. In the case of hole-doping, Mn^{4+} ions will be created. As a result, e_g electrons can hop between neighboring sites and begin to become itinerant, leading to conductivity. In contrast, the three t_{2g} electrons tend to be tightly localized by the strong electron-electron repulsion even in a metallic state. If the MnO_6 octahedra are distorted into the ones with unequal Mn-O bonds, e.g. due to the cooperative JT distortion, the resulting tetragonal crystal environment will further remove the twofold e_g degeneracy. In the case of figure 2.8, the tetragonal MnO_6 octahedron has two longer Mn-O bonds along the crystalline z axis and four shorter ones in the xy plane. This crystal environment results in two different energy levels for the two $d_{x^2-y^2}$ and $d_{3z^2-r^2}$ orbitals as shown in figure 2.8. Therefore the single e_g electron occupies the lower-energy $d_{3z^2-r^2}$ orbital.

According to the JT theorem [74, 75], in the ground state, a local degeneracy cannot occur: a degenerate state is unstable with respect to external perturbations. Therefore, the orbital degeneracy will always be lifted and the ground state will be characterized by one particular set of orbitals being occupied and the other orbitals being empty. The JT distortion is a very effective way to lift the orbital degeneracy in many CTMO. Distortions of different symmetries induce different orbital occupations and vice versa [76]. Unfortunately, the $3d$ orbital degeneracy and the electron filling as a function of the crystal field do not take into account the oxygen orbitals at all.

2.2.4.2 Double exchange

In order to explain the interesting phenomenon of magnetic field dependence of the resistivity in some manganites, a theoretical mechanism named double exchange was elaborated, based on the inter-site charge transfer with FM exchange interaction [41-43].

The single e_g electron of Mn^{3+} can hop to the unoccupied e_g orbitals of Mn^{4+} through an intervenor of O^{2-} ions as shown in figures 2.9(a) and (c). Since the $2p$ orbitals of O^{2-} ions are usually assumed to be fully filled ($2p^6$), the up hopping process has to be accomplished in two steps: one electron in the $2p$ orbitals of O^{2-} moves to the empty e_g orbitals of Mn^{4+} ; then the single e_g electron of Mn^{3+} transfers into the vacated oxygen $2p$ orbital. A concomitant of this process (double exchange) is the role exchange of valence

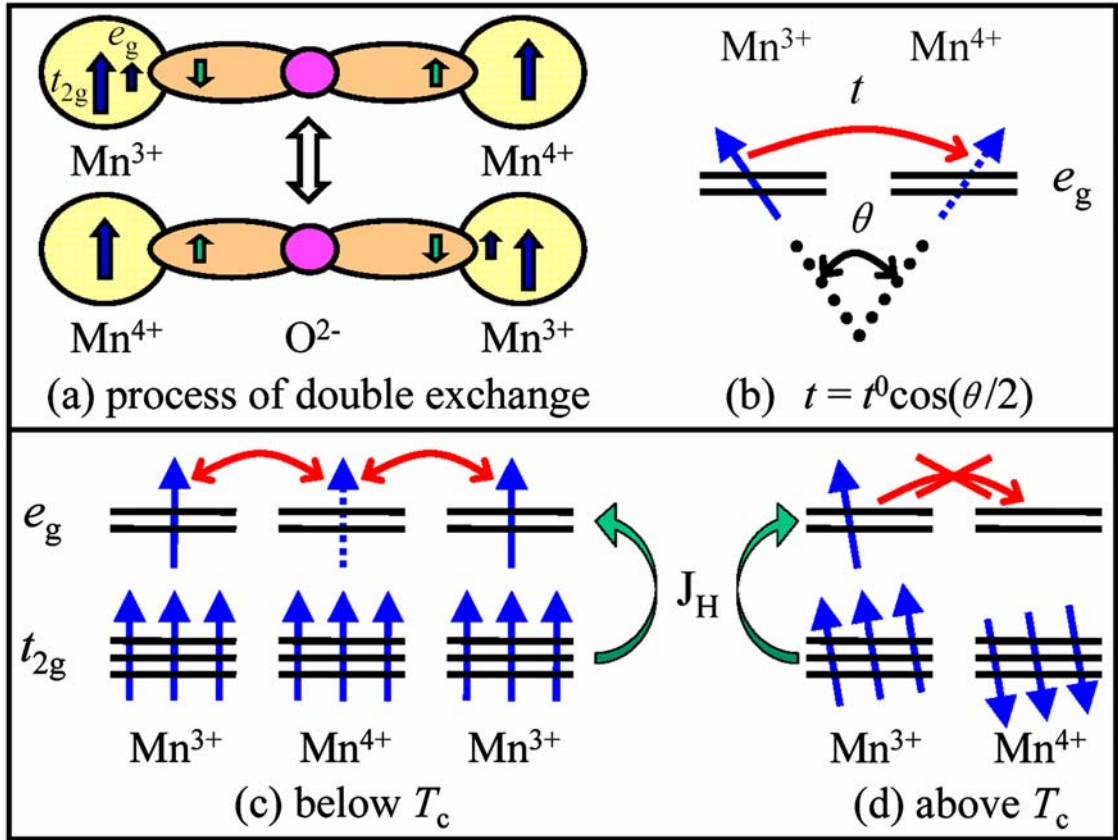


Figure 2.9: Illustration of the double exchange mechanism for Mn ions with different valencies (Mn^{3+} and Mn^{4+}). Here t is the hopping parameter of the e_g electron and J_H is the FM Hund's coupling between e_g and t_{2g} electrons.

states of Mn^{3+} and Mn^{4+} ions as shown in figure 2.9(a), consequently producing the mobile holes on the Mn sites.

In the case of the strong coupling limited with $J_H \gg t$, the inter-site hopping parameter t of the e_g electron between neighboring sites can be roughly evaluated by [42]:

$$t = t^0 \cos(\theta/2), \quad (2.4)$$

where θ is the relative angle between the neighboring spins and t^0 is the value when $\theta = 0^\circ$ as schematically illustrated in figure 2.9(b). Below the Curie temperature T_c , all spins of Mn^{3+} and Mn^{4+} ions have the same direction for the ideal ferromagnetism (figure 2.9(c)). This case maximizes the hopping kinetic energy of the conduction electrons ($\theta = 0^\circ$). Thus the single e_g electron of Mn^{3+} can hop back and forth between Mn^{3+} and Mn^{4+} ions via the oxygen $2p$ states. As a consequence, the FM metallic ground state emerges. When temperature is increased up to the ideal paramagnetic regime (figure 2.9(d)), all spins are completely disordered dynamically, which hampers electron hopping, producing the paramagnetic insulating (PMI) state. Yet at temperatures near T_c , the spins can be easily aligned by an applied magnetic field, more or less enhancing the effective electron hopping and thus decreasing the resistivity and as a result, the CMR effect emerges.

Therefore, the double exchange can only produce the FM interaction of e_g electrons

in some mixed-valence manganites at low temperatures. Based on the strong Hund's coupling and the double exchange mechanism, the CMR effect could be qualitatively but not quantitatively described [22-32]. The shortcoming of a pure double exchange mechanism is the absence of lattice and orbital degrees of freedom, superexchange interaction between the t_{2g} local spins, etc.

2.2.4.3 Superexchange

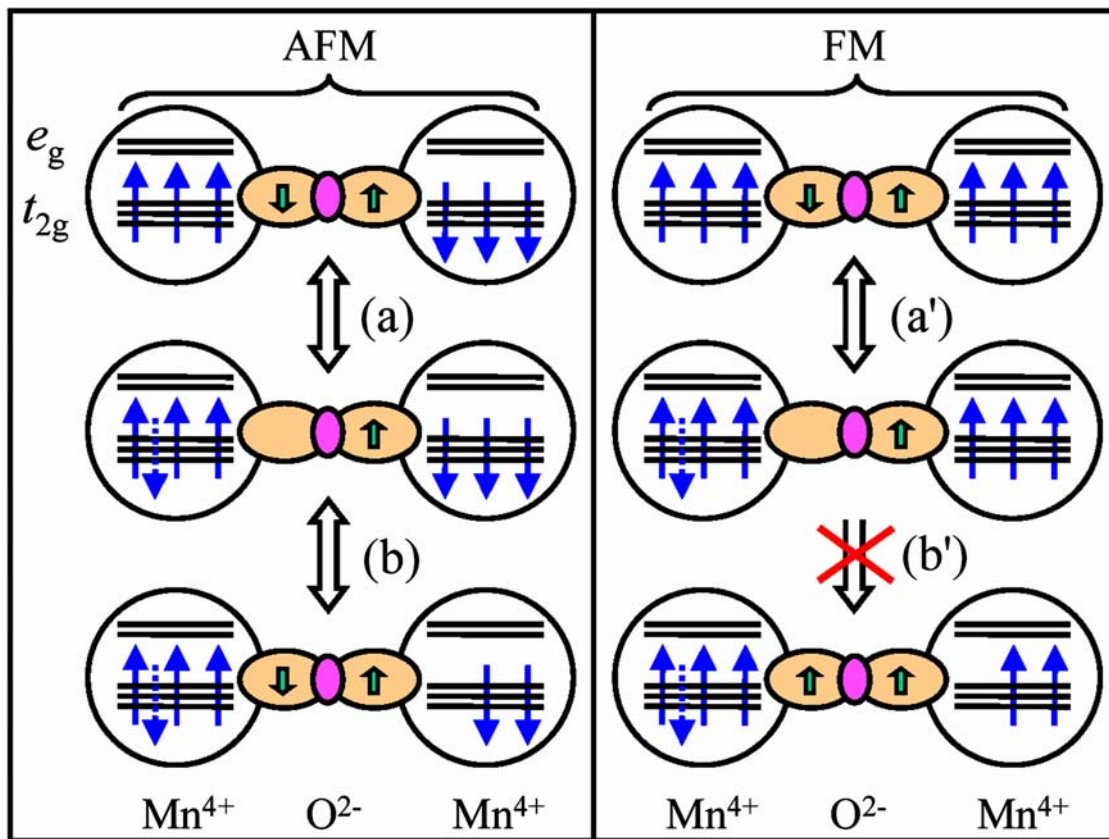


Figure 2.10: Illustration of the superexchange mechanism for Mn^{4+} ($3d^3: e_g^0 t_{2g}^3$) ions with the straight bonds. (left) Antiferromagnetism is indeed realized. (right) Ferromagnetism is rejected assuming non-orthogonal Mn^{4+} orbitals. It is stressed that the bottom configuration in the right is forbidden (see text).

In above discussion, the t_{2g} electrons are viewed as localized spins even in a metallic state. This is justified as the e_g electrons are the ones with highest energy and lie closest to the Fermi level. However, the t_{2g} electron can have overlap with the oxygen $2p$ -states, which can also give rise to the superexchange interaction. Unlike double exchange, this mechanism traditionally applies to the neighboring Mn ions with the same valency via intermediate O^{2-} ions, e.g. $\text{Mn}^{2+}-\text{O}^{2-}-\text{Mn}^{2+}$, $\text{Mn}^{3+}-\text{O}^{2-}-\text{Mn}^{3+}$ and $\text{Mn}^{4+}-\text{O}^{2-}-\text{Mn}^{4+}$.

As illustrated in the left of figure 2.10, the superexchange interaction between two

antiferromagnetically arranged Mn^{4+} ions proceeds through one oxygen $2p$ electron hopping to Mn^{4+} t_{2g} orbitals ((a)) and in order to keep the oxygen $2p$ shell filled, the remaining $2p$ electron makes direct exchange with the other adjacent Mn^{4+} ((b)). In contrast, if the ground state is FM for two Mn^{4+} ions, this direct exchange is forbidden by the Pauli principle as long as the Hamiltonian does not allow spin-flip processes ((b')) in the right of figure 2.10). Therefore the superexchange interaction results in the antiferromagnetic (AFM) coupling of Mn ions.

Furthermore, it turns out that the magnitude as well as the sign of superexchange interaction depends on the orbital character of the localized charge as described by the Goodenough-Kanamori-Anderson (GKA) rules [77-79], which was summarized in detail in [72]. In $\text{LaMn}^{3+}\text{O}_3$, the e_g electron occupies alternating $3d_{3x^2-r^2}$ and $3d_{3y^2-r^2}$ orbitals as shown in figure 2.12(D). This ordering forms MnO_2 planes of filled orbitals with a structural signature of alternating long and short Mn-O bonds, while orbitals perpendicular to the plane remain unoccupied. Superexchange within MnO_2 plane is between filled and empty orbitals thus giving a FM coupling. However, perpendicular to these MnO_2 planes, superexchange is between unoccupied orbitals and leads to AFM coupling [80].

The superexchange and double exchange are two particularly important indirect interactions of electrons via an intermediary in CTMO. Both effects are strongly dependent on the magnetic moments of Mn ions, the overlap integral between orbitals of Mn and O ions, and the Mn-O-Mn bond angle in manganites.

2.3 Complex ordering phenomena and electronic phase separation

With the strong correlation effect, electrons that normally localize on specific atomic sites in CTMO frequently exhibit cooperative electronic ordering phenomena, i.e. charge order, orbital order and spin order. These novel quantum collective behaviors are usually accompanied by concomitant structural, magnetic and metal-insulator phase transitions and so forth. Thus they are believed to play significant roles in controlling these fascinating physical properties. In the following, a short review of these ordering phenomena and electronic phase separation in CTMO is given.

2.3.1 Charge order

Charge order was first proposed by Eugene Wigner in the late 1930s. This concept was later applied to the Verwey transition that occurs in magnetite (Fe_3O_4) at 120 K [81]. For an incomplete doping with holes or electrons, the usual ionic picture of integer valencies leads to a mixed-valence state for most of the transition metals (TMs) such as Cu, Mn, Ni, Fe, etc. For example, in LaMnO_3 and CaMnO_3 , the Mn ion has a valency of +3 and +4, respectively; while in the synthesized $\text{La}_{1-x}\text{Ca}_x\text{MnO}_3$ (hole-doping of LaMnO_3) and $\text{Ca}_{1-x}\text{La}_x\text{MnO}_3$ (electron-doping of CaMnO_3), the Mn ion formally keeps both valence states and the ratio of $\text{Mn}^{3+}/\text{Mn}^{4+}$ depends on the doping level. The relative long-distance assembly chaining of TM ions with the same valency in this kind of mixed-valence

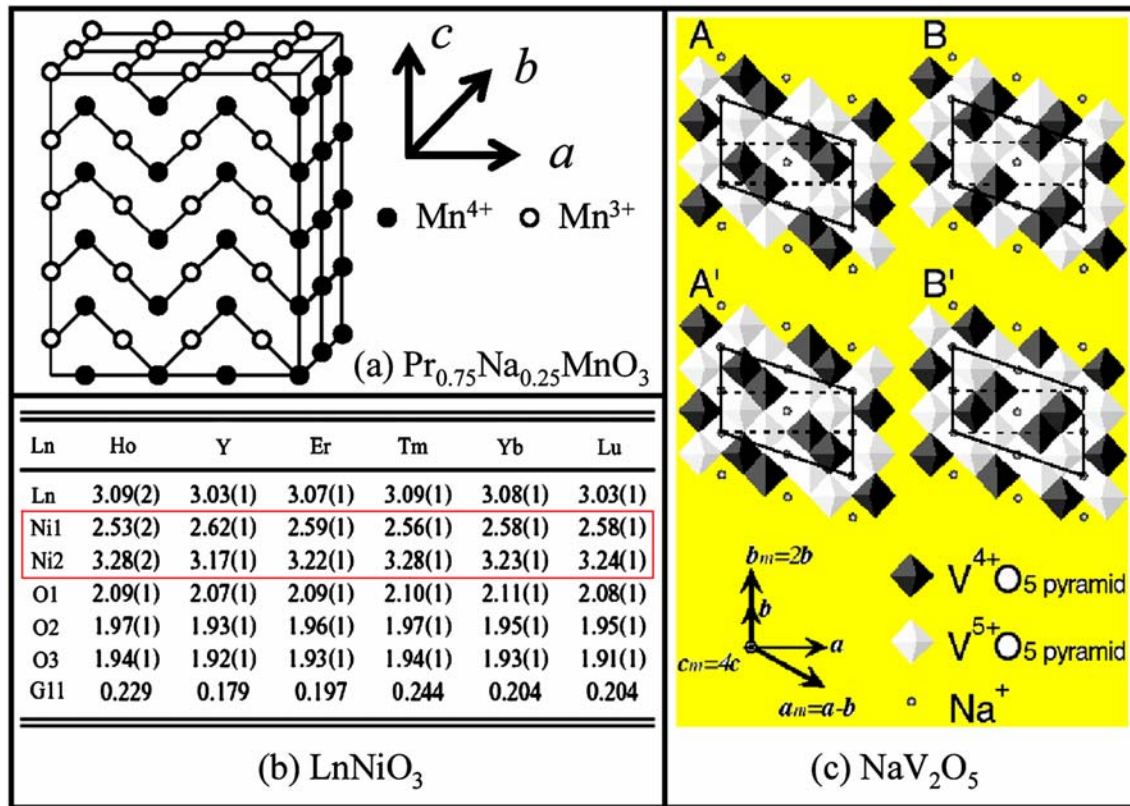


Figure 2.11: (a) Charge-ordered states in $\text{Pr}_{0.75}\text{Na}_{0.25}\text{MnO}_3$ below 220 K, where the Mn^{3+} and Mn^{4+} cations form zigzag chains in crystallographic a - c plane [82]. (b) Valencies determined from the bond valence model for Ln, Ni, and O within the LnO_8 and NiO_6 coordination polyhedra in LnNiO_3 [83]. (c) Zigzag-type charge-order pattern with respect to the configuration of V^{4+}O_5 (black) and V^{5+}O_5 (white) pyramids lying in the a - b plane [84, 85]. There are four types of possible in-plane configuration denoted as A, A', B and B'. Dotted and solid lines represent crystallographic unit cells: orthorhombic ($a \times b \times c$) above $T_c = 35$ K and monoclinic ($a_m \times b_m \times c_m$) below T_c [86].

compounds under certain conditions (doping level, temperature, etc) exhibits the valence states in distinct patterns, forming so-called charge order that can be also viewed as uniformly organized charge carriers. Charge order including all charge carriers of the conduction band leads to an insulating state. In contrast, the charge disorder, i.e. randomly distributing valence states, facilitates the carriers' mobility in favour of a metallic state. Therefore the charge disorder-order transition usually accompanies the metal-insulator transition. Charge order frequently occurs in mixed-valence perovskites, e.g. $\text{Pr}_{0.75}\text{Na}_{0.25}\text{MnO}_3$ (figure 2.11 (a)), half-doped manganites ($\text{La}_{0.5}\text{Ca}_{0.5}\text{MnO}_3$) and nickelates ($\text{La}_{2-x}\text{Sr}_x\text{NiO}_4$), and in self-doped NaV_2O_5 (figure 2.11 (c)), etc.

The description of charge order has been normally made in the frame of the ionic model with integer valencies. This model implies an electronic transfer of an integer number of electrons between two TM charge (oxidation) states in many oxides, the remaining electrons being fixed at the TM d -orbitals. However, this picture of

integer-valency state of TMs is being strongly challenged. For example, the charge difference between the two distinct Mn sites in $\text{Nd}_{0.5}\text{Sr}_{0.5}\text{MnO}_3$ is only 0.16 electrons in a resonant x-ray scattering (RXS) study [87]. This difference is a far cry from $3d^3$ and $3d^4$.

Some CTMO with single-valence TM ions, e.g. LnNiO_3 (Ln = rare-earth ions), CaFeO_3 and BaBiO_3 , etc, display CO state adopting the form of charge disproportionation. Rare-earth LnNiO_3 (Ln = Lu, Ho, Y, Nd, Pr, Sm, etc) perovskites have been investigated for many years [88], where Ni^{3+} ($e_g^1 t_{2g}^6$) has one e_g electron with orbital degeneracy. Most of LnNiO_3 (Ln \neq La) display a first-order metal-insulator transition accompanied by a structural transition from $Pbnm$ to $P2_1/n$ that yields two different crystallographic sites for Ni [89]. The metal-insulator transition temperature increases with decreasing size of the rare earth ion [90]. However, there is no evidence for orbital order in both x-ray and neutron powder diffraction studies in the sense of a cooperative JT distortion at the metal-insulator transition [88]. In addition, theoretical calculations have ruled out the possibility of the proposed OO pattern ($d_{x^2-y^2}$ and d_{z^2}) [91]. Therefore charge order is naturally suspected to be the key to the metal-insulator transition. Indeed, charge order disproportionation in the form of $\text{Ni}^{+3+\delta}-\text{Ni}^{+3-\delta}$ ($\delta \approx 0.3 e^-$) as shown in figure 2.11(b) has been invoked to be present in most of the small rare-earth LnNiO_3 on the basis of a bond valence analysis of the structure in the insulating state [83, 89]. Furthermore, the charge order $\text{Ni}^{+3+\delta}-\text{Ni}^{+3-\delta}$ with a quantitative value of $(\delta + \delta') = (0.45 \pm 0.04) e^-$ in an epitaxial NdNiO_3 film was first reported in a study by the RXS [92]. As open question remains whether the charge carriers go to the ligand oxygen to form bond CO or whether they remain disproportionated in the Ni ions. Recent theoretical calculations on LnNiO_3 perovskites could not provide a definitive answer and more experimental work is required [89, 93].

Sometimes the CO state can be melted by the applied magnetic field [94], or pressure [95], or exposure to x-ray photons [96] in favor of a FM metallic state [97]. With the JT defect alone, i.e. no cooperative JT-effect, the charge correlations are limited to a short range of 10-20 Å [80]. Near T_c , the FM alignment of spins by spontaneous flips or by the application of a magnetic field favors the double exchange and thus melts the short-range charge correlations, driving the insulator-to-metal transition and resulting in the coincident CMR effect [65].

In general, there are two methods to investigate the CO phenomenon: (i) The calculation of BVS's [98, 99] through precisely determined crystallographic bond lengths. The prerequisite of the successful application of this method is the precise quantitative determination of structural parameters, especially the accurate determinations of space group and related bond lengths. The lower crystal symmetry usually permits more distinct crystallographic sites for relevant TMs, which makes it possible to study charge order by the BVS's method. Otherwise, the BVS's method allows one to only determine the averaged formal valence state (only one crystallographic site). (ii) Charge order can be viewed as self-organization of charge carriers in a superstructure. Therefore resonant (also called anomalous) x-ray scattering has been widely used to investigate the different CO patterns by probing possible superstructure reflections near the absorption edge of relevant atomic species [100]. While the BVS's method gives only indirect evidence for CO, RXS allows one to observe CO directly.

2.3.2 Orbital order

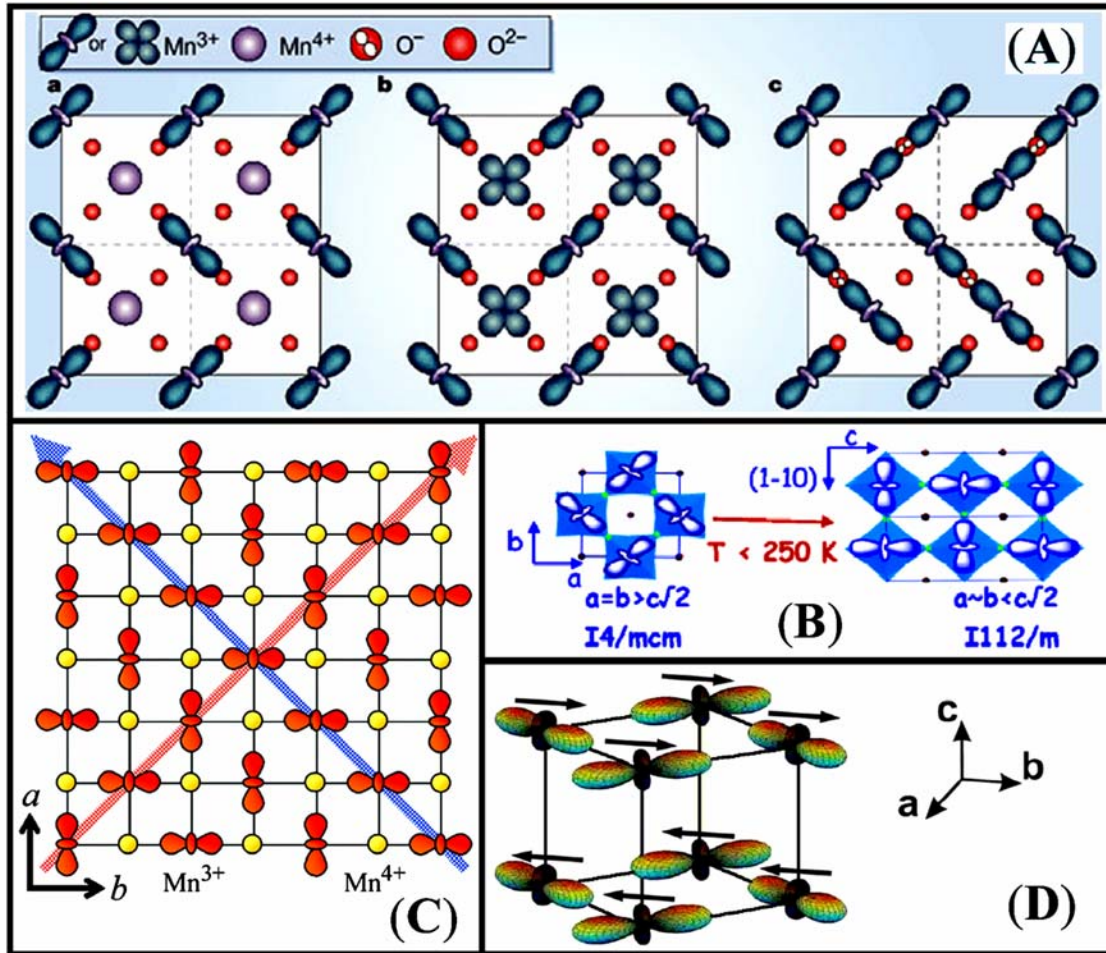


Figure 2.12: (A) $\text{La}_{0.5}\text{Ca}_{0.5}\text{MnO}_3$: the checkerboard charge order originally proposed by Goodenough [77] for Mn^{3+} and Mn^{4+} ions (a), in which the oxygen $2p$ shells are fully filled; CE-type orbital order for two distinct Mn^{3+} sublattices [101], one of which corresponds to $3d_{3x^2-r^2/3y^2-r^2}$ orbitals and another to the $3d_{x^2-y^2}$ orbital (b). This pattern implies that there is incomplete occupancy of the oxygen $2p$ shell; the ordered arrangement of O^- ions between Mn^{3+} pairs in the Zener polaron model (c), suggesting the invalidation of the traditional $\text{Mn}^{3+}/\text{Mn}^{4+}$ CO pattern [16, 102, 103]. Three patterns are projected on the MnO_2 sheet (a - b plane). (B) KCrF_3 : $3d_{z^2}$ OO schemes in different structures [104]. (C) $\text{Pr}_{0.5}\text{Ca}_{0.5}\text{MnO}_3$: orbital order $3d_{3x^2-r^2/3y^2-r^2}$ and charge order of the CE type projected on the MnO_2 sheet (a - b plane) [71]. (D) LaMnO_3 : orbital order $3d_{3x^2-r^2/3y^2-r^2}$ and A-type AFM spin order [105].

As described already, the orbital degeneracy (chapter 2.2.4.1) produces a rich structure of low-energy excitations through quantum orbital fluctuation and OO. In CTMO, preferential occupation of specific d orbitals on the TM ion can lead to the development of a long-range ordered pattern of occupied orbitals. This phenomenon, referred to as

orbital order, is usually observed indirectly from the cooperative JT distortions that result as a consequence of the orbital order [106] and vice versa. For example, the JT distortion happens to Mn^{3+} ions in undoped parent compound LaMnO_3 below 750 K and simultaneously the corresponding orbital order appears as shown in figure 2.12 (D). The half-doped $\text{La}_{0.5}\text{Ca}_{0.5}\text{MnO}_3$ undergoes two phase transitions upon cooling: the first is the FM metallic state at about 220 K; the second is the AFM insulating state at about 160 K. At the second transition, the single e_g electron of Mn^{3+} can occupy one of the two e_g orbitals due to the JT effect, forming an OO pattern as shown in figure 2.12 (A). Many TM ions, e.g. Cu^{2+} ($3d^9$), low-spin Ni^{3+} ($3d^7$), etc, display the JT effect. Orbital order can also be observed in materials with partially filled threefold degenerate t_{2g} -levels of some TM ions such as Ti^{3+} ($3d^1$) or V^{3+} ($3d^2$). The JT effect in these materials is relatively weaker than that in those with e_g orbitals. Besides the JT effect, another mechanism to generate orbital order is the virtual electron hopping between neighboring sites.

An important ordering configuration occasionally emerging in manganese oxides is the *CE* type, in which the orbital order and charge order occurs simultaneously. The most prototypical case is shown in figure 2.12 (C). The *CE*-type charge/orbital pattern is normally realized in half-doped manganites, e.g. $\text{Pr}_{0.5}\text{Ca}_{0.5}\text{MnO}_3$ [107]. In the pseudo cubic perovskite, the *a-b* planes are coupled antiferromagnetically while keeping the same in-plane charge and orbital pattern [71].

The ternary fluoride KCrF_3 has a similar formula with LaMnO_3 , however, one recent study [104] by high-resolution synchrotron x-ray powder diffraction has revealed that the two compounds have strikingly different structures. At 295 K, KCrF_3 has a tetragonal $I4/mcm$ structure. The CrF_6 octahedra are strongly axially distorted, comprising short Cr-F bonds along the *c*-axis and alternating long and short Cr-F bonds in the *a-b* plane with the octahedral distortion parameter $\Delta = 46.2 \times 10^{-4}$. This leads to an antiferrodistortive ordering of the $3d_{3x^2-r^2}$ and $3d_{3y^2-r^2}$ orbitals in the *a-b* plane as shown in figure 2.12 (B). However, upon cooling below 250 K, KCrF_3 shows a phase transition to a monoclinic $I112/m$ structure with an increase in Δ to 60.5×10^{-4} at 150 K, leading to $3d_{z^2}$ OO patterns in the plane defined by the *c*-axis and the $\langle 1-10 \rangle$ base diagonal (figure 2.12 (B)). It will be intriguing to explore within this family of fluorides the synthesis of $\text{Cr}^{2+/3+}$ structural and electronic analogues of the CMR $\text{Mn}^{3+/4+}$ oxides, especially as the monoclinic structure of KCrF_3 can support charge and orbital ordering [104]. It is also interesting to probe the ordering phenomena in this family utilizing the RXS technique.

Orbital order and its fluctuations strongly influence the magnetic correlations and the magnetic (spin) ordering through complex spin-orbital superexchange interactions, as is evident from the GKA [77-79] rules.

2.3.3 Spin order

The strong coupling of spin, charge, orbital and lattice degrees of freedom results in diverse long-range magnetic spin ordering phenomena in CTMO. Most of them can be well explained based on the double-exchange and superexchange interactions as well as the interplay between them. Some frequent spin-order types are schematically shown in figure 2.13.

In CTMO, the strength of spin interactions is strongly dependent on the doping level

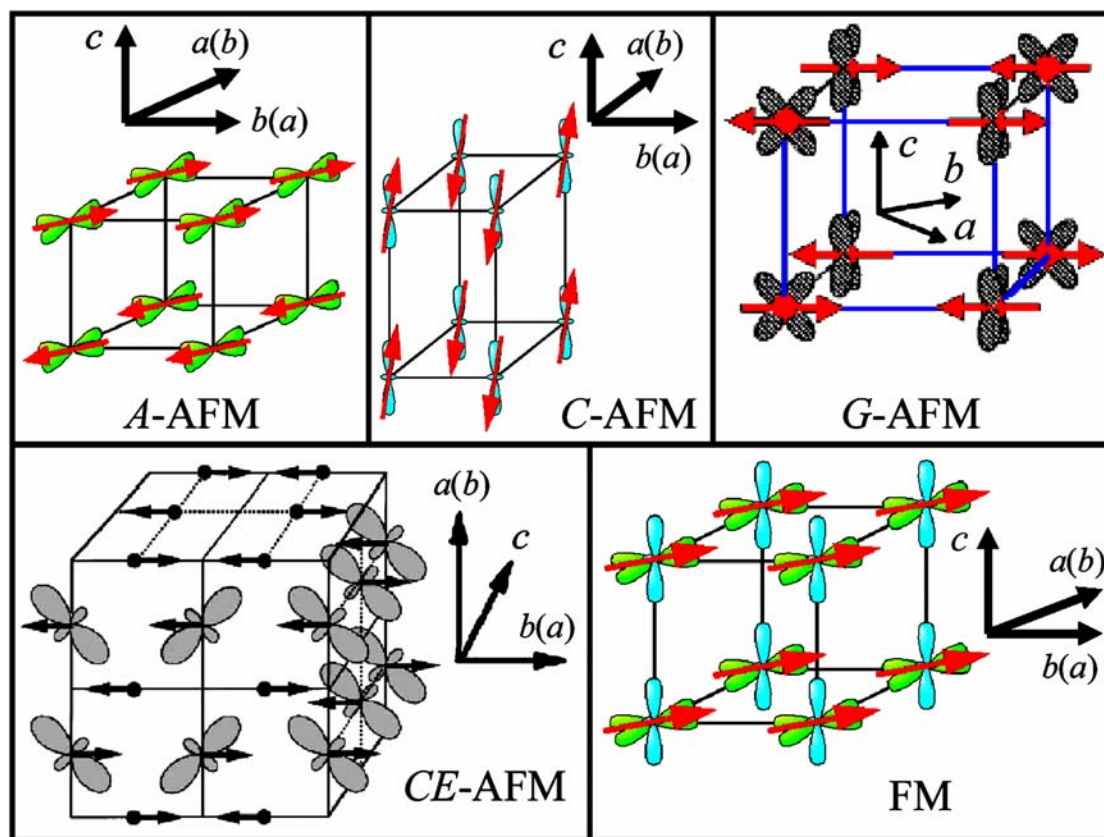


Figure 2.13: Spin order in $\text{Nd}_{1-x}\text{Sr}_x\text{MnO}_3$ at room temperature: ferromagnetic (FM) ($0.3 < x < 0.5$), *A*-type antiferromagnetic (*A*-AFM) ($0.5 < x < 0.7$) and *C*-type antiferromagnetic (*C*-AFM) ($x > 0.7$) [71]. *G*-type antiferromagnetic (*G*-AFM) spin order in YVO_3 below 77 K [108]. *CE*-type antiferromagnetic (*CE*-AFM) spin order in most of the half-doped manganites [27].

and temperature. At room temperature, $\text{Nd}_{1-x}\text{Sr}_x\text{MnO}_3$ shows the FM state for $0.3 < x < 0.5$. When doped further, the compounds show the *A*-type AFM state for $0.5 < x < 0.7$. When doping level is above 0.7, the *C*-type AFM state appears [27, 109]. Above 77 K, YVO_3 shows *C*-type AFM spin order, followed by a transition to the *G*-type AFM below 77 K [108].

The partially filled $3d$ level in CTMO can display both a localized orbital and spin moment, which in general are strongly coupled through the superexchange interaction. In the case of orbital degeneracy, the coupling concerns not only the spins, but also the orbitals at neighboring sites. Actually, this can be described by the GKA [77-79] rules: if the orbitals of two electrons directly overlap, the exchange between the two electrons is strong and AFM; otherwise, the exchange is weak and FM. The strength of superexchange interaction strongly depends on the angle of the bond of TM ion-intermediate ligand (oxygen in CTMO)-TM ion. For example, the 180° superexchange concerning two $3d e_g$ orbitals connected by an oxygen $2p$ orbital is strongly AFM; if the angle gets close to 90° , the strength of superexchange interaction decreases largely; at 90° , the exchange is much weaker and FM.

2.3.4 Electronic phase separation

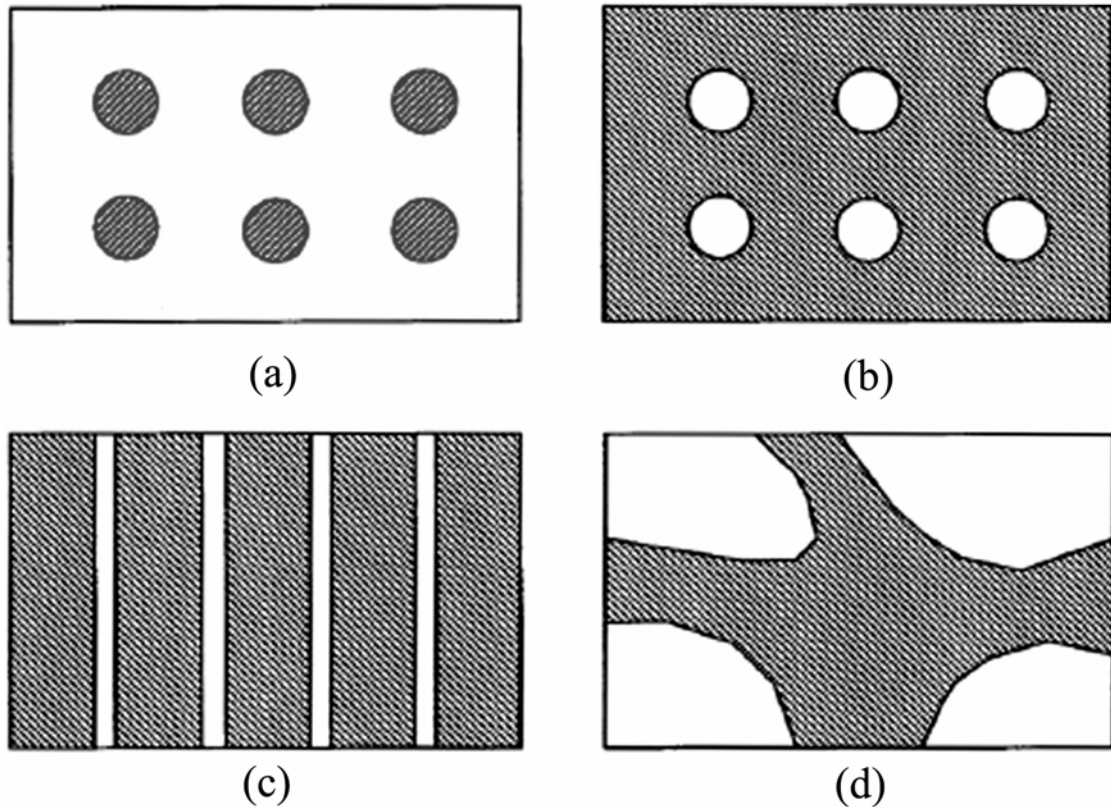


Figure 2.14: Schematic of the electronic phase separation [110]. Shaded portions indicate FM metallic regions; the unshaded portions correspond to AFM insulating regions. (a) FM metallic puddles in an insulating AFM background. (b) Metallic regions with insulating droplets. (c) Charged stripes. (d) Phase separation on the mesoscopic scale.

An amazing phenomenon in certain manganites, often regarded as electronic phase separation, is that multiple phases of different electronic and magnetic properties can coexist within a single, apparently structurally and chemically pure phase. For example, FM regions can be embedded in an AFM insulating background in some manganites. The more interesting aspect in phase separation picture is the scale of the inhomogeneities, varying from nanometers up to even microns as shown in figure 2.14 [110]. Furthermore, these inhomogeneities are in some cases static, while in others they can be strongly affected by a change in temperature [111], magnetic fields [112], etc.

One example of electronic phase separation is the half-doped $\text{Nd}_{0.5}\text{Sr}_{0.5}\text{MnO}_3$ [111]. This material first becomes FM at 250 K, partially transforming to an *A*-type AFM phase around 220 K, followed by a transformation of a substantial fraction to a *CE*-type AFM spin order around 150 K. There exists a complex spatial arrangement of simultaneous ordering of spins, orbitals and charge carriers [27]. The electronic inhomogeneities are currently believed to be largely responsible for the CMR effect in manganites. However, the theoretical understanding of this phenomenon is far from complete. Only one definitive point has been learned that CTMO are intrinsically inhomogeneous on the

nanoscale, owing to strong electronic correlations [110].

The electronic phase separation, depending on the length scale, can be directly probed by neutron and x-ray scattering, transmission electron microscopy, etc. Indirect evidences can be obtained by the magnetization and transport measurements as demonstrated in [113].

The spin-charge-orbital-lattice coupled systems in CTMO offer the most fascinating and challenging arena to test many theoretical ideas, including quantum liquid, solid, and liquid-crystal states [71]. However, the belief of integer $3d$ configurations in ordered states of mixed-valence oxides has been strongly challenged currently by some experiments according to which new theoretical models have been proposed, e.g. the Zener polaron model [16], in which pairs of Mn^{3+} cations share a hole on a bridging O ion. Indeed, the rigid ionic picture is just a starting point and the bonding electrons are shared in states that cannot be assigned solely to TM or oxygen [103].

These challenging ordering phenomena can be investigated by the powerful neutron and x-ray scattering techniques. The basic theories will be described in the next chapter.

Chapter 3

Experimental techniques

Understanding the basic physics and fundamental mechanisms that drive the anomalous macroscopic behavior revealed in CTMO is one of the biggest challenges at the frontier of condensed matter physics. The complementary x-ray and neutron probes (they also share many common characteristics) are the principal and powerful experimental techniques to accomplish this mission. These techniques have been extensively used to probe the structure of materials directly on the atomic scale by diffraction. The crystal and magnetic structures as well as the corresponding phase transitions can be determined from x-ray/neutron powder/single-crystal diffraction and the complex electronic ordering phenomena can be studied by searching the relevant superstructural reflections. The information provided by such experiments allows us to correlate macroscopic behaviours to microscopic origins, providing cogent experimental arguments and then finding the universal principles for establishing detailed theoretical models.

In this chapter, some fundamental aspects of experimental techniques used in this dissertation are described. Elementary scattering theory, atomic form factor and anomalous scattering factors for x-rays, and atomic and magnetic neutron scattering are introduced, followed by the description of the basic principles of powder diffraction and structure determination. The last part treats the resonant soft x-ray scattering.

3.1 Elementary scattering theory: elastic scattering

3.1.1 Scattering geometry and scattering cross section

The scattering experiment is schematically shown in figure 3.1(a). It is assumed that the size of the sample is much smaller than the distance between sample and source and the distance between sample and detector, respectively (Fraunhofer approximation). Thus the sample can be viewed as a ‘point’ object. With monochromatic radiation, the wave field incident on the sample can be considered as a plane wave, which is completely described by a wave vector \underline{k}_i . In the Fraunhofer approximation, the outcome of the interaction is derived by a new plane wave with the wave vector \underline{k}_f . If

$$k_i = |\underline{k}_i| = |\underline{k}_f| = k_f = 2\pi/\lambda, \quad (3.1)$$

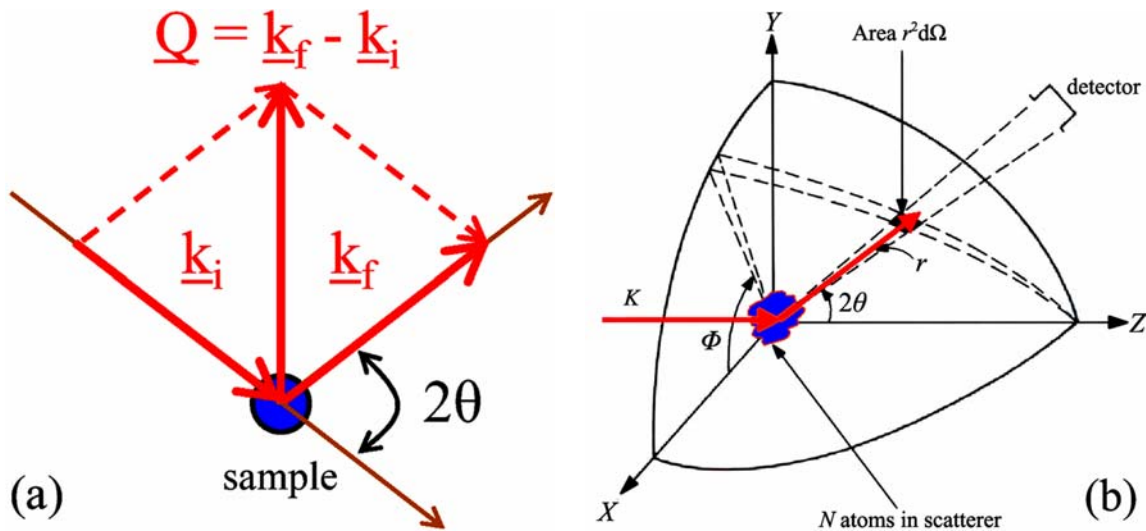


Figure 3.1: (a) A sketch of the scattering process in the Fraunhofer approximation in which the sample is viewed as a ‘point’ object due to the fact that the distance source-sample and sample-detector, respectively, is significantly larger than the size of the sample. (b) Geometry used for the definition of the scattering cross section taken from [14].

i.e. the incident and scattered waves have the same frequency and no energy loss or gain occurs, the interaction process is called elastic scattering. The scattering vector is defined as:

$$\underline{Q} = \underline{k}_f - \underline{k}_i, \quad (3.2)$$

where $Q = |\underline{Q}| = (4\pi \sin\theta)/\lambda$. $\hbar\underline{Q} = \hbar\underline{k}_f - \hbar\underline{k}_i = \underline{p}_f - \underline{p}_i$ represents the momentum transfer during scattering.

A scattering experiment comprises the measurement of the intensity distribution as a function of the scattering vector. The scattered intensity is proportional to the so-called cross section that can be schematically defined by figure 3.1(b) [14]. If n' particles are scattered per second into the solid angle $d\Omega$ seen by the detector under the scattering angle 2θ and into the energy interval between E' and $(E' + dE')$, then the so-called double differential cross section can be defined as:

$$\frac{d^2\sigma}{d\Omega dE'} = \frac{n'}{j d\Omega dE'}, \quad (3.3)$$

where j means the incident beam flux in terms of particles per area and time. If we are not interested in the change of the energy of the radiation during the scattering process, or if the detector is not able to resolve this energy change, then we will describe the angular dependence by the so-called differential cross section:

$$\frac{d\sigma}{d\Omega} = \int_0^\infty \frac{d^2\sigma}{d\Omega dE'} dE'. \quad (3.4)$$

Finally the so-called total scattering cross section gives us a measure for the total scattering probability independent of changes in energy and scattering angle:

$$\sigma = \int_{\Omega} \frac{d\sigma}{d\Omega} d\Omega. \quad (3.5)$$

3.1.2 Scattered intensity [14]

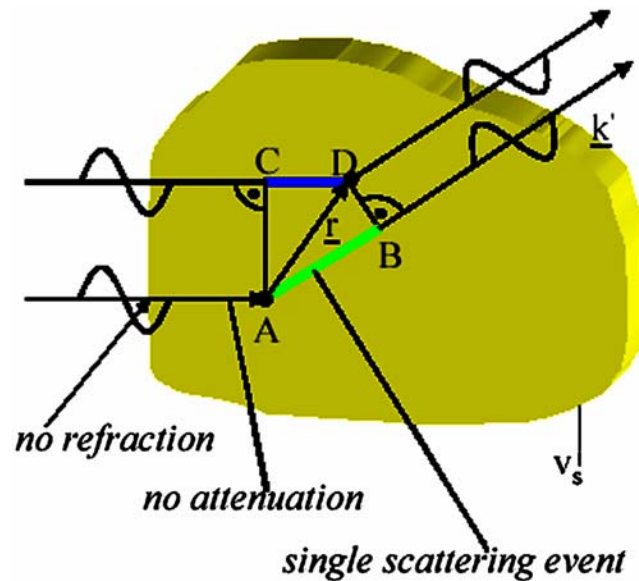


Figure 3.2: A sketch illustrating the phase difference between a beam scattered at the origin of the coordinate system and a beam scattered at the position \underline{r} taken from [14].

With the knowledge of the scattering cross section $d\sigma/d\Omega$, we can determine the arrangement of the atoms in the sample. The relationship between scattered intensity and the structure of the sample is described by the so-called Born approximation, which is often also referred to as kinematic scattering approximation. In this case, refraction of the beam entering and leaving the sample, multiple scattering events and the extinction of the primary beam due to scattering within the sample are being neglected.

Following figure 3.2, the phase difference between a wave scattered at the origin of the coordinate system and at position \underline{r} is given by:

$$\Delta\Phi = 2\pi \cdot \frac{(\overline{AB} - \overline{CD})}{\lambda} = \underline{k}' \cdot \underline{r} - \underline{k} \cdot \underline{r} = \underline{Q} \cdot \underline{r}. \quad (3.6)$$

The scattered amplitude at the position \underline{r} is proportional to the scattering power density, or simply scattering density $\rho_s(\underline{r})$. ρ_s depends on the type of radiation used and its interaction with the sample. Details refer to [14]. Assuming a laterally coherent beam, the total scattering amplitude is given by a coherent superposition of the scattering from all points

within the sample, i.e. by the integral:

$$A = A_0 \cdot \int_{V_s} \rho_s(\underline{r}) \cdot e^{i\mathbf{Q}\cdot\underline{r}} d^3\underline{r}, \quad (3.7)$$

where A_0 denotes the amplitude of the incident wave field. Equation 3.7 demonstrates that the scattered amplitude is connected with the scattering power density $\rho_s(\underline{r})$ by a simple Fourier transform. A knowledge of the scattering amplitude for all scattering vectors \underline{Q} allows us to determine via a Fourier transform the scattering power density uniquely. This is the complete information on the sample, which can be obtained by the scattering experiment. However, one problem is given by the fact that normally the amplitude of the scattered wave is not measurable. Instead only the scattered intensity

$$I \sim |A|^2 \quad (3.8)$$

can be determined. Therefore the phase information is lost and the simple reconstruction of the scattering density via a Fourier transform is no longer possible. This is the so-called phase problem of scattering. There are ways to overcome the phase problem, i.e. by the use of reference waves. Then the scattering density becomes directly accessible.

3.1.3 Pair correlation function [14]

Since the phase information is lost during the measurement of the intensity (equation 3.8), which information can be obtained from the intensity distribution of a scattering experiment?

Substituting equation 3.7 into 3.8, we obtain for the magnitude square of the scattering amplitude, a quantity directly accessible in a scattering experiment:

$$\begin{aligned} I \sim |A(\underline{Q})|^2 &\sim \int \rho_s(\underline{r}') \cdot e^{i\mathbf{Q}\cdot\underline{r}'} d^3\underline{r}' \int \rho_s^*(\underline{r}) \cdot e^{-i\mathbf{Q}\cdot\underline{r}} d^3\underline{r} \\ &= \iint \rho_s(\underline{r}') \rho_s^*(\underline{r}) \cdot e^{i\mathbf{Q}\cdot(\underline{r}'-\underline{r})} d^3\underline{r}' d^3\underline{r} = \iint \rho_s(\underline{R} + \underline{r}) \rho_s^*(\underline{r}) \cdot e^{i\mathbf{Q}\cdot\underline{R}} d^3\underline{R} d^3\underline{r}. \end{aligned} \quad (3.9)$$

This shows that the scattered intensity is proportional to the Fourier transform of a function $P(\underline{R})$:

$$I(\underline{Q}) \sim \int P(\underline{R}) \cdot e^{i\mathbf{Q}\cdot\underline{R}} d^3\underline{R}. \quad (3.10)$$

This function denotes the so-called Patterson function in crystallography or more general the static pair correlation function:

$$P(\underline{R}) = \int \rho_s^*(\underline{r}) \rho_s(\underline{r} + \underline{R}) d^3\underline{r}. \quad (3.11)$$

$P(\underline{R})$ correlates the value of the scattering power density at position \underline{r} with the value at the position $(\underline{r} + \underline{R})$, integrated over the entire sample volume. If, averaged over the sample,

no correlation exists between the values of the scattering power densities at position \underline{r} and $(\underline{r} + \underline{R})$, then the Patterson function $P(\underline{R})$ vanishes. If, however, a periodic arrangement of a pair of atoms exists in the sample with a difference vector \underline{R} between the positions, then the Patterson function will have an extremum for this vector \underline{R} . Thus the Patterson function reproduces all the vectors connecting one atom with another atom in a periodic arrangement.

3.1.4 Form-factor [14]

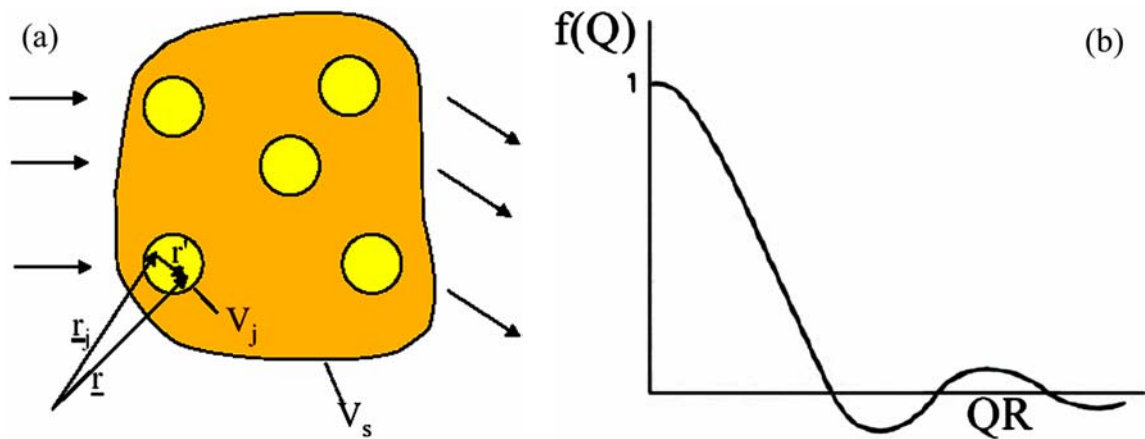


Figure 3.3 taken from [14]: (a) Sketch showing the assembly of N scatterers of finite size and defining the quantities needed for the introduction of the form factor. (b) Form-factor for a homogeneous sphere according to equation 3.15.

Figure 3.3(a) shows an assembly of N scatterers of finite size. These could be atoms in solid, or colloidal particles in a homogeneous solution. In the following, we will separate the interference effects from the scattering within one such particle from the interference effects arising from scattering from different particles. With the decomposition of the vector \underline{r} into the centre-of-gravity-vector \underline{r}_j and a vector \underline{r}' within the particle, the scattering amplitude can be written as:

$$A \propto \int_{V_s} \rho_s(\underline{r}) \cdot e^{i\underline{Q} \cdot \underline{r}} d^3 \underline{r} = \sum_{j=1}^N \int_{V_j} \rho_s(\underline{r}) \cdot e^{i\underline{Q} \cdot \underline{r}} d^3 \underline{r} = \sum_{j=1}^N e^{i\underline{Q} \cdot \underline{r}_j} \int_{V_j} \rho_s(\underline{r}') \cdot e^{i\underline{Q} \cdot \underline{r}'} d^3 \underline{r}' \quad (3.12)$$

$$\Rightarrow A \sim \sum_{j=1}^N A_j(0) \cdot f_j(\underline{Q}) \cdot e^{i\underline{Q} \cdot \underline{r}_j}.$$

The form-factor is defined as the normalized amplitude of scattering from within one particle:

$$f(|\underline{Q}|) = \frac{\int_{V_j} \rho_s(\underline{r}') \cdot e^{i\underline{Q} \cdot \underline{r}'} d^3 \underline{r}'}{\int_{V_j} \rho_s(\underline{r}') d^3 \underline{r}'} . \quad (3.13)$$

For a homogeneous sphere

$$\rho_s(\underline{r}) = \begin{cases} 0 & |\underline{r}| > R \\ 1 & |\underline{r}| \leq R \end{cases} \quad (3.14)$$

the form-factor can be calculated by using spherical co-ordinates:

$$f(|Q|) = 3 \cdot \frac{\sin(QR) - (QR) \cdot \cos(QR)}{(QR)^3} . \quad (3.15)$$

The function 3.15 is plotted in figure 3.3(b). The form-factor takes its maximum value of one. For finite scattering angles 2θ , the form-factor drops due to destructive interference from various parts within one particle and finally for large values of the momentum transfer shows damped oscillations around 0 as a function of $|Q|R$.

3.1.5 Bragg scattering from 3d periodic arrangements of atoms [14]

An example for the application of equations (3.7) and (3.8) is the scattering from a three dimensional lattice of point-like scatterers. This situation corresponds to the scattering of thermal neutrons from a single crystal. In the case of a Bravais lattice with one atom at the origin of the unit cell, we attribute a scattering power α to each atom. The single crystal is finite with N , M and P periods along the basis vectors \underline{a} , \underline{b} and \underline{c} . The scattering power density, which we have to use in (3.7) is a sum over δ -functions for all scattering centers:

$$\rho_s(\underline{r}) = \sum_{n=0}^{N-1} \sum_{m=0}^{M-1} \sum_{p=0}^{P-1} \alpha \cdot \delta[\underline{r} - (n \cdot \underline{a} + m \cdot \underline{b} + p \cdot \underline{c})] . \quad (3.16)$$

The scattering amplitude is calculated as a Fourier transform:

$$A(\underline{Q}) \sim \alpha \sum_{n=0}^{N-1} e^{in\underline{Q} \cdot \underline{a}} \sum_{m=0}^{M-1} e^{im\underline{Q} \cdot \underline{b}} \sum_{p=0}^{P-1} e^{ip\underline{Q} \cdot \underline{c}} . \quad (3.17)$$

Summing up the geometrical series, we obtain for the scattered intensity:

$$I(\underline{Q}) \sim |A(\underline{Q})|^2 = |\alpha|^2 \cdot \frac{\sin^2 \frac{1}{2} \underline{NQ} \cdot \underline{a}}{\sin^2 \frac{1}{2} \underline{Q} \cdot \underline{a}} \cdot \frac{\sin^2 \frac{1}{2} \underline{MQ} \cdot \underline{b}}{\sin^2 \frac{1}{2} \underline{Q} \cdot \underline{b}} \cdot \frac{\sin^2 \frac{1}{2} \underline{PQ} \cdot \underline{c}}{\sin^2 \frac{1}{2} \underline{Q} \cdot \underline{c}} . \quad (3.18)$$

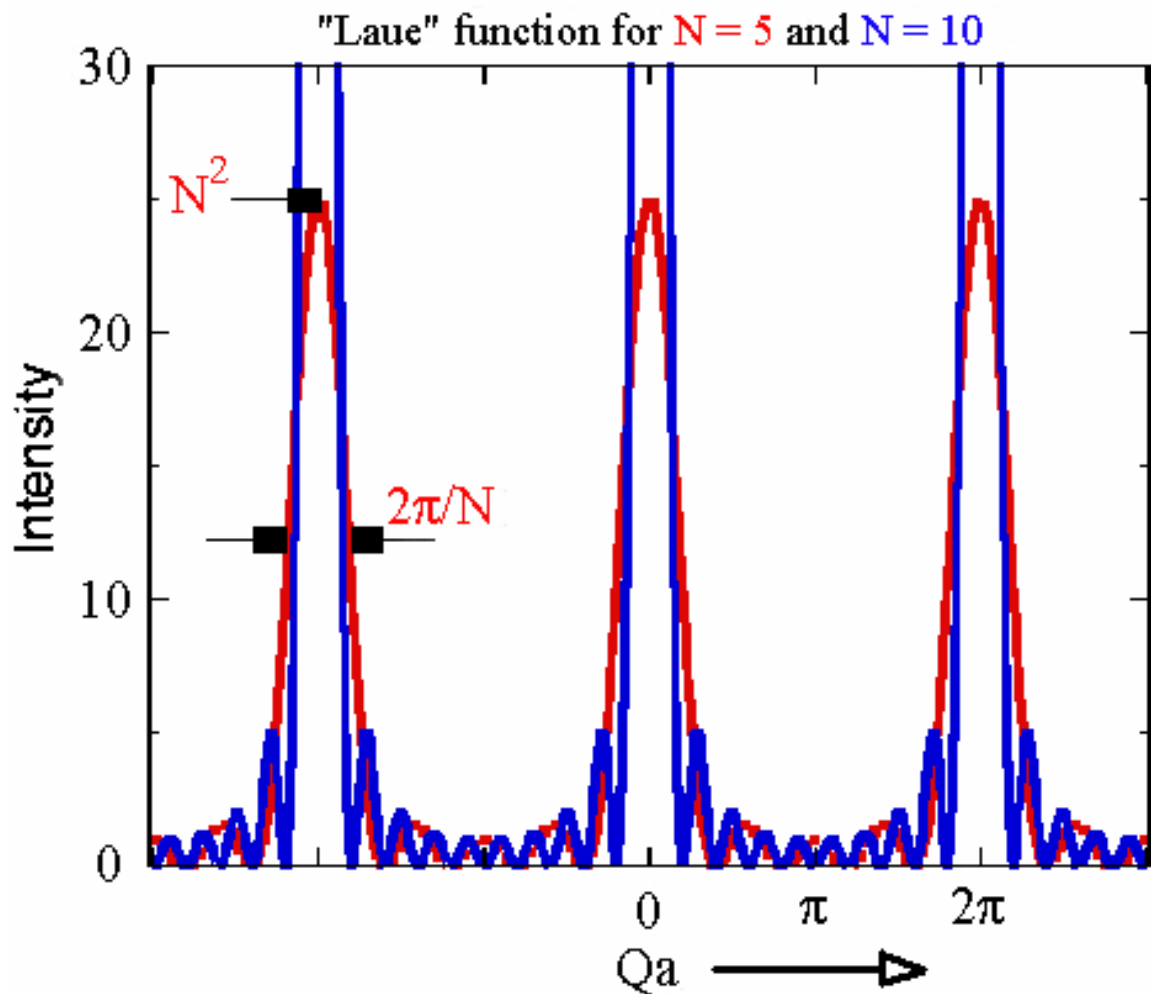


Figure 3.4 taken from [14]: Laue function along the lattice direction \underline{a} for a lattice with five and ten periods, respectively.

The dependence on the scattering vector \underline{Q} is given by the so-called Laue function, which separates according to the three directions in space. One factor along one lattice direction \underline{a} is plotted in figure 3.4.

The main maxima occur at the positions $Q = n \cdot 2\pi/a$. The maximum intensity scales with the square of the number of periods N^2 and the half width is given approximately by $\Delta Q = 2\pi/(N \cdot a)$. The more periods contribute to coherent scattering, the sharper and higher are the main peaks. Between the main peaks, there are $N-2$ site maxima. With increasing number of periods N , their intensity becomes rapidly negligible compared to the intensity of the main peaks. The main peaks are the well known Bragg reflections, which we obtain when scattering from a crystal lattice. From the position of these Bragg peaks in momentum space, the metric of the unit cell can be deduced (lattice constants a , b , c and unit cell angles α , β , γ). The width of the Bragg peaks is determined by the size of the coherently scattering volume (parameters N , M , and P) – and some other factors for real experiments (resolution, mosaic distribution, internal strain, ...).

3.2 Basics of x-ray and neutron scattering

3.2.1 Atomic form factor

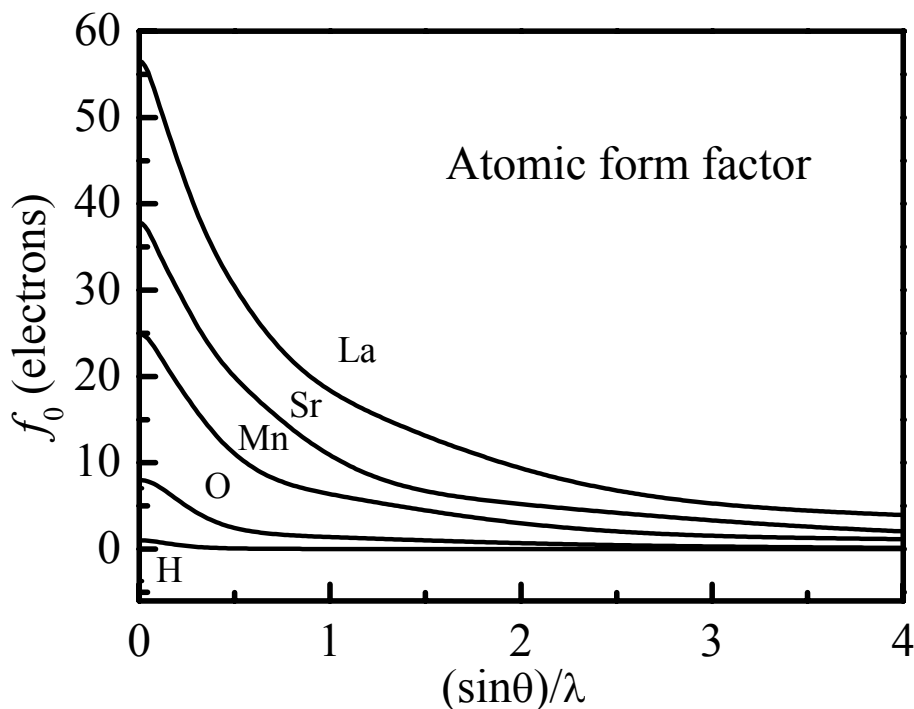


Figure 3.5: X-ray atomic form factors of La, Sr, Mn, O and H as a function of $(\sin\theta)/\lambda$ plotted in order from the top to the bottom.

The atomic form factor $f_0(\underline{Q})$, corresponding to the classic Thomson scattering, is nothing but the Fourier transform of the charge density $\rho(\underline{r})$ of an atom,

$$f_0(\underline{Q}) = \int_V \rho(\underline{r}) \cdot e^{i\underline{Q}\cdot\underline{r}} d\underline{r}. \quad (3.19)$$

This form factor is independent of the wavelength of radiation (if the radiation energy is far away from the absorption edges of concerned atoms) and only depends on the atom type.

For a practical calculation, the normal atomic form factor for x-rays as a function of Bragg angle can be represented by the following exponential function:

$$f_0[(\sin\theta)/\lambda] = c_0 + \sum_{i=1}^4 a_i \exp[(-b_i)(\sin\theta)/\lambda]. \quad (3.20)$$

Thus scattering factors of various chemical elements and ions can be expressed as functions of nine coefficients c_0, a_1-a_4, b_1-b_4 and $(\sin\theta)/\lambda$. All values for x-ray scattering

factors used in this dissertation were taken from *International Tables for X-ray Crystallography* (1999).

Figure 3.5 shows some x-ray atomic form factors f_0 as a function of $(\sin\theta)/\lambda$. For forward scattering of x-rays, full constructive interference is reached. Therefore at zero scattering angle, i.e. $(\sin\theta)/\lambda = 0$, the value of the atomic form factor of a given atom and the sum of the five coefficients ($c_0 + a_1 + a_2 + a_3 + a_4$) in equation 3.20 are both equal to the number of electrons (Z) in the atom, i.e. $f_0(0) = Z$, while $f_0(\infty) = 0$. With increasing $(\sin\theta)/\lambda$, the atomic form factor decreases because at higher scattering angles scattering from different parts of the electron cloud is no longer fully in phase. The heavier atoms (with more electrons) scatter x-rays more strongly than light atoms. Consequently, x-ray scattering is a poor choice for locating light atoms such as hydrogen atoms. In addition, the more extended the electron cloud, the more rapid is the decrease in the atomic form factor with scattering angle. No big contrast exists in the form factors of neutral atoms and ions at high scattering angles; therefore atomic form factors of neutral atoms are normally used in calculations.

3.2.2 Anomalous atomic scattering factor

The normal atomic form factor f_0 for x-rays is wavelength or photon energy (E) independent ($\lambda \approx 12.43/E$, λ in Å and E in keV), describing the contrast scattering ability of different atoms as a function of $(\sin\theta)/\lambda$ or scattering vector Q . This is only true for relatively short wavelengths. Most atoms scatter x-rays anomalously near their absorption edges and thus their scattering factors also depend on the photon energy. The origin of RXS is due to strong dispersion of the atomic scattering factor near an absorption edge of an atom [114]. Taking into account this anomalous scattering, the overall scattering factor of an element becomes complex and can be described by:

$$f(Q, E) = f_0(Q) + f_1(E) + if_2(E). \quad (3.21)$$

The two additional energy dependent terms, $f_1(E)$ and $f_2(E)$, are the real and imaginary components of the anomalous atomic scattering factor.

The anomalous scattering away from the absorption edges is usually at least an order of magnitude lower than the normal scattering at zero scattering angle (figures 3.6(a) and (c)). Thus the influence of anomalous scattering on normal x-ray diffraction is very small and can be neglected. Anomalous scattering is at its maximum when the photon energy is tuned to the corresponding absorption edge of an atom. As an example shown in figure 3.6, both f_1 and f_2 of a free Ni-atom near the Ni $L_{II, III}$ -edges (corresponding to the $2p \rightarrow 3d$ transition) are almost comparable to f_0 (at zero scattering angle), and are significantly larger than those near the Ni K -edge (corresponding to the $1s \rightarrow 4p$ transition). The two anomalous terms are dominated by electrons in the inner shells. These electrons are so spatially confined that the Q -dependence of f_1 and f_2 can be neglected.

The classical optical theorem states that the photoelectric absorption cross section is directly related to the imaginary part $f_2(E)$ in the forward direction (when $Q = 0$),

$$\sigma_{\text{abs}}(E) = (2r_0\lambda)f_2(E) \quad (3.22)$$

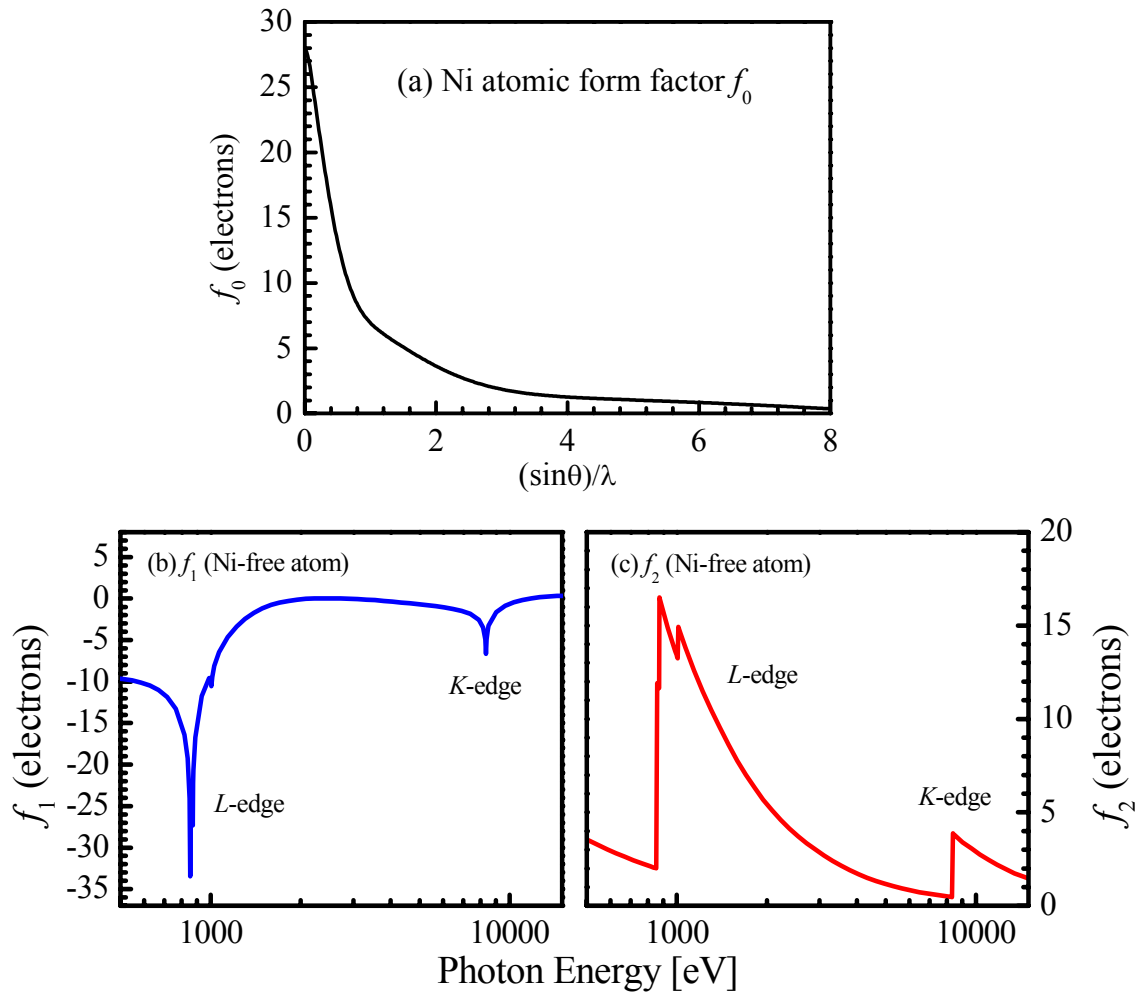


Figure 3.6: (a) X-ray atomic form factor of Ni. (b) and (c) The real (f_1) and imaginary (f_2) components of the anomalous atomic scattering factor of Ni for the free atom [115].

where r_0 is the classical electron radius (2.8×10^{-5} Å). The corresponding mass attenuation coefficient $\mu_m = \mu/\rho$ (μ : absorption coefficient of a material; ρ : density) is

$$\mu_m(E) = (2r_0\lambda \frac{N_A}{A})f_2(E), \quad (3.23)$$

where N_A/A is the number of atoms per gram. The mass attenuation coefficient $\mu_m(E)$ can be experimentally determined from the measurement of the attenuation of the incident beam I_0 after penetrating through a sample with the mass thickness $x = \rho l$ (mass per unit area) (l : thickness) in an x-ray absorption experiment,

$$\frac{I}{I_0} = e^{-\mu l} = e^{-\mu_m x}. \quad (3.24)$$

Consequently, $f_2(E)$ can be obtained from equation 3.23. After the determination of f_2 through absorption studies, the real part f_1 can be relatively precisely calculated using the Kramers-Kronig equation [114]

$$f_1(E) = \frac{2}{\pi} \int_0^{+\infty} \frac{E' f_2(E')}{(E^2 - E'^2)} dE'. \quad (3.25)$$

The anomalous scattering effect is important in determining the absolute configuration of a structure. This effect has been widely applied to investigate the complex ordering phenomena in CTMO.

3.2.3 Neutron scattering length

Whereas x-ray scattering studies rely on the electron densities and electronic states, neutrons are scattered from the nuclei ($\sim 10^{-15}$ m). The wavelength of thermal neutrons (around $\lambda_n = h(2Em_n)^{-1/2} = 1.8$ Å) is much larger than the nuclear radius, which makes the nuclei point-like scatterers. The scattering process may be described by the scattering length $b = b_1 + ib_2$, where b_1 describes scattering and b_2 is the absorption part. For thermal neutrons the so-called *Fermi-pseudo-potential* of a single nucleus is:

$$V(\underline{r}) = \frac{2\pi\hbar^2}{m_n} b\delta(\underline{r} - \underline{R}). \quad (3.26)$$

The scattering length b has been measured as a function of neutron energy. For thermal and lower energies the real part of this scattering length is a constant in the magnitude of femtometer (1 fm = 10^{-15} m). The neutron scattering power by nuclei is thus independent of the scattering angle. Neutron scattering has a unique advantage that makes it possible to observe some light elements, e.g. hydrogen and oxygen, even in the presence of heavier ones due to the contrasts in neutron scattering lengths of elements.

The neutron scattering lengths depend on the strong nucleus-neutron interactions and vary apparently random across the periodic table. They can have positive and negative values, while most of them are positive. Negative values result from resonant scattering where the neutrons penetrate the nuclei and create a compound nucleus, and the emitted neutrons have no phase shift, while the positive values indicate a potential scattering with a π phase shift between the incoming and scattered waves. Even the isotopes of some elements have different neutron scattering lengths, as is the case of hydrogen. Neutron scattering is a versatile probe for investigating not only the crystal structures, but also the dynamics.

3.2.4 Magnetic neutron scattering

Neutrons possess a spin ($S = 1/2$) and a magnetic moment ($\mu_n = \gamma_n \mu_N$; $\gamma_n = -1.91304275(45)$ μ_N ; $\mu_N = 5.05 \times 10^{-27}$ J/T) which can interact with the magnetic field of any unpaired

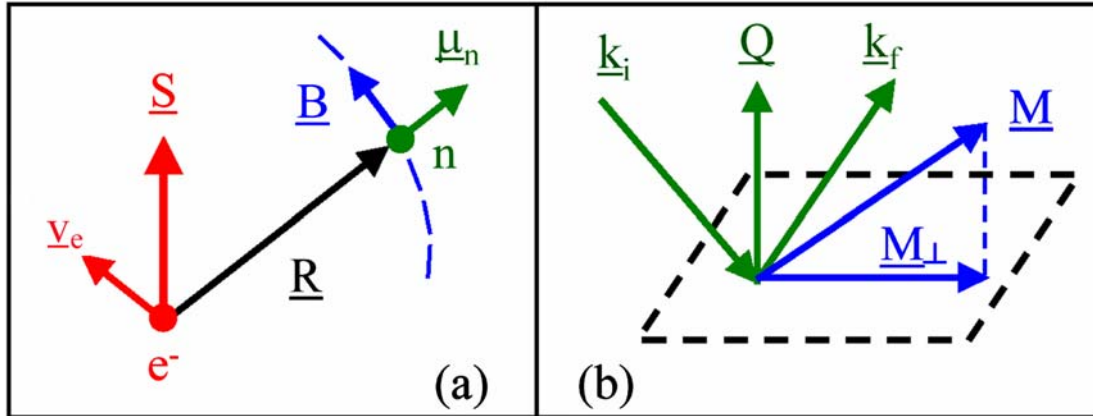


Figure 3.7: (a) Geometry for the derivation of the interaction between neutron and electron. (b) Scattering geometry for the magnetic neutron scattering, only the component \underline{M}_\perp of the magnetization \underline{M} perpendicular to the scattering vector \underline{Q} is of relevance.

electrons in a sample leading to strong magnetic scattering. The scattering process is sensitive to the magnitude and orientation of magnetic moments resulting from the spatial distribution of the electrons. Therefore, magnetic neutron scattering is a unique tool to solve magnetic structures and determine magnetic excitations and fluctuations.

As shown in figure 3.7(a), an electron e^- with spin \underline{S} , moving with a velocity \underline{v}_e , produces a magnetic field \underline{B} at position \underline{R} . This magnetic field interacts with the magnetic dipole moment $\underline{\mu}_n$ of the neutron (n) according to:

$$V_m = -\underline{\mu}_n \cdot \underline{B}. \quad (3.27)$$

The magnetic field \underline{B} arises from a spin (\underline{B}_S) and an orbital part (\underline{B}_L). They are given by:

$$\underline{B}_S = \nabla \times \left(\frac{\underline{\mu}_e \times \underline{R}}{R^3} \right), \quad \underline{\mu}_e = -2\mu_B \cdot \underline{S}; \quad (3.28)$$

$$\underline{B}_L = \frac{-e}{c} \frac{\underline{v}_e \times \underline{R}}{R^3}. \quad (3.29)$$

The magnetic scattering cross section for a process, where the neutron changes its wave vector from \underline{k}_i to \underline{k}_f and the projection of its spin moment to a quantization axis z from σ_z to σ'_z , can be expressed within the first Born approximation:

$$\frac{d\sigma}{d\Omega} = \left(\frac{m_n}{2\pi\hbar^2} \right)^2 \left| \langle \underline{k}_f \sigma'_z | V_m | \underline{k}_i \sigma_z \rangle \right|^2. \quad (3.30)$$

Introducing the interaction potential from equation 3.27 we obtain after some algebra:

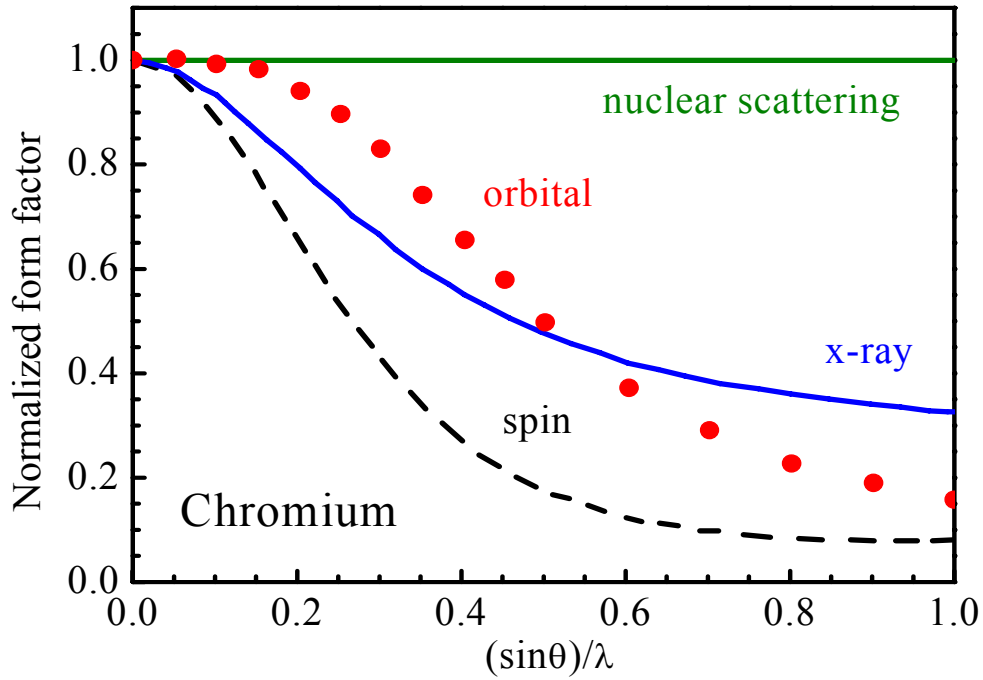


Figure 3.8: Nuclear scattering power, atomic form factor (x-ray) and magnetic form factor (spin and orbital) of Cr (see text) [116, 117].

$$\frac{d\sigma}{d\Omega} = (\gamma_n r_0)^2 \left| -\frac{1}{2\mu_B} \langle \sigma_z' | \underline{\sigma} \cdot \underline{M}_\perp(\underline{Q}) | \sigma_z \rangle \right|^2. \quad (3.31)$$

The pre-factor $\gamma_n r_0 = 5.39$ fm. $\underline{M}_\perp(\underline{Q})$ denotes the component of the Fourier transform of the sample magnetization, which is perpendicular to the scattering vector \underline{Q} :

$$\underline{M}_\perp(\underline{Q}) = \hat{\underline{Q}} \times \underline{M}(\underline{Q}) \times \hat{\underline{Q}}; \quad \underline{M}(\underline{Q}) = \int \underline{M}(\underline{r}) e^{i\underline{Q} \cdot \underline{r}} d^3 r. \quad (3.32)$$

The total magnetization $\underline{M}(\underline{r})$ comprises the spin magnetization and the orbital counterpart. The magnetic neutron scattering geometry can thus be shown schematically in figure 3.7(b), where only the component \underline{M}_\perp of the magnetization \underline{M} perpendicular to the scattering vector \underline{Q} gives rise to the magnetic neutron scattering.

Compared to nuclear scattering (no \underline{Q} -dependence, then so-called constant form factor), magnetic neutron scattering arises from the outer electrons in open shells only, which gives rise to a so-called magnetic form factor. As exemplified in figure 3.8, due to the different distributions of the magnetic field for spin and orbital angular momentum of Cr, a more rapid decrease of the scattering amplitude as a function of momentum transfer results for the spin momentum, while nuclear scattering is independent of the momentum transfer. For the atomic x-ray form factor, the inner electrons also play an important role; therefore, the x-ray form factor drops slower as compared to the magnetic form factor [14].

3.3 Powder diffraction and structure determination

Powder diffraction and structure determination by Rietveld method have been widely recognized to be uniquely valuable for structural analysis of nearly all polycrystalline materials. As shown schematically in figure 3.9, the general procedure is as follows: (a) x-ray/neutron powder diffraction patterns are recorded as numerical functions of a single independent variable, the scattering angle 2θ (or the interplanar distance d , or the value of the scattering vector Q); (b) after refining the collected intensities that are coherently related to the material and the instrumental parameters by the Rietveld method, an extraordinarily rich variety of structural information will be obtained; (c) correlating the microscopic structure information to the macroscopic properties. In this dissertation, the refinable parameters for different samples are tunable. They are described in chapters 7 and 8.1 in details, where the application of the structure determination, e.g. the calculation of the JT distortion parameter Δ and the Mn valence calculation based on the BVS's theory, is also presented.

Any powder diffraction pattern can be described by multiple and discrete Bragg peaks, which have different intensities (including background) in addition to varying positions and shapes. Each of the three components of a Bragg peak is determined by the following three aspects individually or compositively: (1) the crystal structure of the material, including unit cell parameters, disorder, defects, etc; (2) the properties of the measured specimen, including absorption, porosity, preferred orientation, grain size, strain, stress, etc; (3) the instrumental parameters, including geometry, alignment, wavelength, etc. For example, the most important component of a Bragg peak, i.e. the integrated intensity $I_{(hkl)}$, can be expressed as [118]:

$$I_{(hkl)} = K \times p_{(hkl)} \times L_{\theta} \times P_{\theta} \times A_{\theta} \times T_{(hkl)} \times E_{(hkl)} \times |F_{(hkl)}|^2. \quad (3.33)$$

In this equation, K is the scale factor that is a multiplier required to normalize experimentally collected integrated intensities with absolute calculated intensities. Absolute calculated intensity is the total intensity scattered by the content of the unit cell in the direction defined by the length of the corresponding reciprocal lattice vector. Therefore, the scale factor is a constant for a given phase and it is determined by the number, i.e. spatial distribution and states of the scattering atoms in the unit cell. $p_{(hkl)}$ is the multiplicity factor that accounts for the presence of multiple symmetrically equivalent points in the reciprocal lattice. L_{θ} is Lorentz multiplier that is defined by the geometry of diffraction. P_{θ} is the polarization factor that accounts for a partial polarization of the scattered electromagnetic wave. A_{θ} is the absorption multiplier that accounts for absorption of both the incident and diffracted beams and non-zero porosity of the powdered specimen. $T_{(hkl)}$ is the preferred orientation factor that accounts for possible deviations from a complete randomness in the distribution of grain orientations. $E_{(hkl)}$ is the extinction multiplier that accounts for deviations from the kinematical diffraction model. In powders, these are quite small and the extinction factor is nearly always neglected. At last, $F_{(hkl)}$ is the structure factor that is defined by the details of the crystal structure of the material: coordinates and types of atoms, their distribution among different lattice sites and thermal motion. Structure factor in the case of x-ray scattering is given as:

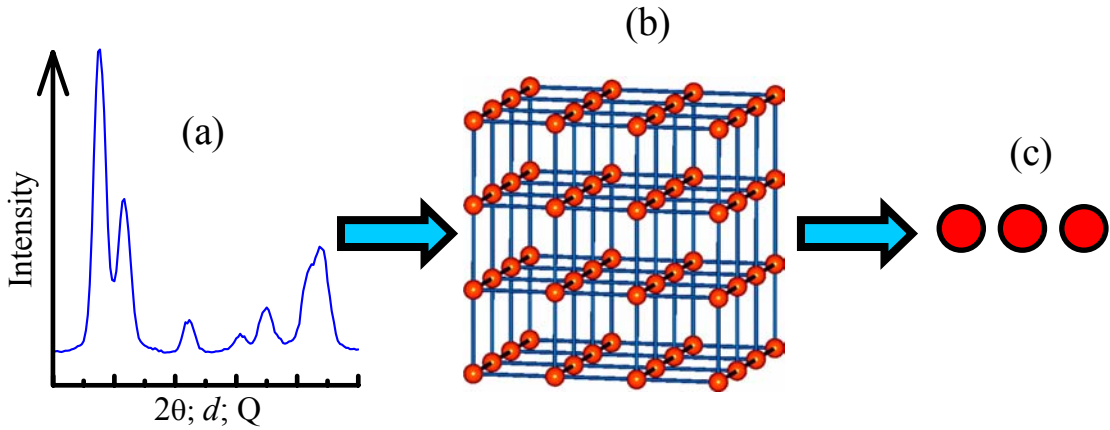


Figure 3.9: Schematic of the process: (a) powder diffraction data collection, (b) structure determination by the Rietveld method and (c) its application (see text).

$$F_{(hkl)} = \sum_{i=1}^n g^i \times t^i[(\sin\theta)/\lambda] \times f_0^i[(\sin\theta)/\lambda] \times \exp[2\pi i(hx^i + ky^i + lz^i)], \quad (3.34)$$

where n is the total number of atoms in the unit cell, g^i is the occupation factor of the i th atom, $t^i[(\sin\theta)/\lambda]$ is the temperature factor, $f_0^i[(\sin\theta)/\lambda]$ is the atomic form factor and (x, y, z) represents fractional coordinates of the i th atom in the unit cell. In the case of nuclear scattering of neutrons the structure factor can be expressed as [119]:

$$F(\underline{H}) = \sum_{i=1}^n g^i \times t^i(\underline{H}) \times b_1^i \times \exp[2\pi i(\underline{H} \cdot \underline{r}_i)], \quad (3.35)$$

where $\underline{H} = Q/2\pi = h\underline{a}^* + k\underline{b}^* + l\underline{c}^*$ (\underline{a}^* , \underline{b}^* and \underline{c}^* are the basis vectors of reciprocal lattice) is the lattice vector of the reciprocal lattice ($|\underline{H}| = (2\sin\theta)/\lambda$), b_1^i is the neutron scattering length of the i th atom (chapter 3.2.3), $\underline{r}_i = x^i\underline{a} + y^i\underline{b} + z^i\underline{c}$ is the vector expressing the position of i th atom in the unit cell of real space ($\underline{H} \cdot \underline{r}_i = hx^i + ky^i + lz^i$). Thus the structure factor has the dimension of a length, as has the scattering length $b_1^i(\underline{H}) = b_1^i = \text{constant of nucleus } i$. In the case of an ordering of the magnetic moments over the whole crystal (periodic magnetic structure) the magnetic structure factor is given by [119]:

$$F_M(\underline{H}) = \sum_{i=1}^n g^i \times t^i(\underline{H}) \times b_M^i(\underline{H}) \times \exp[2\pi i(\underline{H} \cdot \underline{r}_i)] \quad (3.36)$$

with the magnetic scattering amplitude

$$b_M^i(\underline{H}) = (e^2\gamma_n/2m_e c^2) \times f_M^i(\underline{H}) \times \sigma \times m_{\perp}^i(\underline{H}). \quad (3.37)$$

$\frac{1}{2}\sigma$ is the neutron spin operator and $m_{\perp}^i(\underline{H})$ is the projection of the magnetic moment \underline{m}^i onto the scattering plane (hkl). The magnetic form factor $f_M^i(\underline{H})$ is the Fourier transform

of the normalized magnetization density $M_i(\underline{r})$ of the atom or ion i

$$f_M^i(\underline{H}) = \int_V M_i(\underline{r}) \cdot \exp[2\pi i(\underline{H} \cdot \underline{r})] \cdot d\underline{r} \quad (3.38)$$

with $f_M^i(0) = \int_V M_i(\underline{r}) \cdot d\underline{r} = 1$.

This is a function of the reciprocal lattice vector \underline{H} , whereas the atomic form factor f_0^i of x-ray diffraction

$$f_0^i(|\underline{H}|) = \int_V \rho_i(\underline{r}) \cdot \exp[2\pi i(\underline{H} \cdot \underline{r})] \cdot d\underline{r}, \quad (3.39)$$

for a spherical electron density $\rho_i(\underline{r})$, depends only on the length of \underline{H} .

It should be pointed out that the Rietveld analysis is actually the whole-pattern-fitting structure refinement, i.e. profile refinement. Analytical reflection profile shape functions available include two different pseudo-Voigt functions, the Pearson VII function, and Gaussian, Lorentzian, and modified Lorentzian functions, etc. For details refer to [120]. In addition, the dependence of the width H of the reflection profiles measured as full width at half maximum (FWHM) has typically been modeled as (Caglioti *et al.* (1958)):

$$H^2 = U \cdot \tan^2\theta + V \cdot \tan\theta + W, \quad (3.40)$$

where U , V and W are refinable parameters. With the primary structural information, which makes both physical and chemical sense, and suitable peak shape and background functions, the initial structure model can be improved gradually by refining all the parameters in a least-squares procedure until the structure model yields correct integrated intensities close to experimentally observed. The quantity minimized in the least-squares refinement is the residual, S_y :

$$S_y = \sum_i w_i (y_i - y_{ci})^2, \quad (3.41)$$

where $w_i = 1/y_i$, y_i = observed (gross) intensity at the i th step and y_{ci} = calculated intensity at the i th step [120]. This basic idea, extended to the entire powder diffraction pattern, is the foundation of the Rietveld method. In some cases, in particular when the structural model is very crude, it is advisable to analyze first the pattern with the profile matching method in order to determine accurately the space group, profile shape function, background and cell parameters before running the Rietveld refinement. For the analysis of a magnetic structure, one simple method is through a crystallographic-like description using the magnetic unit cell, which describes the magnetic periodicity in the magnetic cell with respect to that of the crystal structure. For magnetic structures described in a magnetic unit cell larger than the crystallographic cell, the coordinates of atoms must be changed consequently, as well as the unit cell parameters. The identification of magnetic reflections is usually accomplished by a careful comparison of powder patterns recorded below and above the magnetic phase transition temperatures. The nuclear structure factors $F(\underline{H})$ can be calculated from the known crystal structure. In this way the scale factor K of

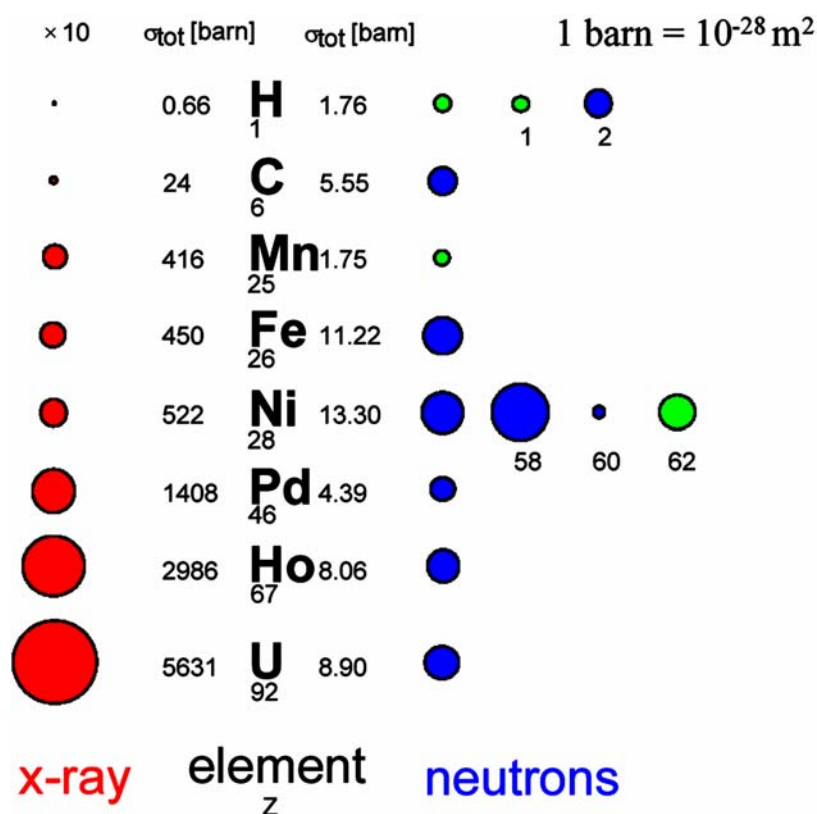


Figure 3.10 taken from [14]: Comparison of the coherent scattering cross-sections for x-rays and neutrons for a selection of elements. The area of the coloured circles represent the scattering cross section, where in the case of x-rays a scale factor 10 has to be applied. For neutrons, the green and blue coloured circles distinguish the cases where the scattering occurs with or without a phase shift of π .

the data can be obtained and the absolute values of the magnitudes of the magnetic structure factors $|F_M(\underline{H})|$ can be determined. The individual orientations of the magnetic moments \underline{m}^i with respect to the basis vectors of the crystal lattice and their magnitudes are then to be calculated [119].

One of the most difficult problems in crystal structure analysis is atom identification, which strongly depends on the scattering power of the atom relative to the other atoms in the structure. The simultaneous Rietveld refinement combining both neutron and x-ray powder diffraction data is an effective technique taking advantage of the different contrast mechanisms for x-rays and neutrons. The observed intensity is proportional to the so-called cross section. It is therefore useful to compare the scattering cross sections for x-rays and neutrons as shown in figure 3.10 [14]. For x-rays, the cross section depends on the square of the number of electrons and thus varies in a monotonic fashion throughout the periodic table. Clearly it will be difficult to determine the lighter atoms' (e.g. hydrogen) positions with x-rays in the presence of heavy elements such as metal ions. In addition, there is a very weak contrast between neighbouring elements as can be seen from the transition metals Mn, Fe and Ni in figure 3.10. For neutrons the cross section depends on the details of the nuclear structure and thus varies in a non-systematic fashion throughout the periodic table. As an example, there is a very high contrast between Mn

and Fe (figure 3.10). With neutrons, the lighter atoms are thus clearly visible even in the presence of heavy elements. Therefore, the structural parameters related to the heavy atoms can be well refined with x-ray diffraction data and the neutron-diffraction data allows one a better determination of the parameters (e.g. atomic positions, site occupancies, thermal parameters, etc) of lighter atoms, e.g. hydrogen and oxygen.

Throughout this dissertation, the software FullProf suit was used for Rietveld refinements. This program has been developed for Rietveld analysis of neutron (nuclear and magnetic scattering) or x-ray powder diffraction data collected at constant or variable step in scattering angle 2θ and it can be freely downloaded from [121]. It can be also used as a profile matching tool, without the knowledge of the atomic positions. Single crystal refinements can also be performed and Time-of-flight neutron data analysis is also available. The successful practical operation of this program largely depends on the experience and the ability of the user to properly select a sequence in which various groups of parameters are refined. Editing a proper PCR file is the critical point. A tested one for structural and magnetic refinements of a powdered $\text{La}_{1/8}\text{Sr}_{7/8}\text{MnO}_3$ single crystal can be found in appendix B.

3.4 Resonant soft x-ray scattering

Soft x-ray scattering techniques employ the excitation of electrons in relatively shallow core energy levels of about 200-2000 eV as shown in figure 3.11. RSXS, a combination of x-ray diffraction and spectroscopy, utilizes the radically altered behavior of the real and imaginary parts of the atomic scattering factor ($f_1 + if_2$) near the absorption edges to probe the periodic electronic structures (charge, orbital and spin degrees of freedom) and other properties of various CTMO.

In a RXS process, a core electron is excited to an unoccupied intermediate band by absorbing incident photons, and then it recombines with the holes in the core levels simultaneously emitting photons with the same energy, as shown schematically in figures 3.12(a) and (b). RXS carries spectroscopic information on the unoccupied bands, e.g. an upper Hubbard band (UHB), and it is element-specific and electronic-shell specific. Therefore, RXS is a spectroscopically-resolved structure probe. As shown in figure 3.12(b), RSXS at the Mn $L_{\text{II, III}}$ -edges (corresponding to $2p \rightarrow 3d$ excitation) is expected to be directly sensitive to the $3d$ valence states, orbitals, spins, etc. By contrast, at the Mn K -edge (figure 3.12(a)), the observed resonances in the hard x-ray regime involve virtual excitations from the $1s \rightarrow 4p$ states, which is thus an indirect probe to the $3d$ states through the JT distortions, $4p$ band structure effects and $3d-4p$ Coulomb interactions. However, compared to resonant hard x-ray scattering, RSXS has some shortcomings: the relatively long wavelength of soft x-rays limits the applicability of RSXS to the systems only with sufficiently long periods (d_{hkl}) satisfying $\lambda < 2d_{hkl}$; the azimuthal analysis in RSXS is difficult to perform currently; the RSXS experiments have to be done in the ultrahigh-vacuum (UHV) diffractometers. The RSXS works presented in this dissertation have been carried out at the two-circle UHV ALICE diffractometer that is described in detail in chapter 4.3. In figure 3.12(c), the vertical scattering geometry is shown, where Ψ is the so-called azimuthal angle which represents the relative orientation of the sample with respect to Q .

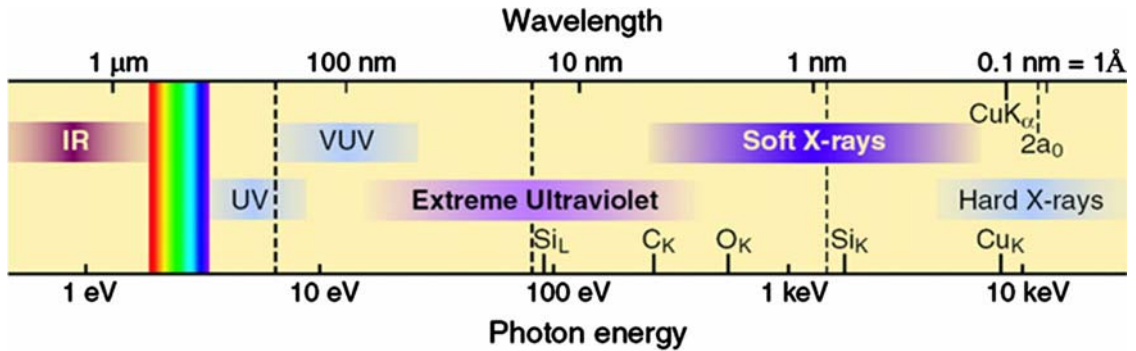


Figure 3.11: The short wavelength region of the electromagnetic spectrum taken from [122]. The oxygen K -edge ($1s \rightarrow 2p$), the transition-metal $L_{II, III}$ -edges ($2p \rightarrow 3d$) and the rare-earth $M_{IV, V}$ -edges ($3d \rightarrow 4f$), are located in the soft x-ray spectral region.

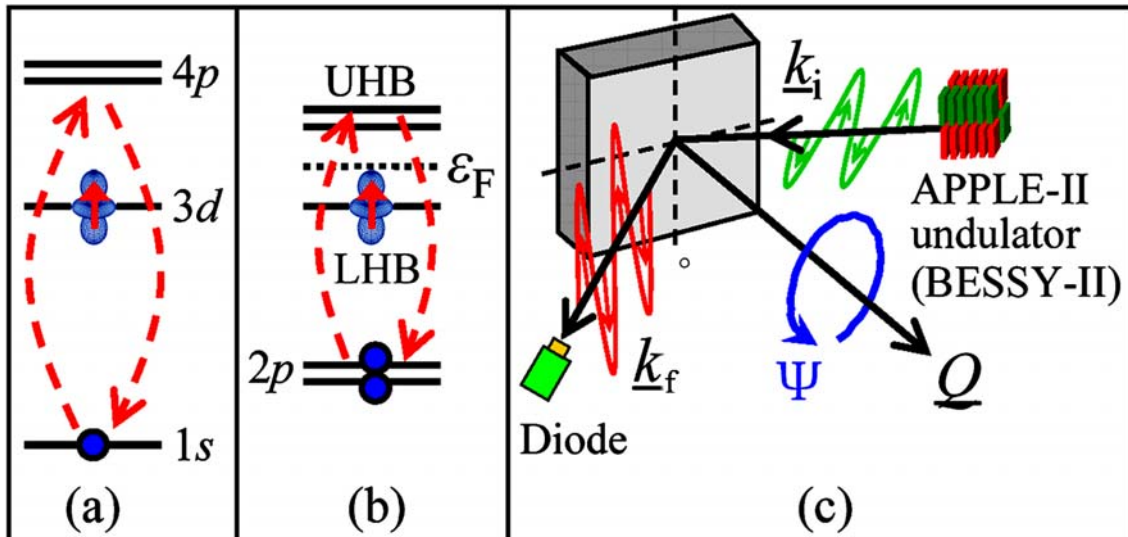


Figure 3.12: A schematic presentation of RXS at the different Mn absorption edges: (a) K -edge and (b) $L_{II, III}$ -edges. (c) Basic notations for the RSXS set-up at the UHV ALICE diffractometer at Berliner Elektronenspeicherring-Gesellschaft für Synchrotronstrahlung (BESSY).

In principle, RXS can be described by the second-order perturbation theory of quantum mechanics. The interaction Hamiltonian H_{int} between the incident radiation and sample can be expressed as:

$$H_{\text{int}} = \frac{e}{m} \underline{A} \cdot \underline{P} + \frac{e^2 \underline{A}^2}{2m}, \quad (3.42)$$

where \underline{A} is the vector potential of the incident photon field. This Hamiltonian produces the transitions between initial $|i\rangle$ and final $|f\rangle$ states, which refer to the combined states of electrons and the electromagnetic field of photons. To obtain the scattering amplitude

for resonant scattering, it is necessary to calculate the transition probability (W) between $|i\rangle$ and $|f\rangle$ induced by H_{int} up to the second order, as shown in the following equation:

$$\frac{d\sigma}{d\Omega} \propto W = \frac{2\pi}{\hbar} \left| \langle f | H_{\text{int}} | i \rangle + \sum_{n=1}^{\infty} \frac{\langle f | H_{\text{int}} | n \rangle \langle n | H_{\text{int}} | i \rangle}{E_i - E_n} \right|^2 \rho(\varepsilon_f), \quad (3.43)$$

where $\rho(\varepsilon_f)$ is the density of states, $|n\rangle$ is the intermediate state. The sum is over all possible $|n\rangle$. The first-order term $\langle f | H_{\text{int}} | i \rangle$ is often called the transition matrix element M_{if} . This gives rise to the classical Thomson scattering factor f_0 . It can be noticed that the $\underline{A} \cdot \underline{P}$ term can now produce scattering via an intermediate state $|n\rangle$ as indicated in the second-order term in equation 3.43. The resonant behavior arises when the denominator tends towards zero. This occurs when the total incident energy, $E_i = \hbar\omega + E_a$ (E_a is the ground state energy for the electron), is equal to the energy of the intermediate state (E_n). It should be noted that the resonant scattering is a coherent process involving only virtual absorption and emission of photons, there exist no discrete steps. The second-order term leads exactly to the dispersion corrections of anomalous atomic scattering factor ($f_1 + if_2$) [123].

After having introduced the basic concepts of experimental techniques, I will introduce the typical experimental set-ups for powder diffraction and RSXS studies in the next chapter.

Chapter 4

Experimental instruments

Powder diffraction (x-ray and neutron) is a fast and non-destructive powerful method for qualitatively and quantitatively analyzing the crystal structure and magnetic ordering of a powdered sample. It is widely used in many laboratories and industries. The RSXS technique is an emerging powerful method for probing the complex ordering phenomena in CTMO.

In this chapter, I describe the instruments used for this dissertation. That the design and construction of a rotating specimen holder for laboratory XRPD and a new portable UHV goniometer for RSXS is part and parcel of the present thesis.

4.1 Laboratory x-ray powder diffractometer

The prerequisite for a quantitative structure refinement using the Rietveld method is the precise and reproducible XRPD data collection. Since for the geometry of our BRUKER AXS D8 ADVANCE system as shown in figure 4.1(a) Bragg reflection occurs mostly from the particles whose crystallographic planes are almost horizontal and since that almost all materials exhibit some degree of preferred orientation [124], the careful sample preparation to obtain a specimen that presents a very large number of randomly oriented, uniformly sized crystallites and the precise measurement to optimize the data quality are particularly crucial.

The sample preparation for XRPD was accurately and concisely discussed in [125]. The universal approach for specimen preparation is as follows: (i) thinly coating a plate (e.g. normal quartz) with some kind of gelatin and flattening it; (ii) sieving the finely ground powder onto the plate and gently taping or shaking the plate to make the powder spread out on it uniformly; (iii) inverting the plate to dislodge the excess powder; (iv) repeating steps (ii) and (iii) until enough powder adheres to the gelatin; (v) waiting for the gelatin to dry. Though good random orientations can be obtained if carefully and properly done, some disadvantages exist in this method: small amount of mass, thin layer of powder, possible background contributions from gelatin and plate, and especially the rough surface.

In order to collect XRPD data with a better quality, we have designed and built a rotating specimen holder as shown in figure 4.1(b). The system consists of a minimotor

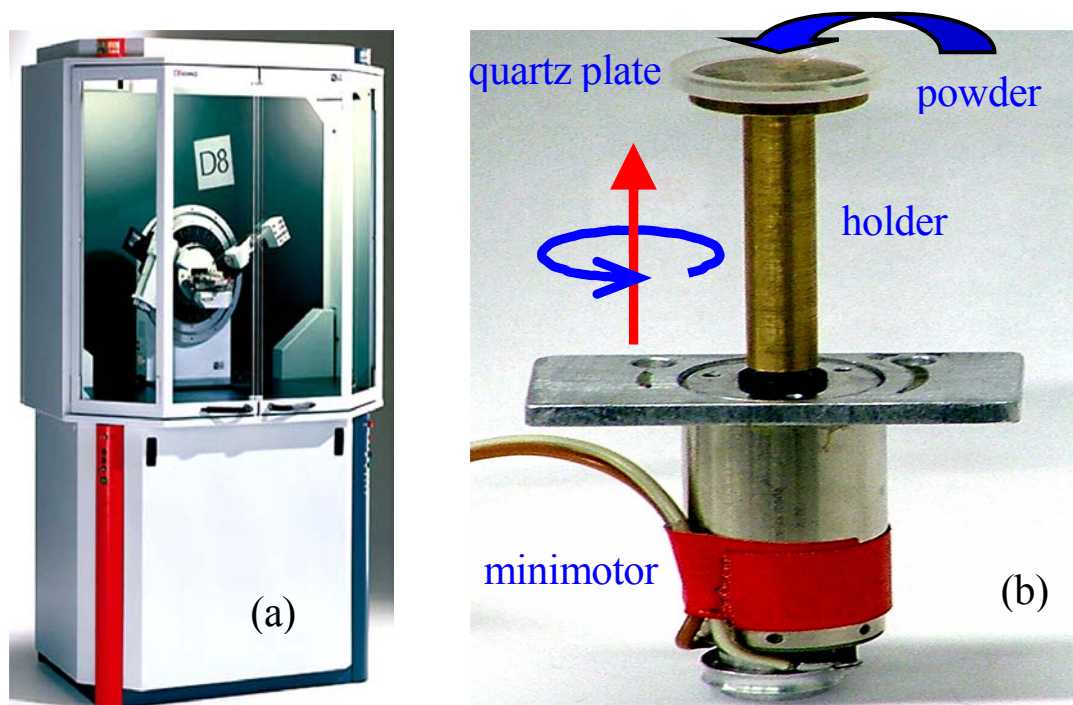


Figure 4.1: (a) Photograph of the BRUKER AXS D8 ADVANCE system used in this dissertation [126]. (b) The system of rotating specimen holder consists of a minimotor, a holder and a cavitary quartz plate.

with a rotating rate of ~ 26 revolutions per minute (rpm), a holder made of pinchbeck alloy and a cavitary quartz plate with a thickness of ~ 1.2 mm. The experimental procedure is as follows: (i) fixing the plate to the holder; (ii) sieving enough finely ground powder into the cavity; (iii) gently pressing the powder with a smooth glass slide to make its surface flat. In this way, a uniformly dense specimen with enough mass and a good surface and free of porosity can be prepared in a very short time. It should be pointed out that the quality of a specimen is one of the important factors affecting the quality of the XRPD data, e.g. influencing the peak position, intensity, shape, etc.

With our x-ray powder diffractometer employing copper $K_{\alpha 1}$ and $K_{\alpha 2}$ radiation ($I_{K_{\alpha 2}}/I_{K_{\alpha 1}} = 0.525$) in combination with the home-made rotating specimen holder, the XRPD study on polycrystalline $\text{La}_{7/8}\text{Sr}_{1/8}\text{Mn}_{1-\gamma}\text{O}_{3+\delta}$ (see details in chapter 7) has been performed at room temperature. Powder samples of $\text{La}_{7/8}\text{Sr}_{1/8}\text{Mn}_{1-\gamma}\text{O}_{3+\delta}$ polycrystals were obtained by carefully crushing and short-time milling the twice sintered, Ar and O_2 annealed rods. The resulting particle size is $\sim 30\text{-}36$ μm . The x-ray generator was operated at 40 kV and 40 mA. XRPD patterns were collected in the angular range $2\theta = 4\text{-}90^\circ$ in a step-scan mode with a step size 0.04° and a counting time 32.2 sec per step in order to obtain data with high counting statistics. Si powder (Alfa Aesar, 99.9985%, always kept in vacuum container at room temperature) was used as an external standard to calibrate 2θ and the intensity ratio of the two wavelengths. The obtained XRPD patterns have a very good quality and are reproducible.

The rotating specimen holder for laboratory XRPD produces a ‘zero-background’ contribution to the collected data and can effectively minimize the problem of preferred orientation as demonstrated in chapter 7, where no appreciable preferred orientation was

observed.

4.2 Neutron powder diffractometers

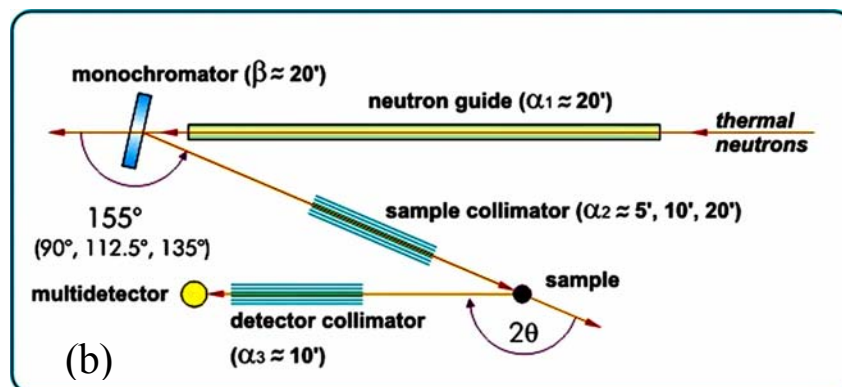
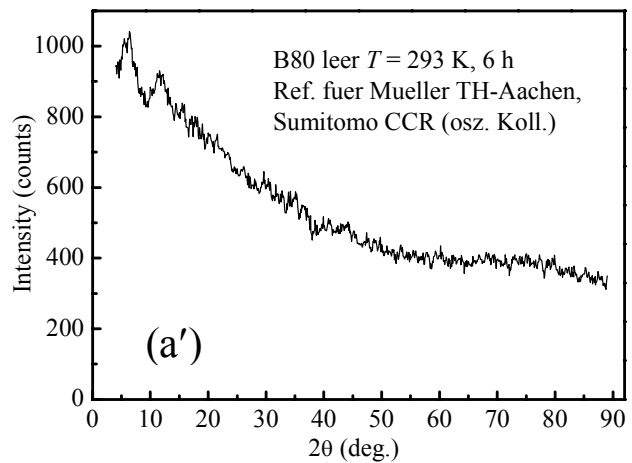
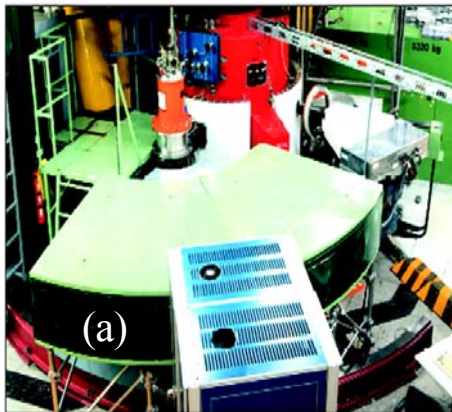


Figure 4.2: (a) Photograph of the SV7-a neutron powder diffractometer at the FRJ-2 [127]. (a') Background measurement at the SV7-a. (b) Principle of the structure powder diffractometer SPODI at the FRM-II [128].

Two neutron powder diffractometers were utilized in this dissertation. They are the SV7-a as shown in figure 4.2(a) at the FRJ-2 research reactor in Jülich [127] and the SPODI at the FRM-II research reactor in Garching [129]. Complementary to our laboratory x-ray powder diffractometer, they were used to collect the NPD data for solving crystal and magnetic structures. Advantages of neutron scattering appear for instance in the determination of magnetic structures, in the localization of light elements (e.g. oxygen) and in the analyses of thermal movements, etc. Apart from routinely working with a high take-off angle (2θ) of 155° as shown in figure 4.2(b), the key use of a thermal neutron guide for the SPODI diffractometer makes it achieve a better resolution and a higher intensity. The use of sample collimator also influences and improves its resolution over a wide 2θ range.

The NPD data for $\text{La}_{7/8}\text{Sr}_{1/8}\text{Mn}_{1-\gamma}\text{O}_{3+\delta}$ polycrystals presented in chapter 7 were collected on the SV7-a diffractometer in the temperature range 10-900 K. The data were acquired in two 2θ spans, from 0 to 45° and from 45 to 90° , with a step size 0.1° and a constant wavelength $\lambda = 1.0959(5)$ Å. For the room temperature measurements, the twice sintered (~ 19 g), Ar annealed (~ 18 g) and O_2 annealed (~ 18 g) samples were sealed in 8 mm diameter and 45 mm high cylindrical vanadium cans mounted on SV7-a without external ω -rotation. For the low temperature measurements, the samples were filled in a vanadium can of 11 mm diameter mounted in a ‘Sumitomo’ closed cycle refrigerator (CCR). The Bragg reflections from the graphite shield are suppressed by a radial oscillating collimator. Background measurements for the empty CCR with an empty vanadium can at the sample position and for the furnace without vanadium can do not show any additional peaks in the diagrams as shown in figure 4.2(a’).

In chapter 8.1, the NPD measurements for powdered single-crystalline $\text{La}_{7/8}\text{Sr}_{1/8}\text{MnO}_3$ are presented in a temperature range from 5 to 300 K. A suitable piece (~ 8 g) cut from the centre of a big single crystal was lightly ground into powder in order to reduce the possible microstrain and get the appropriate particle size of ~ 38 - 44 μm . High-resolution NPD data were collected on the SPODI diffractometer with a vertical focusing monochromator consisting of 17 Ge(551) crystals. The typical step size was 0.05° at constant wavelength $\lambda = 1.5487(5)$ Å. High enough counting statistics make the refinements using the Rietveld method much more reliable.

4.3 RSXS diffractometer

The Berliner Elektronenspeicherring-Gesellschaft für Synchrotronstrahlung (BESSY) operates the only German third-generation synchrotron radiation facility. The electron storage ring BESSY II started its operation in 1998. It is especially dedicated to the vacuum ultra violet and soft x-ray radiation. All the RSXS experiments in this dissertation (chapters 8.2 and 9) were carried out on the UE56/1-PGM elliptically polarized APPLE-II undulator beamline of the BESSY II [130]. The accessible incident photon energy range between 500 eV and 900 eV using the third harmonic of the undulator is ideally suitable for measurements at the L_{II} and L_{III} absorption edges of $3d$ TMs and at the K -edge of oxygen. The monochromator of this beamline is a plane reflection-grating. The 1200 mm^{-1} grid was used for all RSXS measurements. The energy resolution at 700 eV, depending on the exact setting of the exit slit, is $\Delta E/E \approx 2 \times 10^{-4}$ at an exit slit width of typically 100 μm [131].

In the soft x-ray range (200-2000 eV), the strong air absorption of x-rays necessitates the use of a high vacuum environment, which on the other hand can prevent the water and other residual gases, e.g. nitrogen, especially the oxygen (some RSXS studies were performed at the oxygen K -edge), etc, from concentrating on the sample surface measured at low temperatures, guaranteeing reliable scattering experiments. The soft x-ray scattering instrument utilized in this dissertation is the two-circle UHV diffractometer ALICE (figure 4.3) built by Bochum University, Germany [131, 132]. The goniometer is installed in the cylindrical vacuum chamber of 400 mm inner diameter and 310 mm height with a vertical cylinder axis. The chamber is pumped by a 260 l/s turbo-molecular pump and backed by a scroll-type dry roughing pump. The sample change is through a

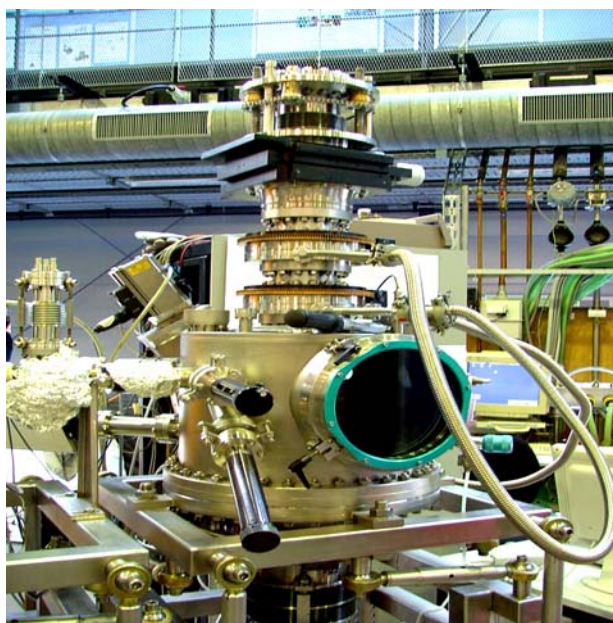


Figure 4.3: The soft x-ray scattering UHV chamber ALICE designed and built in horizontal scattering geometry by Bochum University, Germany, and installed at BESSY II.

200 mm-diameter load-lock window visible in figure 4.3. The time for pumping ($< 1 \times 10^{-6}$ mbar) and decreasing temperature (< 10 K) after sample change is one hour. This diffractometer covers a temperature range of 4–380 K and a variable magnetic field of ± 2.7 kOe. The sample and the detector are driven by two differentially pumped 100 mm-bore rotating platforms with stepper motors and gears external to the vacuum. The stepper motors are controlled via a GPIB interface from a Linux PC. The angular resolution for sample and detector rotation is 0.005° . Two slits are installed in the vacuum chamber in order to optimize the angular resolution. One is ~ 10 cm in front of the sample and the other is installed just before the detector. Both slits were set to $300 \mu\text{m}$ during all measurements such that an angular resolution of $\sim 0.13^\circ$ was obtained. The scattered beam is detected by a Hamamatsu G1127-04 GaAsP photodiode with a dark current below 10 fA, whose signal is measured with a Keithley 6514 electrometer and normalized to the photoelectric current of the refocusing mirror in the beamline optics. Data acquisition is performed by running the standard SPEC software.

4.4 A new portable ultrahigh-vacuum goniometer for RSXS

Most available soft x-ray scattering chambers, including ALICE, host two-circle diffractometers. This geometry leads to severe restrictions for sample rotations around the surface normal (ψ -circle) and sample tilting (χ -circle), which are both essential degrees of freedom for single crystal studies. Therefore, a precise pre-alignment on the sample to be measured becomes crucial. Even when such a perfect pre-alignment is possible, any small mis-orientations that often appear during the cooling of the sample or due to the temperature dependent change of lattice parameters may still easily ruin the efforts. To

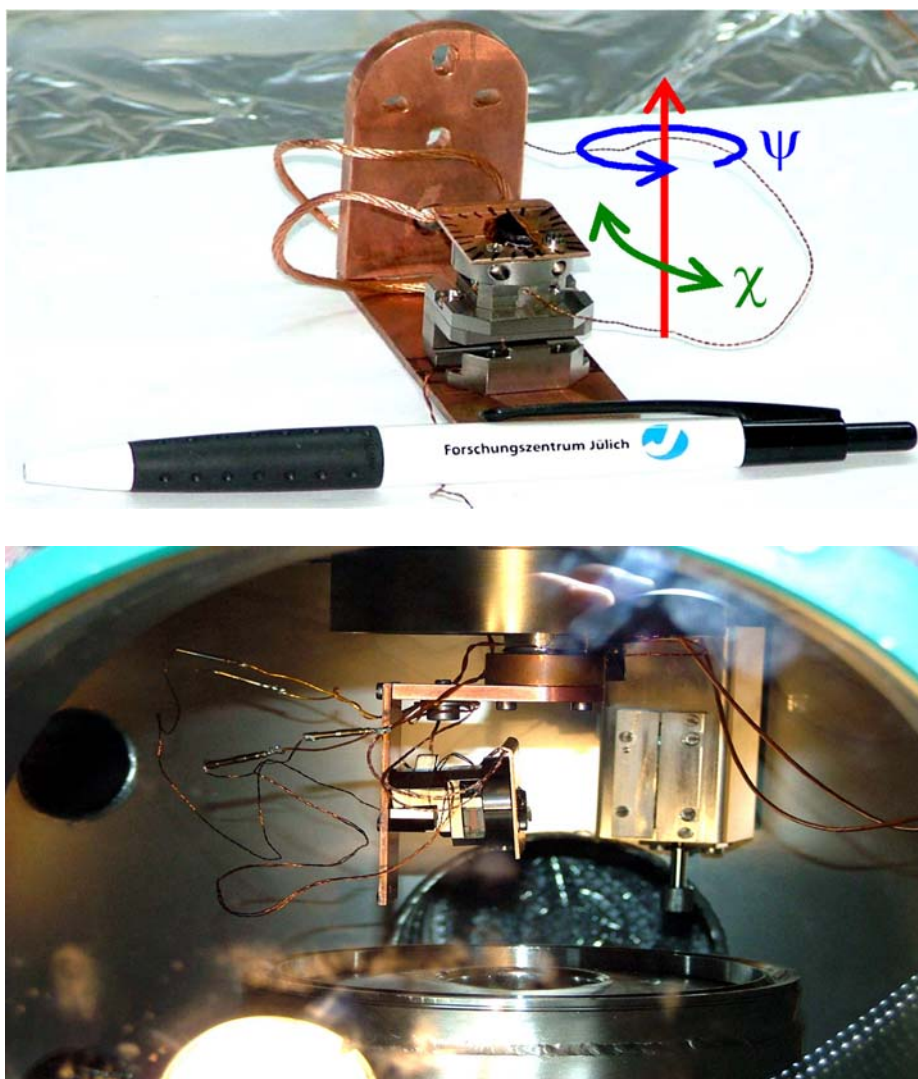


Figure 4.4: (top) The miniature goniometer for sample rotation and tilt in the ψ and χ angles, respectively. (bottom) View into the heart of ALICE chamber through the load-lock window. The x-rays enter from the left window, through a set of slits, and then scatter off the sample (mounted on our goniometer, θ shown here at about -80°) in the centre of the chamber, and are then detected by a photodiode mounted on the 2θ arm (shown here at $\sim 70^\circ$) without polarization analysis.

overcome these limitations, a new portable UHV goniometer has been designed and built for RSXS, which makes it feasible to adjust samples along χ ($\pm 2.5^\circ$, even at temperatures down to 10 K) and ψ (360° , above ~ 220 K) as shown in the upper part of figure 4.4. The system consists of a right-angle shaped sample-holder, two piezo-driven motors, a copper plate, two copper cooling bundles and a silicon-diode thermometer. This miniature goniometer can be easily manipulated and is well compatible with normal two-circle diffractometers as tested in this dissertation. It thus dramatically improves the efficiency of soft x-ray scattering chambers and can be used to unravel the ordering phenomena of lattice, charge, orbital and spin degrees of freedom in CTMO by the RSXS technique as demonstrated in chapters 8.2 and 9. In addition, it makes the measurement of azimuthal

scans (rotating the sample around the scattering vector) possible for the order parameters whose transition temperatures are above ~ 220 K. This measurement is vital to understand the nature of observed resonances.

Single crystals cut and polished such that a face perpendicular to the scattering vector was preferred are mounted on the center of the copper plate braced to our goniometer (upper part of figure 4.4) with the desired orientation nearly normal to the scattering plane. The RSXS data were collected on the ALICE diffractometer equipped with our goniometer as shown in the bottom of figure 4.4 with the incident x-rays linearly polarized either perpendicular (σ polarization) or parallel (π polarization) to the diffraction plane. The scattering geometry for this combination is horizontal, which has been described in chapter 3.4. The sample cooling is realized by connecting the copper plate to the cold finger through two thick enough copper bundles. In this way, the sample temperature can approach 10 K within one hour, strongly depending on how many connecting copper bundles are used. The sample temperature is measured by a silicon diode located ~ 2 mm below the sample bottom, in combination with a Lakeshore 340 temperature controller.

Our miniature goniometer actually has improved the ALICE diffractometer into a more useful ‘four-circle’ one, while the alignment procedure is kept the same as described in [131].

Chapter 5

Synthesis of perovskite manganites

The synthesis condition can modify (more exactly tailor) the material's properties through gently or completely changing its microscopic structures. This interrelationship of synthesis-structure-property is often utilized in materials science. The synthesis of thermodynamically stable perovskites is particularly important in strongly correlated electrons, which sometimes leads to a promising discovery of the unusual physical behaviors.

This chapter describes the route for the optimization synthesis of perovskites taking $\text{La}_{7/8}\text{Sr}_{1/8}\text{MnO}_3$ as a typical sample, trying to obtain a universal recipe for the syntheses of most manganites.

5.1 Solid state reaction

Most of perovskite manganites nowadays have been fabricated through high-temperature solid state reactions. The advantage of this method [133] is the ready availability of starting materials and the low cost for a bunch of sample preparations.

The prerequisite for a complete chemical reaction is that the particle size of raw materials has to be smaller than the diffusion length. This relation [134] is expressed as the following equation:

$$(2Dt)^{1/2} \geq L, \quad (5.1)$$

where $(2Dt)^{1/2}$ is the diffusion length, D is the diffusion constant (depending on the reaction temperature and materials), t is the reaction time and L is the typical particle size. It determines the processing degree of calcining and sintering. The higher the temperature below melting point and the smaller the grain size, the higher the reaction rate of a kinetically favorable reaction. The purpose of calcining is to decompose carbonates at high temperatures (e.g. $\text{SrCO}_3 (\text{s}) = \text{SrO} (\text{s}) + \text{CO}_2 (\text{g})$) in order to get fine-grained corresponding oxides (e.g. SrO from the decomposition of SrCO_3) with large surface area and high reactivity, while the goal of sintering is to obtain a complete chemical reaction through increasing the contact areas of reactants as much as possible by pressing. Solid state reaction is always accompanied by the so-called defect chemistry [135, 136], e.g.

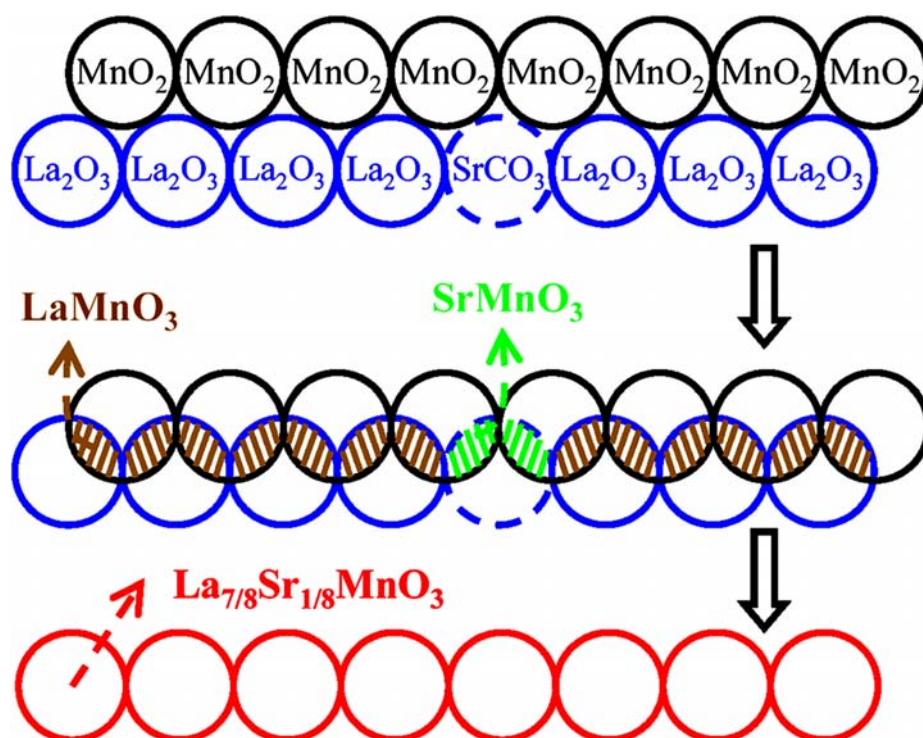


Figure 5.1: The ideal reaction process of raw materials ($\text{La}_2\text{O}_3 + \text{SrCO}_3 + \text{MnO}_2$) for the formation of $\text{La}_{7/8}\text{Sr}_{1/8}\text{MnO}_3$. In order to incarnate the doping level $1/8$, the particles are schematically depicted as spheres with an identical size and periodically arranged. This is actually hard to realize as discussed in the following part 5.2.2.

cation vacancies, excess oxygen, etc, leading to nonstoichiometric compounds. The reasons could be cation loss (wastage, sublimation) or incomplete chemical reaction.

The complicated process of solid state reaction can be simply illustrated with figure 5.1, taking the formation of $\text{La}_{7/8}\text{Sr}_{1/8}\text{MnO}_3$ as an example. This sample belongs to orthorhombic or rhombohedral structure at room temperature, depending on the stoichiometry. In both symmetries, Sr has the same lattice sites as La. Hence it is a dopant. Suppose that very homogenous and fine grains are obtained for the raw materials as shown in the top of figure 5.1. Two kinds of reaction interface exist: one is between MnO_2 and La_2O_3 ; another is between MnO_2 and SrCO_3 . At the first stage, two kinds of nucleus of LaMnO_3 and SrMnO_3 are thus formed in two kinds of surface contact regions, respectively. With nuclei, LaMnO_3 and SrMnO_3 begin to grow but the processing degree is limited to some extent by the certain reaction temperature and time (middle of figure 5.1). This process is accompanied by the formation of $\text{La}(\text{Sr})\text{MnO}_3$ at the interface between LaMnO_3 and SrMnO_3 . For further reactions, three diffusions have to overcome the formed three barriers, i.e. LaMnO_3 , SrMnO_3 and $\text{La}(\text{Sr})\text{MnO}_3$. This can be achieved by increasing the reaction temperature and time or by milling and mixing the intermediate product to produce new grain interfaces, again and again until a pure phase of homogeneously doped $\text{La}_{7/8}\text{Sr}_{1/8}\text{MnO}_3$ forms (bottom of figure 5.1).

One example of the heating-cooling sequence for sintering (to obtain a complete reaction) is schematically shown in figure 5.2. The pressed sample is placed on a Pt-plate and heated in a furnace to 873 K in ~ 4 h, held at this temperature for ~ 6 h if binder is used

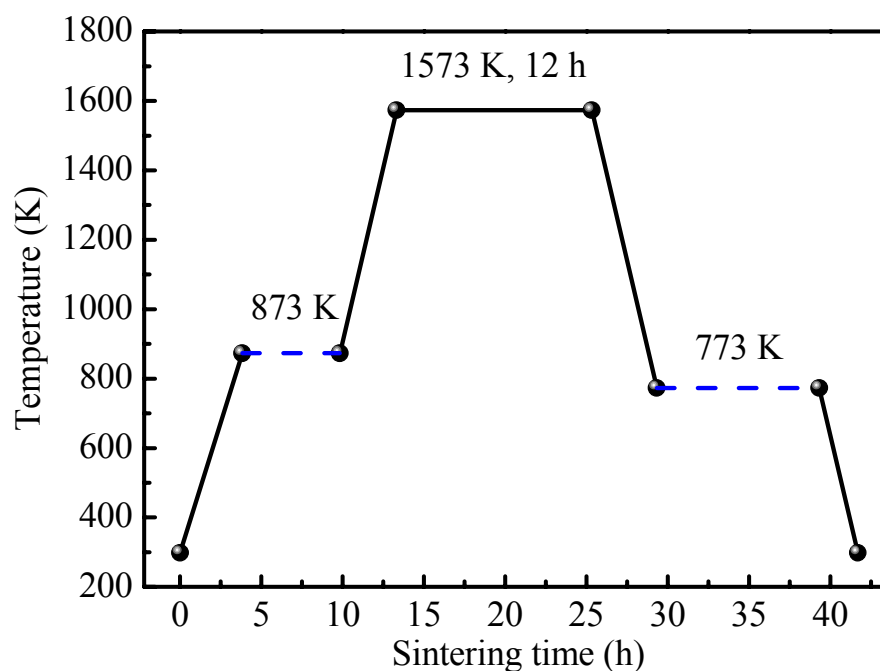


Figure 5.2: Schematic of the heating-cooling process of sintering.

in pressing (burning off the binder), then to the final sintering temperature 1573 K in ~ 3.5 h and held there for ~ 12 h (depending on equation 5.1), allowed to cool to 773 K in ~ 4 h and held there for ~ 10 h if the sample needs to anneal at low temperatures (e.g. to get stoichiometric oxygen content), and finally to the room temperature in ~ 3 h. The heating and cooling programs are determined by the form and reactivity of reactants.

The actual process of solid state reaction is far more complicated than the above description. It may not occur even if thermodynamic considerations favor product formation. Three important factors [133] influence the solid state reaction rate: (i) the area of contact between the reacting materials and hence their surface areas; (ii) the rate of nucleation of the product phase; (iii) the rates of diffusion of starting materials through the various phases, and especially through the intermediate phases. Besides the problems arising from nucleation and diffusion, five additional disadvantages are present: (i) undesirable phases may be formed, e.g. SrMnO_3 or LaMnO_3 during the synthesis of $\text{La}_{1-x}\text{Sr}_x\text{MnO}_3$; (ii) inhomogeneous doping distribution that needless to say is awful for perovskite manganites but is difficult to avoid; (iii) sometimes reaction temperature cannot be high enough to lead to desired reaction rates because of the sublimation of some components; (iv) possible reactions with crucible; (v) monitoring the process of solid state reaction is difficult, though XRPD (only foreign phases with volume fraction in excess of $\sim 5\%$ can be detected) can be carried out periodically. The results of other methods of characterization, e.g. SQUID-Magnetometer (measuring the magnetic properties), inductively coupled plasma with optical emission spectroscopy (ICP-OES) and infrared detection (measuring the composition), and standard four-point probe (measuring the sample resistivity), etc, have to be taken into account to prove the phase purity.

In order to overcome some of the problems associated with solid state reactions, it is absolutely necessary to optimize the processing and synthesis parameters that have a large influence on the properties of final products.

5.2 Process optimization

5.2.1 Starting materials

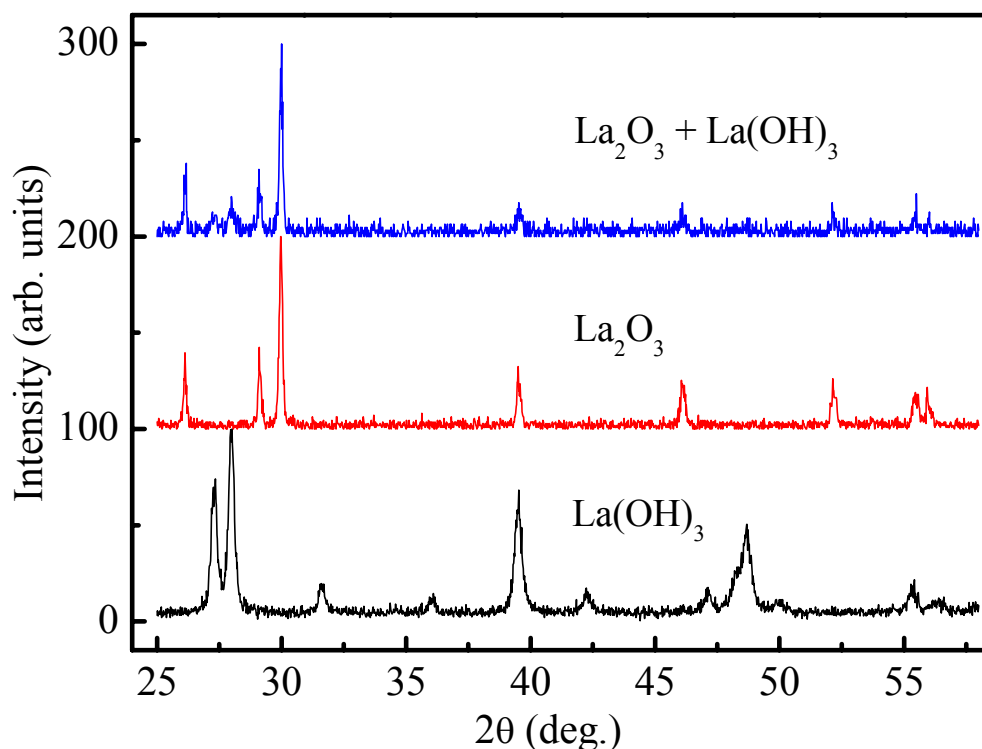


Figure 5.3: XRPD patterns of (top) La_2O_3 normally stored in a plastic bottle in air; (middle) just dried La_2O_3 at 1173 K for 12 h; (bottom) after ~ 2 h exposure of dried La_2O_3 to air.

The selection of suitable starting materials and the correct understanding of their basic properties is the first step to produce a compound with the desired composition and properties. Three basic principles should be observed: (i) Low material cost. The higher the purity, the higher the price. At early stages while assessing the feasibility of the formation of a new compound, starting materials with the relative low purity can be used. (ii) Relative high stable state of starting materials, especially the oxidation state. (iii) High reactivity of starting materials. La_2O_3 (Chempur, 99.99%), MnO_2 (Alfa Aesar, 99.9%) and SrCO_3 (Chempur, 99.999%) were employed for the synthesis of $\text{La}_{1-x}\text{Sr}_x\text{MnO}_3$ in this dissertation.

In most of the publications [8], La_2O_3 was preheated in order to decompose the residual carbonates. In my syntheses, La_2O_3 was dried at 1173 K for 12 h. The XRPD measurement shows that after drying the phase is a pure La_2O_3 within the detection accuracy (middle of figure 5.3). The measuring time was within one hour using the rotating specimen holder described in chapter 4.1. However, after several hours' exposure to air, the volume of the dried La_2O_3 specimen obviously expanded. The remeasurement presents the phase of pure $\text{La}(\text{OH})_3$ (bottom of figure 5.3). Careful reexaminations assure that the transition from La_2O_3 to $\text{La}(\text{OH})_3$ has completed after an exposure of pure La_2O_3

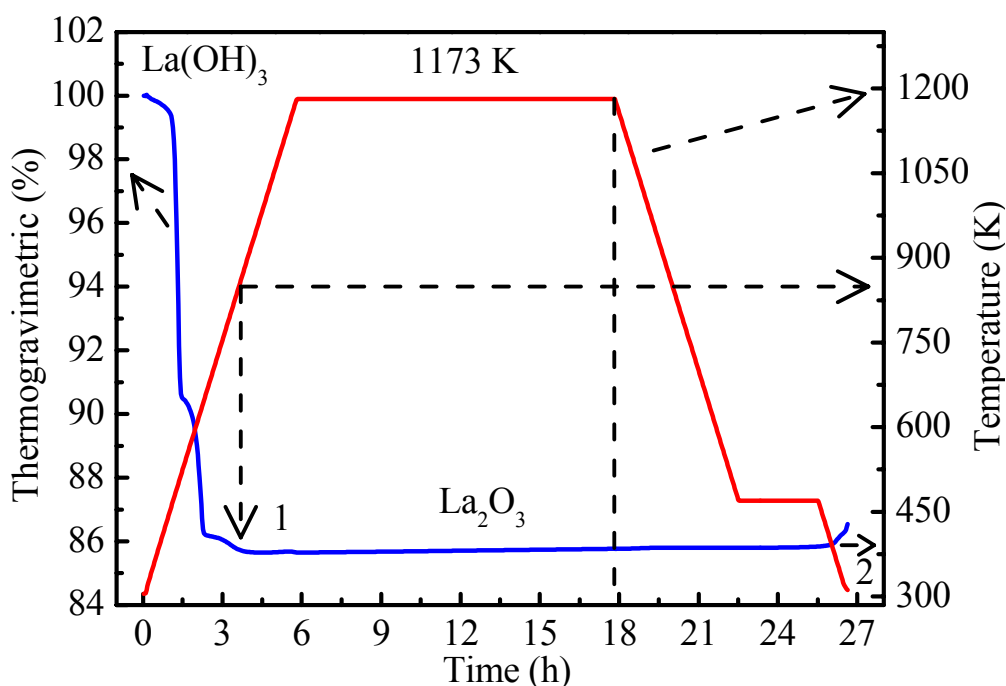


Figure 5.4: Thermogravimetric analysis of $\text{La}(\text{OH})_3$ transformed from La_2O_3 through the ~ 2 h exposure to air.

to air for ~ 2 h, which of course depends on the moisture capacity in the air. This fact was confirmed by the thermogravimetric analysis (TGA) of $\text{La}(\text{OH})_3$ obtained above. In figure 5.4, when the time is below ~ 17.8 h, the dry atmosphere of (79% Ar + 21% O_2) was used to simulate the air; while above 17.8 h, ~ 20 mbar H_2O was artificially added in order to simulate the actual wet air and check the possibility of the transition from La_2O_3 to $\text{La}(\text{OH})_3$. At the point 1 as shown in figure 5.4 corresponding to the temperature of ~ 850 K, the weight decrease of $\text{La}(\text{OH})_3$ is $\sim 14.31\%$. This decrease is well consistent with the ratio of $3\text{H}_2\text{O}/(\text{La}_2\text{O}_3 + 3\text{H}_2\text{O}) = 3 \times 18.02 / (325.81 + 3 \times 18.02) = 14.23\%$, which once more confirms that the exposure of dried La_2O_3 to air resulted in a complete transition from La_2O_3 to $\text{La}(\text{OH})_3$. On the other hand, when fired $\text{La}(\text{OH})_3$ transformed back to La_2O_3 . At the point 2, i.e. 390 K, pure La_2O_3 began to absorb water and change into $\text{La}(\text{OH})_3$. Another surprising fact is that XRPD measurement of La_2O_3 normally stored in a plastic bottle in air displays the existence of a mixed phase ($\text{La}_2\text{O}_3 + \text{La}(\text{OH})_3$) (top of figure 5.3). Chemical analysis by ICP-OES and infrared detection reveals that the actual formula of this mixed phase is $\text{La}_{2.00(6)}\text{O}_{3.98(7)}$. According to this result, the calculated ratio of $\text{La}(\text{OH})_3$ in the mixed phase is $\sim 36.8\%$. Consequently, La_2O_3 can easily absorb moisture in air and then transforms into $\text{La}(\text{OH})_3$. This fact could explain the phenomenon that some bulk manganites related to La automatically decompose into powder after long time exposure to air. Thus the purpose of pre-firing La_2O_3 is not only for decarbonization but also for dehydration. Similar inspections were carried out for MnO_2 and SrCO_3 and one good method for material storage was obtained.

In this dissertation, La_2O_3 was pre-fired in air at 1173 K for 12 h and quickly weighed at ~ 473 K. MnO_2 and SrCO_3 were always kept in dry atmosphere at 388 K. The phase purity of all raw materials was checked by XRPD at room temperature.

5.2.2 Mixing and milling time

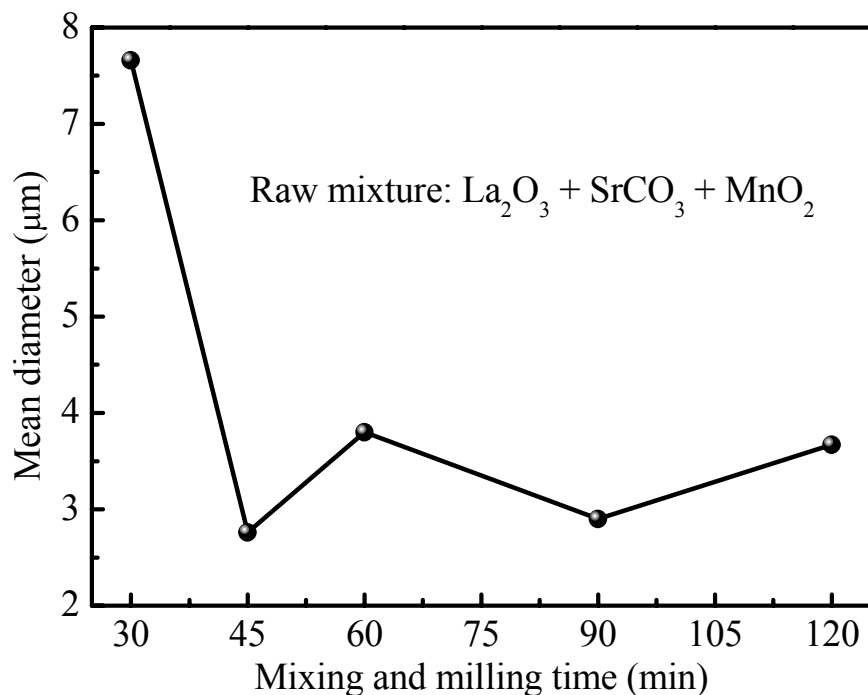


Figure 5.5: Mean diameter of a raw mixture of La_2O_3 , SrCO_3 and MnO_2 for the synthesis of $\text{La}_{7/8}\text{Sr}_{1/8}\text{MnO}_3$ versus ball mixing and milling time.

The goal of mixing and milling raw and intermediate reaction materials with ZrO_2 balls in distilled water or propanol-2 solvent is to get fine grains ($0.5\text{--}4\ \mu\text{m}$) with a narrow and monomodal size distribution [137]. This can maximize the surface contact areas of reactants and hence increase the reaction rates. Any large deviation from the averaged grain size will later result in a possible inhomogeneous reaction state.

The particle size of a raw mixture ($\text{La}_2\text{O}_3 + \text{SrCO}_3 + \text{MnO}_2$) for the synthesis of stoichiometric $\text{La}_{7/8}\text{Sr}_{1/8}\text{MnO}_3$ after different mixing and milling time with the same speed of 200 rpm was analyzed by a particle size analyzer (Mastersizer microplus, version 2.18) whose accuracy is $\pm 1\%$. The results are shown in figure 5.5. As the increase in mixing and milling time, the mean diameter of the mixtures is steeply decreased before 45 min and then becomes nearly constant even up to 120 min. The fluctuant change after 45 min results from the random sampling, which to a turn illustrates the difficulty in getting a homogeneous size distribution. Therefore, the time of 60 min was chosen as the appropriate mixing and milling time for this synthesis. Longer milling time could lead to a more inhomogeneous size distribution and possible contaminations from ZrO_2 balls and container.

In this dissertation, all the syntheses were accompanied by proper mixing and milling after each firing and by isostatic pressing at high enough pressure for sintering (chapter 6.2). This led to dense ($\sim 85\text{--}92\%$ of the theoretical densities) and homogenous samples and ensured a complete reaction.

5.2.3 Reaction temperature and time

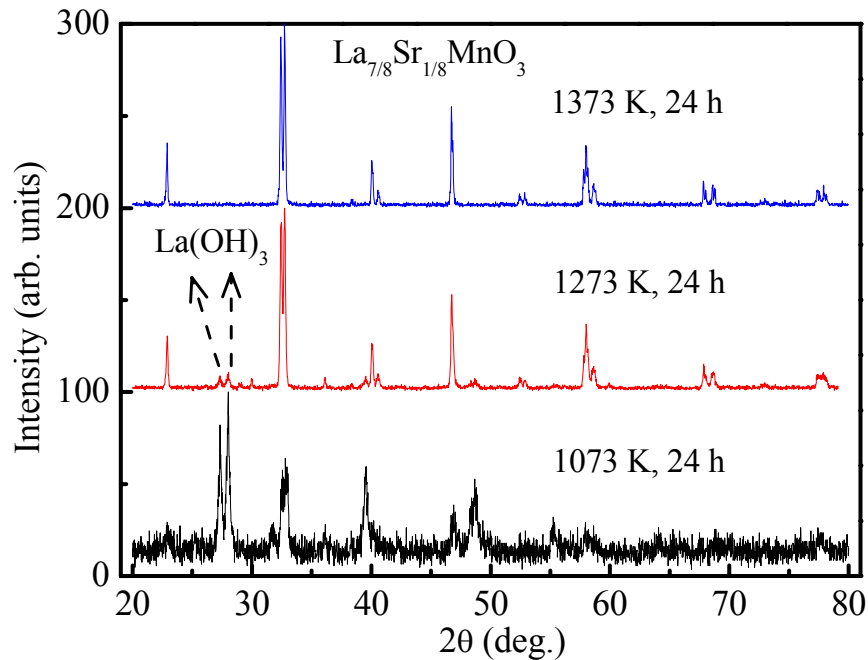


Figure 5.6: XRPD patterns of $\text{La}_{7/8}\text{Sr}_{1/8}\text{MnO}_3$ calcined at temperatures of 1073 K (bottom), 1273 K (middle) and 1373 K (top), respectively, for 24 h at each temperature.

In order to determine the right reaction temperature and time appropriate for the synthesis of $\text{La}_{7/8}\text{Sr}_{1/8}\text{MnO}_3$, a set of polycrystalline samples was prepared. They were calcined in air at 1073, 1273, 1373 and 1473 K, respectively, for 24 h at each temperature. The sample calcined at 1373 K was divided into three parts. They were sintered at 1473, 1573 and 1673 K, respectively, for 24 h at each temperature. All samples were characterized by XRPD and SQUID with the same measuring parameters.

When the calcining temperature is below 1373 K, the trace of $\text{La}(\text{OH})_3$ was always detected as shown in figure 5.6, which was transformed from the residual La_2O_3 in reactants through absorbing moisture in air below 390 K (TGA). It is uncertain that this kind of sample contains unreacted Sr or Mn compounds if their amounts are beyond the detection limit of XRPD method. Such an uncompleted reaction results in non-stoichiometric manganites, e.g. the deficiency of La sites, the increase of Mn^{4+} percentage, T_c and oxygen content, etc. The two calcined samples above 1373 K and all sintered samples belong to rhombohedral structure at room temperature. No unreacted La, Sr or Mn compounds were detected in them.

The magnetization data of all samples are shown in figure 5.7. The effect of uncompleted reaction below 1373 K on magnetization is clearly displayed. Though XRPD measurements show the same structure type for samples heated above 1373 K, there are big differences in their magnetization data, especially in the temperature range of the transition from paramagnetism to ferromagnetism. As the increase in temperature, the above transition becomes sharper and sharper, especially after sintering. This indicates that the step of sintering is indispensable to obtaining a homogenous reaction state.

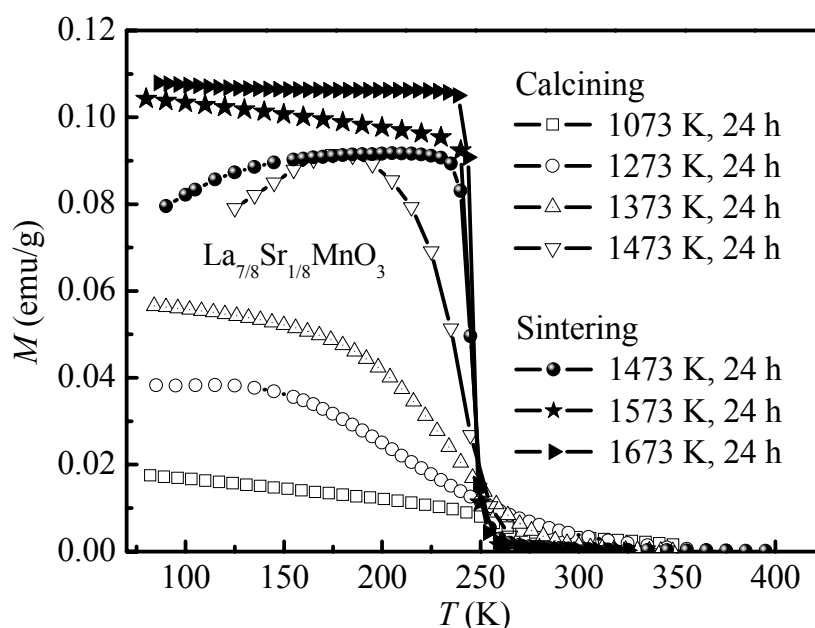


Figure 5.7: Zero-field cooling (ZFC) magnetization M measurements (10 Oe) for calcined and sintered $\text{La}_{7/8}\text{Sr}_{1/8}\text{MnO}_3$ at different temperatures for 24 h at each temperature.

Similar experiments were carried out to explore other synthesis conditions, e.g. the reaction time. Based on all characterizations, it is concluded that the route of two times calcination at 1373 K for 12 h and two times sintering at 1573 K for 12 h is a good recipe to obtain a complete reaction with a homogeneous resultant.

Since the speed of a chemical reaction depends on the temperature and the particle size of reactants, the reaction temperature should be high enough. However, at the same time the problem of sublimation, e.g. Mn_3O_4 whose melting point is 1863 K, becomes more severe, especially for the calcination step due to the low density state without pressing. It is well known that the sublimation of elements or their compounds depends on the temperature, pressure and the relative density. The lower the density, the more likely the sublimation can occur. This makes it difficult to obtain the precise stoichiometry. An alternative route is the sol-gel method [138, 139]. Its advantage is that perovskites can be synthesized at relatively lower temperatures and shorter times due to the smaller size of reactants resulted from solutions. With this method, Dutta *et al.* [8] have successfully prepared single-phase nanocrystalline $\text{La}_{7/8}\text{Sr}_{1/8}\text{MnO}_3$ samples that show an interesting glasslike behavior. La_2O_3 , SrCO_3 and MnO_2 were all converted to their corresponding soluble nitrates. La_2O_3 and SrCO_3 were readily soluble in dilute nitric acid; however, MnO_2 had to be converted to Mn oxalate first using oxalic acid before it could be dissolved in dilute nitric acid. The nitrates were mixed in solution, citric acid was added, and the resulting solution was slowly evaporated to get a pale orange-colored gel. The gel when decomposed at about 573 K resulted in a highly porous black powder. The resulting powder was separated into parts and calcined for 6 h at 973 K, 1173 K and 1473 K. The particle sizes as determined from the x-ray powder data using the Scherrer's formula and the transmission-electron microscopy measurements are 18 nm (973 K), 36 nm (1173 K) and 50 nm (1473 K). The finding of suitable solvents for different starting materials is the prerequisite to successfully utilize the sol-gel method.

5.2.4 Binder effect

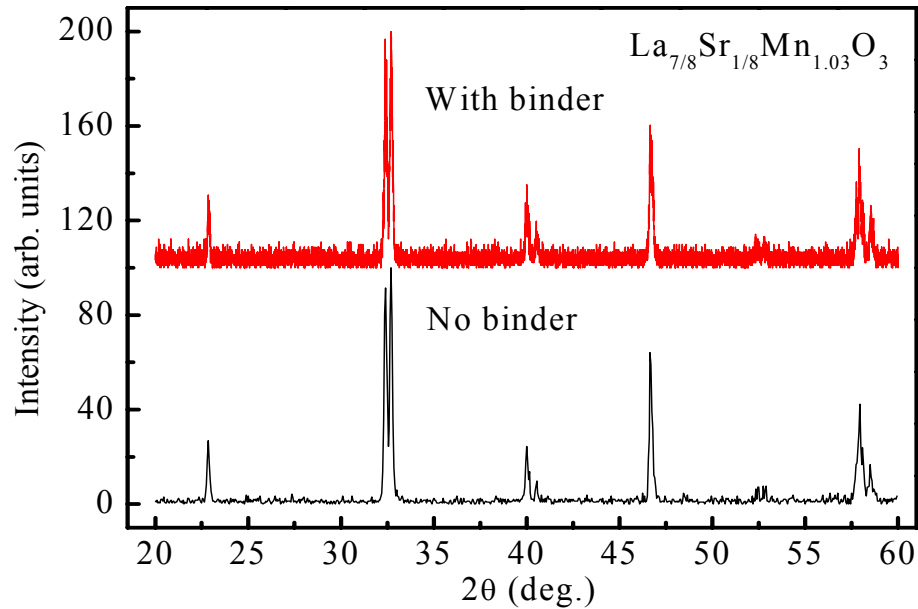


Figure 5.8: XRPD patterns of two sintered $\text{La}_{7/8}\text{Sr}_{1/8}\text{Mn}_{1.03}\text{O}_3$ polycrystals. In the processes: with (top) and without (bottom) binder.

Organic binder is often used in the processing of ceramics from powder to dense counterpart. They easily adsorb to the particle surfaces, improving particle packing. As a consequence, the reaction process is accelerated, decreasing production cost. During subsequent heating, the organic binder can be vaporized, leaving behind little or no residue.

One control experiment has been carried out to test the binder (water-soluble PAF 35F) effect. ~ 10 g $\text{La}_{7/8}\text{Sr}_{1/8}\text{Mn}_{1.03}\text{O}_3$ was prepared. After two times calcination at 1373 K for 12 h, the resulting powder was divided into two parts. They were pressed into pellets with and without binder, respectively. After once simultaneous sintering at 1573 K for 18 h with a simultaneous preheating at 873 K for 6 h to burn off the binder, the two samples were characterized by XRPD and SQUID with the same measuring parameters. The structure is rhombohedral at room temperature for both samples as shown in figure 5.8. However, the background of XRPD data of the sample with binder is distinctly higher than that of the sample without binder. Figure 5.9 also displays a visible contrast in their magnetization data. It should be pointed out that the increase in T_c in figure 5.9 compared to figure 5.7 comes from the arbitrary addition of 3% excess MnO_2 in the raw materials. The purpose of this arbitrary addition is to prepare polycrystals for single crystal growth. The detailed reasons for the change in T_c will be discussed in chapter 7.3.5. The differences in XRPD and SQUID measurements for two kinds of sample are ascribed to the use of binder.

To summarize, though the application of binder during the synthesis can improve reaction rates, residual adsorption has to be removed at elevated temperatures. This process is often very slow. In this dissertation, except for this control experiment, other

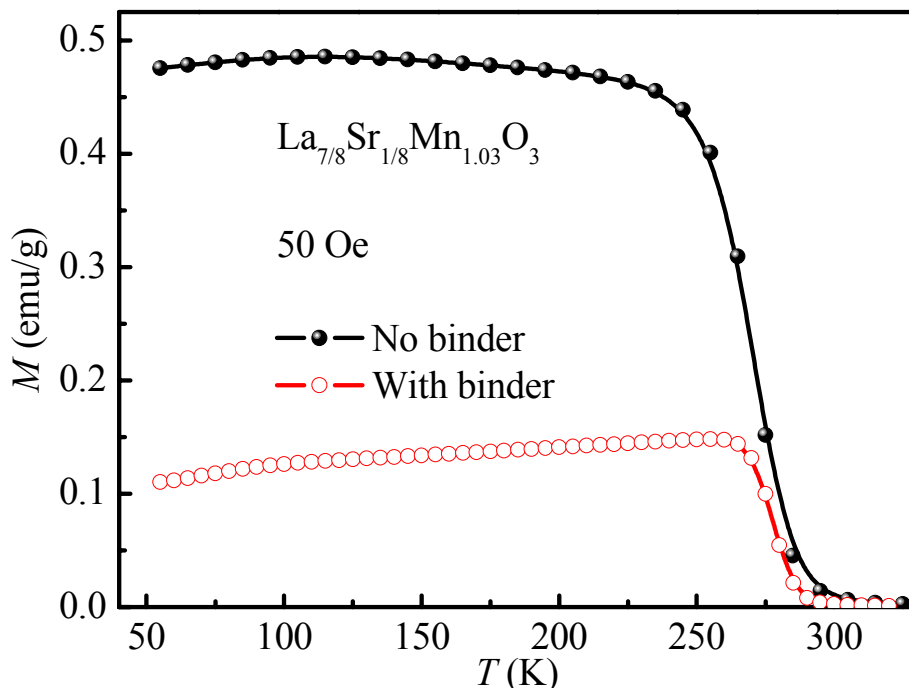


Figure 5.9: ZFC magnetization M measurements of two sintered $\text{La}_{7/8}\text{Sr}_{1/8}\text{Mn}_{1.03}\text{O}_3$ polycrystals. In the processes: with (circles) and without (solid circles) binder.

syntheses did not use any binder. Utilizing the pressing method described in chapter 6.2, dense enough pellets can be prepared without binder.

5.2.5 Other factors

Besides the conditions discussed above, other factors, e.g. concentration of reactants and resultants, pressure (for reactions concerned to gas), annealing (chapter 7), etc, are also important for reactions.

One control experiment, i.e. decomposing SrCO_3 using normal furnace (static air atmosphere) and TGA machine (flowing dry gas mixture of 79% Ar and 21% O_2 at 1 atm, simulating air) was performed. TGA measurement shows that SrCO_3 has been completely decomposed at ~ 1123 K after ~ 6.3 h firing. With normal furnace, I heated SrCO_3 at ~ 1573 K for 8 h. The stoichiometric composition of the resultants measured by ICP-OES and infrared detection methods is $\text{Sr}_{1.00(1)}\text{C}_{0.75(2)}\text{O}_{2.86(2)}$. This indicates that the decomposing ratio is only $\sim 25\%$. The flowing gas can carry the resultant CO_2 out of TGA machine, decreasing CO_2 concentration and thus resulting in the acceleration of the reaction. On the contrary, a gradual increase in CO_2 concentration in normal furnace (always occluded in order to keep stable temperatures) counteracts the decomposing process. Therefore different gas states, static or flowing, have a rather significantly difference in affecting the reaction. This fact is applicable to the synthesis of manganites and can qualitatively explain the effect of annealing.

5.3 Summary

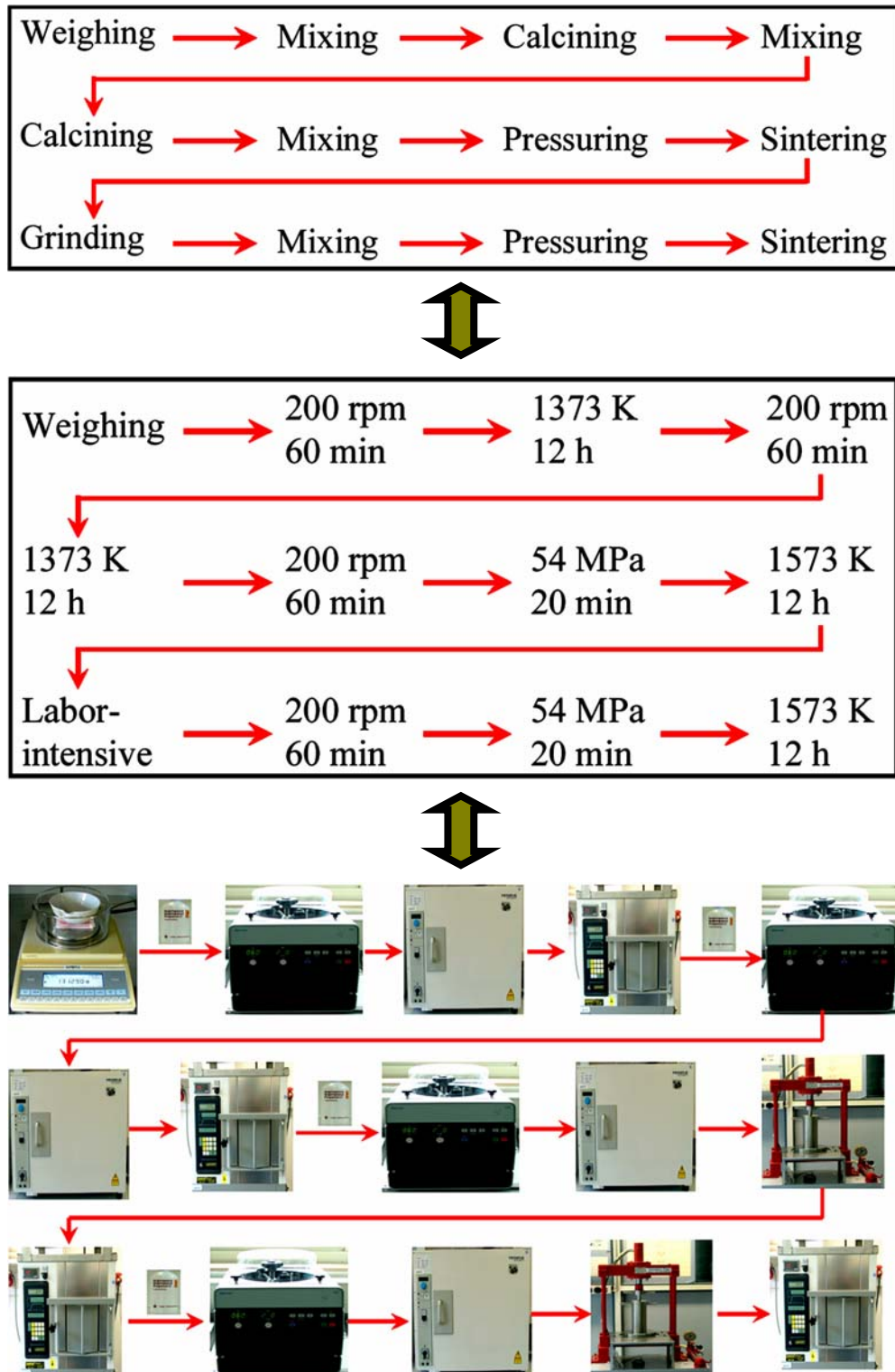


Figure 5.10: (top) Optimum processing route for the synthesis of $\text{La}_{7/8}\text{Sr}_{1/8}\text{MnO}_3$. (middle) Corresponding processing parameters. (bottom) Corresponding apparatuses used in the laboratory for the preparation of electroceramic materials at FZJ GmbH, Germany.

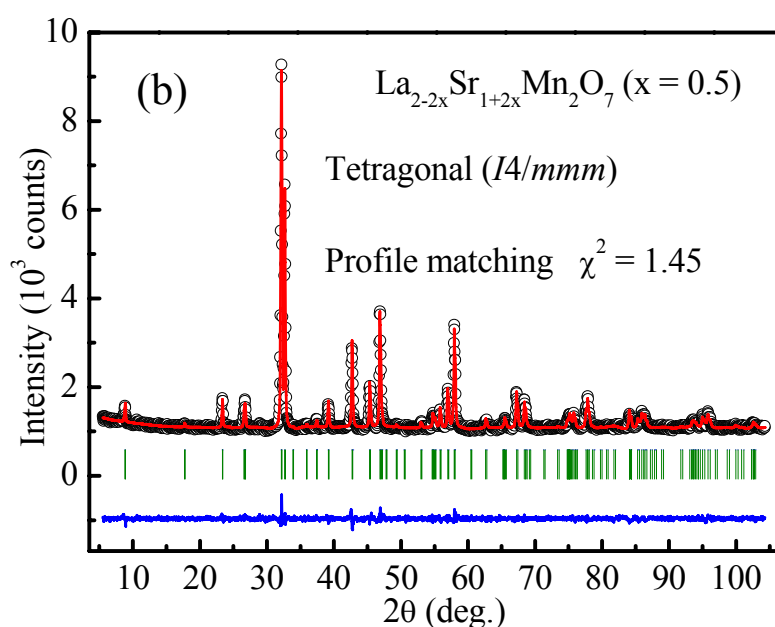
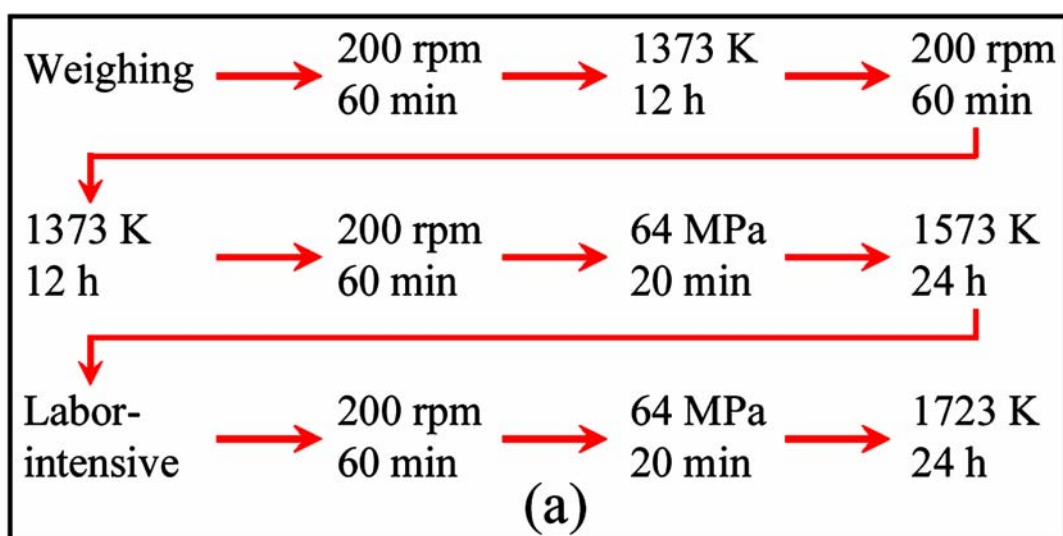


Figure 5.11: (a) Processing parameters for $\text{La}_1\text{Sr}_2\text{Mn}_2\text{O}_7$. (b) Profile matching of the XRPD data of $\text{La}_1\text{Sr}_2\text{Mn}_2\text{O}_7$ at room temperature shows no appearance of impurity phases within the detection accuracy.

Based on hundreds of experiments, a relative good recipe, i.e. two times calcination and two times sintering with mixing and milling after each firing, has been established for preparing high-quality polycrystalline samples as shown in the top of figure 5.10. The middle of this figure shows the corresponding processing parameters for the synthesis of $\text{La}_{7/8}\text{Sr}_{1/8}\text{MnO}_3$ and the bottom corresponds to the instruments used. For other perovskites, the detailed synthesizing parameters, e.g. the reaction temperature and time, can be obtained by the exploration as executed in this chapter for $\text{La}_{7/8}\text{Sr}_{1/8}\text{MnO}_3$. The preparation of perovskite materials is a hard work; in my option, the price of any inappropriate jerry-synthesis is the waste of much more valuable time.

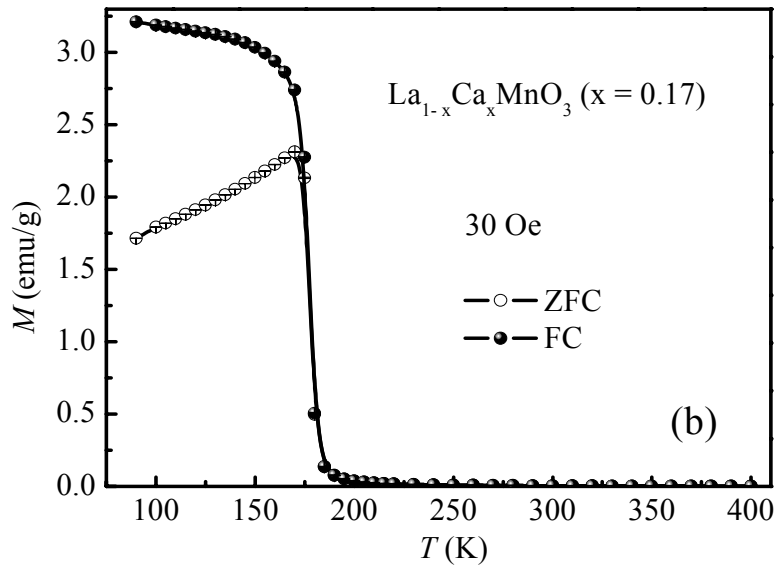
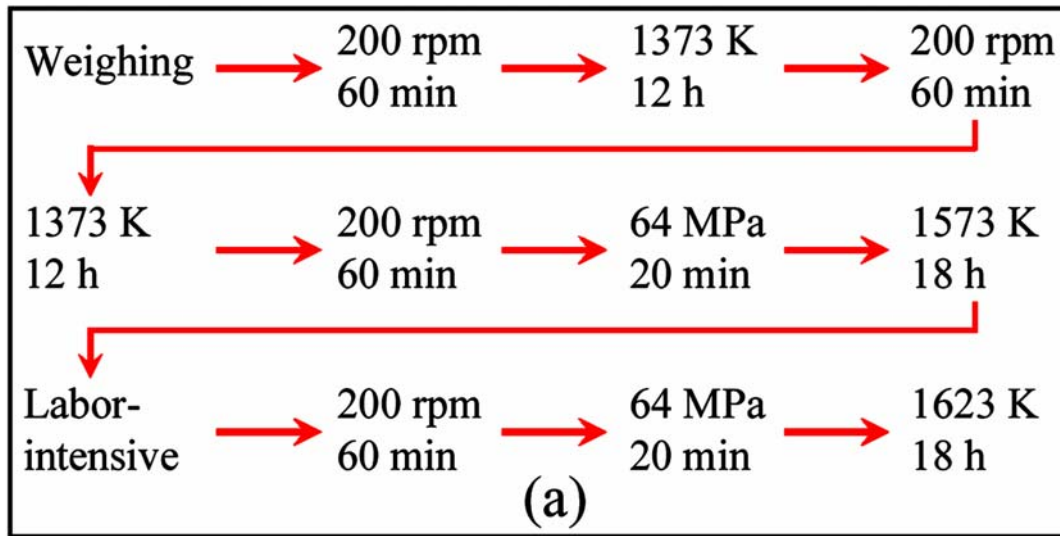


Figure 5.12: (a) Processing parameters for $\text{La}_{0.83}\text{Ca}_{0.17}\text{MnO}_3$. (b) ZFC cooling and field cooling (FC) magnetization M measurements for $\text{La}_{0.83}\text{Ca}_{0.17}\text{MnO}_3$.

Two samples of $\text{La}_1\text{Sr}_2\text{Mn}_2\text{O}_7$ and $\text{La}_{0.83}\text{Ca}_{0.17}\text{MnO}_3$ were prepared using the above optimized preparation route to test its applicability. The double-layered $\text{La}_1\text{Sr}_2\text{Mn}_2\text{O}_7$ manganite was thought to be difficult to synthesize into a single phase. Such that quenching the sintered pellets into dry ice or liquid helium [140] was used to keep the high-temperature phase. However, using the above recipe, it is easy to get a single phase without any quenching or post-annealing as demonstrated in figure 5.11(b). Figure 5.12(b) shows a right and very sharp phase transition for $\text{La}_{0.83}\text{Ca}_{0.17}\text{MnO}_3$ indicative of a very good sample quality. Figures 5.11(a) and 5.12(a) describe the respective processing parameters for $\text{La}_1\text{Sr}_2\text{Mn}_2\text{O}_7$ and $\text{La}_{0.83}\text{Ca}_{0.17}\text{MnO}_3$, respectively. The preparation route of two times calcination and two times sintering seems to be a universal recipe for the synthesis of perovskite manganites, at least for the present testing.

Chapter 6

Floating zone crystal growth of CTMO

6.1 Overview

Since single crystals maintain translational symmetry over macroscopic distances, in contrast with polycrystals, they can give us more reliable information of the structures and intrinsic properties. Therefore, many research scientists starve for a wide variety of single crystals, e.g. CTMO, high T_c superconductors, giant magnetoresistance materials, etc, in order to investigate the fundamental intriguing physics by employing the most advanced synchrotron x-ray and neutron scattering techniques, and so forth. The requirement of these techniques for the quality of single crystals (e.g. size, purity, etc.) is quite rigorous. The lack of large single crystals of CTMO has been a longstanding obstacle in the study of their fascinating physical properties.

A number of single crystal growth techniques have been used for years, e.g. floating zone (FZ), Czochralski, Bridgman, top seeded solution and gas-phase growth, etc. Table 6.1 compares two often used methods: Czochralski and FZ growth. Compared to others, the FZ method with infrared image furnace is a particularly useful one for laboratory crystal growth for preparing research samples because it is crucible-free and thus the grown crystals show the highest purity (the property of single crystals is very sensitive to the purity). The FZ method is thus widely used to grow a wide range of refractory single crystals of CTMO.

Under ideal external physical conditions, the biggest grain inside one polycrystal spontaneously grows on the expense of the smaller ones around it if the active energy is enough. In this way, it gets larger and larger. The amount of grain boundaries becomes smaller and smaller as the gradual increase in the grain size. The final state, single crystal, keeps the lowest energy. Thus it is the stablest state.

Not every compound can be formed easily. It strongly depends on the change of the Gibbs free energy of the reaction ($\Delta G < 0$, favorable; $\Delta G > 0$, unfavorable). In the earlier stages of crystal growth for a new system, it is absolutely necessary to know or to explore the phase diagram for assessing the feasibility of single crystal formation and choosing the appropriate growth parameters. Most of the CTMO have high melting points [141]. The valence state and the degree of stoichiometry of CTMO are very sensitive to the synthesis conditions [142]. Especially, they may decompose near their melting temperatures. Thus they have to be grown under controlled atmospheres with a high

Table 6.1: Comparison of two single crystal growth methods: Czochralski and Floating-zone.

Methods	Czochralski	Floating-zone
Purity	Poor	Highest
Crystal size	Large diameters easy; Large weights	Large diameters possible; Reasonable weights
Mechanical conditions	Gravity stabilizes melt and crystal	Gravity destabilizes melt and crystal; Rotation speed is critical
Thermal condition	Small gradients	Large gradients

enough pressure [143]. To grow large high-quality single crystals of CTMO continuous to be a real challenge for material scientists.

The multidisciplinary nature of single crystal growth makes it lack of scientific understanding [144], though some simulations have been performed [145]. It is thus regarded as more of a craft, or even an art than a science. This chapter is dedicated to this art.

6.2 Preparation of longer and stronger rods

To grow high-quality single crystals, the first and the most important step is to prepare the feed and seed rods. The length of ~2-3 cm for a seed rod is enough, while the longer the better for a feed rod within the limitations of apparatus.

Figure 6.1 schematically shows the process of rod preparation using the usual lopsided pressurizer. First, one has to put the powder material (black) into the mold B, and then increases the pressure N to 30-70 KN using the pressurizer A. After about ten minutes, the powder material will be pressed into a rod with the shape of the mold. The rod prepared in this way has the length of at most ~6 cm (C). With more powder, i.e. a longer rod, it will crack easily (D) due to the inhomogeneously pressed state. Having been sintered, the density of the rod is about 60-75% of the theoretical one, depending on the pressure and the sintering temperature. This method can be manipulated easily and is actually feasible to optimize the powder preparation. However, the rod prepared by this method is not the ideal one for single crystal growth.

Another apparatus for preparing rods is the isostatic pressurizer (A') as shown in figure 6.2. One plastic cylindrical balloon (B') is filled with ~15 g powder material (with fine particle size). One has to remove the air in the filled balloon and then squeeze it with a hydrostatic pressure of 50-70 MPa for about twenty minutes. It is hard to control the initial shape of the evacuated balloon (C'), e.g. the vertical homogeneity, especially at the two ends where the shape is usually irregular and the length perpendicular to the long direction is smaller than the averaged diameter of the rod (the corresponding circle area is decreased). That often results in the crack of the pressed rod (D'). The reason could be

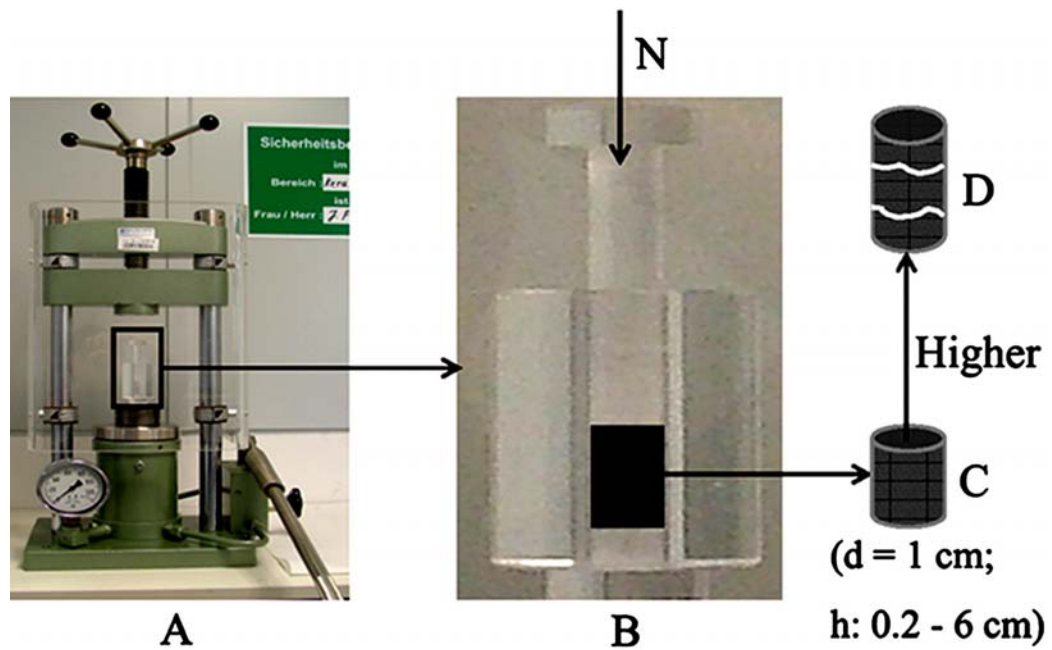


Figure 6.1: Schematic of the short rod preparation using the usual pressurizer.

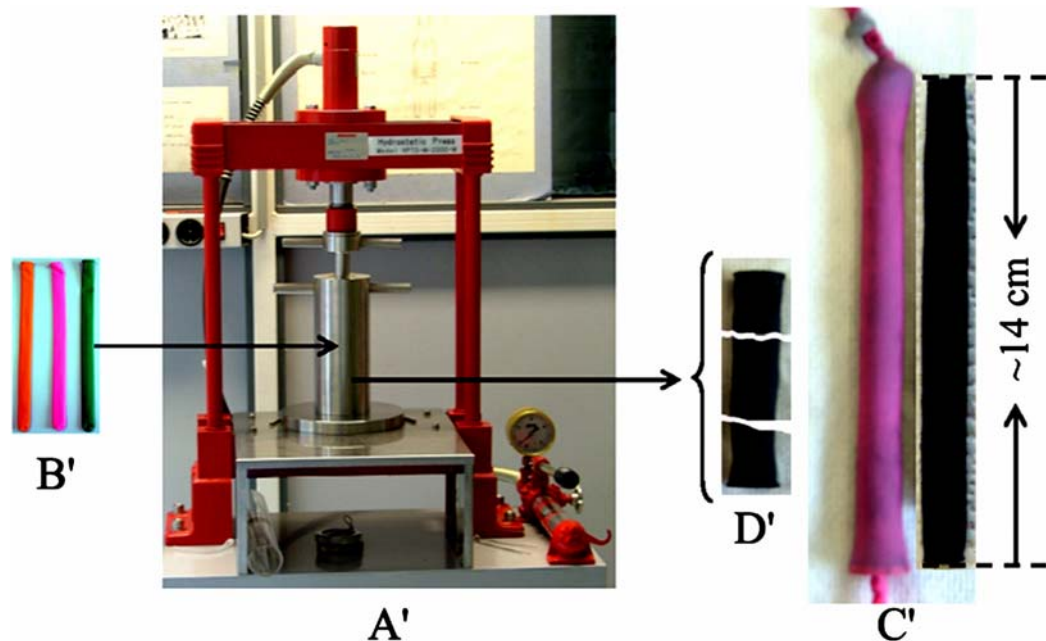


Figure 6.2: Schematic of the long rod preparation using the isostatic pressurizer.

that the added force along the long direction is not enough ($\underline{F} = \underline{P}S$, where \underline{F} is the force, \underline{P} is the isostatic intensity of pressure and S is the area perpendicular to the added force). In addition, the longer the rod, the more difficult the force transfers along the long direction. Sometimes, the rod is well pressed along the diameter direction, while in the long direction it is badly done. Before pressing, if we put two suitable flat plates on the

two ends of the quasi rod, the shape of its two ends can be well controlled and thus the force along the long direction can be increased largely and transferred easily. As a consequence, we can prepare the longer (up to ~14 cm) and stronger (the density of the sintered rod is up to 92% of the theoretical one) feed rods with any diameter needed.

A straight and very uniformly densified feed rod [146] with a homogenous composition distribution is absolutely necessary to achieve and keep a perfectly stable melting zone, preventing it from collapse and providing regular melting when the steady-state growth conditions of the FZ are reached.

6.3 Floating zone furnace and crystal growth

The FZ method grows single crystals by holding the melting zone through obtaining a balance between the surface tension and the hydrostatic pressure. The competing of both forces determines the shape of the melting zone. The obtained crystals are free standing and without contamination by crucible material, which compared to other methods ensures the highest purity of the grown crystals.

A new FZ furnace (figure 6.3, Crystal Systems Inc. Model FZ-T-10000-H-VI-VPO) with four IR-heating halogen lamps as the heat source and four ellipsoidal mirrors as the reflectors has been available at FZJ GmbH, Germany, since 2006 and is fully operational for the growth of CTMO. A similar furnace is also available at the Institute for Crystallography of the RWTH Aachen. Four ellipsoidal mirrors focus the infrared radiation on the focal point to result in a localized high-temperature point in the middle of the cavity, achieving crystal growth temperatures up to ~2000°C with a homogenous temperature distribution. Attaining the maximum temperature takes about thirty minutes. The growth environment is either in vacuum or employing three different kinds of working gases (Ar, N₂ and O₂) individually or simultaneously at pressures up to 8.5 bar.

The FZ furnace is schematically shown in detail in figure 6.4, which also involves the special growth steps: (1) cleaning the whole furnace, especially around the upper shaft 1 because most of the evaporated material adheres there; (2) placing the upper shaft 1 and the bottom shaft 2 to the right positions; (3) fixing the feed rod 3 and the seed rod 4 using upper shaft 1 and bottom shaft 2, respectively, after which the two rods must be coaxial; (4) mounting the quartz tube 5 (the thickness of it is different for one-atmosphere and high-pressure growths), inside which the controlled atmosphere 6 for different growths can be used; (5) placing the two rods very close together so that the point of contact is at the center of the maximum temperature point; (6) gradually increasing the power of the halogen lamp 7 and individually rotating the two shafts oppositely (rotation speed: ~20-40 rpm, which can lead to a uniform composition distribution during growth and guarantee a homogenous temperature distribution in the melting-zone, producing a straight cylindrical crystal); (7) the focused radiation heat by the ellipsoidal mirror 8 will develop a liquid solvent phase called melting zone 9 which is suspended between two rods; (8) moving the two shafts with respect to the mirrors (the speeds are particularly important and different for various compounds) slowly down, the feed rod will be dissolved little by little while the material will solidify on the top of the seed rod; (9) hopefully, after long-time growth, the crystal 10 grown will become single crystalline; (10) after growth, normally some of the evaporated material 11 has sublimated on the wall of the quartz tube.



Figure 6.3: FZ furnace operated at FZJ GmbH, Germany.

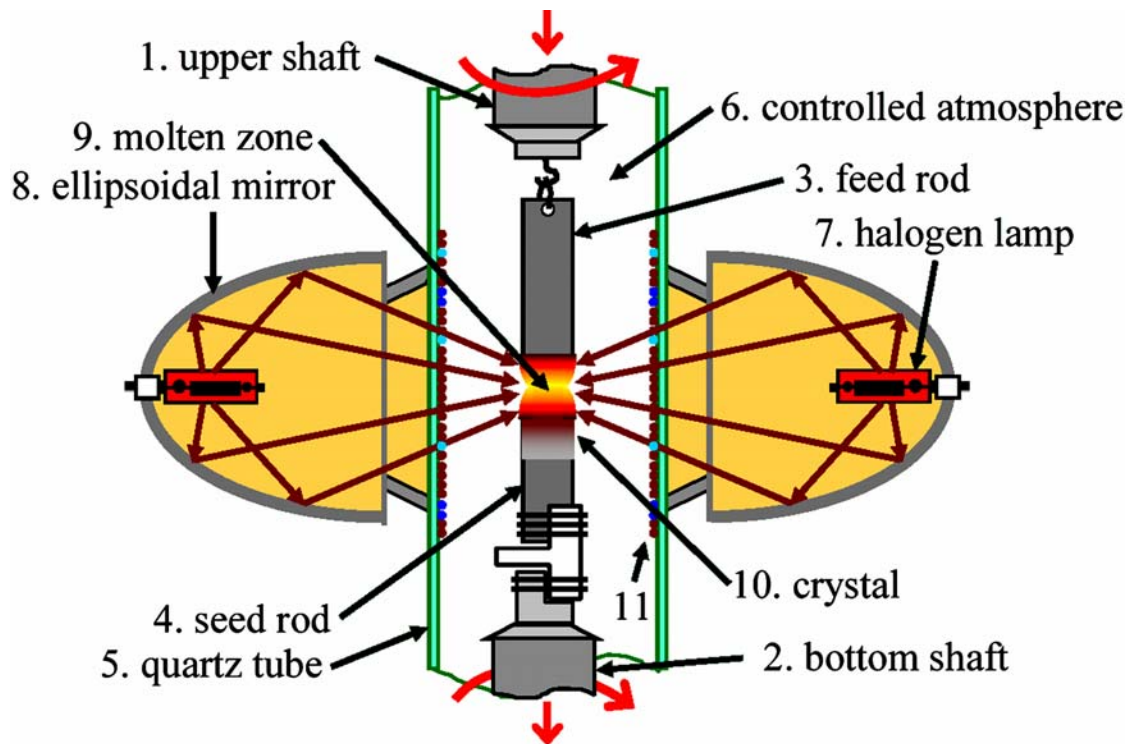


Figure 6.4: Schematic sketch of the FZ furnace and the growth process.

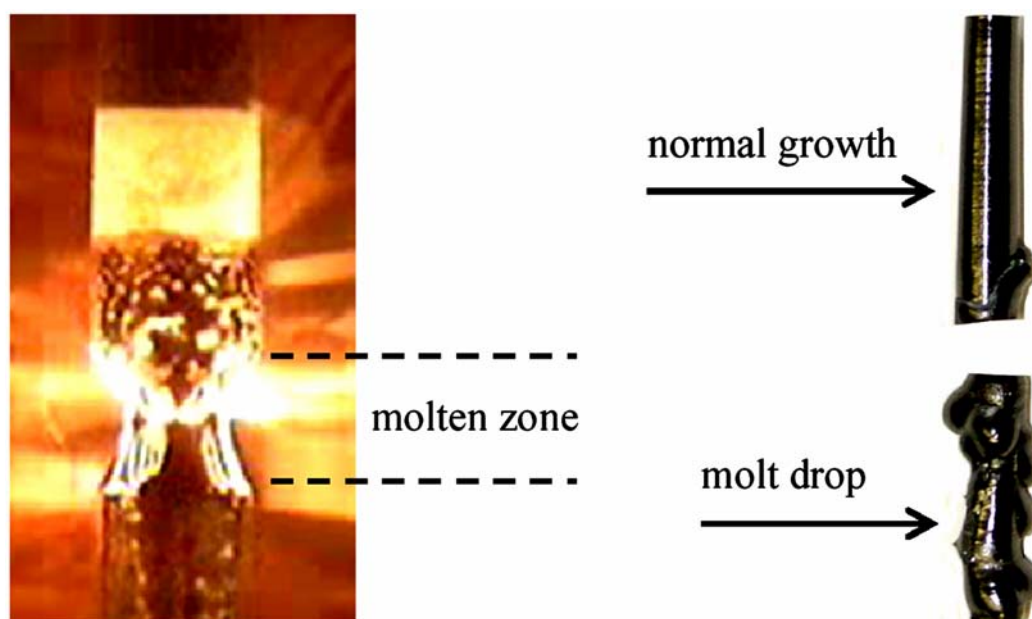


Figure 6.5: (left) An image of a stable melting zone [147]. (right) The crystals grown under a stable state (normal growth) and an unstable state (molt drop).

To form and maintain a stable melting zone between feed and seed rods is the prerequisite for normal single crystal growth. The diameter of the crystal grown is usually larger than that of the feed rod due to the pear shaped melting-zone volume. In order to keep a melting zone stable, the mass of the material melted from the feed rod must be equal to the mass sum of the crystalline material on the seed rod and the evaporated material [148]. The length of a melting zone has a maximum [149], above which the melting zone will collapse. The shape of the liquid solid interface near the seed rod is a good indicator to direct the crystal growth [150]. When temperature is right at the melting point of a sample, it is isothermal. If it is concave to the melting zone, the crystal growth can be developed. To achieve this, the speeds of lowering the feed and seed rods should be controlled independently. Decreasing the temperature fluctuation on the melting zone is critical.

An actual picture of a good growth state is shown in the left of figure 6.5. With this normal growth state, we can keep the melting zone quite stable for long time and get a good result of growth (right-top). Otherwise, e.g. the temperature is too high, some big blobs will spill over from the melting zone sometimes, just sticking on the surface or directly resulting in the separation of feed and seed rods (right-bottom). Carefully controlling the temperature (even only several Kelvin) is absolutely important to avoid this problem. Furthermore, there are another two big problems appearing in the crystal growth with FZ method: (i) The evaporation of some elements or their compounds, e.g. manganese, especially when the temperature of a melting zone is close to their boiling temperatures. Some of the evaporated material deposits on the cold wall of the quartz tube. After growth, it can be collected and identified (XRPD) if enough amount is available. This is the important information to optimize the crystal growth. This problem can be diminished by using a high-pressure atmosphere or arbitrarily adding somewhat excess raw material to compensate for the mass loss by evaporation during melt growth. (ii) The

formation of cracks in crystals grown. This can be diminished by choosing an appropriate growth speed [151] and prolonging the process of cooling to room temperature after growth.

6.4 Necking technique

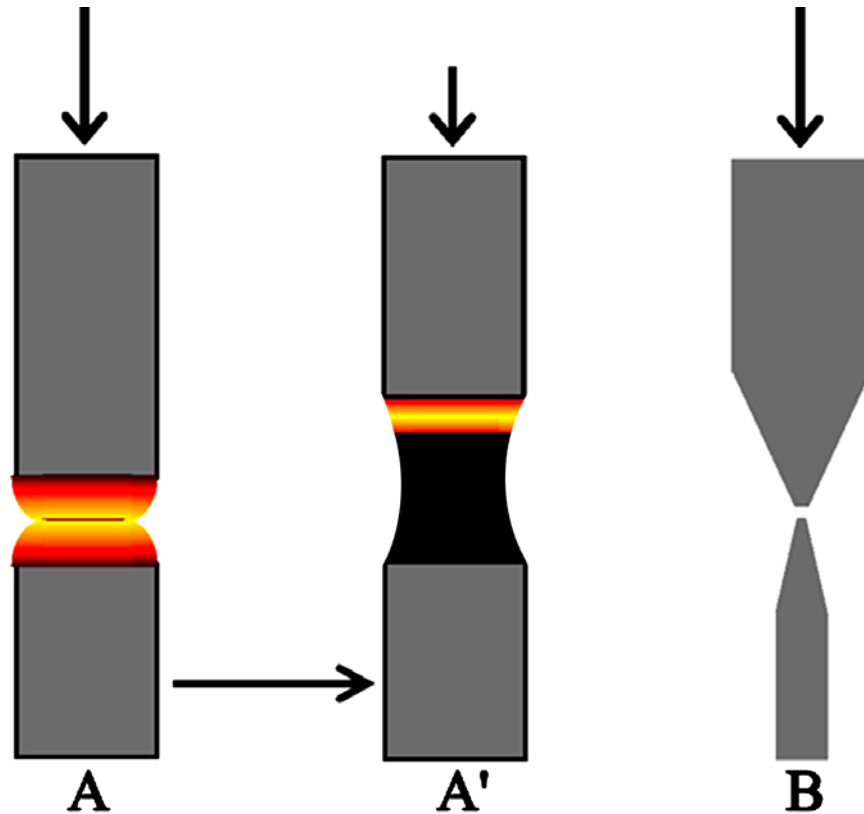


Figure 6.6: Schematics of the necking technique (A and A') and the initial shape of feed and seed rods (B).

For a new compound, the initial crystal growth has to be performed on the polycrystalline seed rod. This makes the crystal growth much more difficult because a polycrystal has too many spontaneous nucleation sites.

Figure 6.6 (A and A') shows one method named necking technique used to select one seed grain. After forming a stable saturated liquid FZ between feed and seed rods (A), we reduce the lowering speed of feed rod whilst keeping that of the seed rod higher. This step makes the crystallization export from the melting zone to the seed rod larger than the solvent import from the feed rod to the melting zone. Thus, the diameter of the grown part will become smaller and smaller. This process is continued until the diameter is $\sim 2\text{-}3$ mm. Then we can recover the lowering speed of feed rod little by little (A'). The purpose of this technique is to grow a small perfect single crystal (during the process of decreasing diameter) around which we can later grow a larger one. However, this technique is very hard to manipulate. It entails slow and painstaking work. Practice makes perfect.

Only experienced crystal grower can do it.

An alternative method is shown in figure 6.6 B, i.e. arbitrarily reducing the contact area between feed and seed rods through designing proper end shapes. The shape designed here for feed and seed rods (already tested in our growths) can not only decrease the dislocation density, improving the crystal perfection, but also decrease the axial temperature gradient for seed rod, especially in the top part.

Both methods have a similar effect on improving crystal quality. For growing a larger single crystal, it is essential that the seed rod used for growth should be single crystalline [152]. In this case, a good single crystal growth mode can be developed. Such a kind of seed crystal can be obtained from the single crystal grown previously.

6.5 Characterizations

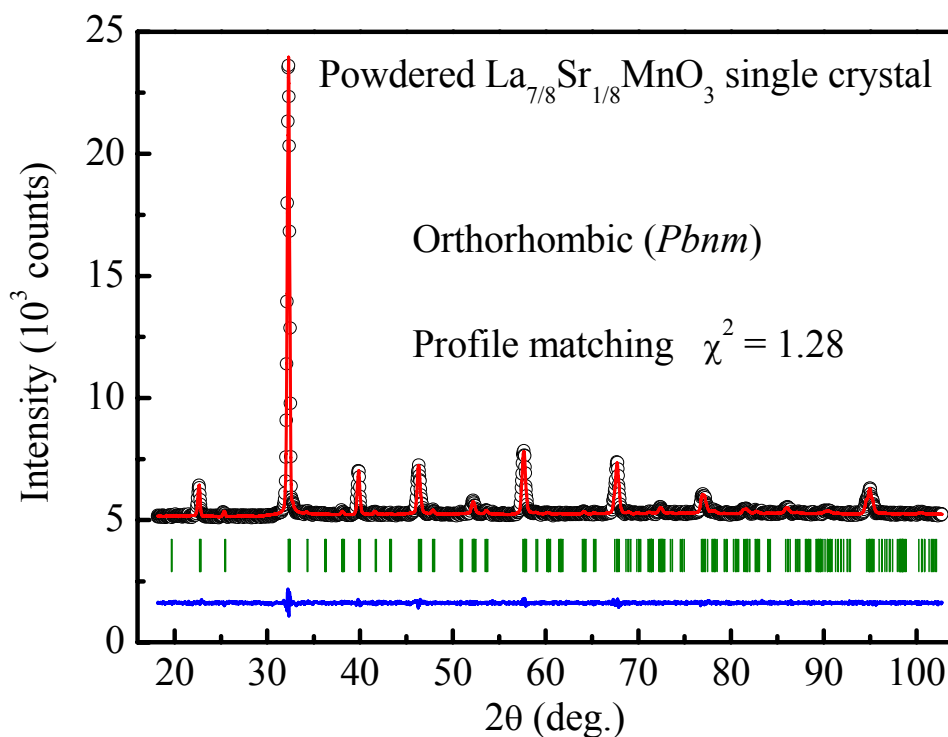


Figure 6.7: Profile matching of the XRPD data of a powdered $\text{La}_{7/8}\text{Sr}_{1/8}\text{MnO}_3$ single crystal at room temperature shows no appearance of impurity phase within the detection accuracy.

Accurate characterization is quite indispensable to optimize the crystal growth, e.g. crystal composition, especially the oxygen content measured by iodometric titration method, high sensitivity TGA or ICP-OES and infrared detection methods, phase purity and structures determined by XRPD (figure 6.7), SQUID (figure 6.8) and physical property measurements (PPMS), etc.

According to the feedback of characterizations on the properties of crystals, we can improve the quality and size of the crystals by adjusting and changing the growing parameters. For example, from the measurement of oxygen content in grown crystals we

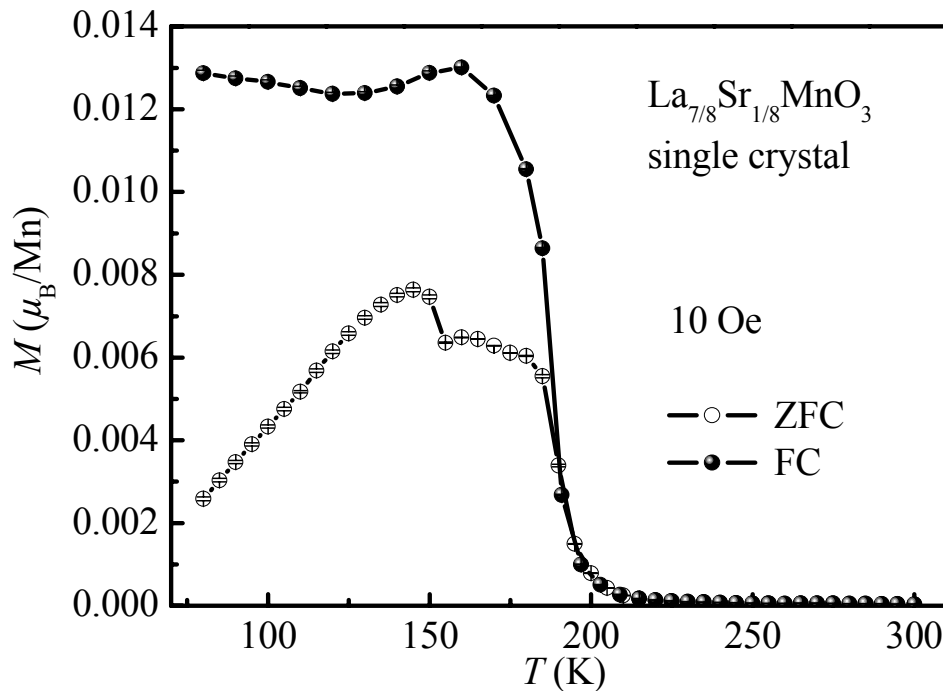


Figure 6.8: Magnetization M measurement with SQUID shows that there are the expected and sharp phase transitions, indicating a good quality of the single crystal.

can adjust the concentration of oxygen gas in the growing environment; from the observation of the crack degree we can change the growth speed and so on.

After obtaining a single crystal, it can be oriented to a particular crystal direction by Laue camera, cut into desired shapes by diamond cutter and polished in the determined orientation by a polishing machine for various subsequent measurements. Different studying techniques demand different single crystals, e.g. the measurements of magnetic and transport properties by PPMS require a high-purity small single crystal, the structure determination by powder diffraction needs a powdered single-crystalline sample, resonant x-ray diffraction demands the single crystals with good surface quality and a large volume ($\sim\text{cm}^3$) is the prerequisite for neutron scattering in order to get a good experimental signal.

6.6 Summary

The procedure of single crystal growth by FZ method is summarized as follows:

- (1) Weighing, ball mixing and milling and calcining the raw powder materials using the method described in detail in chapter 5.
- (2) Isostatic pressing the precursor powder materials into desired feed and seed rods and sintering them.
- (3) Carefully mounting and pre-melting the sintered rods.
- (4) Choosing the suitable growth parameters and forming a stable melting-zone.
- (5) Crystal growth by lowering the feed rod and the seed rod independently.



Figure 6.9: One manganite crystal grown at Institut für Festkörperforschung, FZJ GmbH, Germany.

To explore and optimize the growth parameters for a special kind of material usually takes a long time. You have to change one parameter a time. This process strongly depends on your experience. Thus single crystal growth is a time-consuming and labor-intensive project. However, once you acquire the optimal conditions, it can be grown as a batch production.

Utilizing the FZ method, so far series of single crystals of $\text{La}_{1-x}\text{Sr}_x\text{MnO}_3$, $\text{La}_{1-x}\text{Ca}_x\text{MnO}_3$, TbMnO_3 and GdMnO_3 have been grown successfully with good quality at FZJ GmbH, Germany [153]. Figure 6.9 shows one representative $\text{La}_{0.83}\text{Ca}_{0.17}\text{MnO}_3$ single crystal. We will continue to focus on the growth of large, high-quality single crystals of CTMO, metals and alloys and to explore some new interesting compounds by the FZ and CZ techniques. With them, the electronic and magnetic properties have been investigating by complementary neutron and synchrotron radiation x-ray scattering methods at the instruments of the neutron source at FRJ-II in Jülich (substitution is the JCNS-Jülich Center for Neutron Science in Munich), at the Institute Laue-Langevin (ILL) in Grenoble, at the Synchrotron Radiation Sources in Berlin (BESSY), Grenoble (ESRF) and Argonne, USA (APS).

Chapter 7

Crystal and magnetic properties of $\text{La}_{7/8}\text{Sr}_{1/8}\text{Mn}_{1\pm\gamma}\text{O}_{3+\delta}$ polycrystals

7.1 Introduction

$\text{La}_{1-x}\text{Sr}_x\text{MnO}_3$ is one of the most interesting systems in doped perovskite-type oxides. Recently Hemberger *et al.* [7] have reported the phase diagram of structural, magnetic and electronic properties obtained from investigations of $\text{La}_{1-x}\text{Sr}_x\text{MnO}_3$ single crystals (figure 7.1). This phase diagram is extremely rich. Small changes in external parameters (temperature and doping level) lead to huge changes in the order and physical properties, since the delicate balance between the different degrees of freedom is shifted. At low doping levels $0.1 \leq x \leq 0.15$, this system is a FM insulator, although the canted AFM insulator phase ($x \leq 0.1$) appears to persist up to $x = 0.15$ [2]. For nominal doping level $x = 0.125$ at ambient conditions, the single crystal has an orthorhombic (O) structure [6, 154], but for polycrystalline samples, depending on the preparation methods, different authors [3, 4] have reported either O or rhombohedral (R) structures. Dutta *et al.* [8] have reported the synthesis of nanoparticle $\text{La}_{0.875}\text{Sr}_{0.125}\text{MnO}_3$ samples that have the R structure using the sol-gel method. For the same nominal Sr doping level $x = 0.125$, the structural and magnetic properties reported in the literature [3, 4, 6, 8, 154-157] differ substantially, strongly ascribed to the different preparation methods and synthesis conditions. Normally the Curie temperature T_c of samples with the R structure is a little higher than the T_c of samples with the O structure. It is worth to point out that the difference in T_c of manganites with the same nominal doping level reported in literature is due to the subtle change in magnetic exchange strength resulting from different synthesizing processes. The detailed reasons will be analyzed subsequently in this chapter.

The structural transitions as a function of temperature for $\text{La}_{0.875}\text{Sr}_{0.125}\text{MnO}_3$ single crystals have been reported [5, 157]. Combined with other reports, the temperature dependent phase transitions for nominal $\text{La}_{0.875}\text{Sr}_{0.125}\text{MnO}_3$ manganite are summarized in table 7.1. At $T \approx 450$ K, a transition from a high-temperature R to an O structure occurs. At $T \approx 270$ K, the O structure distorts to the JT distorted orthorhombic (O') phase. Finally O' transforms into another orthorhombic (O'') structure at $T \approx 150$ K [5, 157], at which the average Mn magnetic moment was refined as $\sim 2 \mu_B/\text{Mn}$. Below $T_c \approx 180$ K, a ferromagnetic metallic (FMM) state appears and then transforms into a ferromagnetic

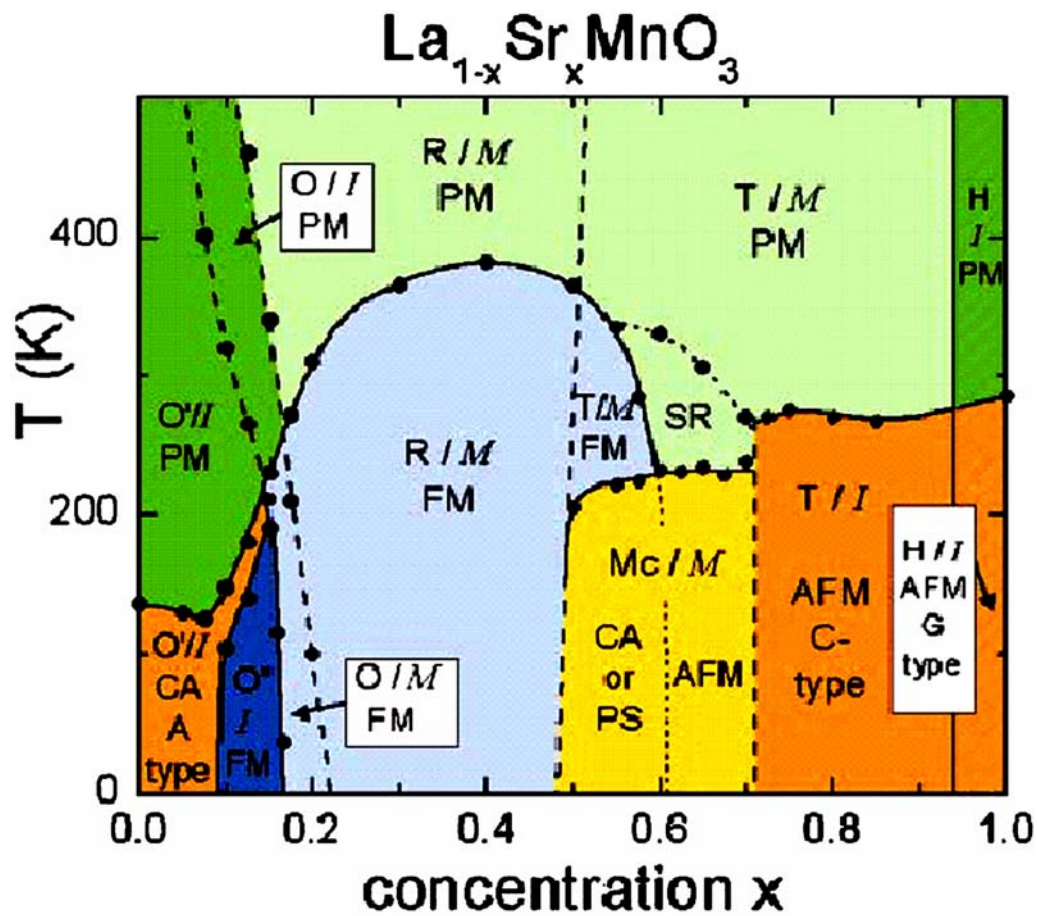


Figure 7.1: Proposed phase diagram for $\text{La}_{1-x}\text{Sr}_x\text{MnO}_3$ manganites [7]. R, O, T, H label the crystallographic phases rhombohedral, orthorhombic, tetragonal and hexagonal. *M* stands for metal, *I* for insulator. Magnetic order is indicated by PM, FM, AFM, CA or PS for paramagnetic, ferromagnetic, antiferromagnetic, canted or phase separated, respectively.

Table 7.1: Temperature dependent phase transitions of nominal single-crystalline $\text{La}_{0.875}\text{Sr}_{0.125}\text{MnO}_3$ (see text).

T (K)	(0, 150)	[150, 180)	[180, 270)	[270, 450)	[450, 900]
Features					
Structure	O''	O'	O'	O	R
Magnetism	FMI	FMM	PMI	PMI	PMI
Others	CO/OO	JT	JT		

insulating (FMI) phase at the temperature of the $O'-O''$ structural transition that is thought to be connected with the charge and orbital order (CO/OO) [5, 6, 9, 154], and the magnetization shows a sudden increase at this temperature. For polycrystalline $\text{La}_{0.875}\text{Sr}_{0.125}\text{MnO}_{3+\delta}$ with an O structure at room temperature, a canted FM order with moments in the crystallographic a - c plane in $Pbnm$ symmetry below $T_c \approx 220$ K was established [3]. The c component of the moment disappears above 220 K, but the a component remains essentially temperature independent with $\sim 1.0 \mu_B$ throughout the temperature range $20 \leq T \leq 220$ K and even up to 300 K. The refined total Mn moment was determined to be $\sim 3.32(7) \mu_B$ at 20 K [3]. The correlation between FM spin orientation and coherent JT distortion was studied [158]. The magnetic structure varies from FM ordered mainly along the b axis ($\text{La}_{0.89}\text{Sr}_{0.11}\text{MnO}_3$, relatively larger coherent JT distortion) to FM almost along the c ($\text{La}_{0.815}\text{Sr}_{0.185}\text{MnO}_3$, without coherent JT distortion due to the hole doping) in $Pbnm$ symmetry. In addition, the parent compound LaMnO_3 undergoes a structural phase transition at $T_{JT} \approx 750$ K [159], above which the OO disappears. On doping with Sr, the JT transition temperature is drastically reduced, becoming $T_{JT} \approx 475$ K at a doping level of 0.1 [160]. However, the R structure known as the high-temperature phase of nominal $\text{La}_{0.875}\text{Sr}_{0.125}\text{MnO}_3$ has received much less attention in the literature, despite the fact that this phase can be induced by an applied magnetic field [161]. T. Ersez [162] has investigated the magnetism of a polycrystalline $\text{La}_{0.875}\text{Sr}_{0.125}\text{MnO}_{3+\delta}$ with the R structure at room temperature and $T_c \approx 250$ K from 11 to 300 K using the NPD method. He found no structural phase transition in the entire temperature range and a strong correlation of magnetic moment with the unit cell dimension, but not with the Mn-O-Mn bond angle. However, the detected trace of Mn_3O_4 raises doubts on the quality of the sample.

Although elaborate investigations have been performed using polycrystals, single crystals and thin films of the nominal $\text{La}_{0.875}\text{Sr}_{0.125}\text{MnO}_3$, the nature of the low-temperature FMI state in this compound is still debated [6, 9, 154, 155, 163]. Besides the peculiar physical properties, the defect chemistry such as cation nonstoichiometry and excess oxygen is also a crucial issue for the exact understanding of manganites because it determines the temperature of O - R transition and the value of T_c , etc. Structural as well as physical properties are very sensitive to the synthesis conditions that can control the relative amount of Mn^{3+} and Mn^{4+} ions. Sublimation of metal ions or their compounds during the high-temperature solid state reactions is unavoidable and excess oxygen (normally detected by TGA or iodometric titration method) in this composition usually exists with normal preparation methods. Taking into account these problems as well as the fact that vacant metal sites and excess oxygen determine hole-doping much more effectively than alkaline-earth substitution, the relative percentage of Mn^{3+} and Mn^{4+} ions, in principle, is governed by the substitutional doping, excess oxygen and cation deficiency. Thus the chemical formula of samples with the nominal composition $\text{La}_{1-x}\text{Sr}_x\text{MnO}_3$ should be expressed as $\text{La}_{1-x-\alpha}\text{Sr}_{x-\beta}\text{Mn}_{1-\gamma}\text{O}_{3+\delta}$. Based on the charge neutrality condition, the hole (i.e. Mn^{4+} content) concentration is $(x + 2\delta + 3\alpha + 2\beta + 3\gamma)$, if we assume the usual ionic picture with integer valencies.

To determine the temperature dependent oxygen content in manganites, one of the popular methods is the high sensitivity TGA, where one must obtain a fixed point for the normalization of oxygen content. Thus the measured oxygen content is relative and not absolute. In addition, this method always uses the flowing working gas or gas mixture, so it is unreasonable to confirm the oxygen content using the observed weight loss, saying

nothing of synthesising the stoichiometric manganites using the synthesis parameters obtained from TGA measurements. The second method is iodometric titration, which determines the average chemical compositions; its accuracy is strongly affected by the homogenization and purity of the measured sample, though it is an arguably good method for determining the mean manganese oxidation state. Another useful method is the high-resolution NPD because of the differences between the neutron scattering lengths of different elements. In particular, due to the negative scattering length of Mn with the associated high contrast, the Mn site occupancy can be determined very accurately, though determining stoichiometry with this method is fraught with the danger of possible correlations between site occupancies and corresponding thermal parameters.

In this chapter, in order to complete the structural studies, solve issues in solid state reactions and clarify the differences between polycrystalline and single-crystalline samples of manganites, detailed comparative studies have been performed. I prepared two sets of polycrystalline $\text{La}_{0.875}\text{Sr}_{0.125}\text{Mn}_{1\pm\gamma}\text{O}_{3+\delta}$ compounds with controlled nonstoichiometry. The first set of samples was treated by air sintering and Ar and O_2 annealings at 1 atm pressure in order to change the oxygen content while keeping the same cation composition and to produce the *O* and *R* structures at room temperature, since the *R* structure can be prepared for polycrystals, but was never observed in $\text{La}_{0.875}\text{Sr}_{0.125}\text{MnO}_3$ single crystals at room temperature. Three samples undergo sharp FM transitions and the $T_c \approx 192$ K of the Ar annealed sample is very close to that of single crystals [5, 157]. I have carried out the simultaneous Rietveld refinement combining both RT NPD and XRPD data being able to precisely determine the site occupancies and measured their interesting magnetic properties. A complete study of the structural transition, magnetic order and coherent JT distortion in the Ar annealed and air sintered samples from 10 to 900 K allows us to relate the magnetic order and properties to the crystal structure and thus resolve many ambiguities from the conflicting reports in literature. The second set of $\text{La}_{0.875}\text{Sr}_{0.125}\text{Mn}_y\text{O}_3$ samples with initial $y = 0.97, 1.00$ and 1.03 was also prepared in order to explore the effect of Mn stoichiometry on the structural and magnetic properties in detail.

7.2 Experimental details

The first set of polycrystalline samples of nominal $\text{La}_{0.875}\text{Sr}_{0.125}\text{Mn}_{1-\gamma}\text{O}_{3+\delta}$ was synthesized from stoichiometric mixtures of starting materials (La_2O_3 , SrCO_3 and MnO_2). The samples were prepared using the conventional standard ceramic method as described in chapter 5. The raw materials were calcined twice in a platinum crucible at 1373 K for 12 h in air in order to carry out decarbonization and pre-reaction. After each firing, the sample was cooled rapidly down to room temperature, followed by an immediate grinding, mixing and milling. The resultant black powder was isostatically pressed into a cylindrical rod of ~ 17 mm in diameter and 80 mm in length with a pressure of 54 MPa. After sintering two times at 1573 K and 1623 K for 18 h at each temperature in air and cooling down to room temperature at a cooling rate of ~ 6.67 K/min on a Pt-plate followed by an immediate grinding, mixing and milling after each firing and pressing after the first firing, two thirds of the product (~ 40 g) was then pressed into two cylindrical rods with almost the same size. The two rods were annealed at 1273 K for 24 h in flowing gases of

high purity argon and oxygen at 1 atm, respectively, and allowed to cool slowly to room temperature on a Pt-plate in the furnace for releasing the internal stress. The second set of $\text{La}_{0.875}\text{Sr}_{0.125}\text{Mn}_y\text{O}_3$ samples with initial $y = 0.97, 1.00$ and 1.03 was synthesized following the general procedure for sample preparation given above. Three $\text{La}_{0.875}\text{Sr}_{0.125}\text{Mn}_y\text{O}_3$ samples were simultaneously calcined three times at 1073 K, 1273 K and 1473 K, respectively, for 12 h, and sintered only once at 1573 K for 12 h in air.

The NPD data for the first set of samples were collected on the powder diffractometer SV7-a at the FRJ-2 reactor in Jülich [127], Germany. The XRPD analysis for all samples was performed on a BRUKER AXS D8 ADVANCE system equipped with our home-made rotating specimen holder. The details about NPD and XRPD measurements have been described in chapter 4.

The dc magnetization measurements between 5 and 400 K were carried out on a Quantum Design MPMS-7 SQUID magnetometer. The ZFC and FC curves were obtained at applied fields of 20 and 60 Oe.

The estimation of cations in the samples was carried out by ICP-OES analysis.

7.3 Room-temperature structural and magnetic properties

7.3.1 Structural studies

Structural parameters of the first set of $\text{La}_{0.875}\text{Sr}_{0.125}\text{Mn}_{1-\gamma}\text{O}_{3+\delta}$ samples at room temperature were determined from the joint refinement of XRPD and NPD data by the Rietveld method (Young, 1993) using the Fullprof program (weight of each pattern for each sample: 0.5) [164]. Values of 8.240, 7.020, -3.730 and 5.803 fm were used for the neutron scattering lengths of La, Sr, Mn and O, respectively, in this dissertation. The NPD and XRPD profiles were modeled using the Pseudo-Voigt profile shape function and the background was determined by automatically selecting points. For each sample, scale factors, zero shifts, lattice constants, atomic positions, isotropic thermal parameters and the occupancies of Mn and oxygen were refined. The ICP-OES results show that there is almost no deviation of the La and Sr contents from the stoichiometry (table 7.2). Refinements for the relative Sr site occupancy while keeping the sum of La and Sr site occupancies fixed at 1 give a composition of 0.125 for Sr within the estimated standard deviation (e.s.d.) for three samples consistent with the chemical analysis. In addition, refinements including all site occupancies in order to remove the introduction of possible systematic errors show almost the same La and Sr contents as the above models and excess oxygen. Therefore the La and Sr site occupancies were fixed to the stoichiometric values during the refinements. The correlation between refined site occupancies and respective thermal parameters is at least smaller than 50% (if it is higher than 50%, the output file of Fullprof will warn).

The crystal structure is orthorhombic ($Pbnm$, $Z = 4$; O) for the Ar annealed sample and hexagonal ($R\bar{3}c$, $Z = 6$; H) for the air sintered and O_2 annealed samples. I transformed the parameters from H into R ($R\bar{3}c$, $Z = 2$) setting while analyzing the data. The NPD and XRPD patterns of three samples are shown in figures 7.2(A) and (B), respectively, together with the calculated patterns and the differences between them. The differences between relative scattering factors for NPD and XRPD experiments are obvious there.

Table 7.2: Refined structural parameters of the Ar annealed, air sintered and oxygen annealed $\text{La}_{0.875}\text{Sr}_{0.125}\text{Mn}_{1-\gamma}\text{O}_{3+\delta}$ samples at room temperature as obtained from refinements of combined XRPD and NPD data. μ represents the refined site occupancy or the measured (ICP-OES) cationic content. Numbers in parenthesis are the e.s.d. of the last significant digit.

Synthesis	Ar	Air	O ₂
Crystal system	<i>O</i>	<i>R</i>	<i>R</i>
Space group	<i>Pbnm</i>	<i>R$\bar{3}c$</i>	<i>R$\bar{3}c$</i>
La/Sr :	<i>4c</i>	<i>2a</i>	<i>2a</i>
<i>X</i>	0.0022(3)	0.25	0.25
<i>Y</i>	0.0212(4)	0.25	0.25
<i>B</i> (La/Sr) (Å ²)	0.85(4)	0.81(4)	0.58(4)
M _{refinement} (La)	0.875	0.875	0.875
M _{ICP-OES} (La)	0.88(1)	0.88(1)	0.88(1)
M _{refinement} (Sr)	0.125	0.125	0.125
M _{ICP-OES} (Sr)	0.12(1)	0.12(1)	0.12(1)
Mn :	<i>4b</i>	<i>2b</i>	<i>2b</i>
<i>B</i> (Mn) (Å ²)	0.36(7)	0.31(7)	0.15(7)
M _{refinement} (Mn)	0.960(8)	0.986(8)	0.985(8)
M _{ICP-OES} (Mn)	0.97(1)	0.98(1)	0.97(1)
O1 :	<i>4c</i>	<i>6e</i>	<i>6e</i>
<i>X</i>	0.0622(9)	0.6994(1)	0.6986(1)
<i>Y</i>	0.4930(4)	0.8006(1)	0.8014(1)
<i>B</i> (O1) (Å ²)	1.23(4)	1.20(3)	1.11(3)
M _{refinement} (O1)	1.044(3)	3.090(2)	3.144(8)
O2 :	<i>8d</i>	—	—
<i>X</i>	0.7305(9)	—	—
<i>Y</i>	0.2763(8)	—	—
<i>Z</i>	0.0332(4)	—	—
<i>B</i> (O2) (Å ²)	1.35(9)	—	—
M _{refinement} (O2)	1.980(3)	—	—
<i>A</i> (Å)	5.5457(1)	5.4771(1)	5.4805(1)
<i>B</i> (Å)	5.5249(1)	—	—
<i>C</i> (Å)	7.8009(1)	—	—
A _{rhom} (°)	—	60.613(1)	60.632(1)
V _{cell} /Mn (Å ³)	59.75(2)	58.90(1)	59.03(1)

(to be continued)

<La(Sr)-O> (Å)	2.776(2)	2.758(1)	2.761(1)
Mn-O(1) (Å)	1.9809(9)		
Mn-O(2) (Å)	2.008(5)		
	1.957(5)		
<Mn-O> (Å)	1.982(2)	1.965(1)	1.968(1)
Mn-O(1)-Mn (°)	159.82(4)		
Mn-O(2)-Mn (°)	161.71(9)		
<Mn-O-Mn> (°)	161.08(4)	163.64(1)	163.38(1)
Reliability factors:	NPD XRD	NPD XRD	NPD XRD
R_p (%)	3.08 2.68	2.77 2.67	2.66 2.66
R_{wp} (%)	4.37 3.44	3.90 3.37	3.77 3.39
χ^2	3.32	2.84	2.65

Insets show magnified NPD and XRPD patterns of the Ar annealed and air sintered samples in selected 2θ regions. One may observe three Bragg reflections, i.e. (4 0 0), (2 2 4) and (0 4 0) in the NPD pattern as shown in the figure (a), and one (1 1 1) in the XRPD pattern as shown in the figure (a') for the Ar annealed sample. For the air sintered sample, the three reflections degenerate into two reflections (2 2 0) and (2 0 8) as shown in the figure (b), and the (1 1 1) reflection disappears as shown in the figure (b') within present detecting accuracy. This shows that the Ar annealed sample has an *O* structure, while the air and O_2 annealed samples belong to the *R* structure.

Refined structural parameters of three $La_{0.875}Sr_{0.125}Mn_{1-\gamma}O_{3+\delta}$ samples are summarized in table 7.2, together with the measured (ICP-OES) cationic contents. The low values of reliability factors represent the good Rietveld refinements. The refined cationic site occupancies are in agreement with the cationic contents obtained from the ICP-OES analysis within the experimental errors. Table 7.2 shows that the oxygen site occupancy decreases by $\sim 2.2\%$ and increases by $\sim 1.7\%$ for the Ar and O_2 annealed samples, respectively, compared with that of the air sintered sample. At the same time the Mn site occupancy seems to decrease by $\sim 2.7\%$ after the Ar annealing. This suggests that the flowing gas of Ar and O_2 decreases and increases the oxygen site occupancy during annealings, respectively. Simultaneously, Ar can carry some sublimational metal ions or their compounds out to some extent, in the present case, especially for Mn ions. For Ar and O_2 annealed, air sintered samples, the averaged Mn-O bond length decreases from 1.982(2) Å (Ar) to 1.968(1) Å (O_2) and 1.965(1) Å (air), while the averaged La(Sr)-O distance also decreases from 2.776(2) Å (Ar) to 2.761(1) Å (O_2) and 2.758(1) Å (air), thus resulting in the decrease of unit-cell volume V per Mn ion from 59.75(2) Å³ (Ar) to 59.03(1) Å³ (O_2) and 58.90(1) Å³ (air), respectively (table 7.2). At the *O-R* structural transition, the mean Mn-O and La(Sr)-O bond lengths and the unit-cell volume V per Mn ion decrease. I am unable to analyze these parameters as a function of preparation atmosphere, i.e. oxygen partial pressure, as discussed in [165] in following discussion due to the unsystematic trend between them and the insufficient number of investigated samples. Both increases of the averaged Mn-O and La(Sr)-O bond lengths suggest that

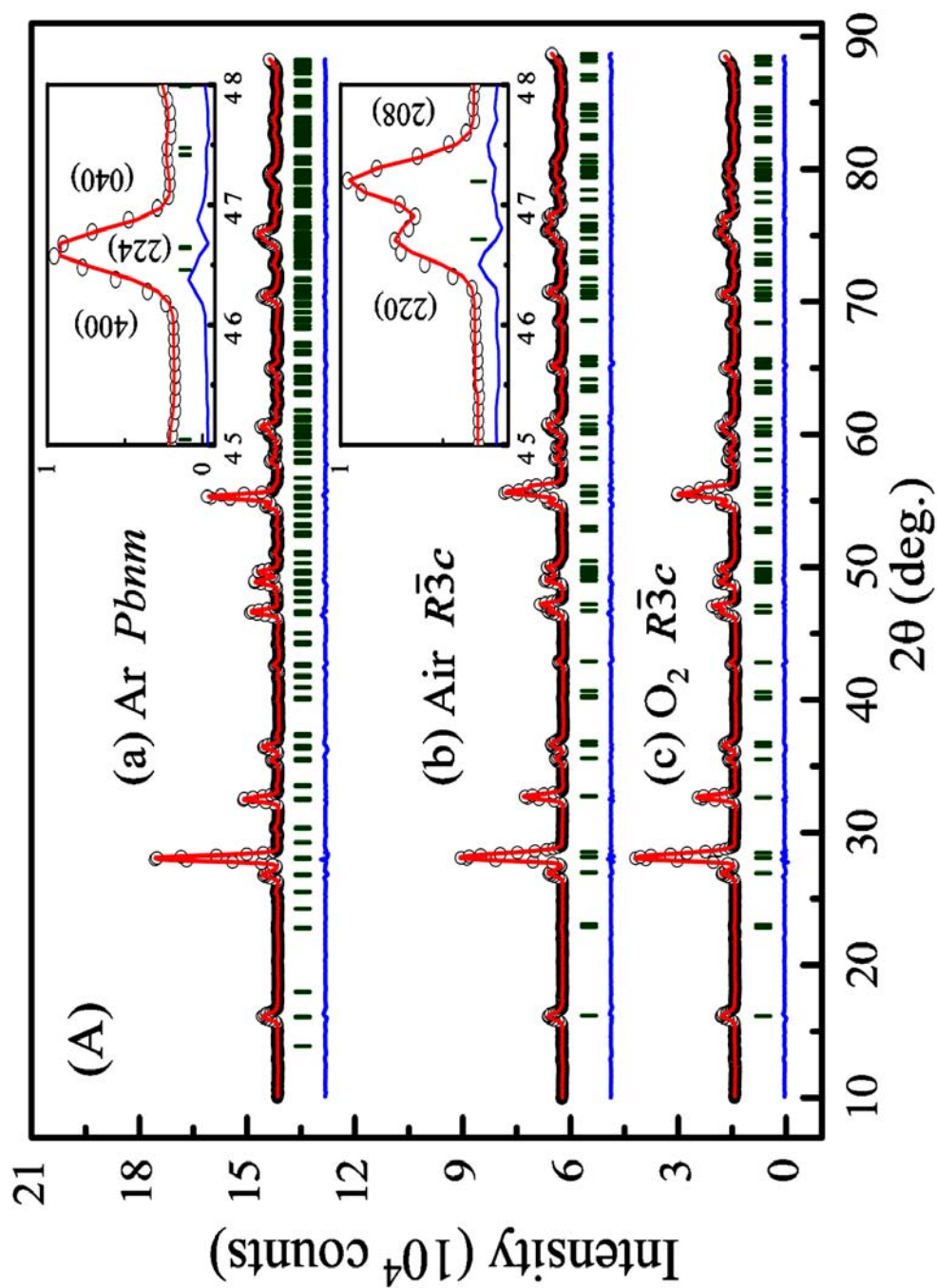


Figure 7.2: Observed (circles) and calculated (solid lines) patterns of neutron (A) and x-ray (B) powder diffraction diagrams for the Ar annealed (a) and (a'), air sintered (b) and (b') and oxygen annealed (c) and (c') $\text{La}_{0.875}\text{Sr}_{0.125}\text{Mn}_{1-\gamma}\text{O}_{3+\delta}$ samples at ambient conditions (to be continued).

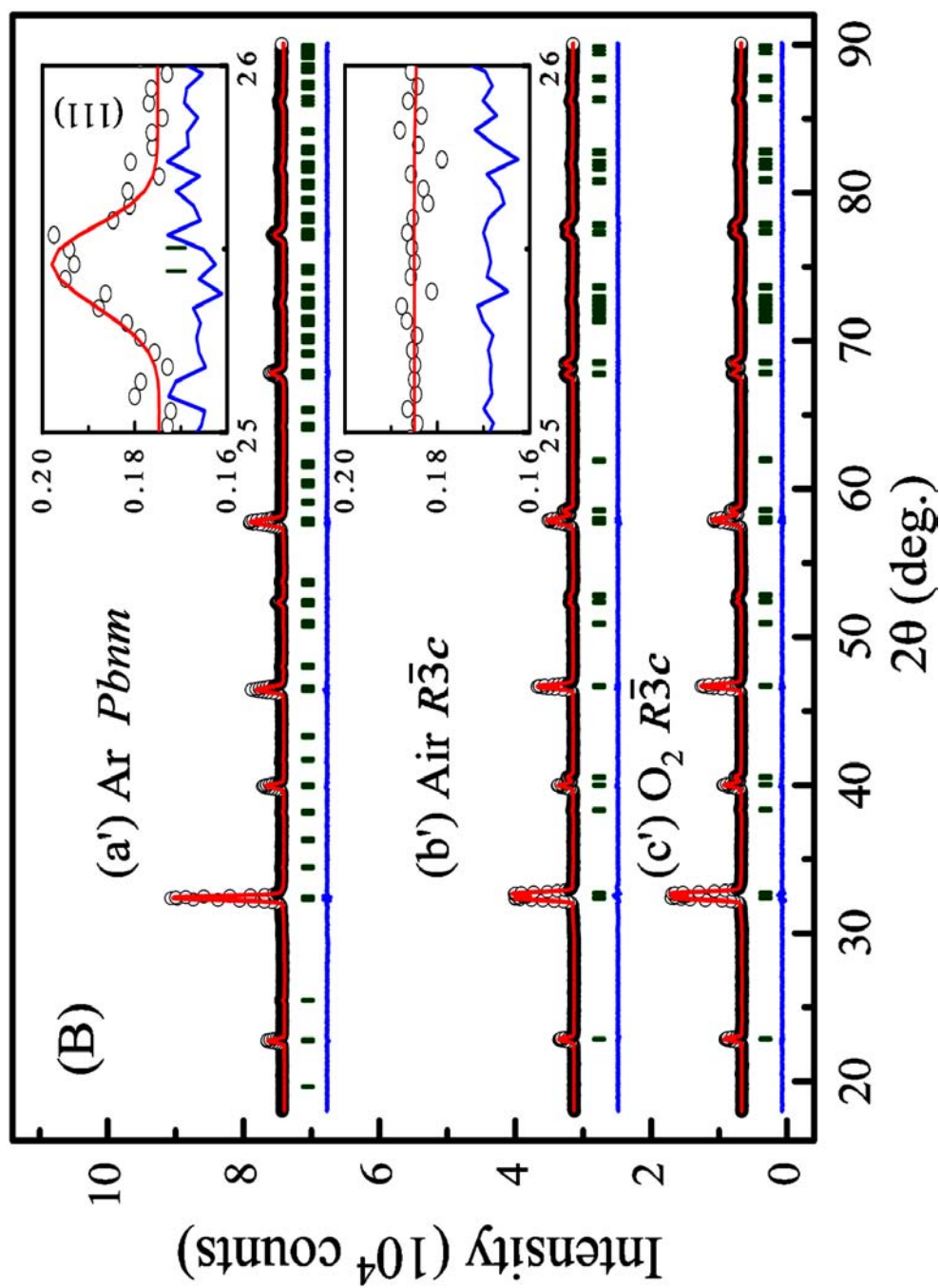


Figure 7.2 (continued): The bars mark the positions of Bragg reflections automatically generated from the space group. The lower curves in each panel represent the difference between the observed and calculated patterns. The insets show magnified patterns in certain 2θ regions.

neither Mn-O nor La(Sr)-O directly controls the structural transition, but influences it indirectly through the tolerance factor (chapter 2.2.2). There are three kinds of Mn-O bonds in the *O* structure: two Mn-O(2) in plane and one Mn-O(1) out of plane. Table 7.2 clearly shows the large differences between them, revealing a very strong JT distortion of the MnO_6 octahedra, which is also evidenced by the values of cell parameters ($a > b > c/\sqrt{2}$). The size of the JT distortion of MnO_6 octahedra can be evaluated by the following equation:

$$\Delta = \left(\frac{1}{6}\right) \sum_{n=1,6} \left[\frac{(d_n - \langle d \rangle)}{\langle d \rangle} \right]^2, \quad (7.1)$$

where $\langle d \rangle = \langle \text{Mn-O} \rangle$ and d_n are the mean Mn-O bond length and the six Mn-O bond lengths along six different directions, respectively. The calculated Δ for the Ar annealed sample is $1.1(2) \times 10^{-4}$. With this distortion the t_{2g} state of the Mn^{3+} ions splits into three states (d_{xy} , d_{yz} and d_{zx}) and e_g state splits into two states ($d_{x^2-y^2}$ and $d_{3z^2-r^2}$). However, there is only one kind of Mn-O bond for the *R* structure, indicating almost no JT distortion and the retention of both t_{2g} and e_g states. The *O-R* structural transition related to an increase of the tolerance factor t suppresses the JT distortion, which is accompanied by the increase of mean Mn-O-Mn bond angles from $161.08(4)^\circ$ (Ar) to $163.38(1)^\circ$ (O_2) and $163.64(1)^\circ$ (air) (tables 7.2 and 7.3). The effective electron transfer interaction between neighboring Mn ions is governed by the superexchange process via O $2p$ states. The relative value of the one-electron bandwidth W of the e_g -band [166] can be estimated by:

$$W \propto \frac{\cos \frac{1}{2}(\pi - \langle \text{Mn-O-Mn} \rangle)}{\langle \text{Mn-O} \rangle^{3.5}}. \quad (7.2)$$

The calculated values of W are listed in table 7.3. The flattening of MnO_6 octahedra caused by the *O-R* transition leads to an increase of the W value, in accordance with the estimated W values at the *O-R* phase boundary caused by hole doping [167]. There are two types of distortion related to MnO_6 octahedra: one is the cooperative rotation corresponding to the mean Mn-O-Mn bond angle ($\langle \text{Mn-O-Mn} \rangle$) and tolerance factor, leading to structural transitions; another is the JT distortion that is inherent to the high-spin ($S = 2$) Mn^{3+} ions, which lifts the double degeneracy of e_g orbitals for the symmetric octahedral environment, resulting in different Mn-O bond lengths. In the more strongly distorted *O* structure, the MnO_6 octahedra are tilted along the c direction, while in the weaker distortion (*R* structure), they are tilted almost along the [111] rotation direction.

It is pointed out that the synthesis conditions have a very important effect on the percentage of Mn^{3+} ions, i.e. $100 \times \text{Mn}^{3+}/(\text{Mn}^{3+} + \text{Mn}^{4+})$, through it seems that a high Mn^{4+} percentage, i.e. $100 \times \text{Mn}^{4+}/(\text{Mn}^{3+} + \text{Mn}^{4+})$, is stable at low preparation temperatures regardless of the starting nominal compositions [165]. The Mn^{3+} and Mn^{4+} contents were evaluated from the refined site occupancies based on the charge neutrality condition (table 7.3). As the oxygen content decreases, the percentage of Mn^{3+} ions increases. This correlation suggests that the JT distortion caused by the *R-O* structural transition promotes Mn^{3+} ions: as the Mn^{4+} percentage decreases with the decrease of oxygen content, the

Mn^{3+} percentage increases, as does the JT distortion. The high percentage of Mn^{4+} ions compensates for the lack of positive charge in the deficient cation sites and the abundance of negative charge in the oxygen sites.

Synthesis	Ar	Air	O ₂
T_c (K)	192(1)	240(1)	237(1)
W ($10^{-4} \times \text{\AA}^{-3.5}$)	899.94(6)	930.66(1)	925.40(1)
V_B (%)	86	59	57
T	0.990(1)	0.993(1)	0.992(1)
$z = 6(1-\gamma)$	5.71(5)	5.74(5)	5.64(5)
Mn^{3+} (cn)	0.67(3)	0.64(3)	0.53(3)
Mn^{4+} (cn)	0.29(3)	0.35(2)	0.46(3)
Mn^{3+} (cn) (%)	70(3)	65(3)	54(3)
$S(S+1)$	4.9(3)	5.0(3)	4.8(3)
$2zS(S+1)$	56(3)	58(3)	54(4)

Table 7.3: The summary of Curie temperature T_c , one-electron bandwidth W of the e_g -band estimated according to equation 7.2, relative concentration of cation vacancies in the B (Mn) sublattice V_B , tolerance factor t , number of nearest magnetic neighbors of Mn ions $z = 6(1-\gamma)$ and calculated Mn^{3+} and Mn^{4+} contents based on the charge neutrality condition for the Ar annealed, air sintered and oxygen annealed $\text{La}_{0.875}\text{Sr}_{0.125}\text{Mn}_{1-\gamma}\text{O}_{3+\delta}$ samples at room temperature. S is the weighted sum of the spin quantum number of Mn^{3+} ($S = 2$) and Mn^{4+} ($S = 3/2$). Numbers in parenthesis are the e.s.d. of the last significant digit.

7.3.2 Magnetic properties

In order to explore the effect of Ar and O₂ annealings on the magnetic properties, I performed magnetization measurements from 5 to 400 K in dc fields of 20 and 60 Oe. The ZFC and FC magnetizations as a function of temperature at an applied field of 20 Oe for three samples are shown in figure 7.3(a). With decreasing temperature, the transitions from paramagnetism to ferromagnetism at T_c are continuous and sharp, indicating a good sample quality with homogeneous composition. The signatures of structural transitions reported for $\text{La}_{0.875}\text{Sr}_{0.125}\text{MnO}_3$ single crystal [5] are not present in the magnetization data here. As far as I know, these features were only observed for single-crystalline but not for polycrystalline samples. The FC magnetization for the Ar and O₂ annealed samples is larger and smaller than that of the air sintered sample, respectively, which indicates that the Ar and O₂ annealings have changed the magnetic states, e.g. the ratio of $\text{Mn}^{3+}/\text{Mn}^{4+}$ or the domain structures, etc. Compared with the air sintered sample, the widths of the FM transition for Ar and O₂ annealed samples are slightly larger, especially for the Ar annealed sample, indicating a slightly broader distribution of the exchange coupling

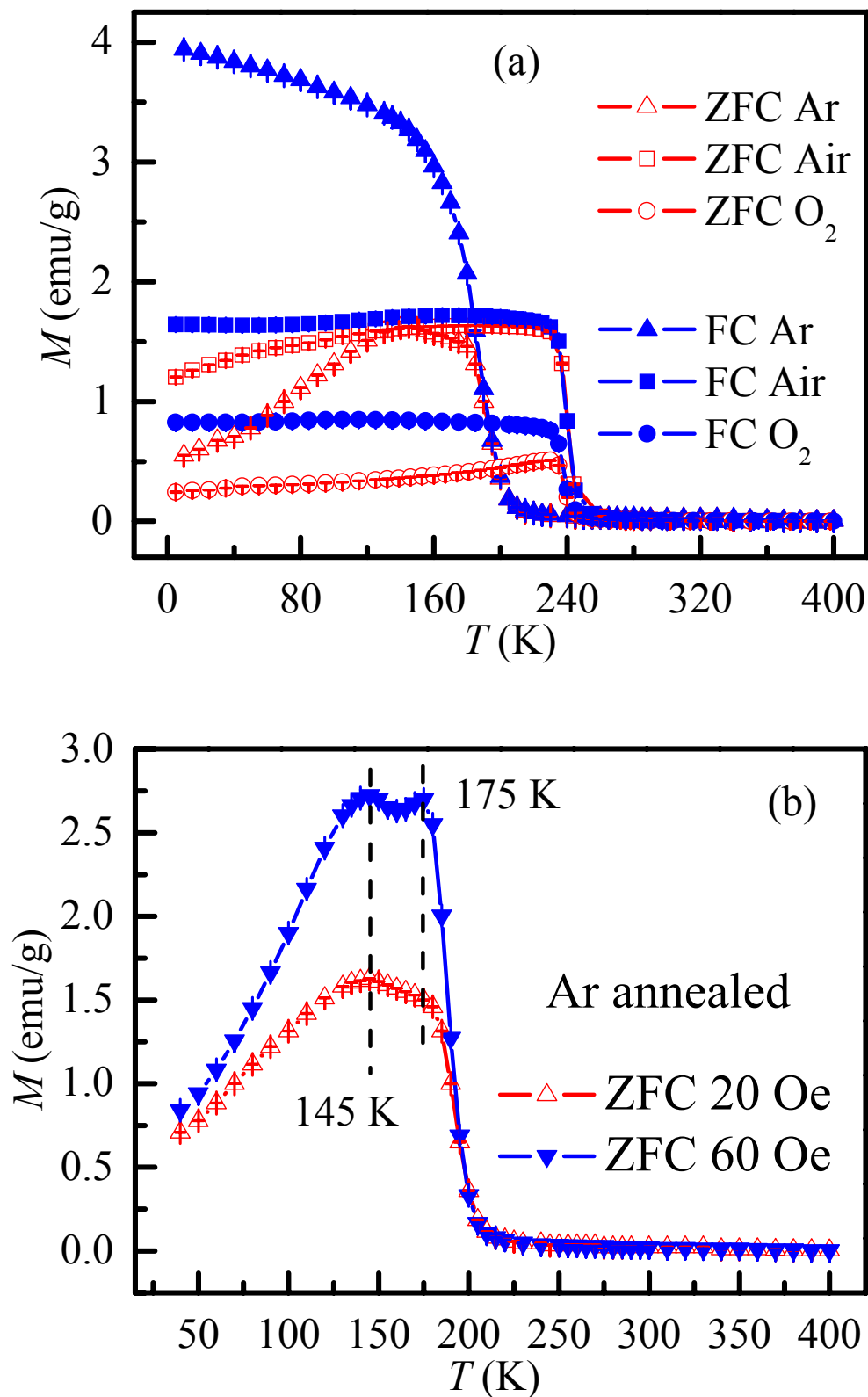


Figure 7.3: (a) ZFC and FC magnetization M versus temperature measured at $H = 20$ Oe for three $\text{La}_{0.875}\text{Sr}_{0.125}\text{Mn}_{1-\gamma}\text{O}_{3+\delta}$ samples and (b) ZFC M at 20 and 60 Oe for the Ar annealed sample. The lines are guides to the eye.

strength between Mn ions. From the inflection point of ZFC curves, I determined the Curie temperature T_c as listed in table 7.3. Thermomagnetic irreversibilities are observed as differences between the ZFC and FC curves for three samples. This is especially pronounced for the O₂ and Ar annealed samples, indicating a less homogenous FM order. At $T \approx 230$ K, just below $T_c = 237$ K, the ZFC magnetization of O₂ annealed sample has a well-defined peak and it continuously decreases towards the lower temperatures, while the FC magnetization is nearly constant below 230 K. Although spin glasses show similar irreversibilities, my study of the magnetization relaxation at 20 K shows no time dependence, and I thus conclude that the behavior comes from the FM domain structures. Similar phenomena are observed for the Ar annealed sample, where I also could not detect any time dependence at $T = 60$ K, and the FC magnetization continuously rises from 192 (T_c) to 5 K. Figure 7.3(b) shows ZFC $M(T)$ curves of the Ar annealed sample at applied fields of 20 and 60 Oe. An interesting feature is that the ZFC magnetization at 60 Oe has two peaks at 145 and 175 K, respectively. In the temperature ranges $145 < T < 159$ K and $159 < T < 175$ K, the value of magnetization decreases and increases, respectively, which corresponds to the behavior observed in the single crystal [5], where well-defined transitions at T_{JT} , T_c and $T_{OO'}$ are observed. According to [5], at $T_c \approx 180$ K a canted magnetic structure appears and at the temperature of $O'-O''$ transition ($T_{OO'} \approx 150$ K) the magnetization increases again. This phenomenon can be repeated and also appears in the measurements of ZFC $M(T)$ at applied fields of 0, 20, 50, 60 and 100 Oe using the corresponding powder sample. From this view, it thus can be deduced that polycrystalline sample can show some typical features characteristic for single crystals with the same nominal composition.

7.3.3 Sources and accommodation of excess oxygen

The refined site occupancies show all three samples contain excess oxygen. Many papers [168-171] have reported the so-called ‘excess oxygen’ problem for manganites, especially when the reaction temperature is relative low, but few of them gave the reasons. Oxygen nonstoichiometry has been found in $\text{La}_{1-x}\text{Sr}_x\text{MnO}_{3+\delta}$ perovskites ($x = 0.0-0.5$) prepared in the temperature range from 873 to 1273 K [164]. For my samples, when the reaction temperature is below 1373 K, XRPD spectra always evidence traces of $\text{La}(\text{OH})_3$ as pointed out in chapter 5. If the composition of this kind of sample is measured by chemical analysis, it shows obviously excess oxygen, part of which definitely comes from the appearance of $\text{La}(\text{OH})_3$. It seems that the appearance of excess oxygen in $\text{La}_{1-x}\text{Sr}_x\text{MnO}_3$ manganites at low doping levels is unavoidable for the conventional solid state reactions.

In refinements, the oxygen site occupancy turns out to be larger than the nominal value 3 for all three samples. The excess oxygen is not accommodated in interstitial sites, i.e. $(\frac{1}{2} 0 0)$ of the primitive perovskite cube and $(\frac{1}{4} \frac{1}{4} \frac{1}{4})$ in the LaO_3 sublattice as this would not be visible in the Rietveld refinements. Thus this is an artifact since the perovskite sites ($Pbnm$: $4c$ and $8d$; $R\bar{3}c$: $6e$) cannot accommodate additional oxygen. This artifact arises from the fact that the La and Sr site occupancies were arbitrarily fixed to be the stoichiometric values of 0.875 and 0.125, respectively. Therefore the observed oxygen deviation from the nominal stoichiometry should be interpreted as cation vacancies in the A (La and Sr) and B (Mn) sublattices, which will be present at elevated

preparation temperatures. Using neutron diffraction and high-resolution transmission electron microscopy methods, Van Roosmalen *et al.* [169] for the first time suggested that the actual composition was $\text{La}_{0.95}\text{Mn}_{0.95}\text{O}_3$ with equal amount of vacancies in the La and Mn sublattices for the formal $\text{LaMnO}_{3.158}$ sample. From simultaneous x-ray and neutron Rietveld refinement, I have arrived at a similar conclusion: the formula of $\text{La}_{0.875-\alpha}\text{Sr}_{0.125-\beta}\text{Mn}_{1-\gamma}\text{O}_{3+\delta}$ should be written as $\text{La}_{0.875-\alpha}\text{Sr}_{0.125-\beta}\text{Mn}_{1-\gamma}\text{O}_3$, but the hole concentration does not change because of the charge neutrality condition. Based on the joint refinements with different models and the above discussion the actual formulae of Ar annealed, air sintered and O_2 annealed samples are $\text{La}_{0.868(1)}\text{Sr}_{0.124(1)}\text{Mn}_{0.952(8)}\text{O}_3$ (Ar), $\text{La}_{0.850(1)}\text{Sr}_{0.121(1)}\text{Mn}_{0.957(8)}\text{O}_3$ (air) and $\text{La}_{0.835(2)}\text{Sr}_{0.119(1)}\text{Mn}_{0.940(8)}\text{O}_3$ (O_2), respectively. There is no the possibility of simultaneously having cation and anion vacancies. To compare the actual distributions of cation vacancies in the *A* and *B* sublattices, I express the formulae as $A_{0.992(2)}B_{0.952(8)}\text{O}_3$ (Ar), $A_{0.971(1)}B_{0.957(8)}\text{O}_3$ (air) and $A_{0.954(2)}B_{0.940(8)}\text{O}_3$ (O_2). For all three samples, I thus observe more vacancies in the *B* (V_B^{vac}) sublattice than that in the *A* (V_A^{vac}) sublattice. I define the relative concentration of cation vacancies in the *B* sublattice compared to the sum of cation vacancies in the *A* and *B* sublattices as V_B (%) = $100 \times V_B^{\text{vac}} / (V_A^{\text{vac}} + V_B^{\text{vac}})$ and the calculated values of V_B for three samples are shown in table 7.3. It is possible that as V_B increases, T_c decreases and the FM transition becomes slightly wider as shown in figure 7.3(a). An increase of the *B* sublattice vacancies leads to a decrease of the strength of magnetic exchange interaction and a widening of its distribution. A recent study of the effects of the presence and distribution of cation vacancies in doped manganites (La, M) $\text{MnO}_{3+\delta}$ (where $M = \text{Na}, \text{Ca}$) on their magnetic properties was reported by Malavasi *et al.* [170]. However, the usual parameters, e.g. Mn-O-Mn bond angle and Mn-O bond length, fail to explain the trend of T_c there. Obviously, only the purely geometrical factor is not sufficient to explain the surprising change of T_c .

To investigate the reasons for the decrease of the Mn site occupancy in Ar and O_2 annealed samples in more detail, studies were conducted with a TGA instrument and an actual furnace with subsequent ICP-OES analysis. I could show that the flowing gas significantly accelerates the reaction compared with the static conditions. In addition, it favors sublimation of the elements. It should be stressed that the Ar and O_2 annealed samples experienced one more firing, mixing and milling than the air sintered sample. To conclude, the Ar and O_2 annealing in the present case can lead to a decrease and an increase of the oxygen site occupancy, respectively, and at the same time may accompany the decrease of Mn ions. Similar behavior was also suggested by Mitsuru Itoh *et al.* [171].

7.3.4 Effect of Ar and O_2 annealings on T_c

I attempt to explore the effects of Ar and O_2 annealings on T_c of $\text{La}_{0.875}\text{Sr}_{0.125}\text{Mn}_{1-\gamma}\text{O}_{3+\delta}$ samples and establish the possible correlations between their structural and magnetic properties among the various and important parameters. The Curie temperature of a Heisenberg ferromagnet with nearest-neighbor interactions only is given in the molecular field approximation as:

$$T_c = 2zJS(S+1)/3k_B. \quad (7.3)$$

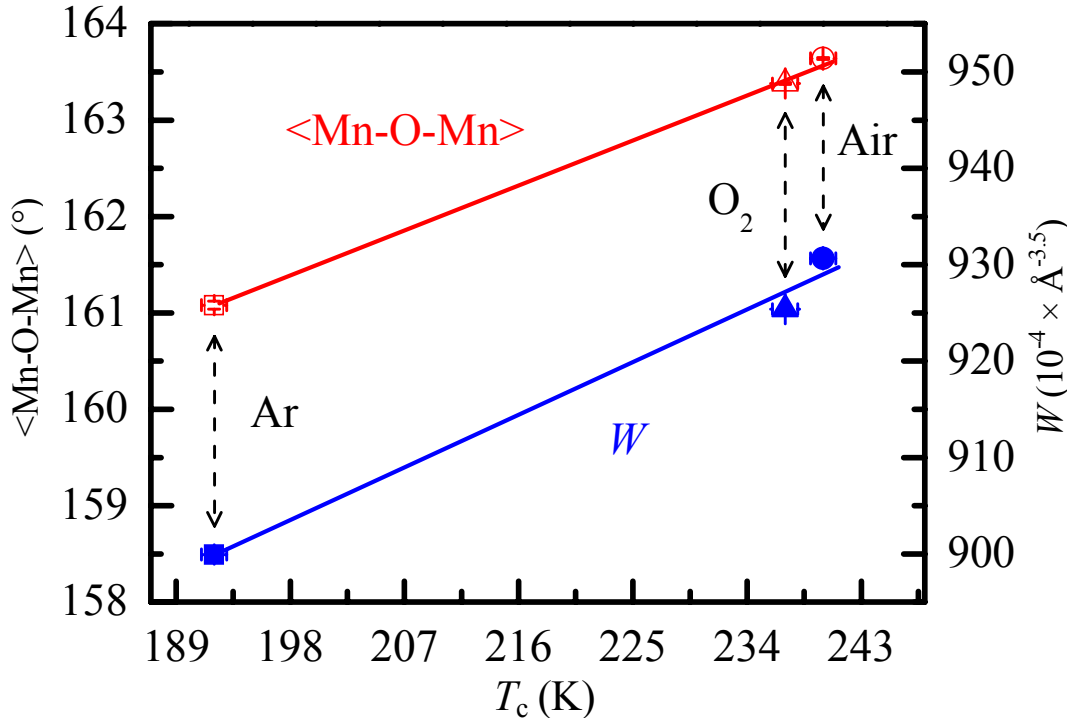


Figure 7.4: Mean Mn-O-Mn bond angle and one-electron bandwidth W of the e_g -band versus Curie temperature T_c for Ar, O₂ annealed and air sintered La_{0.875}Sr_{0.125}Mn_{1- γ} O_{3+ δ} samples. The solid lines are guides to the eye.

Equation 7.3 shows that there are three influencing factors determining the value of T_c and all of them are listed in table 7.3: (i) the number of nearest magnetic neighbors z , i.e. $z = 6(1-\gamma)$; (ii) the spin quantum number S , depending on the Mn content and Mn valence state (Mn³⁺: $S = 2$; Mn⁴⁺: $S = 3/2$) and (iii) the exchange constant J . As can be seen from table 7.3, the value of $2zS(S+1)$ is almost the same for three samples within the e.s.d.. The exchange constant J depends on the mean Mn-O-Mn bond angle and mean Mn-O bond length. As can be seen from equation 7.2, the one-electron bandwidth W of the e_g -band can be used as a measure for the strength of FM double-exchange interaction between Mn³⁺ and Mn⁴⁺ ions. Indeed, I find a nearly linear dependence between W and T_c for three samples as shown in figure 7.4, which indicates that the exchange constant J is the most important determining factor for the drastic differences in T_c for three samples (table 7.3). Clearly, the more neighboring Mn ions with different valencies are present, the stronger is the FM double exchange and thus the Curie temperature T_c .

7.3.5 Effect of Mn stoichiometry on T_c

In order to investigate the individual effect of the number of nearest magnetic neighbors z on the structural and magnetic properties in detail, a second set of La_{0.875}Sr_{0.125}Mn _{γ} O₃ samples with initial $\gamma = 0.97, 1.00$ and 1.03 was prepared. Every sample is a single phase within the detection limit of XRPD method. Although XRPD is not very sensitive to the

Synthesis	0.97	1.00	1.03
Crystal system	R	R	R
Space group	$R\bar{3}c$	$R\bar{3}c$	$R\bar{3}c$
T_c (K)	226(1)	260(1)	295(1)
μ refinement (Mn)	0.970(4)	0.993(3)	1.012(4)
$z = 6(1-\gamma)$	5.82(3)	5.96(2)	6.07(3)
$a = b = c$ (Å)	5.4755(1)	5.4799(1)	5.4857(1)
α_{rhomb} (°)	60.619(1)	60.612(1)	60.603(1)
$V_{\text{cell}}/\text{Mn}$ (Å ³)	58.85(1)	58.98(1)	59.16(1)
R_p (%)	2.65	3.46	3.96
R_{wp} (%)	3.46	4.48	5.08
χ^2	1.37	1.19	1.09

Table 7.4: Refined structural parameters of the three air sintered $\text{La}_{0.875}\text{Sr}_{0.125}\text{Mn}_y\text{O}_3$ samples with initial $y = 0.97, 1.00$ and 1.03 as obtained from refinements of XRPD data, and the summary of the Curie temperature T_c and the number of nearest magnetic neighbors of Mn ions $z = 6(1-\gamma)$. μ represents the refined Mn site occupancy. Numbers in parenthesis are the e.s.d. of the last significant digit.

oxygen structural parameters, the Mn site occupancy can still be determined reliably, as I verified by different refinement procedures. The refined structural parameters are listed in table 7.4, while the observed and calculated XRPD patterns are displayed in figure 7.5. Though the crystal structure for all three $\text{La}_{0.875}\text{Sr}_{0.125}\text{Mn}_y\text{O}_3$ samples is R , the structural distortion decreases as the decrease of α_{rhomb} from $60.619(1)^\circ$ to $60.612(1)^\circ$, and to $60.603(1)^\circ$ for initial $y = 0.97, 1.00$ and 1.03 , respectively. The refined Mn site occupancy is reduced by $\sim 1.8\%$ and $\sim 4.1\%$ for the samples with initial $y = 1.00$ and 0.97 , respectively, compared to that of $\text{La}_{0.875}\text{Sr}_{0.125}\text{Mn}_y\text{O}_3$ with initial $y = 1.03$. This is consistent with the initial compositions and reasonable in consideration of the high-temperature reactions. The calculated numbers of nearest magnetic neighbors z obtained from the refined Mn site occupancies are shown in table 7.4. The decrease of the relative Mn site occupancy results in the decrease of unit-cell volume V per Mn ion and lowers the value of z .

Figure 7.6 shows the ZFC magnetization measured at an applied field of 20 Oe for three $\text{La}_{0.875}\text{Sr}_{0.125}\text{Mn}_y\text{O}_3$ samples. Again, it can be seen that the cationic nonstoichiometry, especially for the B sites, has a very significant effect on the magnetic properties. I estimated the T_c as shown in table 7.4. The T_c is reduced by $\sim 11.9\%$ and $\sim 23.4\%$ for the samples with initial $y = 1.00$ and 0.97 , respectively, compared to that of $\text{La}_{0.875}\text{Sr}_{0.125}\text{Mn}_y\text{O}_3$ with initial $y = 1.03$. Obviously, the strong decrease of T_c from 295(1) K to 260(1) K, and to 226(1) K for initial $y = 1.03, 1.00$ and 0.97 , respectively, is largely due to a decrease in Mn content and thus a decrease of the number of nearest magnetic neighbors z .

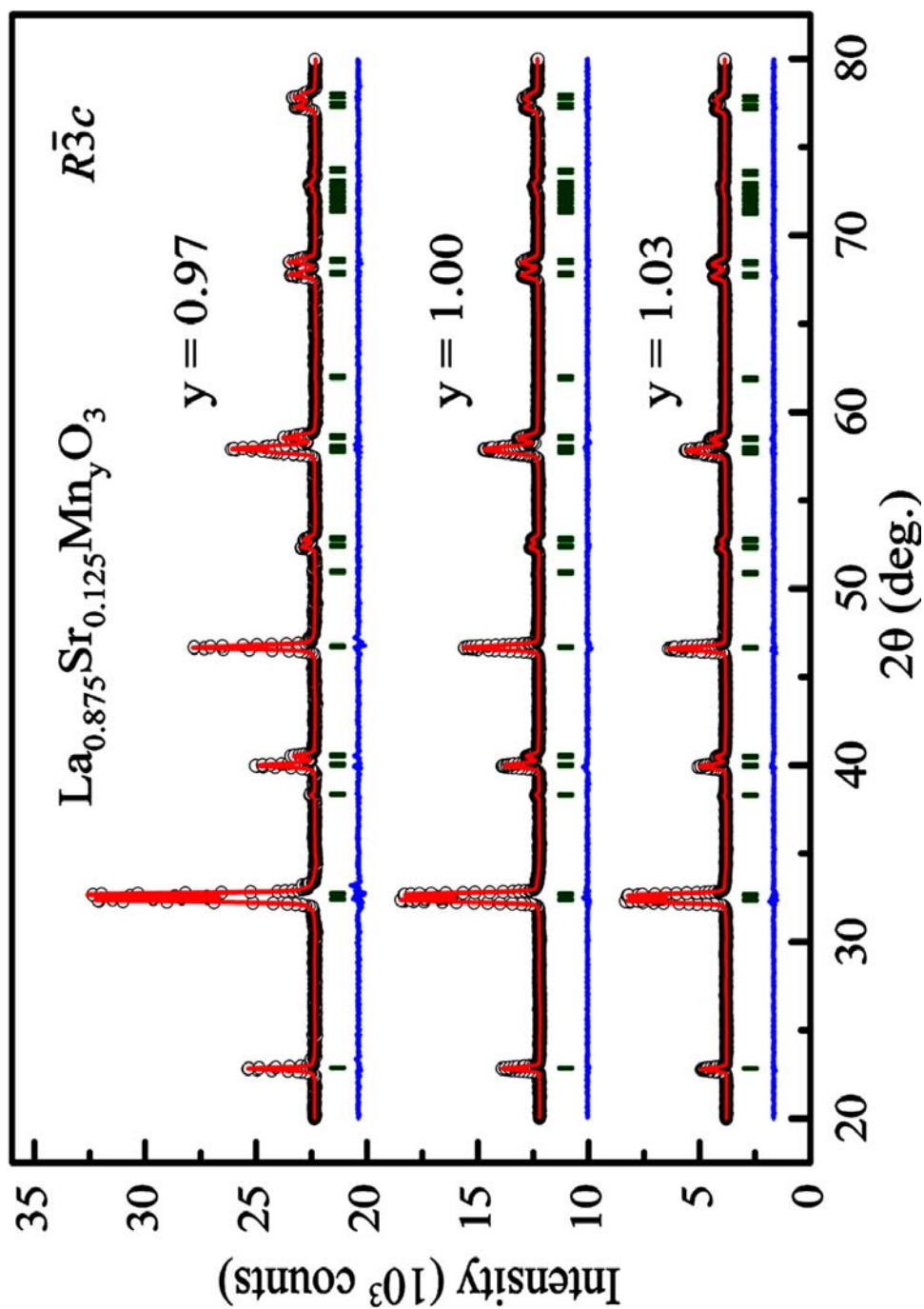


Figure 7.5: Observed (circles) and calculated (solid lines) XRPD patterns of the three air sintered $\text{La}_{0.875}\text{Sr}_y\text{Mn}_{1.25}\text{O}_3$ samples with initial $y = 0.97$, 1.00 and 1.03, belonging to the rhombohedral structure at room temperature. The bars mark the positions of Bragg reflections automatically generated from the space group. The lower curves in each panel represent the difference between the observed and calculated patterns.

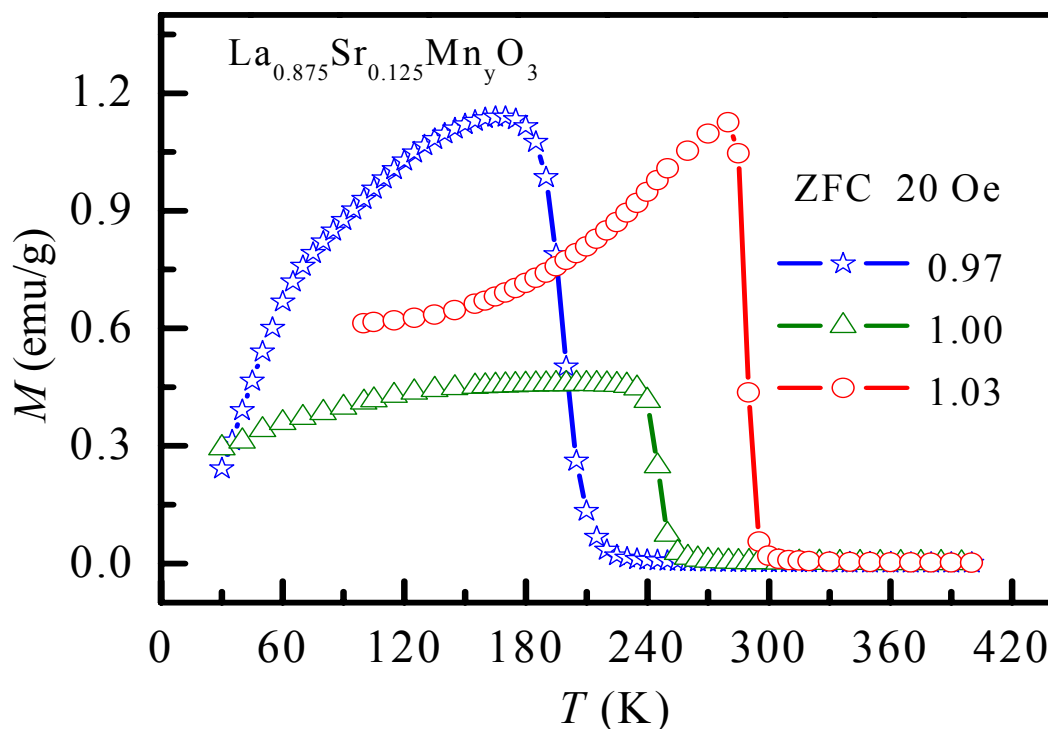


Figure 7.6: ZFC magnetization M versus temperature measured at $H = 20$ Oe for the three air sintered $\text{La}_{0.875}\text{Sr}_{0.125}\text{Mn}_y\text{O}_3$ samples with initial $y = 0.97, 1.00$ and 1.03 , belonging to the rhombohedral structure at room temperature. The solid lines are guides to the eye.

To summarize, the decrease of the total strength of magnetic interactions resulting from a decrease of the single-electron bandwidth W , or the decrease of Mn content, can lead to a drastic decrease of the Curie temperature T_c . In the mixed-valence manganites, the exchange interactions are primarily dominated by the mobile charge carriers, so-called double-exchange coupling. The change of orbital mixing could also be important in determining the T_c . Finally, it should be pointed out that it is almost impossible to change the physical properties of investigated samples using annealing with 1 atm oxygen. A much higher oxygen pressure is needed to investigate its effect.

7.3.6 Conclusions

I have systematically studied the effect of stoichiometry on $\text{La}_{0.875}\text{Sr}_{0.125}\text{Mn}_{1\pm y}\text{O}_{3+\delta}$ manganites with a fixed Sr doping through Ar and O_2 annealings and different initial additions. The structural parameters (lattice constants, atomic coordinates and site occupancies) of air sintered, Ar and O_2 annealed samples were refined. The $\text{La}_{0.875}\text{Sr}_{0.125}\text{Mn}_{1\pm y}\text{O}_{3+\delta}$ samples have been found to exhibit either an orthorhombic (Ar annealed) or a rhombohedral structure (air sintered and O_2 annealed). Depending on the firing atmospheres (air, Ar or O_2), cation vacancies are present in the samples, which leads to drastic changes of the magnetic properties. The one-electron bandwidth W of the e_g -band, the actual concentration of vacancies in the B (Mn) sublattice V_B and the number

of nearest magnetic neighbors are correlated with the decrease of T_c . In conclusion, my results clearly demonstrate how an extremely small change in the stoichiometry can have huge effects on the structural and magnetic properties in these compounds based on the perovskite structure. Comparing the Ar annealed with the air sintered $\text{La}_{0.875}\text{Sr}_{0.125}\text{Mn}_{1-\gamma}\text{O}_{3+\delta}$ sample, only a $\sim 2.2\%$ relative decrease of oxygen content can lead to a structural transition from rhombohedral to orthorhombic and to a decrease of the magnetic transition temperature by $\sim 20\%$. Such a huge response on small changes of parameters is characteristic for this complex system. Only a combined Rietveld refinement of x-ray and neutron-diffraction data allows one to determine the stoichiometry with the required precision to be able to compare results from different samples.

7.4 Temperature dependent structural transition and magnetic order

During the following temperature dependent measurements, two of the first set of samples (Ar annealed and air sintered) were contained in tightly sealed vanadium cans to prevent the case mentioned in [172], i.e. oxygen content fluctuations with measuring temperatures. In addition, the height of the neutron beam is only ~ 3 cm located at the center of the can. Therefore, there were no fluctuations in oxygen content and Mn valence during measurements. As I have analyzed above, for the first set of samples, the crystal structure is O (Ar annealed) or R (air sintered) at room temperature and the corresponding stoichiometries were determined as $\text{La}_{0.868(1)}\text{Sr}_{0.124(1)}\text{Mn}_{0.952(8)}\text{O}_3$ (Ar annealed) and $\text{La}_{0.850(1)}\text{Sr}_{0.121(1)}\text{Mn}_{0.957(8)}\text{O}_3$ (air sintered). It is thus reasonable to fix the site occupancies at the values obtained from room-temperature refinements while analyzing the patterns from different temperatures. I have to point out that for the air sintered sample, at 120 K where a mixed R and O phase exists, the temperature parameters B of La/Sr, Mn and O1, the magnetic moments of Mn and the site occupancies of the O and R structures were constrained to be equal during the structural and magnetic refinements.

7.4.1 Results

The observed and calculated NPD patterns of the Ar annealed and air sintered samples at selected temperatures are shown in figures 7.7(A) and (B), respectively. Observed patterns of the air sintered sample in three Q regions at five selected temperatures are shown in the inset (a), where from the highest intensity to the lowest intensity the five patterns correspond to the temperatures of 10, 65, 120, 180 and 270 K, respectively, with contrast effects to show the structural transition. Insets (b) and (c) only show the contribution of nuclear structure alone for air sintered ($T = 180$ K) and Ar annealed ($T = 10$ K) samples, respectively. In this way, I evidence the major contributions of magnetic scattering to the profiles. In addition, the bottom curve of inset (b) shows that magnetic peaks only appear at the positions allowed by the structural space group $R\bar{3}c$, indicating pure ferromagnetism for the air sintered sample.

The refined structural parameters, calculated tolerance factor t and one-electron

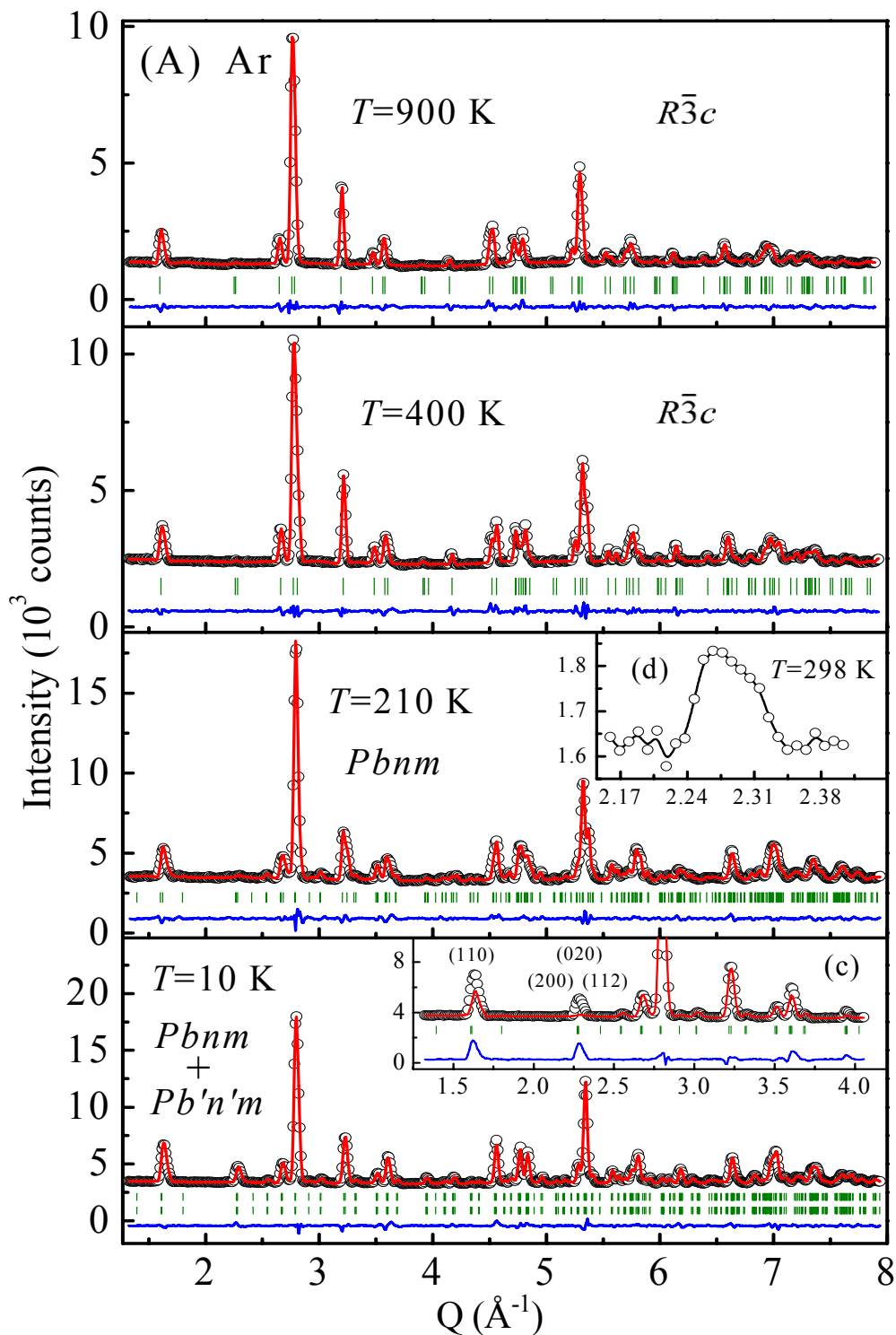


Figure 7.7: Observed (circles) and calculated (solid lines) NPD patterns of (A) the Ar annealed ($T = 10, 210, 400$ and 900 K) and (B) the air sintered ($T = 10, 120, 180$ and 270 K) $\text{La}_{0.875}\text{Sr}_{0.125}\text{Mn}_{1-\gamma}\text{O}_{3+\delta}$ samples. The vertical bars mark the Bragg (top) and magnetic (bottom) peak positions automatically generated from the space group. The line in the bottom of each diagram is the difference between the observed and calculated patterns. Inset (a) shows five observed patterns of air sintered sample in certain Q regions for the temperatures of $10, 65, 120, 180$ and 270 K, respectively (to be continued).

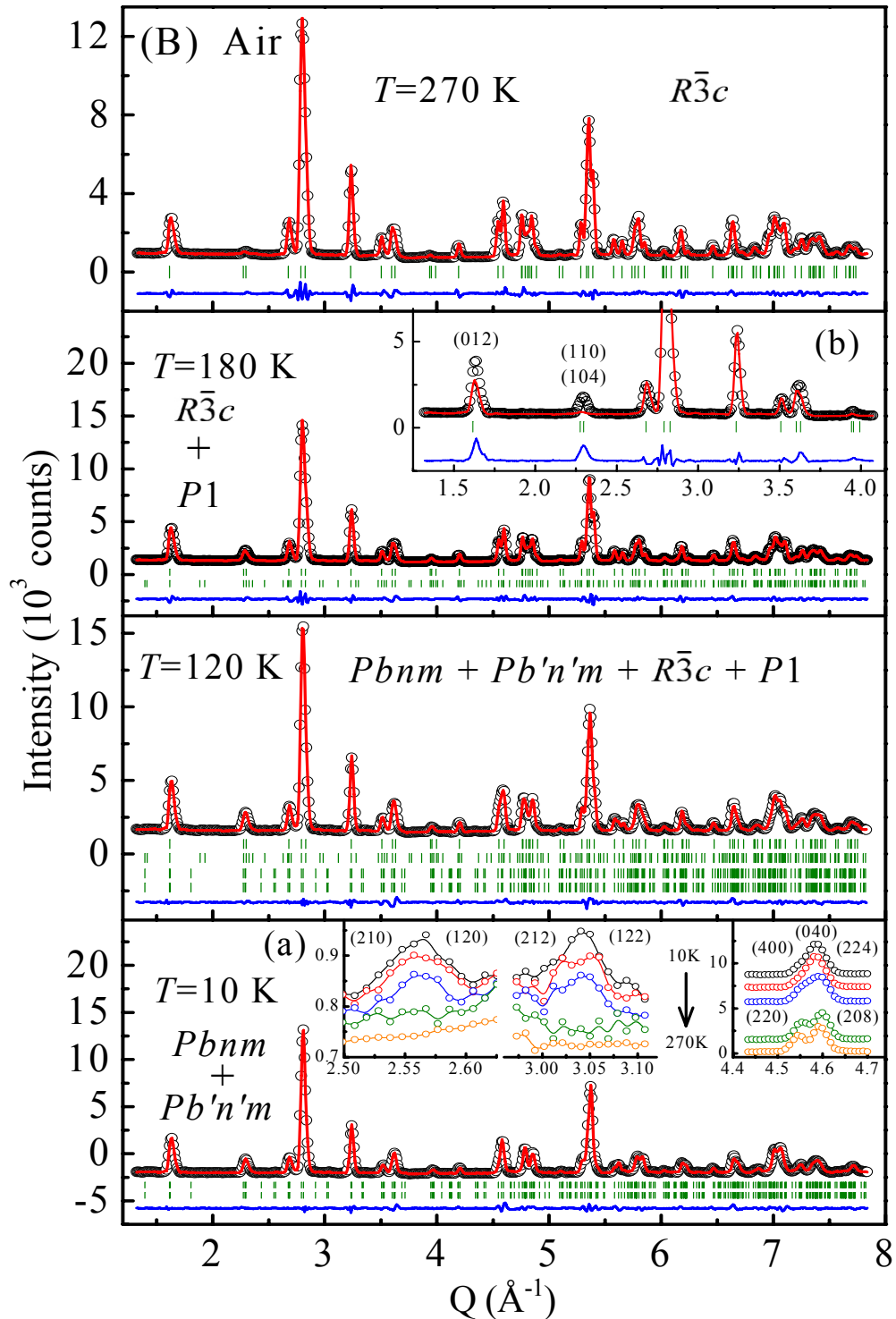


Figure 7.7 (continued): For clarity, the patterns were shifted along the intensity axis with the highest corresponding to the lowest temperature. Inset (b) and (c) show the calculation of the scattering from the nuclear structure only for the air sintered ($T = 180$ K) and Ar annealed ($T = 10$ K) samples, respectively, indicating the major magnetic diffraction peaks. Inset (d) shows the existence of the Bragg peaks indexed as (2 0 0), (0 2 0) and (1 1 2) in the $Pbnm$ symmetry at 298 K for the Ar annealed sample. For the air sintered sample, a coexistence of magnetically ordered O with magnetically ordered R structures occurs.

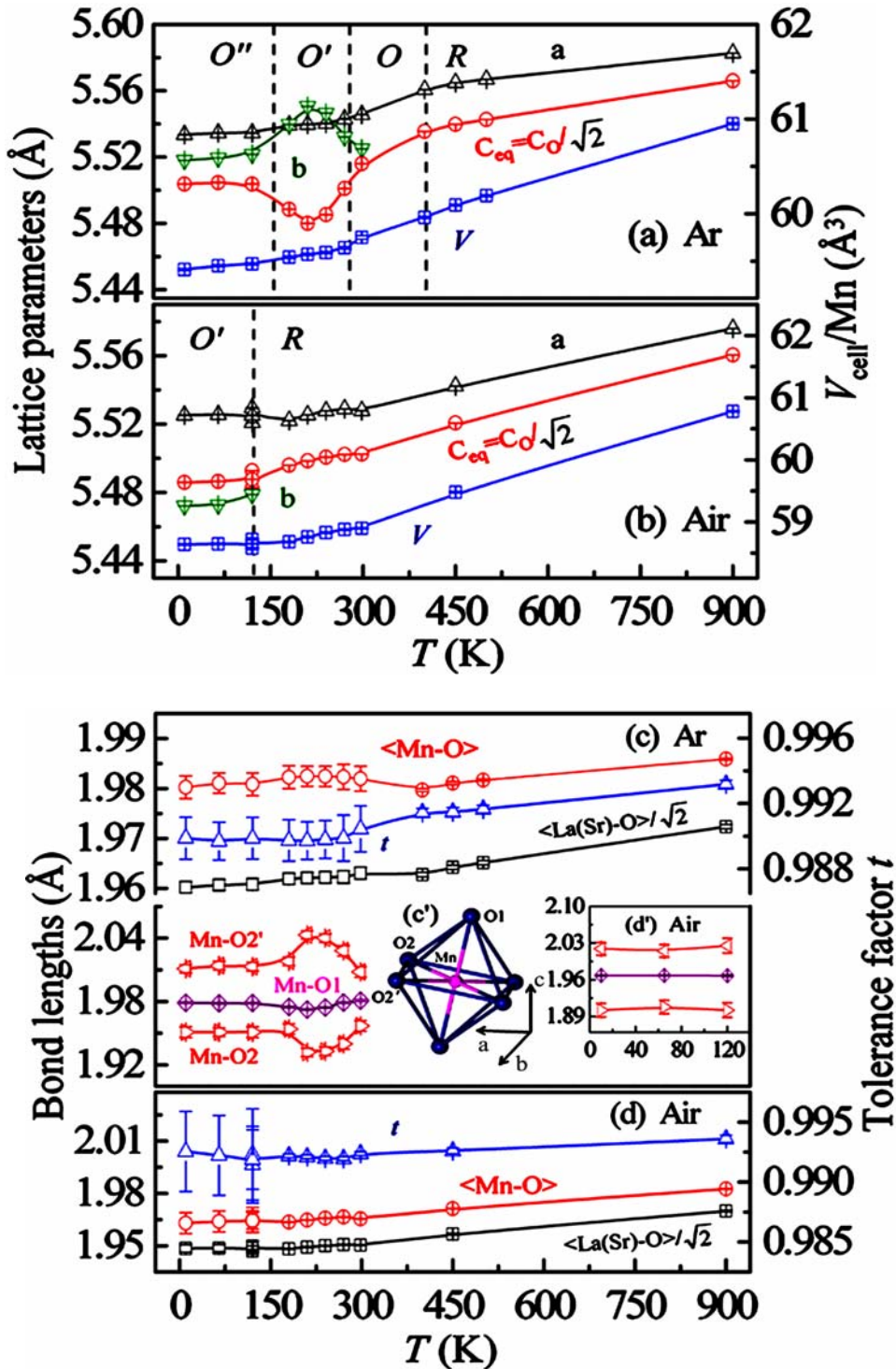


Figure 7.8: (a, b): refined lattice parameters (left) and unit-cell volume V per Mn ion (right) versus temperature for (a) the Ar annealed and (b) the air sintered $\text{La}_{0.875}\text{Sr}_{0.125}\text{Mn}_{1-\gamma}\text{O}_{3+\delta}$ samples. The equivalent lattice parameter c_{eq} for the O and R (hexagonal setting) structures is obtained by $c_{\text{eq}} = c_o/\sqrt{2}$ (O structure: $c_o = c_o$ and R structure: $a_h = (a_o - b_o - c_o)/2$, $b_h = b_o$, $c_h = 2a_o + c_o$ and $c_o = c_o$, so $9c_o \cdot c_o = c_h \cdot c_h + 12a_h \cdot a_h$. Ital. subscripts h and o stand for hexagonal and orthorhombic, respectively). (c, d): mean Mn-O and $\text{La(Sr)-O}/\sqrt{2}$ bond lengths (left) and tolerance factor t (right) versus temperature for (c) the Ar annealed and (d) the air sintered samples (to be continued).

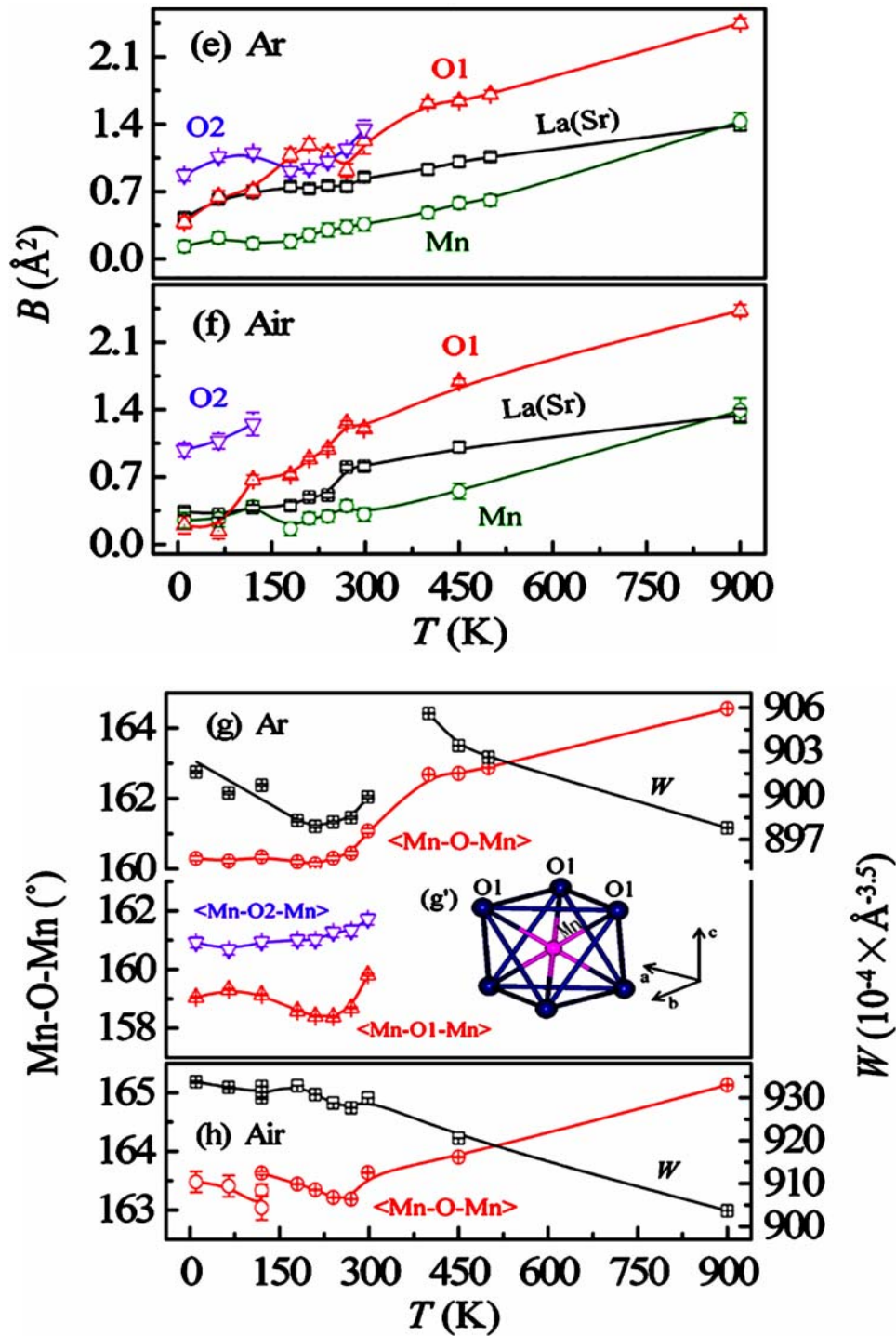


Figure 7.8 (continued): (e, f): temperature variation of the isotropic thermal parameters of La/Sr, Mn and O atoms for (e) the Ar annealed and (f) the air sintered samples. (g, h): mean Mn-O-Mn bond angle (left) and one-electron bandwidth W of the e_g -band (right) versus temperature for (g) the Ar annealed and (h) the air sintered samples. Bottoms of (c) and (g) show the individual Mn-O bond length and Mn-O-Mn bond angle of the Ar annealed sample, respectively. Insets (c') and (g') show schematic illustrations of MnO₆ octahedra in the O and R structures, respectively, illustrating the relevant bond lengths. Inset (d') shows the individual Mn-O bond length of the air sintered sample in the O structural region. The solid lines are guides to the eye.

bandwidth W of the e_g -band are shown in figure 7.8. In order to compare the lattice parameter c with a and b for two samples, I plotted the equivalent c_{eq} for c in (a) and (b). In the O setting c_{eq} equals $c_o/\sqrt{2}$, while for the R setting I transformed the lattice parameters into the O setting and c_{eq} is equal to the converted c_o divided by $\sqrt{2}$. Since for the air sintered sample at 120 K a mixed O and R phase exists, the third set of parameters corresponding to the averaged values was calculated and plotted in addition. Thus one may observe three data points for one parameter at 120 K in (b), (d) and (h). The ideal cubic perovskite structure is usually distorted into a R or an O structure by decreasing the tolerance factor t . For the Ar annealed sample, t increases from 10 to 900 K as shown in (c), while for the air sintered sample it nearly stays constant at a larger value compared to the Ar annealed sample in the entire temperature range as shown in (d). For the Ar annealed sample, in the O structural region shown in the bottom of (g), the bond angle Mn-O2-Mn monotonically increases as a function of temperature but is larger than Mn-O1-Mn bond angle. The latter, however, has a larger variation. This leads to the $\langle\text{Mn-O-Mn}\rangle$ nearly remaining constant below ~ 180 K (close to T_c) and then increasing smoothly, but showing a large change in the slope above $T_{\text{OR}} \approx 400$ K as shown in (g). By contrast, for the air sintered sample shown in (h), $\langle\text{Mn-O-Mn}\rangle$ shows small variations below $T_c = 240$ K and then significantly increases up to 900 K. Insets (c') and (g') show schematic illustrations of MnO_6 octahedra in the O and R (hexagonal setting) structures, respectively, illustrating the relevant bond lengths. Bottom of figure (c) and inset (d') show the individual Mn-O bond length for Ar annealed and air sintered samples in the O structural region, respectively. For both samples, in the orthorhombic phase, the relation $\text{Mn-O2} < \text{Mn-O1} < \text{Mn-O2}'$ holds, while in the rhombohedral phase all Mn-O bond lengths are equal. Large variations of the Mn-O2' and Mn-O2 bond lengths in temperature range $180 < T < 298$ K as shown in the bottom of (c), with coincident changes of the lattice parameters as shown in (a), confirm that a very strong coherent JT distortion takes

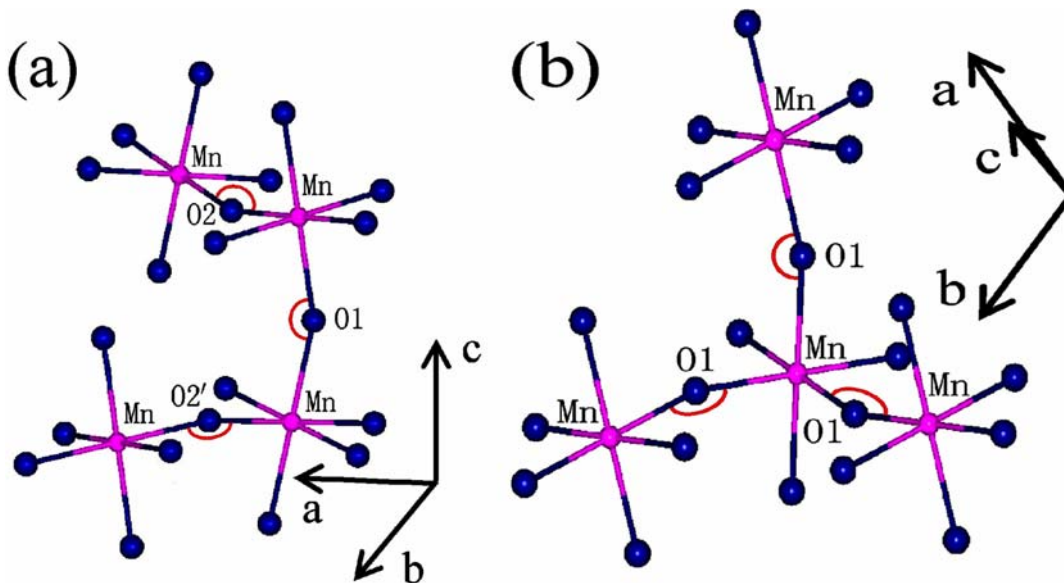


Figure 7.9: Schematic illustration of (a) Mn-O1-Mn, Mn-O2-Mn and Mn-O2'-Mn (= Mn-O2-Mn) bond angles in the O structure of the Ar annealed sample at 180 K and (b) Mn-O1-Mn in the R (hexagonal setting) structure of the air sintered sample at 180 K.

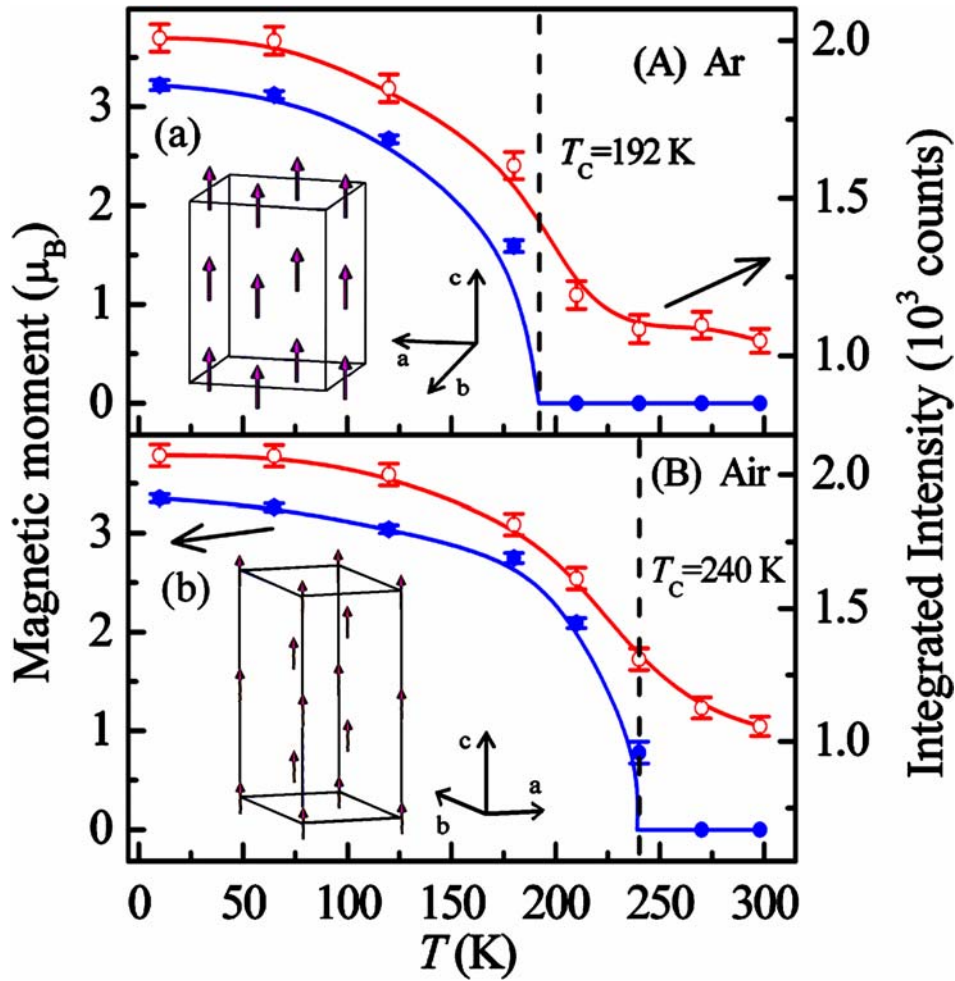


Figure 7.10: Refined Mn moment (left) and integrated intensity (right) observed at $Q = (1\ 1\ 0)$ and $(0\ 0\ 2)$ of the O structure and $Q = (0\ 1\ 2)$ of the R (hexagonal setting) structure versus temperature for (A) the Ar annealed and (B) the air sintered $\text{La}_{0.875}\text{Sr}_{0.125}\text{Mn}_{1-\gamma}\text{O}_{3+\delta}$ samples. Insets (a) and (b) show schematic illustrations of the ordered moments in the FM space groups of $Pbnm$ and $P1$, respectively. T_c is the onset temperature of FM ordering based on SQUID measurements. The solid lines are guides to the eye.

place for the Ar annealed sample. This is also reflected in the very large variation of the Mn-O1-Mn bond angle in the same temperature range as shown in the bottom of (g). Figures 7.9(a) and (b) schematically illustrate the Mn-O1-Mn, Mn-O2-Mn and Mn-O2'-Mn bond angles in the O structure and the Mn-O1-Mn in the R structure, respectively. For O structure the bond angle Mn-O2-Mn is equal to Mn-O2'-Mn. Two kinds of distortion related to MnO_6 octahedra have been distinguished: (i) the cooperative rotation mainly corresponding to Mn-O1-Mn bond angle; (ii) the JT distortion, inherent to high-spin ($S = 2$) Mn^{3+} ions, leading to large variations in bond lengths of Mn-O2 and Mn-O2' lying in acclivitous a - b plane of $Pbnm$ symmetry. Figure 7.10 shows the temperature dependences of the refined Mn moments and integrated intensities observed for Bragg reflections with magnetic intensity contributions for two samples. Insets (a) and (b) show schematic illustrations of the ordered moments for Ar annealed and air sintered samples, respectively. The T_c determined from the temperature dependences of the

Table 7.5: Refined structural parameters of the Ar annealed $\text{La}_{0.875}\text{Sr}_{0.125}\text{Mn}_{1-y}\text{O}_{3+\delta}$ sample. The R structure was refined using the H setting. The atomic positions for space group $R\bar{3}c$: La/Sr (0 0 1/4), Mn (0 0 0) and O1 (x 0 1/4); for $Pbnm$: La/Sr (x y 1/4), Mn (1/2 0 0), O1 (x y 1/4) and O2 (x y z). Numbers in parenthesis are the e.s.d. of the last significant digit.

Synthesis	Ar												annealed			
	10	65	120	180	210	240	270	300	400	450	500	900				
T (K)																
Crystal system	O	H	H	H	H											
Space group	$Pbnm$	$R\bar{3}c$	$R\bar{3}c$	$R\bar{3}c$	$R\bar{3}c$											
La/Sr :	$4c$	$6a$	$6a$	$6a$	$6a$											
x	-0.003(1)	0.001(1)	-0.002(1)	-0.004(1)	-0.005(1)	-0.004(1)	0.001(1)	0.0022(3)	0	0	0	0				
y	0.0241(5)	0.0235(5)	0.0240(5)	0.0246(6)	0.0226(6)	0.0219(6)	0.0203(6)	0.0212(4)	0	0	0	0				
O1 :	$4c$	$18e$	$18e$	$18e$	$18e$											
x	0.0647(8)	0.0638(8)	0.0644(8)	0.0656(8)	0.0662(7)	0.0664(7)	0.0657(8)	0.0622(9)	0.4464(3)	0.4465(3)	0.4470(3)	0.4522(3)				
y	0.494(1)	0.493(1)	0.494(1)	0.491(1)	0.492(1)	0.493(1)	0.494(1)	0.4930(4)	0	0	0	0				
O2 :	$8d$	—	—	—	—											
x	0.728(1)	0.729(1)	0.729(1)	0.730(1)	0.734(1)	0.734(1)	0.732(1)	0.7305(9)	—	—	—	—				
y	0.2796(7)	0.2794(7)	0.2791(7)	0.2788(7)	0.2803(6)	0.2797(6)	0.2791(7)	0.2763(8)	—	—	—	—				
z	0.0334(4)	0.0344(4)	0.0338(4)	0.0341(3)	0.0352(3)	0.0347(3)	0.0340(4)	0.0332(4)	—	—	—	—				
R_p (%)	3.81	3.63	3.73	3.68	3.73	3.65	3.61	2.88	3.39	3.67	3.44	3.28				
R_{wp} (%)	5.34	4.93	5.13	4.91	4.84	4.77	4.85	3.91	4.58	4.86	4.57	4.43				
χ^2	3.73	3.14	3.41	3.17	3.09	2.97	3.07	3.32	2.00	2.27	2.00	1.84				
R_{mag} (%)	4.40	4.15	3.65	6.65	—	—	—	—	—	—	—	—				

Table 7.6: Refined structural parameters of the air sintered $\text{La}_{0.875}\text{Sr}_{0.125}\text{Mn}_{1.7}\text{O}_{3.6}$ sample. The R structure was refined using the H setting. Numbers in parenthesis are the e.s.d. of the last significant digit.

Synthesis	Air												Sintered		
	10	65	120	180	210	240	270	300	450	900					
Crystal system	O	O	O	H											
Space group	$Pbnm$	$Pbnm$	$Pbnm$	$R\bar{3}c$											
La/Sr :	$4c$	$4c$	$4c$	$6a$											
x	0.002(1)	0.002(1)	0.008(1)	0	0	0	0	0	0	0	0	0	0		
y	0.010(1)	0.010(1)	0.011(2)	0	0	0	0	0	0	0	0	0	0		
O1 :	$4c$	$4c$	$4c$	$18e$											
x	0.0605(8)	0.0605(7)	0.062(2)	0.4494(8)	0.4485(2)	0.4481(2)	0.4480(2)	0.4494(2)	0.4502(3)	0.4540(4)					
y	0.499(2)	0.499(2)	0.501(3)	0	0	0	0	0	0	0	0	0	0		
O2 :	$8d$	$8d$	$8d$	—	—	—	—	—	—	—	—	—	—		
x	0.752(3)	0.751(3)	0.756(3)	—	—	—	—	—	—	—	—	—	—		
y	0.263(1)	0.263(1)	0.260(2)	—	—	—	—	—	—	—	—	—	—		
z	0.0325(4)	0.0327(4)	0.0340(6)	—	—	—	—	—	—	—	—	—	—		
R_p (%)	3.76	3.84	2.97	3.98	3.42	3.15	3.11	2.72	2.94	3.61					
R_{wp} (%)	5.36	5.32	4.11	5.25	4.63	4.28	4.25	3.64	4.00	4.99					
χ^2	3.97	3.90	2.34	3.72	2.90	2.49	2.45	2.84	1.54	2.36					
R_{mag} (%)	2.33	2.26	2.69	2.97	2.72	4.34	—	—	—	—					

profiles of (1 1 0), (0 0 2) in the O structure and (0 1 2) in the R structure are consistent with the values determined based on SQUID measurements. Tables 7.5 and 7.6 show the refined atomic positions and reliability factors at all explored temperatures for the Ar annealed and air sintered samples, respectively.

7.4.2 Discussion

Inset (a) of figure 7.7 in the Q ranges 2.5-2.6 \AA^{-1} and 3.0-3.1 \AA^{-1} shows the presence of Bragg reflections (2 1 0), (1 2 0) and (2 1 2), (1 2 2), respectively, at 10, 65 and 120 K. These peaks belong to the O structure and are absent at 180 and 270 K. In the Q range 4.4-4.7 \AA^{-1} of inset (a), one may observe a symmetric structural and magnetic peak indexed as (4 0 0), (0 4 0) and (2 2 4) in the O structure at 10 and 65 K. This peak splits into two peaks at 180 and 270 K, corresponding to nuclear as well as FM reflections, which are indexed as (2 2 0) and (2 0 8) in the R structure. At 120 K, the shape of the peak becomes clearly asymmetric, indicating the existence of a mixed R and O phase at this temperature. The coalescence of (2 2 0) and (2 0 8) of R setting in the O structure within present resolution results not only from the structural changes, but also from the contribution of the magnetic peaks at 10, 65 and 120 K. I thus conclude that there is a structural transition from R to O between 180 and 65 K for the air sintered sample, unlike the case in [162]. In particular, at 120 K, a mixed R and O phase is observed with the refined weight percentage of 49.2(14) wt% and 50.8(14) wt%, respectively, which yields the smallest reliability factors (table 7.6). With a single phase, no satisfactory refinement can be achieved. By contrast, this transition from R to O happens in the Ar annealed sample between 400 and 298 K (table 7.5). To summarize: for the Ar annealed sample, I found the O structure between 10 and 298 K and the R structure between 400 and 900 K (table 7.5); for the air sintered sample, I observe a pure O structure only below 65 K and the R structure between 180 and 900 K, while at 120 K a phase mixture was observed (table 7.6).

For the Ar annealed sample as shown in figure 7.8, the lattice parameters very slowly increase from 10 to 120 K ($c_o/\sqrt{2} < b_o < a_o$; O'' phase). From 120 to 298 K, a rapid development of a large breathing-mode distortion corresponding to larger b_o than $c_o/\sqrt{2}$ is observed, whereas a_o continuously increases. At temperatures close to 180 and 270 K, the temperature variation curves of a_o and b_o cross one another ($c_o/\sqrt{2} < a_o < b_o$; O' phase). From 298 to 400 K, as reported in $\text{La}_{1-x}\text{Sr}_x\text{MnO}_3$ with $x = 0.1$ [160], the lattice parameters should satisfy relation $b_o < c_o/\sqrt{2} < a_o$, belonging to the so-called O phase. From 400 to 900 K, i.e. in the rhombohedral phase, a_h and c_{eq} increase more rapidly than in the O region. I can conclude that the Ar annealed sample follows the phase-transition sequence of the $\text{La}_{0.875}\text{Sr}_{0.125}\text{MnO}_3$ single crystal [157] O'' - O' - O - R in the temperature range investigated. The differences between lattice parameters of O'' and O phases are by far smaller than those of O' phase. It should be mentioned that the true crystal structures of O' and O'' phases for $\text{La}_{1-x}\text{Sr}_x\text{MnO}_3$ samples with $x = 0.11$ - 0.125 were reported to be monoclinic and triclinic, respectively, in the studies with high resolution synchrotron powder x-ray diffraction [172] and resonant x-ray scattering [173] techniques. However, I did not observe any splitting of Bragg peaks within our instrument resolution, which would have indicated the existence of the two lower-symmetry structures, and therefore

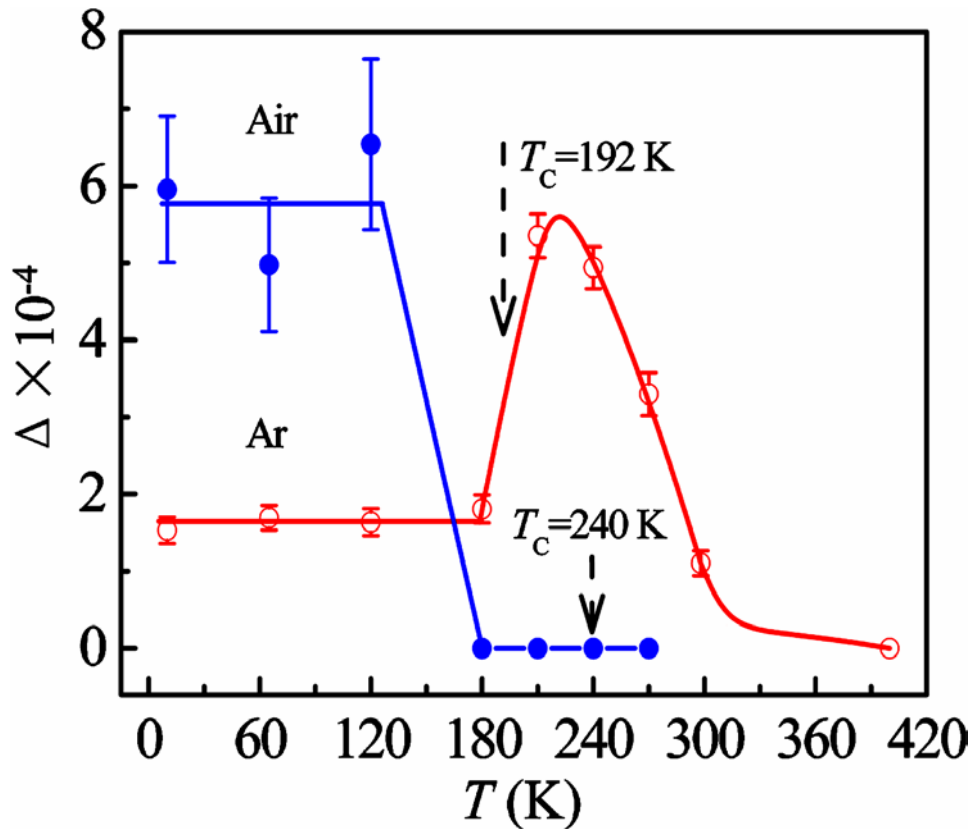


Figure 7.11: Temperature variation of the coherent JT distortion parameter Δ of MnO_6 octahedra for Ar annealed and air sintered $\text{La}_{0.875}\text{Sr}_{0.125}\text{Mn}_{1-\gamma}\text{O}_{3+\delta}$ samples. T_c (Ar) = 192 K and T_c (Air) = 240 K are based on the SQUID measurements. The solid lines are guides to the eye.

refined the data within an orthorhombic model. For the air sintered sample, I note nearly linear increases for a_h and c_{eq} in the R structural region from 180 to 900 K, while in the O region from 10 to 120 K, a_o , $c_o/\sqrt{2}$ and b_o remain nearly constant as shown in figure 7.8. Moreover, from 10 to 120 K, the lattice parameters satisfy the relation of $b_o < c_o/\sqrt{2} < a_o$, indicating that the air sintered sample belongs to the O phase. Compared to the $x = 0.125$ single-crystal data [157], the structural changes for my samples are less distinct. However, compared to [174], the Sr content in my samples is more stoichiometric in agreement with the refined room-temperature data. This indicates that one of the reasons for the differences in structural and physical properties between polycrystals and single crystals is the possible composition fluctuations and inhomogeneities.

According to equation 7.1, I calculated the coherent JT distortion parameter Δ for both samples as shown in figure 7.11. For the Ar annealed sample, Δ remains constant below 180 K and then drastically increases, showing a peak at ~ 210 K. On further warming, it is strongly reduced, especially when T approaches to $T_{\text{JT}} \approx 298$ K. The value of Δ at $T_{\text{JT}} \approx 298$ K is somewhat smaller than that in $10 < T < 180$ K. Above 400 K, i.e. in the R structural region, Δ vanishes completely. For the air sintered sample, Δ for the O structure below 120 K is comparable to that of Ar annealed sample at its maximal value at 210 K. Its contrast value is consistent with contrast Mn-O2' and Mn-O2 bond lengths as

shown in the inset (d') of figure 7.8. In view of a large Δ below 120 K, resulting from big differences between three bond lengths and suggesting strongly distorted MnO_6 octahedra, the orthorhombic structure for air sintered sample is more alike the O' than the O phase. The coherent JT transition temperature is reduced to ~ 170 K. For comparison, the coherent JT transition temperature of the parent compound LaMnO_3 is about 750 K [159]. On doping with Sr, T_{JT} is drastically reduced, becoming $T_{\text{JT}} \approx 475$ K for a doping level of 0.1 [160]. Here, it is once more reduced to $T_{\text{JT}} \approx 298$ K for the Ar annealed sample with Sr doping level 0.125, which is rather close to the reported value $T_{\text{JT}} \approx 270$ K for the single crystal [157]. Moreover, it is surprisingly decreased to ~ 170 K for the air sintered sample. It is worth mentioning that the coherent JT transition temperature strongly depends on the Mn^{3+} concentration which can easily be changed by substitution and nonstoichiometry, e.g. Mn site vacancies and excess oxygen, etc. For the Ar annealed sample, the onset of large coherent JT distortion leads to a phase transition from O to O' , accompanied by Mn^{3+} orbital order which is reflected by the bond lengths in the MnO_6 octahedra, i.e. the long Mn-O2' and short Mn-O2 bonds lying in the acclivitous a - b plane and the medium Mn-O1 almost along the c axis in the $Pbnm$ symmetry. In [174], this transition is considered as a disorder-order transition, during which the randomly disordered and highly distorted MnO_6 octahedra in the O phase form a long-range order in the O' phase. The FM transition temperature ($T_c \approx 192$ K) is much smaller than the R - O structural transition temperature $T_{\text{RO}} \approx 400$ K. Below $T \approx 180$ K, the long-range FM order partly suppresses the coherent JT distortion, resulting in the O' to O'' transition and the short-range order of highly distorted MnO_6 octahedra in the O'' phase, which indicates a strong coupling between the distortion of MnO_6 and the FM order. The structural features of O'' phase are similar to those of O phase, as is the JT distortion parameter Δ , whereas the magnetic states are severely different (O'' phase: FM order; O phase: paramagnetic state). The air sintered sample shows the effect of FM transition in the R structural region on the structural properties and the vestiges of R - O structural transition in the FM ordering state. The R - O structural transition is responsible for the appearance of a large coherent JT distortion, though in the whole O structural region the FM order has already set in ($T_{\text{RO}} \approx 180$ K $<$ $T_c \approx 240$ K). Thus here exist strong couplings between FM order, coherent JT distortion and structural transition. For both samples, the increase of T_c is accompanied by a shift of T_{RO} to lower temperatures, which seems to be universal for the lightly doped $\text{La}_{1-x}\text{Sr}_x\text{MnO}_3$ [174]. At T_{JT} and T_{OR} transition temperatures, the unit-cell volume V per Mn ion displays anomalies in accordance with the case of LaMnO_3 [175], but unlike [9].

Equation 7.2 shows that both the decrease of $\langle \text{Mn-O-Mn} \rangle$ and the increase of $\langle \text{Mn-O} \rangle$ result in the decrease of one-electron bandwidth W . So W can be interpreted as a generalized parameter, combining the effects of $\langle \text{Mn-O-Mn} \rangle$ and $\langle \text{Mn-O} \rangle$. The calculated values of W for two samples are shown in figures 7.8(g) and (h). For the Ar annealed sample, a band widening happens from $T_c \approx 192$ to 10 K, which is owned to the small decrease of $\langle \text{Mn-O} \rangle$ bond length consistent with less insulating bonds as well as the slight increase of $\langle \text{Mn-O-Mn} \rangle$ bond angle, in agreement with a stronger orbital overlap of Mn-O bonds in the O'' phase [174]. For the air sintered sample, W decreases slowly in the entire temperature range. The decrease of $\langle \text{Mn-O} \rangle$ bond length and the increase of $\langle \text{Mn-O-Mn} \rangle$ bond angle from $T_c \approx 240$ to 120 K lead to a widening of the band, consistent with the creation of itinerant electrons and the development of metallic bonds in the FM phase [174].

For the Ar annealed sample, the peak at $\sim 2.27 \text{ \AA}^{-1}$, allowed not only for nuclear scattering but also for magnetic scattering and indexed as $(2\ 0\ 0)$, $(0\ 2\ 0)$ and $(1\ 1\ 2)$ in the $Pbnm$ symmetry, has a remaining nuclear contribution at $T = 298 \text{ K}$ above $T_c \approx 192 \text{ K}$ as shown in the inset (d) of figure 7.7. This is unlike the case in [3], where this peak vanishes at temperatures above $T_c \approx 220 \text{ K}$ (probably owe to the short counting time) and the authors established a canted FM model and an AFM state for the sample below and above T_c , respectively. I did not detect any reflection forbidden by the crystal structure and pure ferromagnetism below $T_c \approx 192 \text{ K}$, such as $(0\ 0\ 3)$ (detected by monitoring [176]) and $(0\ 0\ 1)$ (detected with triple-axis neutron spectrometer [2]), within the present data accuracy. The magnetic reflections $(0\ 0\ l)$ are absent, indicating a moment aligned along c . Thus for both samples, my data are consistent with pure FM order of the Mn moments along c with space groups $Pb'n'm$ and $P1$ for the O and R structures, respectively. The theoretical saturation moments are $4 \mu_B$ and $3 \mu_B$ for Mn^{3+} and Mn^{4+} ions, respectively. Assuming quenched orbital angular momentum ($L = 0$; $J = S$), I calculated the effective saturation values of spin moments using the Mn^{3+} and Mn^{4+} contents (table 7.3), which are evaluated from the refined site occupancies of RT data based on the charge neutrality condition. The calculated moments of $3.55(13) \mu_B$ (Ar) and $3.60(13) \mu_B$ (air) are in good agreement with the refined values of $3.22(5) \mu_B$ (Ar) and $3.35(4) \mu_B$ (air) for the two samples, respectively, considering the crude assumptions, especially the purely integer valencies.

The FM order below T_c is not changed by the different nuclear structures, O and R . On the other hand, the FM ordering temperature is strongly dependent on these structural transitions resulting from different synthesis conditions and decreases from 240 K (air) to 192 K (Ar).

7.4.3 Conclusions

I have performed a comparative NPD investigation of the crystal and magnetic structures in the temperature range from 900 to 10 K for Ar annealed and air sintered $\text{La}_{7/8}\text{Sr}_{1/8}\text{Mn}_{1-\gamma}\text{O}_{3+\delta}$ samples with O and R structures at room temperature, respectively. The behavior of Ar annealed polycrystalline material is similar to the case of a single crystal. A series of structural transitions $R-O-O'-O''$ takes place successively with decreasing temperature from 900 to 10 K . The refined FM moment is $3.22(5) \mu_B/\text{Mn}$ at 10 K with spin orientation along the c axis in $Pbnm$ symmetry. The estimated JT transition temperature is drastically reduced to $\sim 298 \text{ K}$, compared with that of LaMnO_3 ($T_{JT} \approx 750 \text{ K}$) [159] and that of $\text{La}_{0.9}\text{Sr}_{0.1}\text{MnO}_3$ ($T_{JT} \approx 475 \text{ K}$) [160]. For the air sintered sample, a structural transition from R to O has been observed for the first time to occur between 180 and 65 K . In particular, at 120 K , a mixed R ($49.2(14) \text{ wt}\%$) and O ($50.8(14) \text{ wt}\%$) phase exists. The structural transition temperature is severely decreased compared to $T_{RO} \approx 400 \text{ K}$ for the Ar annealed sample. The refined FM moment is $3.35(4) \mu_B/\text{Mn}$ at 10 K , being parallel to the c axis in $R\bar{3}c$ symmetry. Air sintering, leading to the R structure at room temperature, results in a remarkable decrease of the coherent JT transition temperature by $\sim 43\%$ compared to that of Ar annealed sample, though no significant change in the magnitude of coherent JT distortion parameter Δ was observed. In addition, the refined moments and the FM transition temperatures are consistent with the calculated effective saturation values of the spin moments and SQUID measurements, respectively, for both

samples. Moreover, this study shows the existence of strong couplings between FM ordering, JT distortion and structural transition. For the Ar annealed sample, the appearance of FM ordering below $T_c \approx 192$ K only partially suppresses the coherent JT distortion, but it is completely removed by the *O-R* structural transition for both samples.

Chapter 8

Complex ordering phenomena in $\text{La}_{7/8}\text{Sr}_{1/8}\text{MnO}_3$ single crystals

8.1 Introduction

The parent compound LaMnO_3 is an AFM insulator ($T_N = 140$ K) with an orbital order (figure 2.12(D)) induced by the cooperative JT effect of Mn^{3+} ions below $T_{JT} = 750$ K [177]. With Sr doping, the JT distortion is gradually suppressed, which leads to a FMI state and finally to a FMM state. The classical double-exchange mechanism originally formulated by Zener [41] and the strong Hund's coupling are able to qualitatively explain the FMM phase observed at intermediate hole-doping levels of 0.2-0.4 [178]. However, the nature of the unusual FMI state in lightly doped $\text{La}_{1-x}\text{Sr}_x\text{MnO}_3$ with $x \approx 0.10$ -0.15 [38] has attracted much attention and given rise to many controversies [9, 155, 156, 163, 179, 180].

Numerous publications were focused on the hole-doped $\text{La}_{1-x}\text{Sr}_x\text{MnO}_3$ ($x \approx 1/8$) manganite with the FMI phase below $T_{\text{CO/OO}} \approx 150$ K. First-order structural transitions from O ($c/\sqrt{2} < b \approx a$) in the PMI state to O' ($c/\sqrt{2} < a < b$) with the cooperative JT distortion at $T_{JT} \approx 270$ K and subsequently to O'' ($c/\sqrt{2} < b < a$) with similar behaviors to O phase at $T_{\text{CO/OO}} \approx 150$ K in the $Pbnm$ symmetry were reported for a $\text{La}_{7/8}\text{Sr}_{1/8}\text{MnO}_3$ single crystal with $T_c \approx 180$ K [157], where the FM moment $\sim 3.6 \mu_B/\text{Mn}$ was detected. The structure of a $\text{La}_{7/8}\text{Sr}_{1/8}\text{MnO}_3$ single crystal between T_{JT} and $T_{\text{CO/OO}}$ was confirmed to be the monoclinic by high-resolution synchrotron powder x-ray diffraction (SPXD) but without the information of atomic positions [172], where the assignment of triclinic symmetry to the FMI phase was regarded to be tentative not confirmative by the profile matching method without atomic position parameters. This assignment was confirmed by the RXS technique [173]. However, this technique definitely cannot determine a complete structure model standing the test because of the small number of observed reflections (Bragg and superstructure), though it could be a useful method to test the structure symmetry by observing the very weak Bragg peaks. It was revealed that the FMI phase at this doping level belongs to the triclinic ($P\bar{1}$) structure and has a superstructure with the unit cell of $\sim 2a_c \times 4b_c \times 4c_c$, where a_c , b_c and c_c are lattice parameters in the pseudocubic perovskite notation, in a study by the convergent-beam electron diffraction together with selected-area electron diffraction [181]. Up to now, the detailed actual structure of this

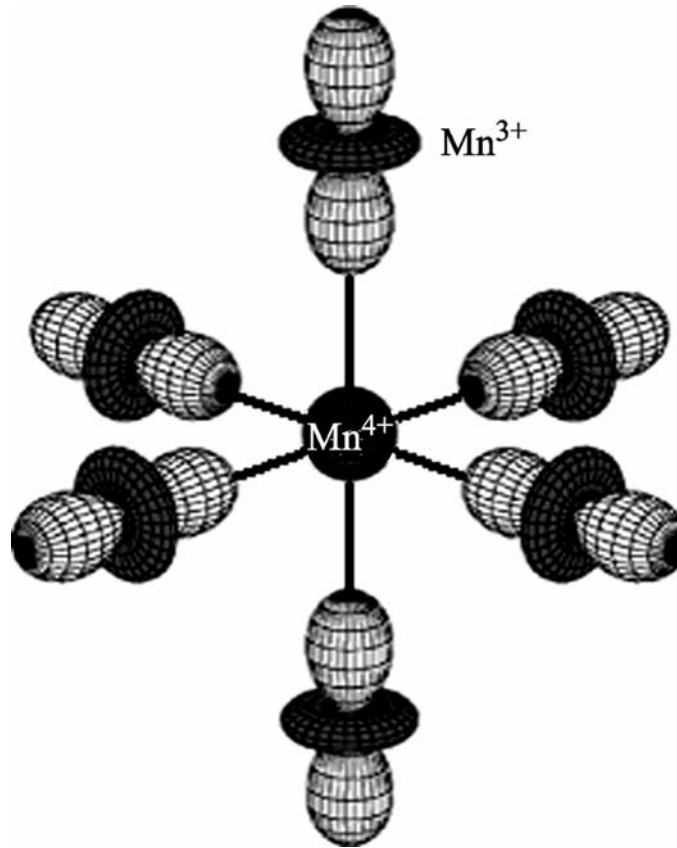


Figure 8.2: The orbitals of Mn³⁺ ions are directed towards a hole forming an orbital polaron around a Mn⁴⁺ site (sphere). The formation of an orbital polaron not only leads to a FM object that is stabilized by the double-exchange mechanism, but also traps a hole reducing the kinetic energy of the charge carriers, which consequently could lead to the FMI state. Taken from [9].

natural explanation for the coexistence of FM and insulating properties. Recently, it was reported that $\text{La}_{7/8}\text{Sr}_{1/8}\text{MnO}_3$ displays a non-uniform charge distribution below 30 K, comprised of two interconnected Mn subsystems with different spin, orbital and charge couplings, in a study using the nuclear magnetic resonance technique [180].

Although the importance of charge and orbital degrees of freedom on understanding the microscopic origin of the FMI phase in $\text{La}_{1-x}\text{Sr}_x\text{MnO}_3$ ($x \approx 1/8$) has been realized, the exact and detailed CO/OO model is still a puzzle just because of the bewildering structures. Another current argument is how the CO/OO takes place. The present understanding of these complex ordering phenomena is largely based on the traditional ionic model, in which the valence electrons are completely localized at the cation sites. However, it cannot be discarded that the actual charge non-stoichiometry of total Mn ions deviated from the normal doping level in manganites may result from the oxygen charge holes, namely that the itinerant electrons may be mutually shared by Mn and oxygen together. Thus the CO description has to include the oxygen holes as suggested in [103]. The CO in $\text{La}_{1-x}\text{Sr}_x\text{MnO}_3$ ($x \approx 1/8$) is among the most puzzling. Up to date, no hard experimental evidence concerning the occurrence of CO in this compound has been obtained. Therefore, this compound still remains an outstanding example to tackle the complex ordering phenomena in highly correlated CTMO.

In this chapter, the first part presents the results of crystal and magnetic structure studies carefully carried out on a powdered $\text{La}_{1-x}\text{Sr}_x\text{MnO}_3$ ($x \approx 1/8$) single crystal utilizing the NPD technique from 5 to 300 K along with its interesting magnetic properties. The structural information obtained from this study provides the basis for establishing the correct charge- and orbital- order model from single crystal anomalous x-ray scattering. The second part reports the RXS investigations on the complex ordering phenomena of $\text{La}_{1-x}\text{Sr}_x\text{MnO}_3$ ($x \approx 1/8$) in the hard and soft x-ray regimes, especially the first direct observation of the hole ordering in this compound obtained via the RSXS technique.

8.2 Lattice and magnetic order

8.2.1 Experimental details

Detailed preparation procedures for $\text{La}_{7/8}\text{Sr}_{1/8}\text{MnO}_3$ polycrystals have been described in chapter 5. Just here in order to particularly make amends for the Mn sublimation and evaporation during the processes of high-temperature reactions and single crystal growth, respectively, 3 at% excess Mn was added in the form of MnO_2 raw material. High-quality single crystals of $\text{La}_{1-x}\text{Sr}_x\text{MnO}_3$ ($x \approx 1/8$) were grown by an optical floating-zone method (chapter 6). The details about the subsequent high-resolution NPD data collection on the SPODI instrument [129] are described in chapter 4. For Rietveld analysis of the NPD data, the pseudo-Voigt function was chosen to model the peak profile shape; the background contribution was determined using a linear interpolation between automatically selected data points; the scale factor, zero shift, profile shape parameters, half width parameters, asymmetry, lattice parameters, atomic positions, isotropic thermal parameters as well as the site occupancies of La(Sr) and Mn atoms were refined. The dc magnetization measurements between 5 and 400 K were performed on a Quantum Design MPMS-7 SQUID magnetometer. The magnetization curves were acquired on heating from low temperature after cooling in zero magnetic field and with applied fields of 20, 120 and 7×10^4 Oe, respectively. A hysteresis loop from -70 to 70 kOe at 5 K was also measured. The estimation of the density was carried out on a home-made densitometer.

8.2.2 Results

The NPD data at 300 K was refined using an orthorhombic ($Pnma$) model, while the data in the temperature range $T_{\text{CO/OO}} < T < T_{\text{JT}}$ (i.e. 170, 220 and 265 K) were verified to correspond to a monoclinic ($P12_1/c1$, M') structure by comparing these two competing models. The data at 5 and 100 K (i.e. in the FMI regime) were also refined using the monoclinic ($P12_1/c1$, M'') model. An attempt was made to refine them with a triclinic ($P\bar{1}$) model, but the goodness of fit χ^2 has not decreased largely despite 11 additional parameters in refining the 5 K data. The appearance of excess oxygen in $\text{La}_{1-x}\text{Sr}_x\text{MnO}_3$ compounds at low doping levels is due to the corresponding cation vacancies [10]. Therefore, the La/Sr (fixed at the ratio 7/1) and Mn (constrained to be the same for Mn1 and Mn2) site occupancies were first refined with the 220 and 265 K NPD data that have high enough counting statistics and no magnetic contributions. By refining them with

different procedures and models, the actual formula $\text{La}_{0.848(2)}\text{Sr}_{0.121(2)}\text{Mn}_{0.984(4)}\text{O}_3$ was obtained within e.s.d. for the studied powdered single crystal. In the subsequent refinements, the occupancy parameters of La/Sr and Mn were allowed to vary at other temperatures, but they remained almost the same as the obtained actual formula within the e.s.d.. It should be stressed that the actual molecular weight was used for various calculations in this chapter, e.g. in the transformation of the magnetization unit from emu per gram to μ_B per Mn ion.

Figure 8.3 exhibits a comparison between refinements with the two structure models, orthorhombic (a, b, c and d) and monoclinic (a', b', c' and d'), at 220 K. The differences between observed and calculated patterns in different 2θ regions confirm that the space group $P12_1/c1$ is much more suitable for the observed NPD data. Comparing figures 8.3(a), (c) and (d) to the corresponding (a'), (c') and (d'), we can see that some overlapped and unrecognized peaks in $Pnma$ symmetry are separated and appreciated by the space group $P12_1/c1$, respectively. The refined structural parameters with these two competing models are shown in table 8.1, where an obvious deviation of the structure angle β from 90° and significant decreases in the reliability factors once more support the choice of M' structural model for the observed NPD data. The two crystal unit-cells of orthorhombic ($Pnma$) and monoclinic ($P12_1/c1$) structures and their respective MnO_6 octahedra are contrastingly illustrated in figures 8.4(a) and (b), respectively, where the Mn and O2 sites in $Pnma$ space group decompose into Mn1, Mn2 sites and O2, O3 sites in $P12_1/c1$ symmetry, respectively, while O1 still retains one site.

Magnetic refinements have been done assuming an identical magnetic moment for Mn1 and Mn2 ions in $P12_1/c1$ symmetry. Various FM models were tried with spin orientations parallel to the a , b and c axes or their combinations. Only the two models with ordered Mn moments along the b and c axes, respectively, can lead to the convergence of the refinement reached. With further testing, the best fit was obtained using the model with total Mn moment located in the crystallographic b - c plane. This can be verified by the insets (b) and (c) of figure 8.5, where the refined results with FM models of $F_y F_z$ (moments along the b and c axes) and F_z , respectively, are shown. In inset (b), the model $F_y F_z$ can produce a much more comparable intensity (solid line) to the observed one (circles) than that of F_z model (dashed). In inset (c), the sum of the intensities generated by crystal structure (dashed) and $F_y F_z$ magnetic model is already enough for the observed peaks (circles). The observed intensity of (0 1 1) peak does not need any supplement from F_z magnetic structure except that from the crystal structure. The characteristic A -AFM (1 0 0) peak appears at 5 K as shown in the inset (a) of figure 8.5. With increasing temperature to 100 K, the peak (1 0 0) disappears, indicating a transformation from A -AFM to FM and different temperature evolutions for them. It should be pointed out that the (1 0 0) peak at 100 K was shifted in the intensity axis in order to clearly show the 5 K data. Having identified the correct FM model at 100 and 170 K, a suitable AFM model was tried to be refined with the 5 K NPD data as the procedure used for the FM model. Finally, it was determined as A_y (moment along the b axis). The refined results at 5 K are plotted in figure 8.5, where the calculated pattern consists of three contributions: crystal structure, FM ($F_y F_z$) and AFM (A_y) models.

Figure 8.6 shows the temperature dependence of the unit-cell parameters from 5 to 300 K. It is worth pointing out that I tried to refine the NPD data at 300 K using the monoclinic symmetry and the obtained unit-cell volume shown as the symbol of \diamond in panel (c), in addition to the monoclinic angle $\beta = 89.97(2)^\circ$, is identical to the obtained

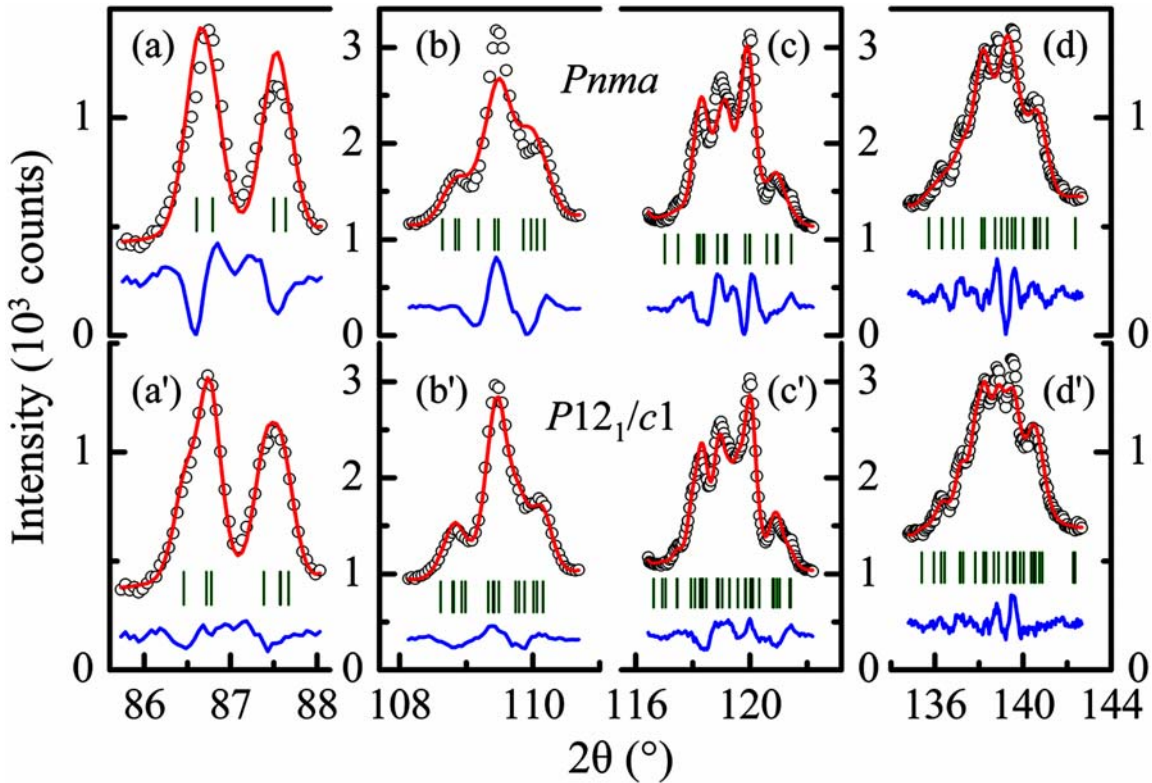


Figure 8.3: Observed NPD data (circles) of a powdered $\text{La}_{1-x}\text{Sr}_x\text{MnO}_3$ ($x \approx 1/8$) single crystal within four 2θ regions and the corresponding calculated intensities (solid lines) with space groups of $Pnma$ (a, b, c and d) and $P12_1/c1$ (a', b', c' and d') at 220 K. The vertical lines mark the positions of Bragg reflections automatically generated from the space groups. The lower curve in each panel represents the difference between experimental and calculated patterns.

ones for $Pnma$ setting within e.s.d.. This attempt proves that if an actual orthorhombic structure is refined with a lower symmetry, the refined parameters will stay identical within the e.s.d. and have no such big differences as certified in my data at 170, 220 and 265 K. The panel (a) definitely represents a breathing-mode distortion. It is worth noting that there are two crossovers in the lattice parameters b and c around $T_{\text{CO/OO}}$ and T_{JT} , respectively, implying a change in the sign of the orthorhombic strain in the b - c plane, namely $S = 2(b-c)/(b+c)$. This is related to the huge decrease in the JT effect below $T_{\text{CO/OO}}$ and above T_{JT} , corresponding to the decrease of the structure angle β and the appearance of the two anomalies in unit-cell volume. The change in the sign of S as shown in the inset (a') of figure 8.7 for Sr doped $\text{La}_{1-x}\text{Sr}_x\text{MnO}_3$ ($x \approx 1/8$) manganite is the distinct difference with the Ca doped manganite having the same nominal hole concentration where the sign of S keeps unchanged [182].

The temperature variation of the ZFC and FC dc magnetization $M(T)$ at $H = 20$ and 120 Oe for the studied $\text{La}_{1-x}\text{Sr}_x\text{MnO}_3$ ($x \approx 1/8$) single crystal are plotted in figure 8.8(a). Figure 8.8(b) shows temperature dependence of the ZFC and FC magnetic moment μ_{B} per Mn ion at 70 kOe (unconnected up and down triangles, respectively), where the strong magnetic field induced magnetization appears above T_{c} . The refined values of the total FM moments at 5, 100 and 170 K and the value of the AFM moment at 5 K using the two

Table 8.1: Comparison of the refined structural parameters of a powered $\text{La}_{1-x}\text{Sr}_x\text{MnO}_3$ ($x \approx 1/8$) single crystal and the reliability factors for refinements with monoclinic and orthorhombic models at 220 K. In space group $Pnma$, the angle Mn1-O1-Mn2 means Mn1-O1-Mn1. Number in parenthesis is the e.s.d. of the last significant digit.

Crystal system	Monoclinic ($P 12_1/c 1$)	Orthorhombic ($Pnma$)
a (Å)	7.7370(6)	5.5624(6)
b (Å)	5.5487(8)	7.7360(6)
c (Å)	5.5633(7)	5.5478(5)
β (°)	90.145(2)	90
La/Sr:	$4e$	$4c$
x	0.2515(3)	0.0256(2)
y	-0.0041(2)	0.25
z	-0.0253(2)	-0.0040(3)
$B(\text{La/Sr})(\text{Å}^2)$	0.58(2)	0.56(3)
Mn1:	$2c(0, 0, 0.5)$	$4b(0, 0, 0.5)$
Mn2:	$2d(0.5, 0, 0.5)$	
$B(\text{Mn1}, 2)(\text{Å}^2)$	0.53(4)	0.65(6)
O1:	$4e$	$4c$
x	0.2507(6)	0.4927(4)
y	0.0678(2)	0.25
z	0.5072(3)	0.0690(3)
$B(\text{O1})(\text{Å}^2)$	0.95(2)	0.96(3)
O2:	$4e$	$8d$
x	0.0342(4)	0.2846(2)
y	0.7381(7)	0.0341(1)
z	0.7113(4)	0.7347(4)
O3:	$4e$	
x	0.4657(3)	
y	-0.2290(7)	
z	0.2201(4)	
$B(\text{O2}, 3)(\text{Å}^2)$	1.08(2)	1.13(2)
Mn1, 2-O1(Å)	1.976(5), 1.966(5)	1.972(1)
Mn1-O2(Å)	2.097(3), 1.887(3)	2.067(2), 1.916(2)
Mn2-O3(Å)	2.027(3), 1.958(3)	
$\langle \text{Mn-O} \rangle$ (Å)	1.985(2)	1.985(1)
Mn1-O1-Mn2(°)	157.87(19)	157.49(1)
Mn1-O2-Mn1(°)	160.80(13)	160.98(7)
Mn2-O3-Mn2(°)	160.81(13)	
$\langle \text{Mn-O-Mn} \rangle$ (°)	159.83(9)	159.82(3)
R_p (%), R_{wp} (%)	2.97, 3.85	3.74, 5.18
χ^2	1.40	2.52
R_B (%), R_F (%)	2.63, 2.05	3.06, 2.28

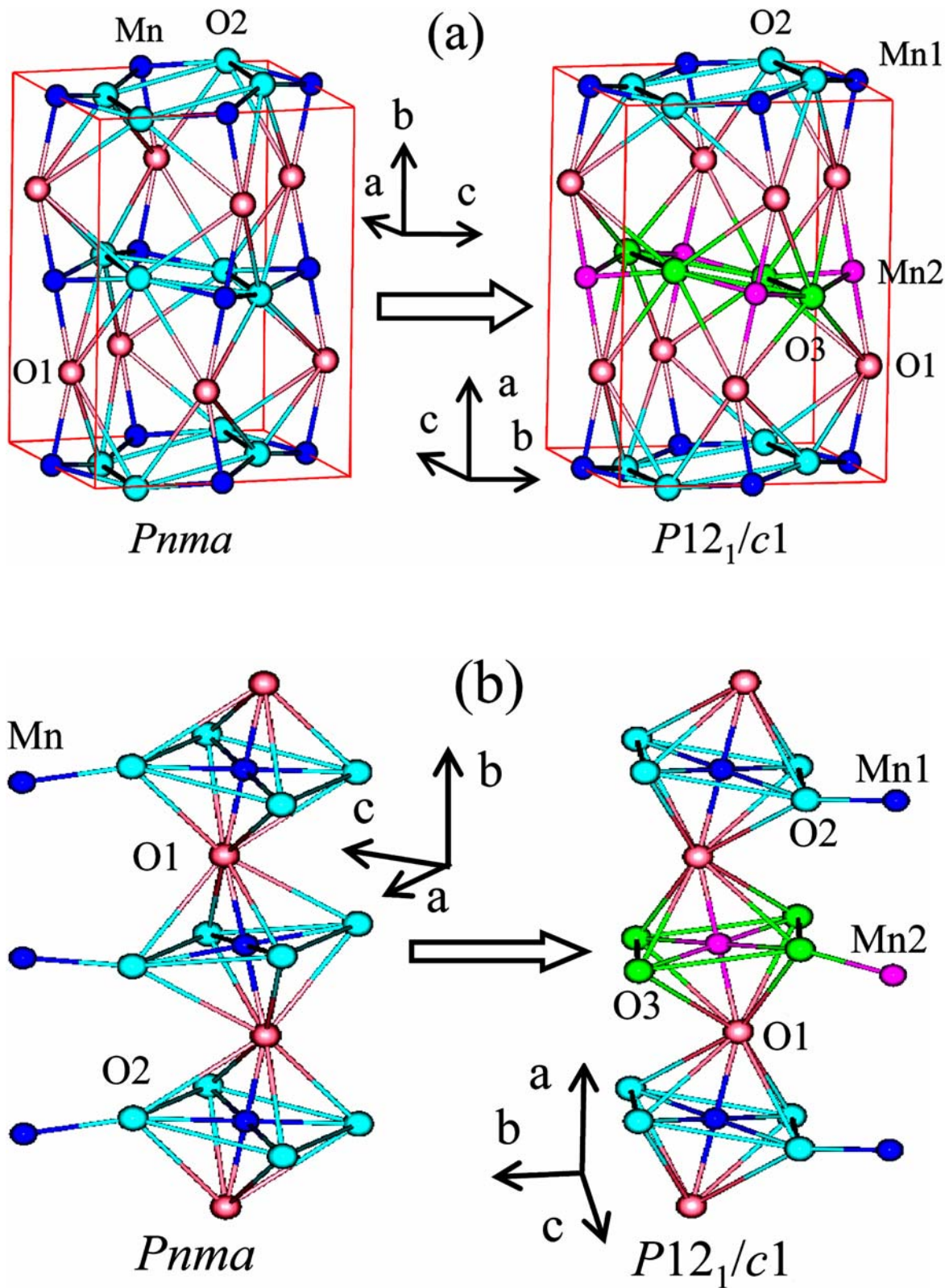


Figure 8.4: Schematic illustrations of (a) the crystal structure unit-cells and (b) the corresponding MnO_6 octahedra in orthorhombic ($Pnma$) and monoclinic ($P12_1/c1$) models.

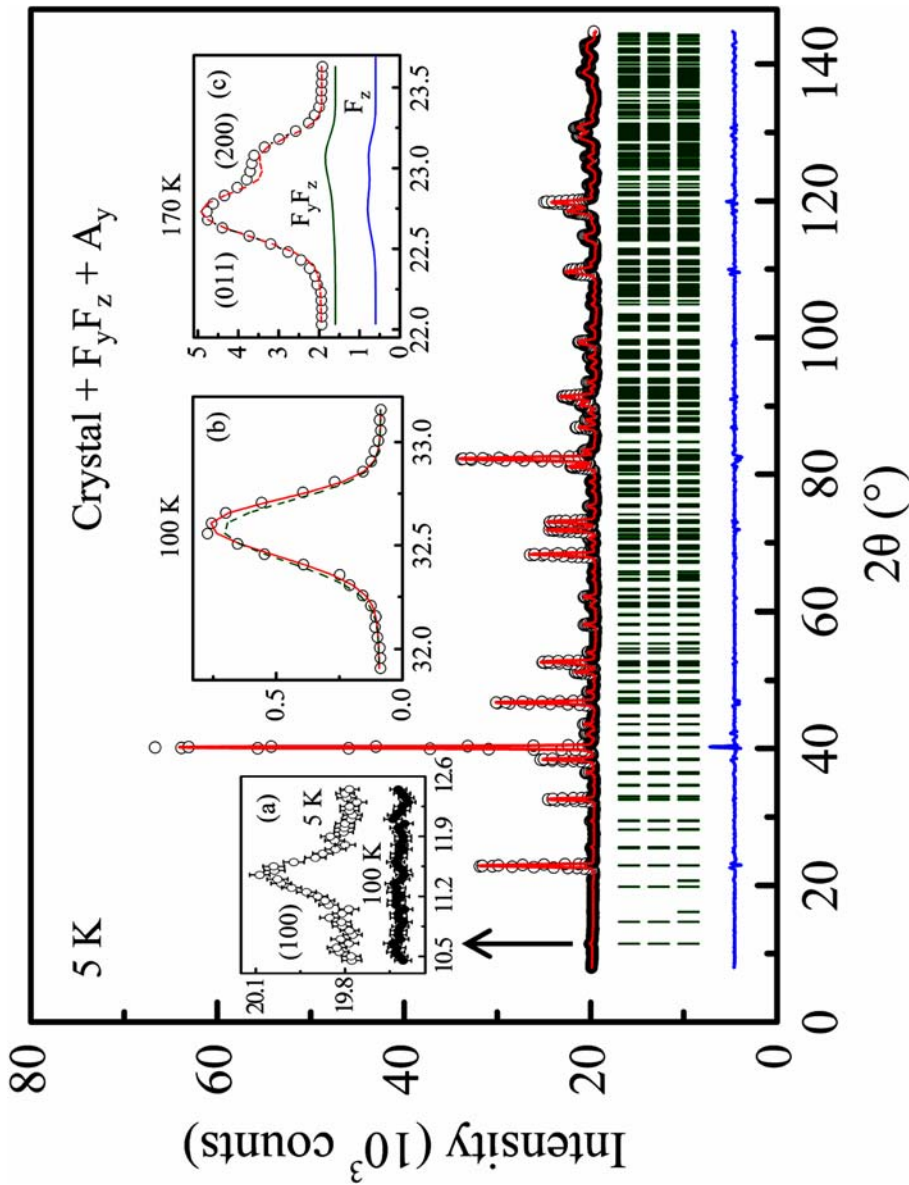


Figure 8.5: Rietveld refinement plot of the NPD data of a powered $\text{La}_{1-x}\text{Sr}_x\text{MnO}_3$ ($x \approx 1/8$) single crystal in $P12_1/c1$ symmetry at 5 K. The contributions to the calculated intensity (solid line) are from crystal, FM ($F_y F_z$) and A -AFM (A_y) structures. F_y , F_z and A_y denote the FM moments along the b and c axes and the A -AFM moment along the b axis, respectively. Inset (a) shows the presence of an A -AFM peak (1 0 0) at 5 K. Insets (b) and (c) contrastingly show the quality of the fit for refinements with different FM models $F_y F_z$ and F_z (see text).

competing structures $P12_1/c1$ (squares) and $Pnma$ (solid triangles) are also plotted in figure 8.8(b). Although the goodness of fit χ^2 for $P12_1/c1$ model has decreased a lot, the refined values of the magnetic moments are identical within e.s.d.. The temperature dependences of the ZFC reciprocal susceptibility $\chi^{-1}(T) = H/M$ in unit of (g Oe)/emu at $H = 20, 120$ and 7×10^4 Oe are shown in figure 8.9(a). Figure 8.9(b) depicts the hysteresis loop measured at 5 K and the inset (b'') shows the enlarged view for small fields. Obviously, a very small hysteresis effect is displayed, which indicates that the single crystal is an extremely soft ferromagnet. The Curie temperature $T_c = 187(1)$ K was

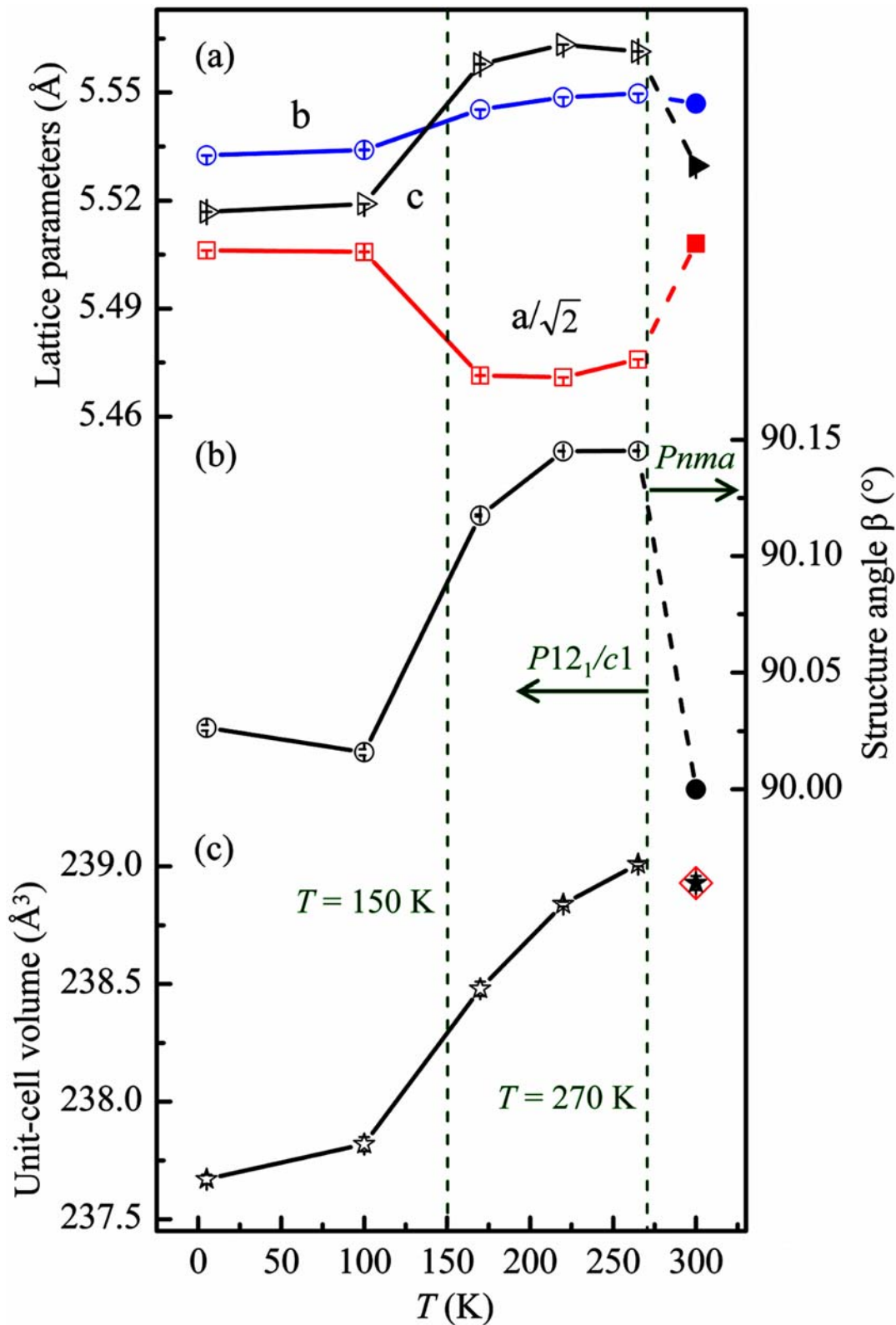


Figure 8.6: Temperature variations of (a) the lattice parameters, (b) the crystal structure angle β and (c) the unit-cell volume of a powered $\text{La}_{1-x}\text{Sr}_x\text{MnO}_3$ ($x \approx 1/8$) single crystal. The symbol \diamond in panel (c) represents the refined unit-cell volume using $P12_1/c1$ space group for the observed 300 K NPD data.

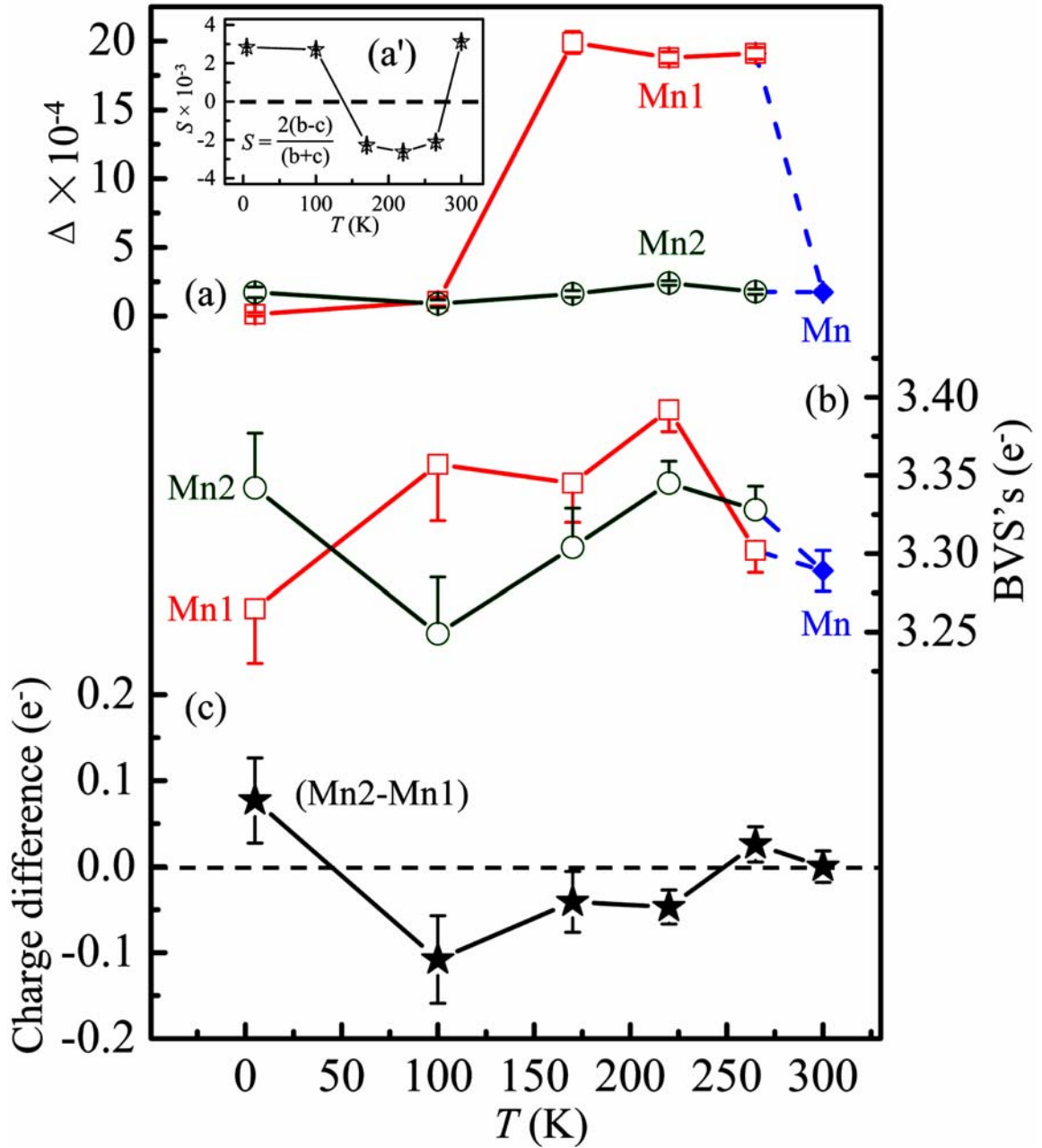


Figure 8.7: Temperature variations of (a) the size of cooperative JT distortion of MnO_6 octahedra Δ (defined in equation 7.1), (b) the BVS's of the Mn ($Pnma$) and Mn1, Mn2 ($P12_1/c1$) calculated from the refined parameters and (c) the charge difference between Mn1 and Mn2. Inset (a') shows the orthorhombic strain in the b - c plane, namely $S = 2(b-c)/(b+c)$, in $P12_1/c1$ symmetry.

evaluated as the temperature where the absolute value of the slope dM/dT of ZFC $M(T)$ curve at 20 Oe reaches its maximum. With decreasing temperature, the transitions from paramagnetism to ferromagnetism at T_c in figure 8.8(a) are continuous and sharp indicative of a good sample quality with a homogeneous composition distribution. Here the signatures of CO/OO and JT transitions are obviously displayed in the low-field data (20 and 120 Oe), which is distinct from the polycrystalline data (figure 7.3(a)). The values

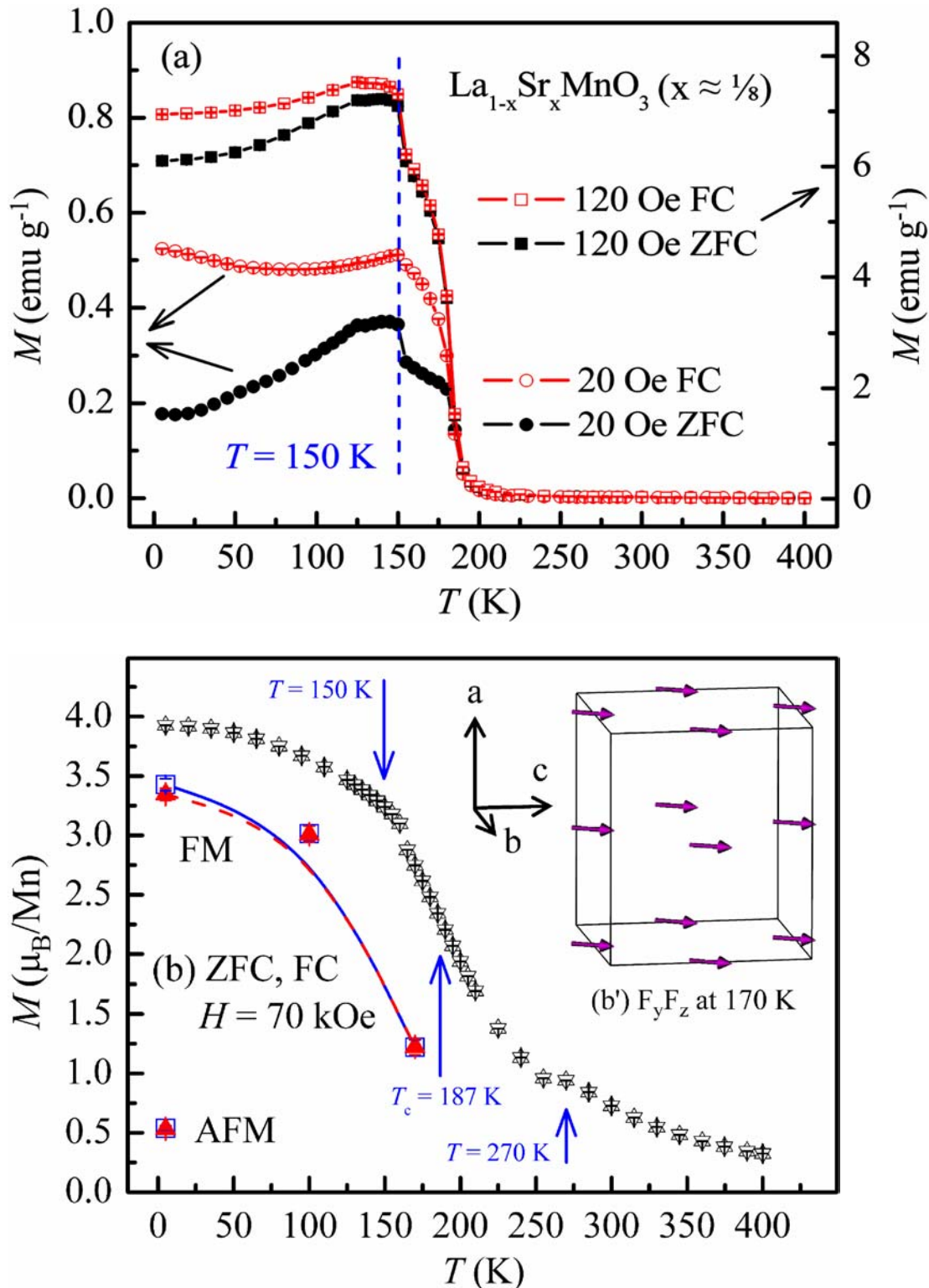


Figure 8.8: (a) ZFC and FC magnetization M at 20 and 120 Oe versus temperature for a powered $\text{La}_{1-x}\text{Sr}_x\text{MnO}_3$ ($x \approx 1/8$) single crystal. (b) Temperature dependence of the ZFC (up triangles) and FC (down triangles) magnetic moment μ_B per Mn ion at 70 kOe and the refined FM (5, 100 and 170 K) and A-AFM (5 K) moments ($P12_1/c1$: squares; $Pnma$: solid triangles). Inset (b') illustrates the magnetic structure unit-cell $F_y F_z$ in $P12_1/c1$ symmetry at 170 K. F_y and F_z denote the FM moments along the b and c axes, respectively.

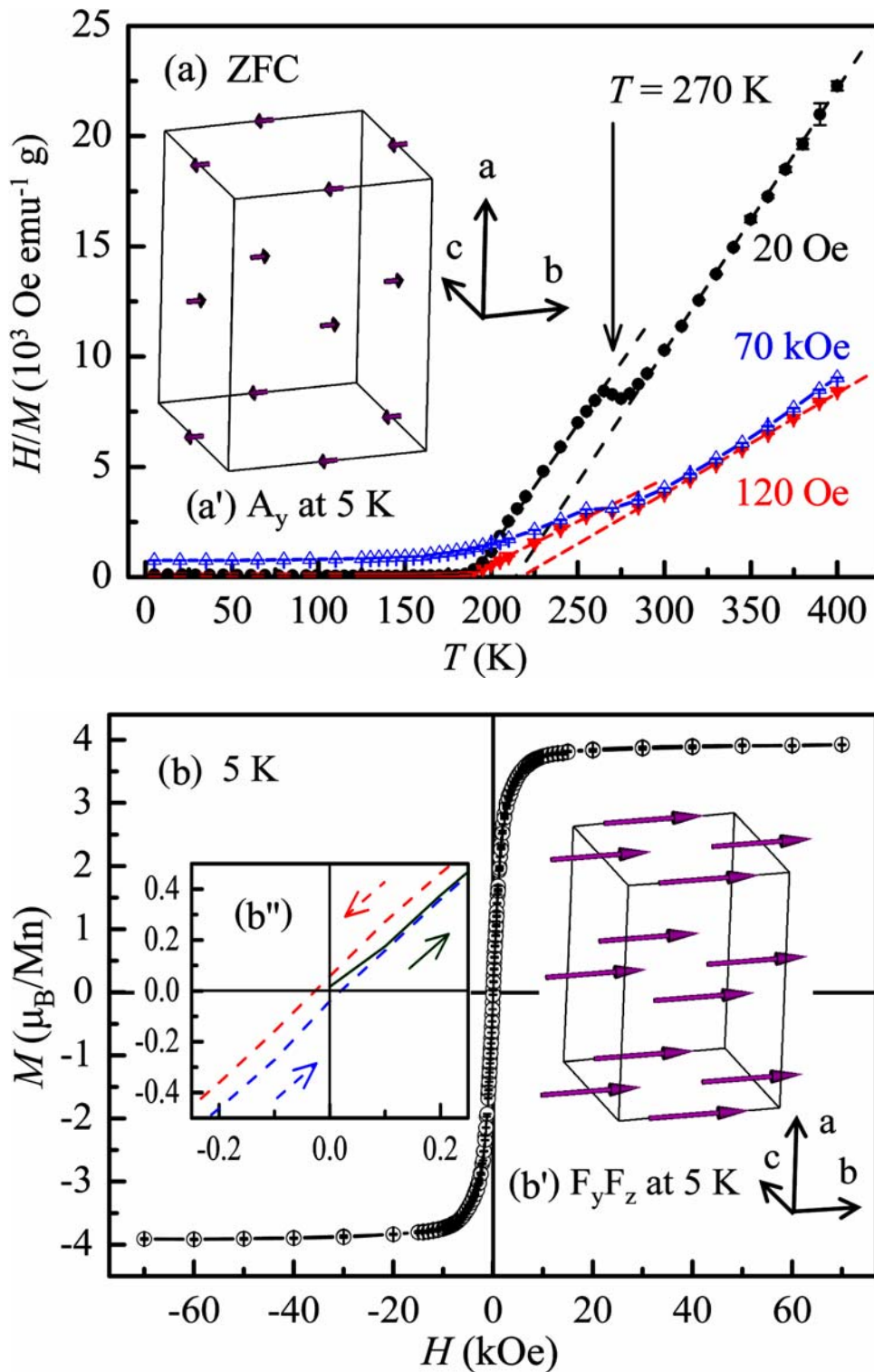


Figure 8.9: (a) Temperature variation of the ZFC H/M at 20, 120 and 7×10^4 Oe with the dashed lines showing the fits of the data at 20 and 120 Oe to the Curie-Weiss law below and above T_{JT} . (b) A hysteresis loop at 5 K. Insets (a') and (b') illustrate the magnetic structure unit-cells A_y and $F_y F_z$ at 5 K in $P12_1/c1$ symmetry, respectively. Inset (b'') depicts the enlarged view of the hysteresis loop in a limited region. A_y , F_y and F_z denote the A -AFM moment along the b axis and the FM moments along the b and c axes, respectively.

of $T_{\text{CO/OO}}$ and T_{JT} were determined as the temperatures where the obvious inflections happen to the measured curves. It is interesting to note that the value of $T_{\text{CO/OO}}$ increases from ~ 150 to ~ 160 K as increasing the magnetic field from 20 via 120 to 7×10^4 Oe, while that of T_{JT} decreases from ~ 273 to ~ 263 K in this process. It is noteworthy that the apparent thermomagnetic irreversibility is shown as the difference between ZFC and FC curves at 20 Oe. This difference gets smaller with increasing magnetic field to 120 Oe. Finally, it is completely removed at 70 kOe. The shape of the curves in figure 8.9(a) is characteristic of the normal ferromagnets, which implies that the single crystal is ferromagnetic. It should be pointed out that the FC $\chi^{-1}(T)$ curves at 20 and 120 Oe are nearly the same as the corresponding ZFC curves at $T_c < T < T_{\text{JT}}$ and they are just a little lower at $T_{\text{JT}} < T < 400$ K. Therefore, figure 8.9(a) shows the ZFC $\chi^{-1}(T)$ curves only. Within $\Delta T_{\text{JT}} \approx 10$ K, a sharp change occurs around $T_{\text{JT}} \approx 273$ K. In the temperature ranges $T_c < T < T_{\text{JT}}$ and $T_{\text{JT}} < T < 400$ K, the value of $\chi^{-1}(T)$ increases linearly with increasing temperature. This behavior can be well fitted for the molar susceptibility by the Curie-Weiss law:

$$\chi(T) = \frac{C}{T - \theta_p} = \frac{N_A \mu_{\text{eff}}^2}{3k_B(T - \theta_p)}, \quad (8.1)$$

where C is the Curie constant, θ_p is the paramagnetic Curie temperature, $N_A = 6.022 \times 10^{23} \text{ mol}^{-1}$ is the Avogadro's number, $\mu_{\text{eff}} = g\mu_B \sqrt{J(J+1)}$ is the effective paramagnetic moment and $k_B = 1.38 \times 10^{-23} \text{ J/K}$ is the Boltzmann constant. The paramagnetic Curie temperatures $\theta_{p-20}^{M'} = 188.3(1) \text{ K}$, $\theta_{p-20}^O = 213.9(4) \text{ K}$ at 20 Oe and $\theta_{p-120}^{M'} = 185.0(1) \text{ K}$, $\theta_{p-120}^O = 216.8(2) \text{ K}$ at 120 Oe were determined by extrapolating the corresponding linear portions of $\chi^{-1}(T)$ curves between T_c and T_{JT} in the M' structural region and above T_{JT} up to 400 K in the O structural region to $\chi^{-1}(T) = 0$. The corresponding Curie constants $C_{20}^{M'} = 0.008909(3)$, $C_{20}^O = 0.008398(8)$, $C_{120}^{M'} = 0.025849(9)$ and $C_{120}^O = 0.021963(9)$ in unit of (emu K)/(g Oe) were also determined from the corresponding inverse slopes of the linear portions of $\chi^{-1}(T)$ curves. With these Curie constants, the effective paramagnetic moment per formula unit $\mu_{\text{eff}-20}^{M'} = 4.05(1) \mu_B$, $\mu_{\text{eff}-20}^O = 3.94(1) \mu_B$, $\mu_{\text{eff}-120}^{M'} = 6.91(1) \mu_B$ and $\mu_{\text{eff}-120}^O = 6.37(1) \mu_B$ were calculated.

8.2.3 Discussion

One may argue the choice of M' (170, 220 and 265 K) and M'' (5 and 100 K) models for the observed NPD data. It may be also argued that the decrease of the goodness of fit χ^2 from 2.52 to 1.40 in table 8.1 is due to the increase in the number of refined parameters, which is increased by 6. However, the improvement of the refinements is very obvious. The refined monoclinic angle $\beta = 90.145(2)^\circ$ at 220 K largely deviates from 90° , which is due to the right decomposition of the overlapped peaks with high enough counting statistics. It should be mentioned that an increase in the number of refined parameters can lead to a decrease in χ^2 , e.g. turning the isotropic thermal parameters into anisotropic ones, the χ^2 has decreased from 2.50 to 1.90 in the NPD refinement of a $\text{Na}_{0.5}\text{Pr}_{0.5}\text{TiO}_3$ sample

with *Pbnm* symmetry in [183], but the prerequisite is the right selection of the structure model. It is noteworthy that so far there has been no definitive conclusion that the FMI phase of $\text{La}_{1-x}\text{Sr}_x\text{MnO}_3$ ($x \approx 1/8$) belongs to the triclinic symmetry from the NPD and SPXD studies alone.

The presence of *A*-AFM (1 0 0) peak at 5 K may result from the regional superexchange interactions between Mn ions. In addition, this appearance could be produced by the configuration of the canted FM structure or the localized magnetic polarons with weak couplings. Moreover, this behavior, i.e. small AFM regions embedded in a long-range ordered FM state, is similar to the restricted spin-frozen picture in a certain geometrical environment that is probably induced by the ordered cation vacancies. The reasons for the existence of AFM domains may be also the source of the reported phase separation [172] and charge order [155] in the FMI regime. In other words, the AFM and FM domains probably belong to different structures. This is supported by the fact that the spin orientations of the main FM component F_y and the AFM moment A_y at 5 K are both along the *b* axis. In the same domain the FM and AFM states are usually hard to coexist, say nothing of having the same spin direction. Indeed, this system tends to nanoscale phase separation [173]. However, the dissimilarity in the structural parameters of the two phases is too small to be detected from the present NPD data. The angle between total FM spin moment and crystallographic *b* axis was defined as Ψ and when the moment turns away from the *b* axis towards the *c* axis in *b-c* plane, the value change of Ψ is positive. With increasing temperature from 5 via 100 to 170 K, the estimated values of Ψ are $\sim 0.3^\circ$, $\sim 12.0^\circ$ and $\sim 59.7^\circ$, respectively. The corresponding FM unit-cells $F_y F_z$ at 170 K, A_y and $F_y F_z$ at 5 K in *P12₁/c1* symmetry are illustrated as the inset (b') of figure 8.8 and the insets (a') and (b') of figure 8.9, respectively.

From the refined lattice parameters and actual formula $\text{La}_{0.848(2)}\text{Sr}_{0.121(2)}\text{Mn}_{0.984(4)}\text{O}_3$, the theoretical density was calculated as $6.40(1) \text{ g/cm}^3$ well consistent with the measured one $6.41(1) \text{ g/cm}^3$, indicative of a very good accuracy of refinements. This agreement also hints that the cation vacancy is the main crystal defect. In addition, the Mn ions can locate on *A* (La/Sr) sites to form antisite defect since the mean *A* site radius is much larger than that of the *B* (Mn) sites (La^{3+} : $r_{\text{CN}=12} = 1.36 \text{ \AA}$, Sr^{2+} : $r_{\text{CN}=12} = 1.44 \text{ \AA}$, Mn^{3+} : $r_{\text{Low-Spin}} = 0.58 \text{ \AA}$ and $r_{\text{High-Spin}} = 0.645 \text{ \AA}$ and Mn^{4+} : $r_{\text{CN}=6} = 0.53 \text{ \AA}$, where CN means the coordination number. Taken from [184]), but not vice versa. To calculate the actual cation vacancies in *A* and *B* sublattices, the refined formula was expressed as $A_{0.969(3)}B_{0.984(4)}\text{O}_3$. Therefore, the percentages of cation vacancies in *A* (V_A^{vac}) and *B* (V_B^{vac}) sublattices are 3.1(3)% and 1.6(4)%, respectively. These values are smaller than the corresponding ones of the air sintered and O_2 annealed $\text{La}_{7/8}\text{Sr}_{1/8}\text{Mn}_{1-\gamma}\text{O}_{3+\delta}$ polycrystals (chapter 7), especially for the *B* sublattice. This is ascribed to a better oxygen stoichiometry and an initial 3 at% excess Mn addition for the single-crystalline sample. It was thus confidently determined that the actual average valency for Mn ions is $3.214(7)+$ and subsequently evaluated that in a purely ionic model the Mn^{3+} and Mn^{4+} contents are 0.722(15) and 0.262(14), respectively, based on the charge neutrality condition. The theoretical saturation moments are $4 \mu_B$ and $3 \mu_B$ for Mn^{3+} and Mn^{4+} ions, respectively. Supposing that the orbital angular momentum is quenched ($L = 0$, $J = S$, neglecting the spin-orbital coupling), the theoretical saturation value of spin moments was calculated as $M_s^{\text{calc}} = 3.67(7) \mu_B/\text{Mn}$ using the Mn^{3+} and Mn^{4+} contents obtained above. This value is a little higher than the refined FM moment $3.43(5) \mu_B/\text{Mn}$ at 5 K but slightly lower than the measured one $3.9265(9) \mu_B/\text{Mn}$ at 70 kOe and 5 K. It is of interest that if we add the refined FM moment to the AFM moment

0.54(2) μ_{B}/Mn at 5 K, the sum 3.97(5) μ_{B}/Mn agrees quite well with the measured one. This result implies that a large enough applied field can break the special AFM ordering by flipping one part of spins and making the independent spins interact with each other again. This leads to the melting of the AFM domain into the FM domain and the magnetic melting of the charge order. The driving force for this transformation is possible of the internal molecular field induced by the spontaneous magnetization. The additional part of the measured moment at 5 K compared to the theoretical one may result from the unquenched orbital angular momentum or the formation of the localized magnetic polarons [185]. Furthermore, the possible magnetic polarons most probably have the identical cores with the AFM domains. It is noticed that no significant contribution from the small AFM component observed in the NPD experiment appears in the $M(H)$ curve as shown in figure 8.9(b), probably ascribing to the low value of the spin-flop field at which the transformation from AFM to FM domain has completed. Indeed, the saturation field for this compound is only ~ 1.5 kOe.

For nominal $\text{La}_{1-x}\text{Sr}_x\text{MnO}_3$ compounds, the theoretical value of the effective paramagnetic moment at each composition can be evaluated by:

$$\mu_{\text{eff}}^{\text{theo}} = g\mu_{\text{B}}[x\sqrt{S_4(S_4 + 1)} + (1-x)\sqrt{S_3(S_3 + 1)}], \quad (8.2)$$

where $g \approx 2$ ($L = 0$, $J = S$) is the Lande factor assuming quenched orbital moments, $1 \mu_{\text{B}} = 9.27 \times 10^{-24}$ J/T is the Bohr magneton, $S_4 = 3/2$ and $S_3 = 2$ are the spin quantum numbers of Mn^{4+} and Mn^{3+} ions, respectively, x is the hole concentration (Mn^{4+} content) and $(1-x)$ is the Mn^{3+} content. The calculated $\mu_{\text{eff}}^{\text{theo}}$ for actual $\text{La}_{0.848(2)}\text{Sr}_{0.121(2)}\text{Mn}_{0.984(4)}\text{O}_3$ is 4.55(9) μ_{B}/Mn . It is interesting that this value is slightly larger than $\mu_{\text{eff}-20}^{M'} = 4.05(1) \mu_{\text{B}}/\text{Mn}$ and $\mu_{\text{eff}-20}^O = 3.94(1) \mu_{\text{B}}/\text{Mn}$ at 20 Oe, but significantly smaller than $\mu_{\text{eff}-120}^{M'} = 6.91(1) \mu_{\text{B}}/\text{Mn}$ and $\mu_{\text{eff}-120}^O = 6.37(1) \mu_{\text{B}}/\text{Mn}$ at 120 Oe. The decrease in the observed effective paramagnetic moments at 20 Oe may indicate a regional spin-frozen state thanks to the anisotropy of possible clusters. In principle, a magnetic cluster with a certain size or a certain combination of clusters with different sizes, in precondition of the charge neutrality, can also lower the value of the effective moment. On the other hand, the enhancements at 120 Oe may originate from the existence of magnetic clusters with the short-range FM interactions [186]. Correlating the appearance of AFM domains at 5 K, the possible sites where the clusters are formed may be the same as those for the AFM regions. The sites surrounded by the cation vacancies could serve as this source. The possible forms of magnetic clusters are either a localized cluster of Mn^{3+} ions around one or more Mn^{4+} ions (the holes are in common) or one or more Mn^{3+} ions as the cores (Mn^{4+} ions are sharing the mutual electrons). It is noted that an increase in the applied field aligns or frees the abnormal spins and causes the possible magnetic polarons, leading to a formation or growth of the FM clusters. As a result, charge disorder in the PMI state is somewhat modified by the magnetic field, leading to an increase in the number of itinerant electrons. In addition, the magnetic field can affect the hopping degree of charge carriers inside the magnetic clusters. Therefore, it is concluded that there is a field-induced change in the paramagnetic state. A similar behavior was reported in a $\text{Sm}_{0.65}\text{Sr}_{0.35}\text{MnO}_3$ manganite [187]. Another important feature is that there is no big change in $\theta_p^{M'}$ at 20 and 120 Oe. This feature also appears to θ_p^O . While the value of θ_p^O is

significant larger than that of $\theta_p^{M'}$ at 20 and 120 Oe. This fact indicates that an increase in the magnetic field does not significantly alter the value of J above T_c , since θ_p is proportional to the strength (J) of the exchange couplings. Thus the field-induced change in the PMI state discussed above is limited to the local cluster ranges. However, a relative enhancement of J in the O structure compared to that of the M' structure above T_c does not induce the long-range magnetic order in PMI regime above T_{JT} probably due to the JT transition. Moreover, the small difference between ZFC $\chi^{-1}(T)$ curves at 120 and 7×10^4 Oe above T_c is probably correlated to the expansion of the magnetic clusters at a larger field, while the clearly positive value of $\chi^{-1}(T)$ at 70 kOe below T_c is ascribed to an increase in the FM moment.

The increase in $T_{CO/OO}$ from ~ 150 to ~ 160 K and the decrease in T_{JT} from ~ 273 to ~ 263 K with increasing magnetic field from 20 to 7×10^4 Oe reveal that a large magnetic field favors the FMI state and stabilizes the O structure, consequently decreasing the temperature range of the JT distorted phase consistent with [188]. Two possible reasons can be given for the observed difference in ZFC and FC curves at 20 Oe below T_c : one is the freezing of the magnetic clusters around crystal defects, e.g. cation vacancies, intrinsic stress formed during the rapid cooling after single crystal growth or during the sample preparation for the SQUID measurements, etc; another is the pinning effect of the crystal defects on magnetic domains, preventing the enlargement of the domain volumes and the turn of the domain directions to the applied field orientation. The gradual disappearance of the difference with increasing applied field to 120 and 7×10^4 Oe clearly demonstrates that a large enough magnetic field, e.g. 70 kOe, is able to destroy the freezing and pinning effects.

According to equation 7.1, the calculated JT distortion size as a function of temperature is shown in the panel (a) of figure 8.7. For the Mn2 site, Δ remains nearly constant in the entire temperature range and the mean Δ of all temperatures is calculated as $1.7(1) \times 10^{-4}$. However, the Mn1 site shows a huge cooperative JT effect at 170, 220 and 265 K, but at 5 K Δ reduces to $1.4(9) \times 10^{-5}$, one order of magnitude lower than that of Mn2 site at 5 K. Here the value of Δ for Mn1 sites in the JT region is significantly larger over that of the air sintered and Ar annealed $\text{La}_{7/8}\text{Sr}_{1/8}\text{Mn}_{1-\gamma}\text{O}_{3+\delta}$ polycrystals (chapter 7), owing to the fact that the single crystal is closer to ideal stoichiometry. It is reasonable to deduce that Mn1 may play a role of Mn^{3+} with the e_g orbital order. This orbital order in the JT regime for a $\text{La}_{7/8}\text{Sr}_{1/8}\text{MnO}_3$ single crystal was considered to be similar to that of LaMnO_3 , i.e. C -type orbital order, in a RXS study [173]. However, this type was suggested to transform into G -type orbital order [172]. One fact is that the orbital order formed in the JT regime for $\text{La}_{7/8}\text{Sr}_{1/8}\text{MnO}_3$ is completely different from the one in the FMI state of $\text{La}_{7/8}\text{Sr}_{1/8}\text{MnO}_3$ and the one of LaMnO_3 . The two permitted Mn1 and Mn2 sites in $P12_1/c1$ symmetry offer an opportunity to explore their respective electric configurations at the two distinct crystallographic sites. Based on the BVS's method [98], the evaluated oxidation states of Mn ($Pnma$) and Mn1, Mn2 ($P12_1/c1$) from the refined parameters are shown in the panel (b) of figure 8.7. The calculated BVS's value for Mn is $3.29(1)^+$, in agreement with the analytical valency $3.214(7)^+$ based on the refined site occupancies. Therefore, the above calculations with ionic Mn^{3+} and Mn^{4+} configurations are valid. However, the degree of the charge disproportion between Mn1 and Mn2 is not apparent, e.g. the relative maximum difference is $0.11(5) e^-$ at 100 K and thus within just two standard deviations. Similar results were widely reported in the half-doped manganites with the so-called charge order. The CO/OO transition of

$\text{Nd}_{0.5}\text{Sr}_{0.5}\text{MnO}_3$ was explained as a structural transition in a RXS study, where two non-equivalent crystallographic Mn sites with a charge difference of $0.16 e^-$ were present at low temperatures [87]. It is of interest to notice that Mn1 and Mn2 at 5 K seem to exchange their charge states compared to the tendency in the JT regime shown in the panels (b) and (c) of figure 8.7.

Finally, it is stressed that the distortion from monoclinic to triclinic symmetry for $\text{La}_{1-x}\text{Sr}_x\text{MnO}_3$ ($x \approx 1/8$) below $T_{\text{CO/OO}}$ is too weak to be detected within the resolution of the NPD method: there is no observed indication for the possible peak splitting, much less for the superstructure reflections. But the symmetry reduction is detected by the RXS technique with single crystals, where the superstructure reflections can be observed against the background in contrast to powder samples. Here the unit-cell size is thus constrained to be similar to that in the orthorhombic perovskite basis. One cannot specify a unique space group and determine the superstructure unit-cell size merely based on the superlattice reflections observed in electron microscope (microdomain scale) and RXS studies. Nonetheless, it may be possible to identify the correct space group and the averaged unit-cell size by comparing the possible competing models through a combined Rietveld refinement with many patterns and some constraints using high-resolution NPD and SPXD data with enough counting statistics. This method is an arguably good resolver on the complicated structure of archaic Fe_3O_4 with the intriguing Verwey transition at ~ 120 K [189].

8.2.4 Conclusions

The crystal and magnetic structure of a powdered single-crystalline $\text{La}_{1-x}\text{Sr}_x\text{MnO}_3$ ($x \approx 1/8$) perovskite have been studied. Although visual inspection of the NPD patterns shows no obvious evidence for the appearances of monoclinic and triclinic structures below T_{JT} and $T_{\text{CO/OO}}$, respectively, it has been confirmed that the sample has an orthorhombic (O) structure at 300 K and a monoclinic (M') one at 170, 220 and 265 K by comparing the competing models. The 5 and 100 K NPD data were also refined using a monoclinic (M'') model. The refined lattice parameters, monoclinic angle β and unit-cell volume, in addition to the temperature dependence of the $M(T)$ curves at 20, 120 and 7×10^4 Oe, present characteristic discontinuities at the critical transition temperatures $T_{\text{CO/OO}}$ for charge and orbital order and T_{JT} for JT distortion. Short-range A -AFM domains indicated by the appearance of a broad (1 0 0) peak in $P12_1/c1$ setting are embedded in the long-range ordered FM domains at 5 K. In addition, they have an identical spin orientation. Increasing temperature to 100 K or the applied field to 70 kOe, the AFM domains are melted. The angle Ψ between total FM spin moment and crystallographic b axis increases from $\sim 0.3^\circ$ via $\sim 12.0^\circ$ to $\sim 59.7^\circ$ in the b - c plane with increasing temperature from 5 via 100 to 170 K. The enhancements in the effective paramagnetic moments at 120 Oe compared to the corresponding theoretical values are attributed to the presence of magnetic clusters. The BVS's results show no obvious charge disproportion between two distinct Mn1 and Mn2 sites in spite of a big difference existing between their JT distortion sizes. These results reveal the importance of spin, charge and lattice interactions in manganites.

8.3 Evidence of hole ordering from RSXS

8.3.1 Introduction

The interesting FMI phase in $\text{La}_{1-x}\text{Sr}_x\text{MnO}_3$ ($x \approx 1/8$) below $T_{\text{CO/OO}} \approx 150$ K is currently thought to be related to the CO/OO phenomena. The proposed orbital-polaron model [9] has more or less evidenced the occurrence of OO. However, the above calculated charge disproportion between Mn1 and Mn2 (maximum is $0.11(5) e^-$) based on the BVS's theory falls into the shade in contrast with the traditionally proposed integral charge difference one e^- between Mn^{3+} and Mn^{4+} ions. In order to solve the puzzle of CO in this compound, RXS experiments have been carried out on a single-crystalline $\text{La}_{1-x}\text{Sr}_x\text{MnO}_3$ ($x \approx 1/8$) sample in the hard x-ray (Mu-CAT, APS) and soft x-ray (UE56/1-PGM-b, BESSY-II) regimes.

8.3.2 Results and discussion

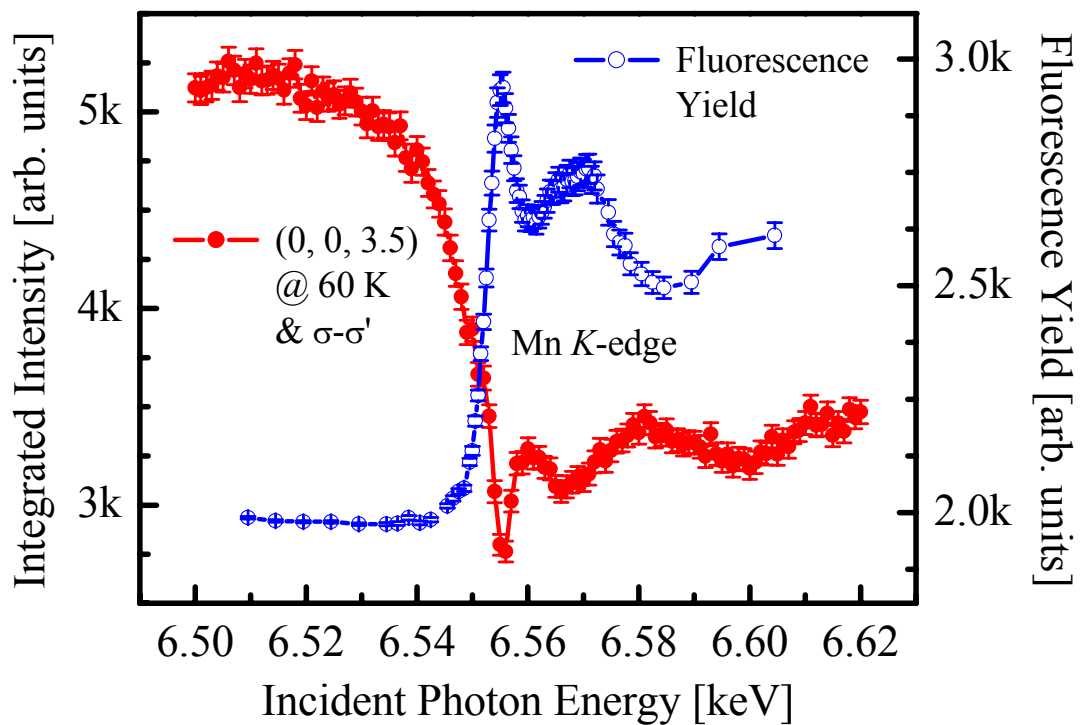


Figure 8.10: No appreciable resonant enhancement of the CO reflection (0 0 3.5) in $Pbnm$ symmetry in $\text{La}_{1-x}\text{Sr}_x\text{MnO}_3$ ($x \approx 1/8$) can be observed at the Mn K -edge at 60 K.

Although various superstructural unit-cell sizes were proposed for the FMI phase of $\text{La}_{1-x}\text{Sr}_x\text{MnO}_3$ ($x \approx 1/8$) in different studies [155, 156, 163, 179, 181], one common feature is that the CO should take place at $Q = (0\ 0\ 1/2)$ in the orthorhombic $Pbnm$ perovskite notation. In order to be consistent with the literature, I use the orthorhombic $Pbnm$

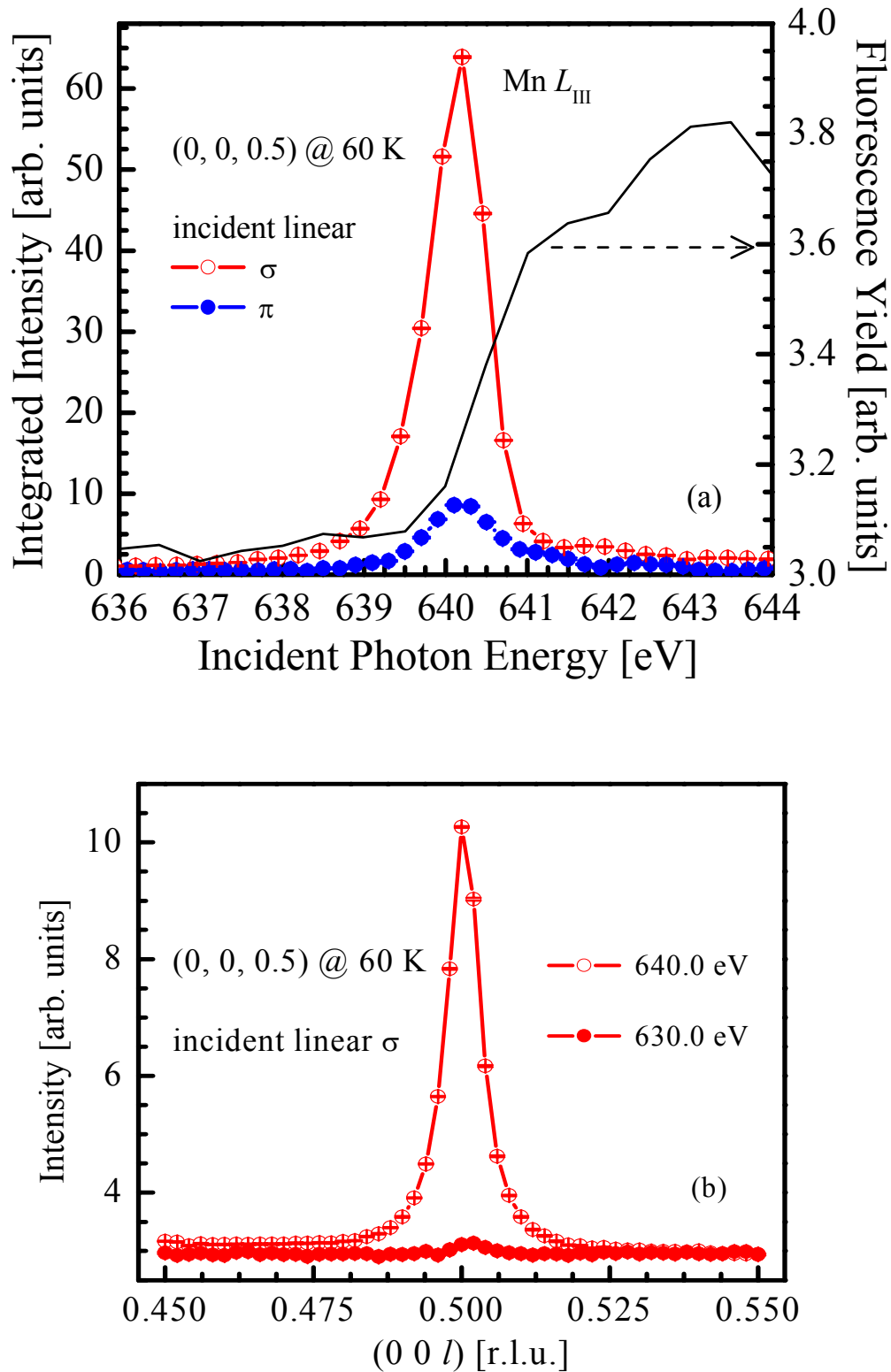


Figure 8.11: (a) A significant resonant enhancement of the CO reflection $(0, 0, \frac{1}{2})$ in $Pbnm$ symmetry in $\text{La}_{1-x}\text{Sr}_x\text{MnO}_3$ ($x \approx \frac{1}{8}$) is clearly seen at the Mn L_{III} -edge at 60 K. (b) Longitudinal scans of $(0, 0, \frac{1}{2})$ in $Pbnm$ symmetry at different incident photon energies with incident σ polarization at 60 K.

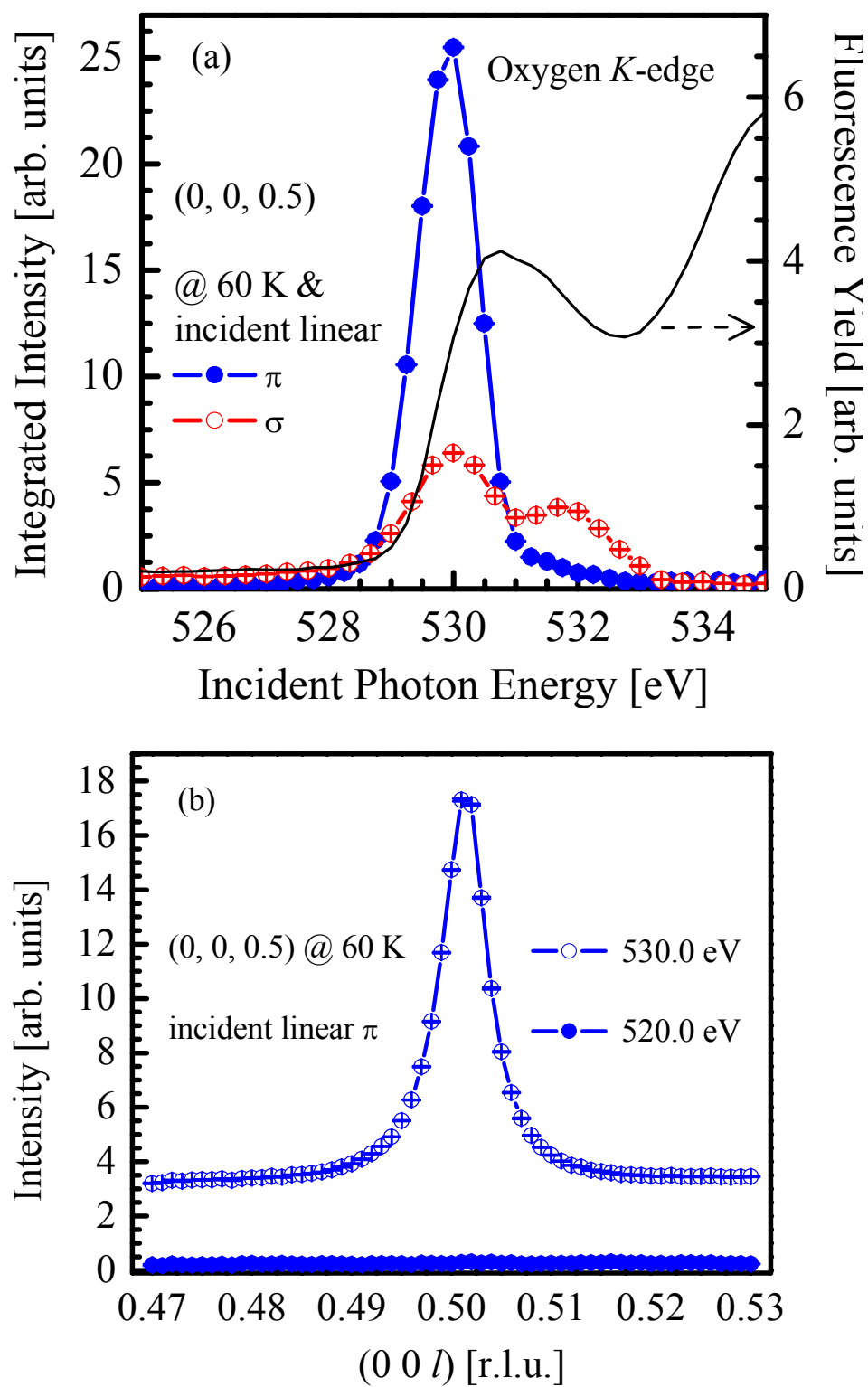


Figure 8.12: (a) A significant resonance enhancement of the CO reflection $(0\ 0\ \frac{1}{2})$ in $Pbnm$ symmetry in $\text{La}_{1-x}\text{Sr}_x\text{MnO}_3$ ($x \approx \frac{1}{8}$) is clearly seen at the oxygen K -edge at 60 K. (b) Longitudinal scans of $(0\ 0\ \frac{1}{2})$ in $Pbnm$ symmetry at different incident photon energies with incident π polarization at 60 K.

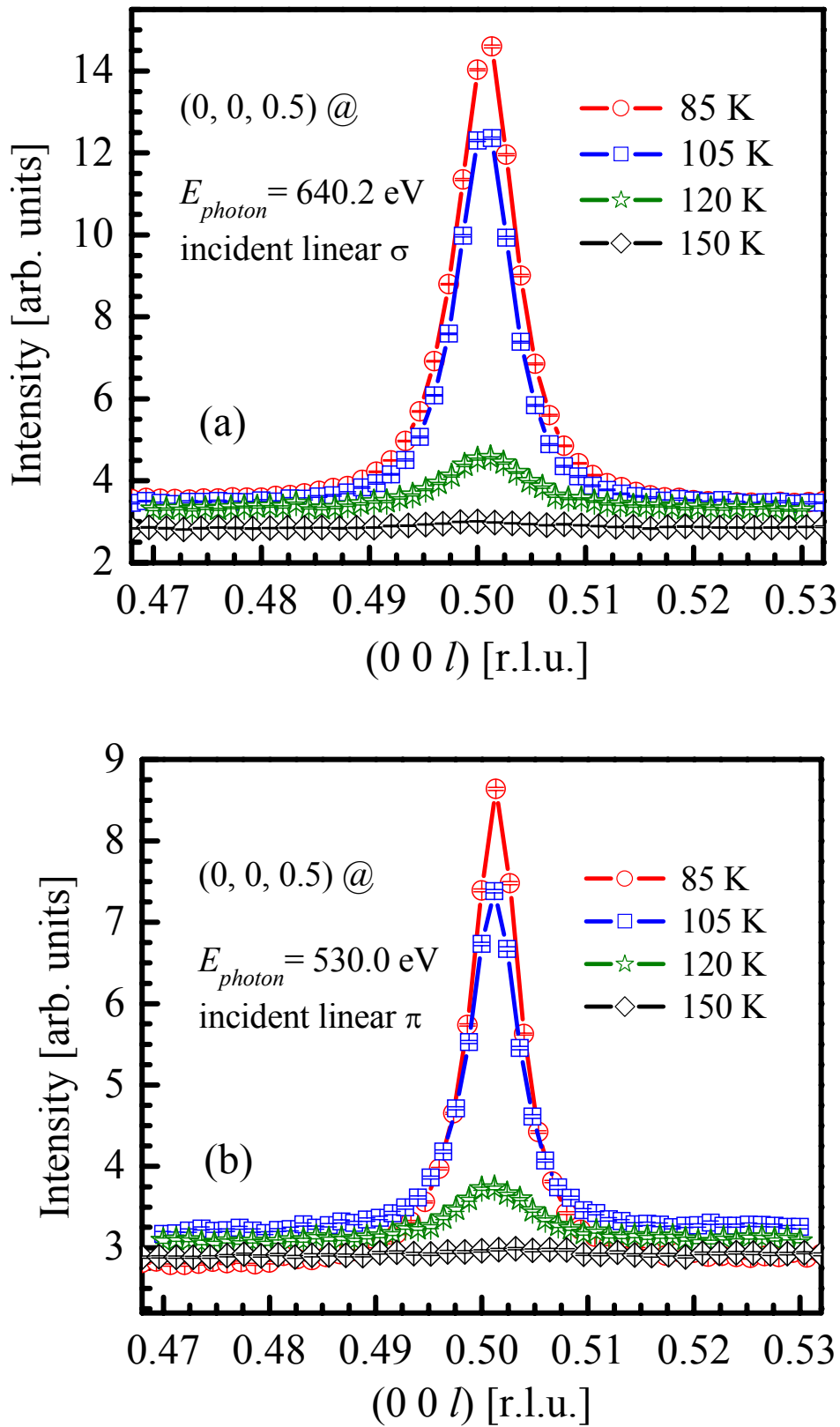


Figure 8.13: Temperature dependence of the CO reflection $(0, 0, \frac{1}{2})$ in $Pbnm$ symmetry in $\text{La}_{1-x}\text{Sr}_x\text{MnO}_3$ ($x \approx \frac{1}{8}$) at: (a) 640.2 eV (Mn L_{III} -edge) with incident σ polarization and (b) 530.0 eV (oxygen K -edge) with incident π polarization.

symmetry for $\text{La}_{1-x}\text{Sr}_x\text{MnO}_3$ to discuss my RXS data. The transformation of orthorhombic $Pbnm$ and $Pnma$ symmetries can be found in appendix C and a comparison of orthorhombic $Pnma$ and monoclinic $P12_1/c1$ symmetries is shown in table 8.1. In the classic ionic scenario, the CO in manganites occurs with Mn^{3+} and Mn^{4+} ions being arranged periodically. This ordering pattern can be detected by the measure of the chemical shift in $1s$ core level, since this chemical shift will lead to an occurrence of the resonant enhancement of the CO reflections at the Mn K -edge via the $1s \rightarrow 4p$ dipolar transition. Figure 8.10 shows the energy dependence of the integrated intensity of a CO reflection (0 0 3.5) in $Pbnm$ symmetry taken in the hard x-ray region, where no appreciable resonance was observed at the Mn K -edge (~ 6.554 keV). This result urges us to rethink the origin of the so-called CO reflections, from the lattice modulations induced by doping effect or purely electronic reasons. The inexistence of the resonance of CO reflection at the Mn K -edge may also indicate the failure of the classic ionic CO model.

If the possible resonance at the Mn K -edge were observed, it is also an indirect evidence of the order in Mn $3d$ states, which is strongly influenced by the JT distortions, $4p$ band structure effects and $3d-4p$ Coulomb interactions. In contrast, the observed resonant enhancement at the Mn $L_{II, III}$ -edges by RSXS in the soft x-ray region, corresponding to $2p \rightarrow 3d$ excitations, is thought to be the direct experimental evidence for the $3d$ valence states, orbitals, spins, etc. This technique, i.e. RSXS, has hugely enhanced sensitivity to the CO of $3d$ electrons via the dipolar transition to an unoccupied $3d$ sub-band, instead of via the indirect chemical shift effects. As shown in figure 8.11(a), a strong resonant enhancement of a CO reflection (0 0 $\frac{1}{2}$) in $Pbnm$ symmetry in $\text{La}_{1-x}\text{Sr}_x\text{MnO}_3$ ($x \approx \frac{1}{8}$) at the Mn L_{III} -edge (~ 640.0 eV) at 60 K has been clearly observed. Figure 8.11(b) shows a big contrast between longitudinal scans of (0 0 $\frac{1}{2}$) in $Pbnm$ symmetry at the strongest resonance energy (~ 640.0 eV) and off (~ 630.0 eV) this resonance, where the resonant effect around the Mn absorption L_{III} -edge is apparently shown. Another striking observation is that the CO reflection (0 0 $\frac{1}{2}$) in $Pbnm$ symmetry is also enhanced around the oxygen K -edge at 60 K (figure 8.12), where two clear features exist in the integrated intensity of (0 0 $\frac{1}{2}$) in $Pbnm$ symmetry with the incident σ polarization as shown in figure 8.12(a).

These resonances at the Mn L_{III} -edge and the oxygen K -edge display very strong incident σ or π polarization dependence. As shown in figure 8.13, their resonant intensities nearly disappear above ~ 150 K. These temperature dependences clearly correspond to the FMI phase transition in this compound, indicating that the physics behind these resonances could be one of the important reasons for this phase transition. These observations by RSXS technique enable us to finally confirm that the ordering of doped holes does take place in this compound, however, in a quite different fashion compared to that in the classic ionic ordering scenario, in which integer $3d^n$ configurations of Mn ions and fully filled oxygen $2p$ shells are assumed. The holes in this compound are indeed shared between the Mn and O sites.

8.3.3 Conclusions

We have performed resonant scattering studies on the CO phenomenon of $\text{La}_{1-x}\text{Sr}_x\text{MnO}_3$ ($x \approx \frac{1}{8}$) in the hard and soft x-ray regions. Strong resonant enhancements of the CO superstructural reflection are observed around the Mn L_{III} -edge and the oxygen K -edge

but not at the Mn K -edge. These results give a strong evidence that due to oxygen $2p$ -Mn $3d$ hybridization, the hole from doping is partly localized on the oxygen sites. This situation is similar to the so-called Zhang-Rice singlets proposed for high T_c cuprates.

Chapter 9

Soft x-ray resonant scattering study of $\text{La}_1\text{Sr}_2\text{Mn}_2\text{O}_7$

9.1 Introduction

Strongly correlated electron systems such as $3d$ TM oxides present exciting fundamental properties, e.g. the superconducting behavior and the extraordinary CMR effect in complex manganites. Their rich structural, magnetic and electronic properties are governed by the interplay of lattice, spin, charge and orbital degrees of freedom. Identification of the ordered phases is a prerequisite for understanding the physical properties and unusual phenomena.

Among all possible experimental techniques, RXS stands out since this technique has a unique sensitivity to the charge and orbital ordering due to its spectroscopic characteristics. In addition, charge, orbital and magnetic correlations can be studied in one experiment simultaneously. With the application of RXS in the hard x-ray regime [190], significant progress on the experimental quest of orbital degree of freedom in $3d$ TM compounds has been made recently. However, the resonance at the K -edge of $3d$ TMs is due to dipolar excitations from the $1s$ to $4p$ band and thus indirectly reflects the $3d$ electronic states through Coulomb interactions between $3d$ and $4p$ bands, band valence or JT distortion effects. An alternative way is the emerging RSXS technique, i.e. RXS in the soft x-ray range. This is a powerful method for directly probing the ordered phases individually since the RSXS process depends on the anisotropy of the empty electronic levels as determined not only by the orbital filling on the resonant atom, but also by the geometrical distribution of its neighbours. Utilizing this method, the first direct observation of magnetic ordering at the $L_{\text{II, III}}$ manganese absorption edges in $\text{La}_{2-2x}\text{Sr}_{1+2x}\text{Mn}_2\text{O}_7$ with $x = 0.475$ was reported [191], where the resonant enhancement of Bragg (0 0 2) reflection was also recorded at the Mn $L_{\text{II, III}}$ -edges and this resonance is weaker than that of the A -AFM (0 0 1) reflection. Some recent studies [191-194] show strong resonant enhancements of the expected superlattice reflections around the Mn $L_{\text{II, III}}$ -edges ($2p \rightarrow 3d$) which are known to be very sensitive to details of the $3d$ electronic states, supporting direct and definitive evidences for the ordering of charge, orbital and spin degrees of freedom in various manganites.

In order to extract meaningful information from the observed resonances and unravel

competing degrees between charge, orbital, spin and lattice, simulating the energy dependent signal is absolutely necessary. Normally, this kind of calculation is based on the multiple-scattering theory and the finite difference method in a certain crystal field. A theoretical calculation [195] resulting in a good general agreement with the observed energy spectra of the orbital ($\frac{1}{4} \frac{1}{4} 0$) reflection in $\text{La}_{0.5}\text{Sr}_{1.5}\text{MnO}_4$ shows that scattering at the Mn L_{III} -edge is primarily associated with the cooperative JT distortion, while that at the Mn L_{II} -edge is particularly sensitive to the OO. These assignments of different features to different origins were experimentally tested in more detail recently [196].

Room-temperature lattice parameters of $\text{La}_1\text{Sr}_2\text{Mn}_2\text{O}_7$ ($a = b = 3.879 \pm 0.002 \text{ \AA}$, $c = 19.996 \pm 0.007 \text{ \AA}$) [197] were determined previously. The c axis is so long that RSXS can access not only the A -AFM (0 0 1) superlattice reflection but also the Bragg (0 0 2) reflection even at the Mn L_{III} -edge. In this chapter, the results of a detailed RSXS study on the energy and temperature dependences of Bragg (0 0 2) and A -AFM (0 0 1) reflections in 50% hole-doped $\text{La}_1\text{Sr}_2\text{Mn}_2\text{O}_7$ are being reported. In particular, the unforeseen huge resonant enhancements of (0 0 2) at the La $M_{\text{IV},\text{V}}$ -edges (M_{IV} -edge: $3d_{3/2} \rightarrow 4f$; M_{V} -edge: $3d_{5/2} \rightarrow 4f$) were observed for the first time and the possible reasons for this resonance were explored. It was confirmed that the complex energy spectra of (0 0 1) over the Mn $L_{\text{II},\text{III}}$ -edges (L_{II} -edge: $2p_{1/2} \rightarrow 3d$; L_{III} -edge: $2p_{3/2} \rightarrow 3d$) consist of six unique features that are from the same order parameter: spin ordering. This is supported by the observation that integrated intensities of (0 0 1) at the six corresponding x-ray energies show a similar temperature dependence.

9.2 Double-layered $\text{La}_1\text{Sr}_2\text{Mn}_2\text{O}_7$

The formula of Ruddlesden-Popper manganites is expressed as $(\text{Ln}, \text{X})_{n+1}\text{Mn}_n\text{O}_{3n+1}$, where Ln and X are trivalent rare-earth and divalent alkaline-earth ions, respectively. When $n = 2$, the compounds such as $\text{La}_{2-2x}\text{Sr}_{1+2x}\text{Mn}_2\text{O}_7$ consist of MnO_2 bilayers separated by rock-salt-type $(\text{Ln}, \text{X})_2\text{O}_2$ blocking bilayers. They are stacked vertically along the c axis ($I4/mmm$; $Z = 2$) as shown in figure 9.1(a) taking the half-doped $\text{La}_1\text{Sr}_2\text{Mn}_2\text{O}_7$ as an example, where the structural parameters were taken from [198]. It should be pointed out that no structural phase transition was reported for $\text{La}_1\text{Sr}_2\text{Mn}_2\text{O}_7$ with decreasing temperature even down to 10 K [198]. However, this compound undergoes a transition into the CE -type charge-orbital ordered state at $\sim 225 \text{ K}$ [199]. This state starts melting at $\sim 170 \text{ K}$, where the A -AFM structure (figure 9.2) begins to form. The CO/OO breaks down below $\sim 100 \text{ K}$ but recovers again below $\sim 50 \text{ K}$. This reentrant behavior was discussed in terms of a polaron model [199]. Below $\sim 170 \text{ K}$, magnetic spins are ferromagnetically aligned in the a - b plane but antiferromagnetically coupled along the c axis. The (0 0 1) superlattice reflection corresponds to this long-range A -AFM ordering along the c axis. In addition, the minor CE -AFM structure was reported to coexist with the major A -AFM ordering below $\sim 145 \text{ K}$ and be drastically but not completely suppressed below $\sim 100 \text{ K}$, which was viewed as an effective phase separation [200]. This suppression is accompanied by the first-order phase transition from a CO/OO state to the A -AFM state [199, 200].

The resonant enhancement of CO/OO reflections in $\text{La}_1\text{Sr}_2\text{Mn}_2\text{O}_7$ has been investigated at the Mn K -edge [199, 201]. The subsequent *ab-initio* calculations [202]

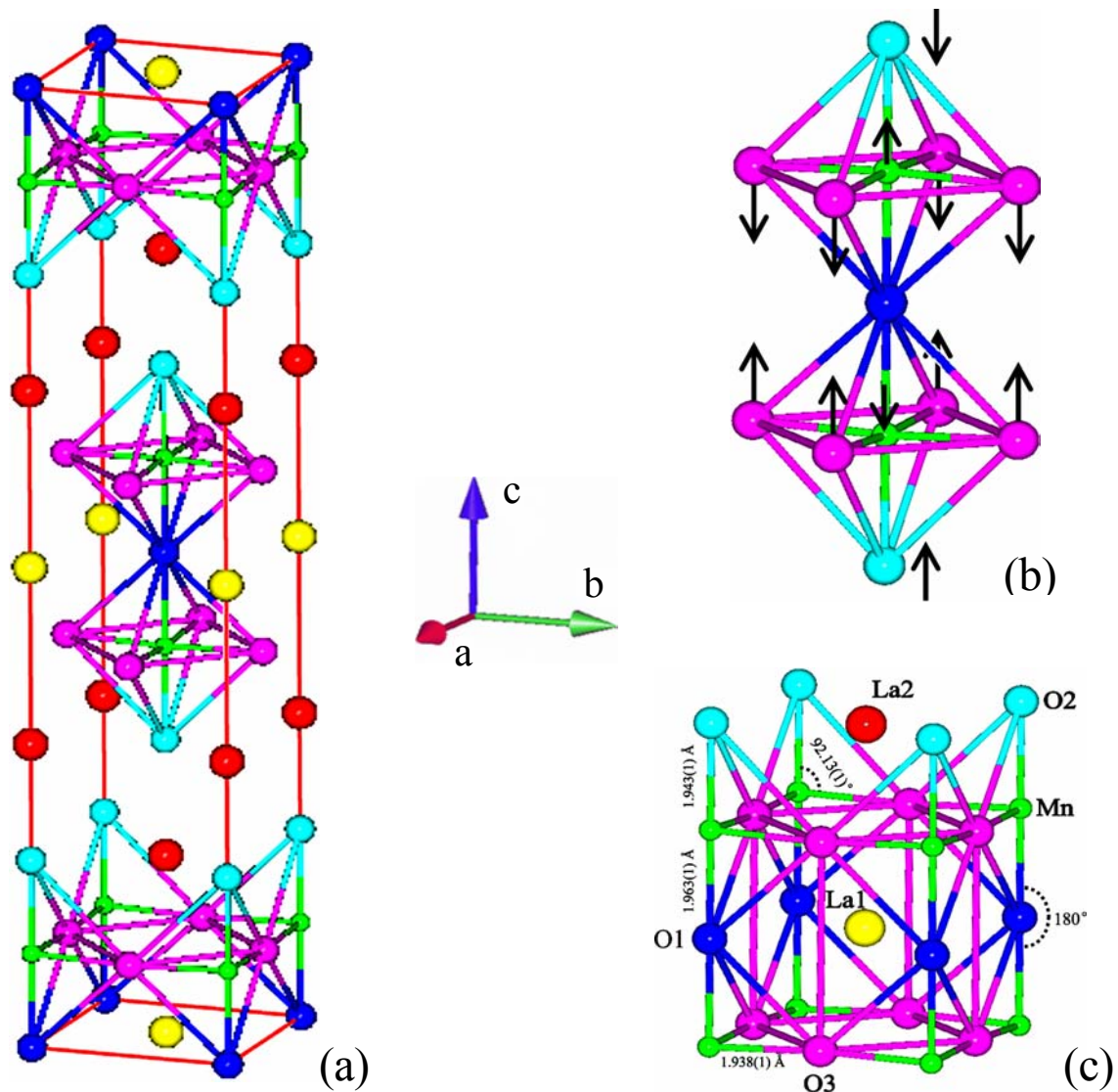


Figure 9.1: (a) Structural ($I4/mmm$; $Z = 2$) unit-cell of $\text{La}_1\text{Sr}_2\text{Mn}_2\text{O}_7$ at RT, where Mn: $(0\ 0\ z = 0.098(1))$, La1/Sr1: $(0\ 0\ \frac{1}{2})$, La2/Sr2: $(0\ 0\ z = 0.3161(7))$, O1: $(0\ 0\ 0)$, O2: $(0\ 0\ z = 0.195(1))$ and O3: $(0\ \frac{1}{2}\ z = 0.0944(6))$. The structural parameters were taken from [198]. (b) MnO_6 octahedra along the c axis and the corresponding distortion mode. (c) Local environments for La1 and La2 sites.

based on the multiple scattering and finite difference method show that JT distortion of MnO_6 octahedra alone is mainly responsible for the observed RXS signal at the Mn K -edge in charge/orbital ordered state, whereas the contribution of OO is only about one percent of that of the JT distortion. Theoretical modeling to the observed resonant energy spectra of OO and magnetic ordering reflections in $\text{La}_1\text{Sr}_2\text{Mn}_2\text{O}_7$ at the Mn $L_{II, III}$ -edges shows the presences of a relatively weaker JT distortion and a $\text{Mn}^{3+}/\text{Mn}^{2+}$ -type valence fluctuation [203]. However, this simulation cannot even describe the main experimental signals correctly, saying nothing of the subtle features. Thus identifying the origins of various features in energy spectra is critically important for understanding the physics

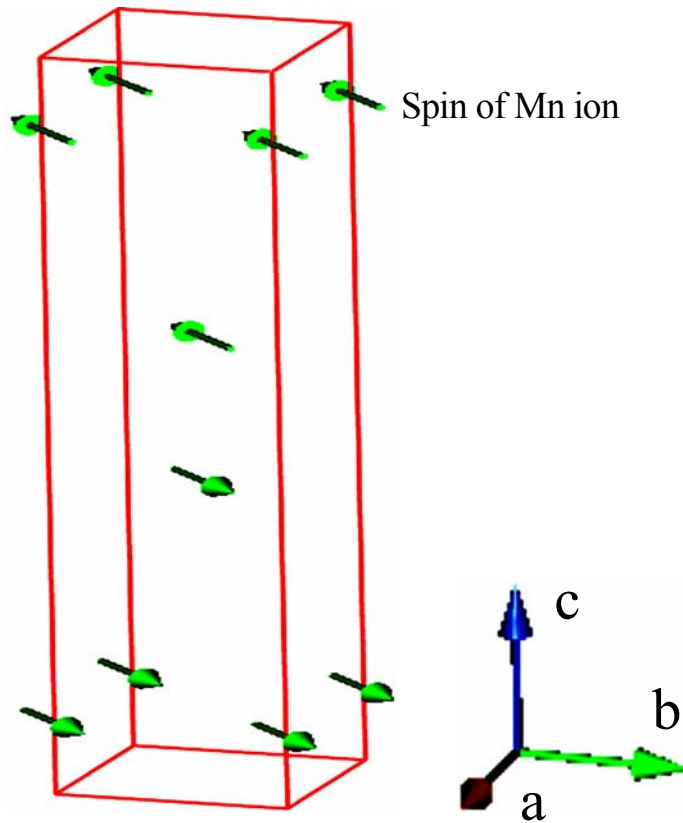


Figure 9.2: Arrangement of the *A*-AFM magnetic spins of Mn ions in $\text{La}_1\text{Sr}_2\text{Mn}_2\text{O}_7$.

behind the scattering process and then establishing a correct theoretical model.

9.3 Diffraction data

The left of figure 9.3(a) shows the observed intensity of Bragg (0 0 2) reflection versus incident x-ray energy at 300 K. Resonant enhancement of the diffraction intensity was observed close to the Mn $L_{\text{II,III}}$ absorption edges, while there is no strong incident linear polarization (σ or π) dependence and no obvious shift of peak positions. The intensity ratio between two main peaks at the Mn L_{III} -edge keeps the numerical relationship with σ and π polarizations. Compared to [191] where $\text{La}_{1.05}\text{Sr}_{1.95}\text{Mn}_2\text{O}_7$ was investigated, the resonance observed here has a different spectral shape and much clearer features, i.e. an obvious peak splitting at the Mn L_{III} -edge, probably ascribing to different Mn $3d$ electronic states and different scattering factors of (0 0 2) resulting from different doping levels. The longitudinal scans in θ - 2θ direction through Bragg (0 0 2) peak at the Mn L_{II} -edge were shown in the left of figure 9.3(b). The correlation length ξ indicates the x-ray penetrating depth and can be roughly evaluated by:

$$\xi = \frac{c}{2\pi}k, \quad (9.1)$$

where c is the lattice parameter in direct space and k is the half width at half-maximum in

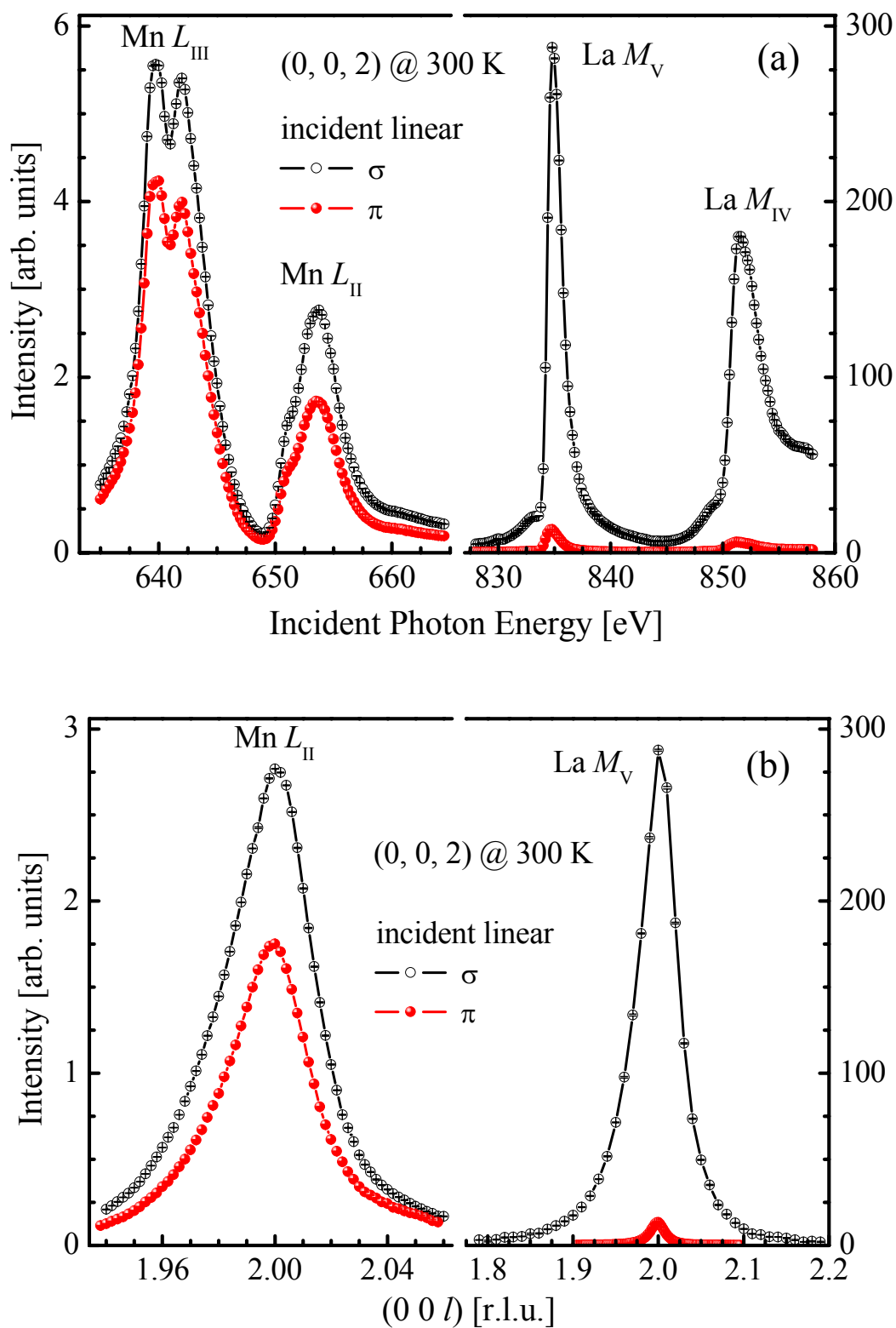


Figure 9.3: (a) Energy dependence of Bragg (0 0 2) reflection in $\text{La}_1\text{Sr}_2\text{Mn}_2\text{O}_7$ recorded over the Mn $L_{\text{II,III}}$ - and the La $M_{\text{IV,V}}$ -edges at constant wave vector with incident linear σ and π polarizations at 300 K. (b) Corresponding longitudinal scans at the Mn L_{II} - and the La M_{V} -edges.

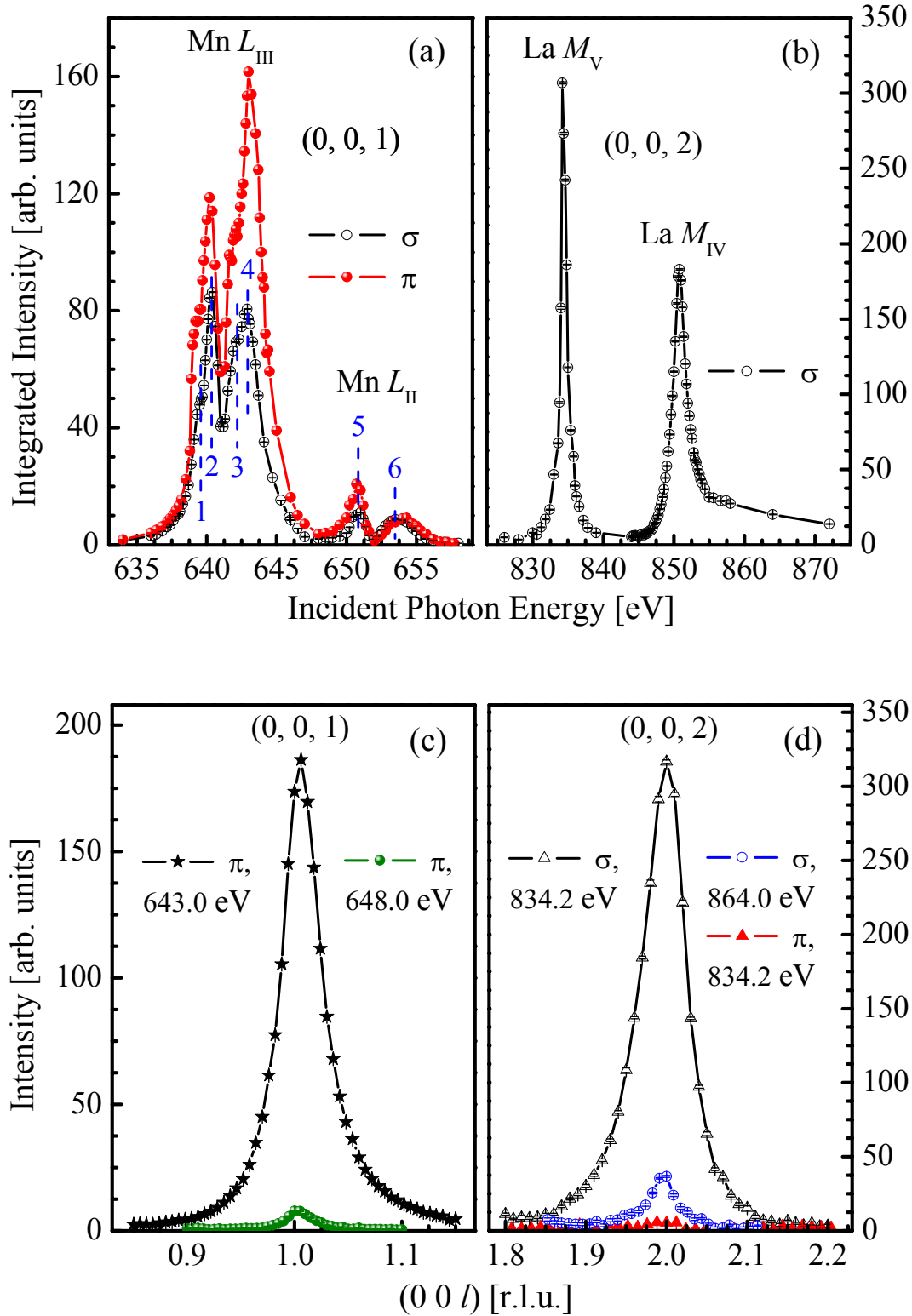


Figure 9.4: (a) Energy dependence of A -AFM $(0, 0, 1)$ reflection in $\text{La}_1\text{Sr}_2\text{Mn}_2\text{O}_7$ recorded over the $\text{Mn } L_{\text{II, III}}$ -edges and (b) Bragg $(0, 0, 2)$ reflection over the $\text{La } M_{\text{IV, V}}$ -edges with incident linear σ and π polarizations at 15 K. The intensity was integrated from the longitudinal scan. (c) and (d) Corresponding longitudinal scans of two reflections at and off their strongest resonance energies ~ 643.0 eV ($\text{Mn } L_{\text{III}}$ -edge) and ~ 834.2 eV ($\text{La } M_{\text{V}}$ -edge).

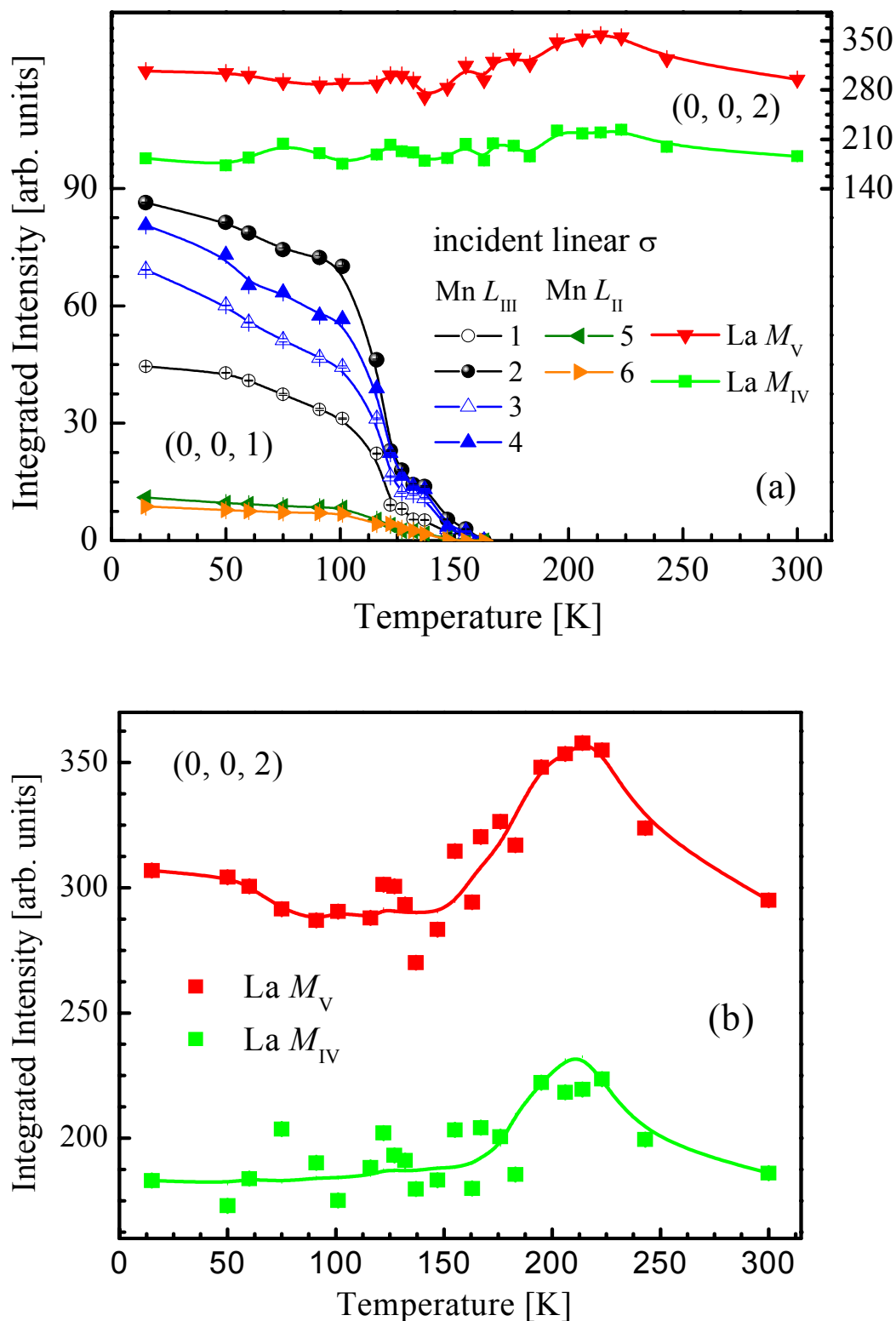


Figure 9.5: (a) Temperature dependent integrated intensity (measured in the longitudinal direction) of A -AFM $(0\ 0\ 1)$ reflection in $\text{La}_1\text{Sr}_2\text{Mn}_2\text{O}_7$ recorded at six energies corresponding to the six clear features 1, 2, 3, 4, 5 and 6 as labeled in the energy spectra in figure 9.4(a), and $(0\ 0\ 2)$ reflection at the $\text{La } M_{IV,V}$ -edges. (b) Magnified temperature dependence of Bragg $(0\ 0\ 2)$ reflection.

units of reciprocal lattice units (r.l.u.). From the Lorentzian fitting results, correlation lengths were calculated as $\sim 160.77 \text{ \AA}$ (σ) and $\sim 170.94 \text{ \AA}$ (π). The resonance of Bragg (0 0 2) reflection at the La $M_{\text{IV}, \text{V}}$ -edges ($3d \rightarrow 4f$) with incident linear σ polarization shown in the right of figure 9.3(a) was observed for the first time. The La M_{IV} and M_{V} spectra involve only a single resonant peak each. This resonant enhancement is extremely large and has dramatic polarization dependence at the La $M_{\text{IV}, \text{V}}$ -edges, especially at 15 K as shown in figure 9.4(b) where no appreciable intensity was observed with the incident π polarization. Figure 9.4(d) comparatively shows the longitudinal scans of (0 0 2) at ($\sim 834.2 \text{ eV}$) and off ($\sim 864.0 \text{ eV}$) the strongest resonance at 15 K, where the almost vanishing observed intensity at $\sim 834.2 \text{ eV}$ with incident π polarization is also shown and the remaining intensity may be due to the non-perfect polarization of the primary beam. The contrast in enhancements at and off the strongest resonance energy is up to two orders of magnitude, while the corresponding correlation length is increased from $\sim 102.04 \text{ \AA}$ to $\sim 172.41 \text{ \AA}$.

Figure 9.4(a) shows the energy dependence of the integrated intensity of A -AFM (0 0 1) reflection through the Mn $L_{\text{II}, \text{III}}$ -edges at 15 K. A similar observation at the same doping level was previously reported in [203] where only observed intensity without polarization analysis was recorded at 20 K, but the present data are far more precise. The spectra show very strong polarization dependence and are dominated by scattering at the Mn L_{III} -edge. Six distinct features are present: four peaks (2, 4, 5 and 6) and two shoulders (1 and 3). The longitudinal scans with incident linear π polarization at two energies $\sim 648.0 \text{ eV}$ and $\sim 643.0 \text{ eV}$ (where the strongest resonance occurs) are shown in figure 9.4(c). The calculated corresponding correlation lengths are $\sim 240.38 \text{ \AA}$ and $\sim 145.99 \text{ \AA}$, respectively. All the correlation lengths ξ of (0 0 1) and (0 0 2) calculated above demonstrate that incident x-rays penetrate through at least five unit cells of the single crystal. Therefore, RSXS is not a technique with surface sensitivity only.

The temperature dependences of A -AFM (0 0 1) superlattice reflection at six energies corresponding to the six clear features 1, 2, 3, 4, 5 and 6 as labeled in figure 9.4(a) and Bragg (0 0 2) reflection at the La $M_{\text{IV}, \text{V}}$ -edges with incident linear σ polarization upon warming are shown in figure 9.5(a). The integrated intensities of (0 0 1) at six energies decrease little by little with increasing temperature from 15 K to the Néel temperature $T_{\text{N}} \approx 160 \text{ K}$ and then disappear simultaneously, exhibiting a similar transition tendency. An interesting stepwise feature around 130 K is clearly exposed. On first inspection, the intensity of the (0 0 2) Bragg reflection seems to be a constant in entire temperature range. At 15 and 300 K two comparable integrated intensities were observed. However, the magnified view as shown in figure 9.5(b) exhibits a broad peak around 220 K, especially at the La M_{V} -edge where the larger integrated intensity presents more reliable information.

Meanwhile, an attempt to search for possible resonant magnetic exchange scattering at the oxygen K -edge and the La $M_{\text{IV}, \text{V}}$ -edges was made. However, no appreciable resonance of (0 0 1) above the background was observed.

9.4 Discussion

The intensity ratio between the two main features 2 and 4 at the Mn L_{III} -edge in energy spectra of A -AFM (0 0 1) reflection shown in figure 9.4(a) is reversed with different

polarizations. Polarization dependence is a sensitive probe of the valence states. Comparing to the rough theoretical calculations [203], the energy spectrum with π polarization observed here is probably ascribed to the $\text{Mn}^{3+}/\text{Mn}^{4+}$ -type valence state, while the one with σ polarization mostly comes from the $\text{Mn}^{3+}/\text{Mn}^{2+}$ -type. The contrast intensity between both spectra results from different orientations of magnetic spins relative to the incident linear σ or π x-ray. The six temperature dependences of (0 0 1) shown in figure 9.5(a) display a similar trend and disappear above $T_N \approx 160$ K indicative of the same origin for them: A -AFM ordering. The origin of the six main features in energy spectra of (0 0 1) in figure 9.4(a) was thus confirmed. However, the development of a correct magnetic model in theory for simulating observed resonances and making the actual physics clear still remains a real challenge. The variation of magnetization versus temperature measured at an applied magnetic field $H = 5$ T was previously reported with $H // a$ - b plane and $H // c$ axis in [197], where two maxima located at ~ 10 and ~ 220 K in addition to two shoulders near 125 and 240 K were observed. The shoulder near 125 K is probably correlated to the stepwise feature around 130 K observed in the temperature dependence of (0 0 1) shown in figure 9.5(a). This may be induced by the setting up of CE -type spin ordering [200] observed in neutron diffraction studies around this temperature. There the effect of CE -AFM structure was also displayed in the temperature dependent intensity of (0 0 1) but in a different manner. Furthermore, below the temperature region for this stepwise feature, the transition is pretty sharp consistent with the confirmed first-order phase transition from a charge-orbital state with the CE -AFM spin arrangement to the A -AFM state [199, 200]. No resonant enhancement of (0 0 1) reflection occurs at the oxygen K -edge and the La $M_{\text{IV}, \text{V}}$ -edges. This indicates that the holes introduced by doping taking part in producing the A -AFM ordering mainly are located on the Mn sites. This is in contrast to the situation in $\text{La}_{1-x}\text{Sr}_x\text{MnO}_3$ ($x \approx 1/8$) reported in chapter 8.3.

Superlattice reflections corresponding to the propagation vector $Q = (1/4 \ 1/4 \ 0)$ in $\text{La}_1\text{Sr}_2\text{Mn}_2\text{O}_7$ were believed to be relevant to the $3d$ OO ($3x^2-r^2/3y^2-r^2$) of Mn^{3+} ions which is accompanied by the CO of 1:1 $\text{Mn}^{3+}/\text{Mn}^{4+}$ species [204]. X-ray, neutron and electron diffraction studies [199, 204] indicate that the coupled CO/OO developed below ~ 225 K starts melting at the A -AFM transition temperature (~ 170 K) and collapses at lower temperatures below ~ 100 K. However, in a subsequent RXS study [201], the CO wave vector $(1/2 \ 1/2 \ 0)$ was confirmed to be different with that of the OO. The recent direct observation of the orbital $(1/4 \ 1/4 \ 0)$ reflection [203] using RSXS technique at the Mn $L_{\text{II}, \text{III}}$ -edges shows that the OO develops at ~ 225 K and persists down to ~ 20 K with a small change in the gradient of the observed intensity below ~ 100 K. Therefore, it seems that the OO causes an occurrence of the CO and subsequently drives the formation of long-range A -AFM spin ordering. The breakdown of CO is due to the FM spin coupling in a - b plane in the A -AFM state. In addition, the change in temperature dependent integrated intensity of (0 0 2) at the La M_{V} -edge shown in figure 9.5(b) seems to be inversely correlated to that of the OO reported in [203], indicating a possible interplay between OO and temperature dependent lattice modulations. To summarize, complicated cooperation and competition between spin, charge, orbital and lattice exist in double-layered $\text{La}_1\text{Sr}_2\text{Mn}_2\text{O}_7$.

It is interesting to explore the reasons for the huge resonant enhancement of Bragg (0 0 2) reflection at the La $M_{\text{IV}, \text{V}}$ -edges. This peak is allowed for the tetragonal structure of this compound. The observed intensity in RSXS is mainly determined by the anomalous

atomic scattering factor (chapter 3.2.2) of resonant atoms. This factor is a function of the incident photon energy E and can be expressed as $f(E) = f_1(E) + if_2(E)$, where the imaginary part $f_2(E)$ is related to the absorption coefficient and the real part $f_1(E)$ can be deduced from $f_2(E)$ through the mutual Kramers-Kronig relation [114]. The x-ray absorption spectrum of this compound at the La $M_{IV, V}$ -edges needs to be measured for a quantitative calculation of the anomalous scattering factor. However, the high absorption coefficients of rare earths at the $M_{IV, V}$ -edges imply the strong resonance possible.

The anomalous atomic scattering factor shows a tensorial character and its anisotropy is mainly related to the distortion of the local environment. During the RSXS process, in principle, the excited electron is sensitive to any anisotropy around the absorbing ions, e.g. the anisotropy of charge, orbital, spin or lattice. When measured at symmetry-allowed peaks [205], RSXS provides: (i) structural information, e.g. neighbor types and bond disorders of neighbor atoms; (ii) spectroscopic sensitivities, e.g. valence, empty orbital or bonding information of the resonant atoms. Thus the origins of (0 0 2) resonance could be any or some of the above items induced by possible local and asymmetric lattice modulations, JT distortion, tilting of MnO_6 octahedra, novel interplay of lattice dynamics with spin, charge and orbital, etc.

There are two types of distortion related to MnO_6 octahedra in manganites: (i) one is the JT distortion that is inherent to the high-spin ($S = 2$) Mn^{3+} ions, resulting in different Mn-O bond lengths, which is accompanied by OO of the occupied Mn $3d$ orbitals; (ii) another is the cooperative rotation corresponding to the Mn-O-Mn bond angle and tolerance factor, leading to lattice modulations and forming the octahedral tilt ordering. An x-ray-scattering study of the octahedral tilt ordering in $\text{Pr}_{1-x}\text{Ca}_x\text{MnO}_3$ with $x = 0.4$ and 0.25 and in LaMnO_3 was reported [206], where the observation of octahedral tilt ordering was achieved by tuning the incident x-ray energy to the L_I , L_{II} , and L_{III} absorption edges of Pr and La, respectively. The observed resonances were thought to be induced by the anisotropies formed due to the octahedral tilt ordering at rare-earth sites. However, no coupling between tilt ordering and corresponding OO was observed there. The structural data of $\text{La}_1\text{Sr}_2\text{Mn}_2\text{O}_7$ as a function of temperature is somewhat not complete [207] and the existing structural parameters were strongly challenged by the study [208] using a single-crystal diffractometer. The proposed $I4/mmm$ tetragonal symmetry for $\text{La}_1\text{Sr}_2\text{Mn}_2\text{O}_7$ determines that the out-of-plane Mn-O-Mn bond angle along the c axis is 180° and the JT distortion size Δ , which is defined as the ratio of the averaged apical and the equatorial Mn-O bond lengths, is close to unity even down to 10 K [198] (figures 9.1(b) and (c)). Therefore no octahedral tilt ordering exists in $\text{La}_1\text{Sr}_2\text{Mn}_2\text{O}_7$. However, the distortion mode developed for MnO_6 octahedra based on Mn-O bond lengths as shown in figure 9.1(b) indeed exists, which was confirmed by a Raman spectroscopy study [209] on this compound. Raman spectroscopy is a very sensitive probe of the local or dynamical structural changes. This scattering method can be used to study the complex interplay of lattice dynamics with ordering parameters in manganites. In [209], the major intensity of out-of-plane spectra (polarization of incident or scattered light along the crystalline c axis) was assigned to this stretching mode (figure 9.1(b)) and is independent of temperature. In addition, two tiny intensities in out-of-plane spectra were attributed to the Raman allowed modes in the original structure: atomic motion of La and Sr ions along the c direction. Moreover, the rest appreciable intensities were thought to be from the activated modes, i.e. the coupling between lattice distortion and CO/OO. This octahedral distortion mode has little effect on the local environment of La1 sites that locate at the center of four

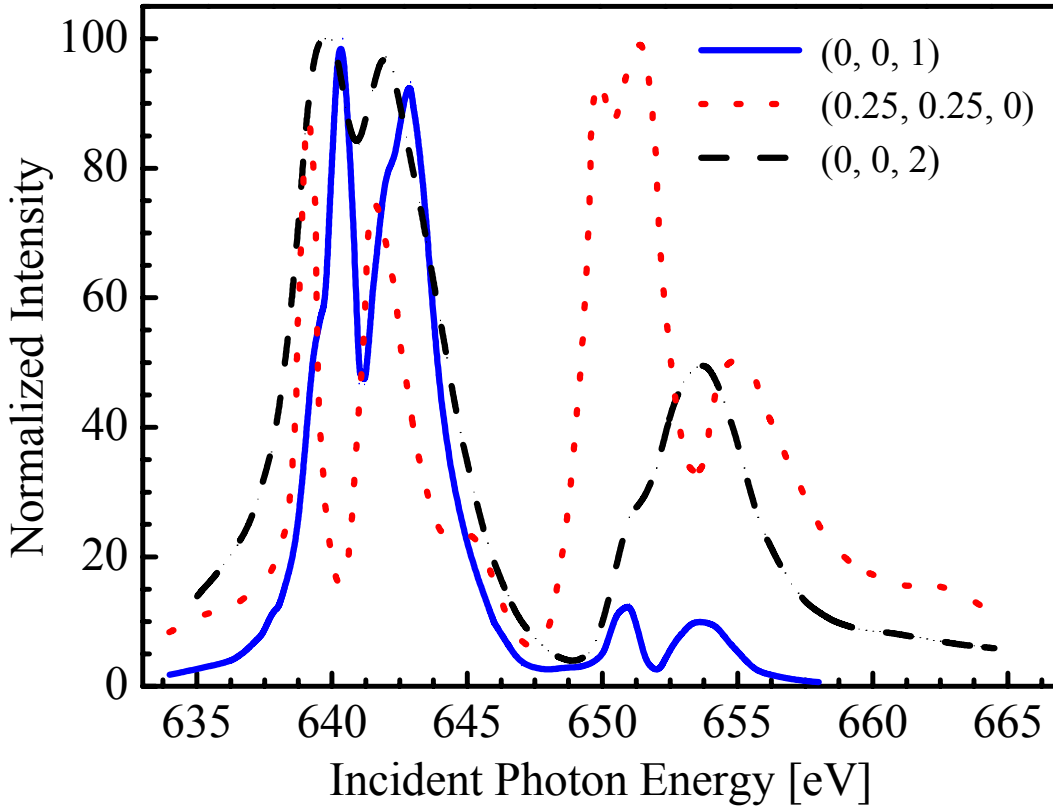


Figure 9.6: Comparison between three resonant energy spectra through the Mn $L_{II,III}$ -edges for $\text{La}_1\text{Sr}_2\text{Mn}_2\text{O}_7$: A -AFM (0 0 1) reflection at 15 K; OO (0.25 0.25 0) reflection at ~ 20 K [203]; Bragg (0 0 2) reflection at 300 K. Incident photon energy of (0.25 0.25 0) was calibrated by the difference between energy dependent intensity of (0 0 1) in [203] and the corresponding one observed here. Observed intensity was normalized to 100.

double- MnO_6 octahedra as shown in figure 9.1(c), while it has a profound effect on that of the La2 sites due to the asymmetric action. Indeed, based on the reported structural parameters at RT in [198], the calculated local distortion parameters Δ of La1 and La2 sites by Fullprof suit [164] are 3.2×10^{-5} and 1.4×10^{-3} , respectively. The strongly produced anisotropy of La2 sites may lead to the resonant enhancement of (0 0 2) at the La $M_{IV,V}$ -edges. In addition, the observed coupling between OO and temperature dependent integrated intensity of (0 0 2) at the La M_V -edge is in agreement with the Raman spectroscopy study [209]. The incident σ polarization means that the electric-field vector of incoming photons is parallel to the scattering plane. From the dramatic contrast between observed intensities of (0 0 2) at the La $M_{IV,V}$ -edges with different incident polarizations shown in figure 9.3 (300 K) and figures 9.4(b) and (d) (15 K), it can be concluded that the anisotropy of electronic states around La2 sites induced by the distortion of MnO_6 octahedra is nearly collinear.

Furthermore, some interesting information can be obtained by qualitatively comparing three resonant energy spectra through the Mn $L_{II,III}$ -edges as shown in figure 9.6: A -AFM (0 0 1) reflection at 15 K, OO (0.25 0.25 0) reflection at ~ 20 K [203] and Bragg (0 0 2) reflection at 300 K. At the Mn L_{III} -edge, the two peak positions of

(0.25 0.25 0) reflection correspond to that of the two shoulders of (0 0 1) reflection. Big contrasts exist at the Mn L_{II} -edge, where the (0.25 0.25 0) reflection triply splits. Figure 9.6 clearly demonstrates that three reflections have different origins. Theoretical modeling to the three resonances is indispensable for further understanding.

9.5 Conclusions

A systematic RSXS study at the Mn $L_{\text{II, III}}$ -edges on the A -AFM structure and at the La $M_{\text{IV, V}}$ -edges on the possible lattice modulations in $\text{La}_1\text{Sr}_2\text{Mn}_2\text{O}_7$ has been accomplished. At 15 K, well below $T_{\text{N}} \approx 160$ K, dramatic enhancements of A -AFM (0 0 1) and Bragg (0 0 2) reflections at the Mn $L_{\text{II, III}}$ - and the La $M_{\text{IV, V}}$ - edges were observed, respectively. The formation of OO below $T_{\text{OO}} \approx 220$ K leads to the growth of CO and successively to the setting up of A -AFM spin ordering, whereas the CO and the A -AFM phases compete with each other. The temperature dependences of (0 0 1) resonance at the six featured energies show a similar trend indicative of the same origin: A -AFM ordering. However, the resonant intensity of (0 0 2) persists throughout the investigated temperature range but is strongly affected by the OO, indicative of a strong interaction between them. This study carefully carried out reveals a heretofore neglected lattice modulation that is indicated by the resonances at La sites. This observation specially emphasizes the importance of lattice degree of freedom for understanding the anomalous physical properties in manganites.

Chapter 10

Summary and outlook

The research area of solid state physics contains many aspects, most of which are presented in this dissertation, e.g. instrumentation development, materials synthesis, designing and carrying out experiments, data collection and analysis, results publication, etc. The motivations and the main results of this dissertation are summarized here.

Chapter 4:

(1) Powder diffraction (x-ray and neutron) is a most useful method for qualitatively and quantitatively analyzing the crystal structure and magnetic ordering of a powdered sample. For laboratory XRPD, preferred orientation more or less exists in a normally prepared specimen, especially for powdered single-crystalline samples. In order to overcome this problem, one rotating specimen holder has been designed and built, which not only can effectively minimize the problem of preferred orientation but also produces a 'zero-background' contribution to the collected data, increasing XRPD data quality and then the refinement accuracy with these data by the Fullprof suite.

(2) The setup of two-circle diffractometers for most of the RSXS chambers leads to severe restrictions for sample rotations around the surface normal (ψ -circle) and sample tilting (χ -circle), which are both essential degrees of freedom for single crystal studies. To overcome these limitations, a new portable UHV goniometer has been designed and built, which makes it feasible to adjust samples along χ ($\pm 2.5^\circ$, even at temperatures down to 10 K) and ψ (360° , above ~ 220 K) and dramatically improves the efficiency of soft x-ray scattering chambers and can be widely used to unravel the ordering phenomena of lattice, charge, orbital and spin degrees of freedom in CTMO by the RSXS technique.

Chapter 5:

Most of perovskite manganites nowadays have been fabricated through high-temperature solid state reactions. This traditional method has its advantages, but it also has some intrinsic drawbacks (see details in chapter 5). In order to overcome some of them, it is absolutely necessary to optimize the processing and synthesis parameters that have a profound effect on the properties of final products.

In this chapter, the preparation parameters for $\text{La}_{7/8}\text{Sr}_{1/8}\text{MnO}_3$ manganite have been optimized from the selection and treatment of starting materials, to the mixing and milling speed and time for raw and intermediate mixtures, to the reaction temperature and time for calcining and sintering, to the binder effect and to other factors (e.g. atmosphere concentration). The observation of the transition from La_2O_3 to $\text{La}(\text{OH})_3$ after the exposure of pure La_2O_3 to the air for ~ 2 h demonstrates that the purpose of pre-firing La_2O_3 is not only for decarbonization but also for dehydration. This transition could explain the phenomenon that some bulk manganites relevant to La prepared at low temperatures automatically decompose into powder samples after long time exposure to air. The appropriate mixing and milling speed and time are determined as 200 rpm and 60 min. The application of binder during synthesis can improve reaction rates; however, the residual adsorption has to be removed at elevated temperatures. This process is often very slow. It is thus suggested not using any binder while pressing powder sample into bulk one. The results obtained from decomposing SrCO_3 using normal furnace (static air atmosphere) and TGA machine (flowing dry gas mixture of 79% Ar and 21% O_2 at 1 atm, simulating air) can qualitatively explain the effect of annealing with different atmospheres. Finally, one good recipe for preparing high-quality polycrystalline $\text{La}_{7/8}\text{Sr}_{1/8}\text{MnO}_3$ samples, i.e. two times calcination (1373 K, 12 h) and two times sintering (1573 K, 12 h), has been established. This synthesis route, i.e. two times calcining and two times sintering, has been tested in the syntheses of $\text{La}_1\text{Sr}_2\text{Mn}_2\text{O}_7$ and $\text{La}_{0.83}\text{Ca}_{0.17}\text{MnO}_3$ and it seems to be a universal one at least for the present testing. The most important contribution of this chapter is the establishment of the route for optimizing the synthesis of polycrystalline manganites.

Chapter 6:

Improving the crystal quality and growing new single crystals are the sine qua non of investigating the novel properties of CTMO. A straight and very uniformly densified feed rod with a homogenous composition distribution is crucial for establishing a stable melting zone that is the prerequisite for any single crystal growth. One method has been established for preparing such kind of feed rods. The FZ furnace and the crystal growth process have been described in details, especially some valuable tricks, e.g. when will one begin to grow crystals and how to keep the melting zone stable. The principles of necking technique and an alternative method for this technique have been introduced. The characterizations of grown crystals, the in-depth experiments employing complementary neutron and synchrotron radiation x-ray scattering methods to obtain a deeper understanding of the related physics, and the whole procedure of single crystal growth by FZ method have been summarized. I believe that this chapter is particularly useful for the newcomers to this field.

Chapter 7:

(1) $\text{La}_{1-x}\text{Sr}_x\text{MnO}_3$ is one of the most interesting systems in doped perovskite-type manganites. For the same nominal Sr doping level $x = 1/8$, structural and magnetic properties reported in the literature differ substantially, strongly ascribed to the different preparation methods and synthesis conditions. Besides peculiar physical properties, the defect chemistry such as cation nonstoichiometry and excess oxygen is also a crucial issue

for the exact understanding of manganites. This system contains technologically interesting manganite materials. Therefore a full understanding of the possible tuning of the physical properties in polycrystals and single crystals is desirable before such applications become possible.

In this part, in order to resolve many ambiguities from the conflicting reports in literature and solve issues in solid state reactions, structural and magnetic properties of air sintered and Ar and O₂ annealed La_{7/8}Sr_{1/8}Mn_{1-γ}O_{3+δ} polycrystalline samples have been studied systematically. From the simultaneous refinement of RT XRPD and NPD data, it has been found that the crystal structure is orthorhombic (*Pbnm*, $Z = 4$; *O*) for the Ar annealed sample and rhombohedral ($R\bar{3}c$, $Z = 2$; *R*) for the air sintered and O₂ annealed samples. At the *O-R* structural transition, the averaged Mn-O-Mn bond angle increases from 161.08(4)° (Ar) to 163.38(1)° (O₂) and 163.64(1)° (Air). Ar and O₂ annealings cause a decrease of the Curie temperature T_c from 240(1) K (Air) via 237(1) K (O₂) to 192(1) K (Ar). The Curie temperature is reduced by ~20% for the sample with orthorhombic structure (Ar) as compared with that of the samples with rhombohedral structure (Air and O₂). The decrease of T_c is explained by the decrease of total strength of magnetic interactions, due to the decreased <Mn-O-Mn> bond angle and increased <Mn-O> bond length, and by the decrease of number of nearest magnetic neighbors. The possible reasons for the decrease of Mn site occupancy after Ar and O₂ annealings and the sources of apparent excess oxygen have been discussed. Thus it is shown that the actual distributions of cation vacancies in *A* (La and Sr) and *B* (Mn) sublattices induced by the changes of Mn and oxygen contents through Ar and O₂ annealings play an important role in the structural and magnetic properties. Comparing the Ar annealed with the air sintered sample, a decrease as small as ~2.2% of the relative oxygen content leads to a remarkable large ~20% effect on the magnetic transition temperature. Only a combined refinement of XRPD and NPD data allows one to determine the stoichiometry with the required precision to be able to compare results from different samples.

(2) In order to complete the structural studies, a systematic temperature dependent NPD study of polycrystalline La_{7/8}Sr_{1/8}Mn_{1-γ}O_{3+δ} compounds has been performed. In the temperature range between 10 and 900 K, the structural and magnetic phases and transitions for two different samples were investigated: one Ar annealed with an orthorhombic *Pbnm* ($Z = 4$; *O*) structure at room temperature and one air sintered with a rhombohedral $R\bar{3}c$ ($Z = 2$; *R*) structure at room temperature. At higher temperatures, above 400 K, both samples exhibit a rhombohedral structure. For the Ar annealed sample, a JT transition occurs in the orthorhombic phase at about 298 K with very large variations in the Mn-O2' and Mn-O2 bond lengths and Mn-O1-Mn bond angle on cooling from 298 K to 180 K. For this sample the FM moment at 10 K in the magnetic space group *Pb'n'm* amounts to 3.22(5) μ_B/Mn. By contrast, the air sintered sample undergoes upon cooling a structural transition from rhombohedral to orthorhombic with a mixed phase of nearly equal *R* and *O* repartition at 120 K. This transition was observed for the first time. The FM order develops in this sample at about 240 K with a moment of 3.35(4) μ_B/Mn at 10 K. The coherent JT distortion in its orthorhombic phase occurs below some 170 K. In addition, the coherent JT distortion parameter Δ, the tolerance factor *t* and the one-electron bandwidth *W* of the *e_g*-band have been determined.

Chapter 8:

(1) The interesting FMI phase of single-crystalline $\text{La}_{1-x}\text{Sr}_x\text{MnO}_3$ ($x \approx 1/8$) below ~ 150 K has not been understood completely. This is just because of the bewildering crystal structures. In addition, the structure information of the JT region has also not been established correctly. In order to unclosethese structures and clarify the differences between polycrystalline and single-crystalline samples of manganites, a high-resolution NPD study on the crystal and magnetic structure of a powdered $\text{La}_{1-x}\text{Sr}_x\text{MnO}_3$ ($x \approx 1/8$) single crystal has been carried out. The structural information obtained from powdered single-crystalline $\text{La}_{1-x}\text{Sr}_x\text{MnO}_3$ ($x \approx 1/8$) is of particular interest because the information of CO/OO pattern is usually obtained from single-crystal x-ray investigations at a synchrotron. Careful analysis of the NPD data and comparison of the Rietveld refinement results for competing structure models reveal that the sample is orthorhombic ($Pnma$, O) above the JT transition temperature (T_{JT}) and monoclinic ($P12_1/c1$, M') in the JT regime. The NPD data below the charge/orbital ordering temperature ($T_{\text{CO/OO}}$) were also refined with monoclinic ($P12_1/c1$, M'') model because the goodness of fit χ^2 of the tentative refinement with triclinic ($P\bar{1}$) structure has not decreased largely due to the heavily overlapped peaks. The refined lattice parameters show an obvious breathing-mode distortion between $T_{\text{CO/OO}}$ and T_{JT} , accompanied by a large deviation of the monoclinic angle β from 90° , signifying a very strong cooperative JT distortion. A FM moment $3.43(5) \mu_{\text{B}}/\text{Mn}$ in addition to an AFM moment $0.54(2) \mu_{\text{B}}/\text{Mn}$ is mainly along the b axis in $P12_1/c1$ symmetry at 5 K. With increasing temperature, the AFM domains are transformed into FM ones above 100 K and the FM spin orientation turns from the b to the c axis in crystallographic b - c plane below $T_{\text{c}} = 187(1)$ K. The magnetization measurements especially at 70 kOe besides 20 and 120 Oe show typical anomalies around $T_{\text{CO/OO}}$ and T_{JT} . The measured moment $3.9265(9) \mu_{\text{B}}/\text{Mn}$ at 70 kOe and 5 K is well consistent with the sum $3.97(5) \mu_{\text{B}}/\text{Mn}$ of the refined FM and AFM moments at 5 K, implying that the FM regions grow on expense of the AFM regions. The applied magnetic field can affect the PMI state in the range of magnetic polarons. Based on the size of JT distortion and the BVS's theory, the CO/OO phenomenon is briefly discussed. In this study, the structural information of the JT regime in single-crystalline $\text{La}_{1-x}\text{Sr}_x\text{MnO}_3$ ($x \approx 1/8$) has been established for the first time, which provides obvious evidence that the CO/OO pattern occurring in this regime is completely different with that of LaMnO_3 .

(2) For $\text{La}_{1-x}\text{Sr}_x\text{MnO}_3$ manganites, of particular interest are compositions close to $x = 1/8$, where a double transition from a PMI phase to a FMM phase and then to a FMI phase occurs with decreasing temperature. The exact nature of the FMI phase in lightly doped $\text{La}_{1-x}\text{Sr}_x\text{MnO}_3$ ($x \approx 1/8$) is still being strongly debated in spite of intensive investigations. The CO in this phase is among the most puzzling. Up to now, no hard experimental evidence concerning the occurrence of CO has been obtained. In this part, the first direct observation of the hole ordering was obtained via the soft x-ray resonant scattering technique. The expected resonance of the CO reflection ($0\ 0\ 1/2$) in $Pbnm$ symmetry is not observed at the Mn K -edge in the hard x-ray regime. However, it indeed occurs at the Mn L_{III} -edge in the soft x-ray regime, where the RSXS is a direct probe of the $3d$ electronic states of TMs. Most surprisingly, the resonant enhancement of this CO reflection also occurs at the oxygen K -edge. In addition, the temperature dependences of ($0\ 0\ 1/2$) in $Pbnm$ symmetry at the Mn L_{III} -edge and the oxygen K -edge correspond to

the FMI transition temperature ~ 150 K. These observations strongly challenge the classic ionic picture of integer valence states for $3d$ TMs and definitively confirm that the doped holes in this compound are indeed shared by the Mn and oxygen sites together in analogy to the so-called Zhang-Rice singlets proposed for the high T_c cuprates.

Chapter 9:

The spin ordering and the possible lattice modulations of a bilayered $\text{La}_1\text{Sr}_2\text{Mn}_2\text{O}_7$ single crystal have been systematically studied by the RSXS. Huge resonances of A -AFM $(0\ 0\ 1)$ and Bragg $(0\ 0\ 2)$ reflections at the Mn $L_{\text{II, III}}$ -edges and the La $M_{\text{IV, V}}$ -edges were observed, respectively. In particular, the unexpected dramatic enhancements of Bragg $(0\ 0\ 2)$ reflection show a very strong σ polarization dependence. This observation indicates the occurrence of possible lattice modulations. The possible driving forces were briefly discussed. In addition, six obvious features were confirmed to exist in the energy dependence of $(0\ 0\ 1)$ near the Mn absorption edges. The temperature dependences of $(0\ 0\ 1)$ demonstrate that these six features purely originate from the spin ordering, supporting detailed and definitive experimental data for theoretical modeling a correct magnetic model. Moreover, the temperature dependence of $(0\ 0\ 2)$ inversely interplays with that of the OO. The formation of OO below $T_{\text{OO}} \approx 220$ K leads to the growth of CO and successively to the setting up of A -AFM spin ordering, whereas the CO and the A -AFM phases compete with each other. To summarize, complicated cooperation and competition between spin, charge, orbital and lattice exist in double-layered $\text{La}_1\text{Sr}_2\text{Mn}_2\text{O}_7$.

Apart from the development of data analyzing techniques, solving complicated structures of perovskites, I think, ultimately depends on the development of experimental techniques, e.g. the improvement of detecting resolutions for NPD and SPXD methods, etc.

Quantitatively understanding the physics of observed resonances is still a difficult issue. To clarify these resonances, microscopic theoretical modeling, e.g. *ab-initio* band structure calculation, is urgently needed and will definitely be the subjects of further investigations.

Appendix

A List of Abbreviations

<i>A</i> -AFM	<i>A</i> -type antiferromagnetic
AFM	antiferromagnetic
at%	atomic percent
BESSY	Berliner Elektronenspeicherring-Gesellschaft für Synchrotronstrahlung
BVS's	Bond-valence sums
CCR	closed cycle refrigerator
CO	charge ordering
CO/OO	charge and orbital order
CMR	colossal magnetoresistance
CTMO	complex transition metal oxides
e.s.d.	estimated standard deviation
FC	field cooling
FM	ferromagnetic
FMI	ferromagnetic insulating
FMM	ferromagnetic metallic
FRJ	Forschungszentrum Jülich
FRM	Forschungsneutronenquelle Heinz Maier-Leibnitz
FWHM	full width at half maximum
FZ	floating zone
GKA	Goodenough-Kanamori-Anderson
h	hour
<i>H</i>	hexagonal
ICP-OES	inductively coupled plasma with optical emission spectroscopy
JT	Jahn-Teller
<i>M</i>	magnetization
min	minute
MS	giant magnetostriction
NPD	neutron powder diffraction
<i>O</i>	orthorhombic
OO	orbital ordering
PMI	paramagnetic insulating
PPMS	physical property measurements
<i>R</i>	rhombohedral
rpm	revolutions per minute
RSXS	resonant soft x-ray scattering
RT	room-temperature
RXS	resonant x-ray scattering
SPXD	synchrotron powder x-ray diffraction
SQUID	superconducting quantum interference device

T	temperature
T_c	Curie temperature
TGA	thermogravimetric analysis
T_{JT}	Jahn-Teller transition temperature
TM	transition metal
TMs	transition metals
T_N	Néel temperature
UHB	upper Hubbard band
UHV	ultrahigh-vacuum
Wt%	weight percent
XRPD	x-ray powder diffraction
ZFC	zero-field cooling
μ_B	Bohr magneton

B An example of the PCR files for Rietveld refinement by Fullprof

```

COMM      Crystal and magnetic structure of powdered single-crystalline La7/8Sr1/8MnO3 at 5 K
! Current global Chi2 (Bragg contribution) = 1.800
! Files => DAT-file, PCR-file: 5k10h
!Job Npr Nph Nba Nex Nsc Nor Dum Iwg Ilo Ias Res Ste Nre Cry Uni Cor Opt Aut
  1  5  3  48  2  0  0  1  0  0  1  0  0  0  0  0  0  0  0  0  0  1
!Ipr Ppl Ioc Mat Pcr Ls1 Ls2 Ls3 NLI Prf Ins Rpa Sym Hkl Fou Sho Ana
  0  0  1  1  1  0  0  0  0  3  10  0  0  1  4  1  1
!lambda1 Lambda2      Ratio      Bkpos      Wdt      Cthm      muR      AsyLim      Rpolarz ->Patt1
  1.5487  1.5487      1.00      103.05     16.0     0.0       0.0      180.0       0.0
!NCY  Eps  R_at  R_an  R_pr  R_gl      Thmin      Step      Thmax      PSD      Sent0
  22  0.3  1.0   1.0  1.0   1.0       8.00     0.05     144.50   0.00   0.00
!2Theta/TOF/E(Kev) Background for Pattern# 1
   9.600    410.667    0.000
  13.750    387.000    0.000
  15.450    380.000    0.000
  19.450    373.000    0.000
  21.800    347.000    0.000
  24.000    338.667    0.000
  27.700    332.000    0.000
  31.250    326.333    0.000
  33.750    327.000    0.000
  35.650    318.333    0.000
  37.550    355.000    0.000
  42.800    359.000    0.000
  45.650    338.000    0.000
  45.700    340.667    0.000
  49.450    327.333    0.000
  51.800    333.667    0.000
  56.400    281.333    0.000
  57.200    272.333    0.000
  60.000    289.000    0.000
  63.650    273.667    0.000

```

```

66.250    299.333    0.000
70.050    308.667    0.000
74.150    368.000    0.000
76.450    274.000    0.000
77.200    290.333    0.000
80.600    331.667    0.000
85.600    285.667    0.000
85.850    276.333    0.000
88.650    312.333    0.000
94.200    265.333    0.000
94.850    253.333    0.000
98.350    288.333    0.000
102.200   270.667    0.000
103.650   250.333    0.000
108.300   272.667    0.000
108.550   341.667    0.000
113.550   281.000    0.000
116.050   320.667    0.000
117.700   397.000    0.000
121.500   380.000    0.000
124.150   275.000    0.000
128.150   323.000    0.000
128.550   421.667    0.000
134.200   318.000    0.000
135.300   277.333    0.000
137.700   404.000    0.000
141.300   420.667    0.000
144.250   330.000    0.000
! Excluded regions (LowT HighT) for Pattern# 1
    0.00      8.00
    144.50   180.00
!
    34      !Number of refined parameters
!
! Zero   Code   SyCos   Code   SySin   Code   Lambda   Code MORE ->Patt# 1
    0.10022 21.00  0.00000  0.00  0.00000  0.00  0.00    0.00  0
!-----
! Data for PHASE number: 1 ==> Current R_Bragg for Pattern# 1: 0.00
!-----
Crystal structure of powdered single-crystalline La7/8Sr1/8MnO3 at 5 K
!Nat Dis Ang Pr1 Pr2 Pr3 Jbt Irf Isy Str Furth ATZ Nvk Npr More
    7 0 0 1.0 1.0 1.0 0 0 0 0 0 941.724 0 5 1
!Jvi Jdi Hel Sol Mom Ter Brind RMua RMub RMuc Jtyp Nsp_Ref Ph_Shift
    0 3 0 0 0 0 1.000 0.0000 0.0000 0.0000 1 0 0
!
! Max_dst(dist) (angles) Bond-Valence Calc.
    2.3000 180.0000 BVS
! N_cations N_anions Tolerance(%) / Name or cations/ and Anions
    3 1 0.00
LA+3 SR+2 MN+3
O-2
!
P 1 21/C 1 <--Space group symbol

```

```

!Atom Typ      X      Y      Z      Biso      Occ      In Fin N_t Spc /Codes
Mn1  MN        0.00000 0.00000 0.50000 0.33771  0.50000  0  0  0  0
          0.00    0.00    0.00    191.00    0.00
Mn2  MN        0.50000 0.00000 0.50000 0.33771  0.50000  0  0  0  0
          0.00    0.00    0.00    191.00    0.00
La1  LA        0.25074 -0.00734 -0.02198 0.37691  0.87500  0  0  0  0
          71.00    81.00    91.00    201.00    0.00
Sr1  SR        0.25074 -0.00734 -0.02198 0.37691  0.12500  0  0  0  0
          71.00    81.00    91.00    201.00    0.00
O1   O         0.24936 0.06687 0.50544 0.86364  1.00000  0  0  0  0
          101.00   111.00   121.00   211.00    0.00
O2   O         0.04018 0.72405 0.72245 0.63294  1.00000  0  0  0  0
          131.00   141.00   151.00   221.00    0.00
O3   O         0.47099 -0.23343 0.22529 0.63294  1.00000  0  0  0  0
          161.00   171.00   181.00   221.00    0.00
!-----> Profile Parameters for Pattern # 1
! Scale      Shape1      Bov      Str1      Str2      Str3      Strain-Model
  1.6528     0.04889     0.00000  0.00000  0.00000  0.00000  0
 11.00000    241.000    0.000    0.000    0.000    0.000
! U          V          W          X          Y          GauSiz   LorSiz Size-Model
  0.126511  -0.104837  0.115123  0.004581  0.000000  0.000000  0.000000  0
  261.000   251.000   231.000   271.000   0.000    0.000    0.000
! a          b          c          alpha      beta      gamma     #Cell Info
  7.786890  5.532544  5.516849  90.000000  90.026382  90.000000
 31.00000   41.00000  51.00000  0.00000   61.00000  0.00000
! Pref1     Pref2     Asy1     Asy2     Asy3     Asy4
  0.00000   0.00000  0.49040  0.09271  -0.68207  -0.09821
  0.00    0.00    281.00  291.00  301.00  311.00
!-----
! Data for PHASE number:  2 ==> Current R_Bragg for Pattern# 1:  0.00
!-----
Ferromagnetic structure of powdered single-crystalline La7/8Sr1/8MnO3 at 5 K
!
!Nat Dis Mom Pr1 Pr2 Pr3 Jbt Irf Isy Str Furth      ATZ      Nvk Npr More
  4  0  0  1.0 1.0 1.0  1  0 -1  0  0      0.000    0  5  0
!
P 1 21/C 1          <--Space group symbol
!Nsym Cen Laue MagMat
  1  1  2  1
!
SYMM x, y, z
MSYM u, v, w, 0.000
!
!Atom Typ  Mag Vek  X      Y      Z      Biso  Occ      Rx      Ry      Rz
! Ix      Iy      Iz      beta11 beta22 beta33  MagPh
Mn1  MMN3  1  0  0.00000 0.00000 0.50000 0.33771 1.00000  0.000  3.428  -0.017
          0.00    0.00    0.00    191.00    0.00    0.00  321.00  331.00
          0.000  0.000  0.000  0.000  0.000  0.000  0.000
          0.00    0.00    0.00    0.00    0.00    0.00
Mn2  MMN3  1  0  0.00000 0.50000 0.00000 0.33771 1.00000  0.000  3.428  -0.017
          0.00    0.00    0.00    191.00    0.00    0.00  321.00  331.00
          0.000  0.000  0.000  0.000  0.000  0.000  0.000
          0.00    0.00    0.00    0.00    0.00    0.00

```

```

Mn3 MMN3 1 0 0.50000 0.00000 0.50000 0.33771 1.00000 0.000 3.428 -0.017
      0.00 0.00 0.00 191.00 0.00 0.00 321.00 331.00
      0.000 0.000 0.000 0.000 0.000 0.000 0.000
      0.00 0.00 0.00 0.00 0.00 0.00 0.00
Mn4 MMN3 1 0 0.50000 0.50000 0.00000 0.33771 1.00000 0.000 3.428 -0.017
      0.00 0.00 0.00 191.00 0.00 0.00 321.00 331.00
      0.000 0.000 0.000 0.000 0.000 0.000 0.000
      0.00 0.00 0.00 0.00 0.00 0.00 0.00
!-----> Profile Parameters for Pattern # 1
! Scale      Shape1      Bov      Str1      Str2      Str3      Strain-Model
  1.6528      0.04889      0.00000  0.00000  0.00000  0.00000  0
  11.00000    241.000     0.000   0.000   0.000   0.000
! U          V          W          X          Y          GauSiz   LorSiz Size-Model
  0.126511 -0.104837  0.115123  0.004581  0.000000  0.000000  0.000000  0
  261.000   251.000   231.000   271.000   0.000     0.000     0.000
! a          b          c          alpha     beta      gamma    #Cell Info
  7.786890  5.532544  5.516849  90.000000 90.026382 90.000000
  31.00000  41.00000  51.00000  0.00000   61.00000  0.00000
! Pref1     Pref2     Asy1     Asy2     Asy3     Asy4
  0.00000  0.00000  0.49040  0.09271 -0.68207 -0.09821
  0.00     0.00     281.00  291.00  301.00  311.00
!-----
! Data for PHASE number: 3 ==> Current R_Bragg for Pattern# 1: 0.00
!-----
Antiferromagnetic structure of powdered single-crystalline La7/8Sr1/8MnO3 at 5 K
!
!Nat Dis Mom Pr1 Pr2 Pr3 Jbt Irf Isy Str Furth      ATZ      Nvk Npr More
  4 0 0 1.0 1.0 1.0 1 0 -1 0 0      0.000  0 5 0
!
P -1                      <--Space group symbol
!Nsym Cen Laue MagMat
  1 1 1 1
!
SYMM x, y, z
MSYM u, v, w, 0.000
!
!Atom Typ  Mag Vek  X      Y      Z      Biso  Occ      Rx      Ry      Rz
!  Ix      Iy      Iz      beta11 beta22 beta33  MagPh
Mn1 MMN3 1 0 0.00000 0.00000 0.50000 0.33771 1.000 0.000 -0.537 0.000
      0.00 0.00 0.00 191.00 0.00 0.00 341.00 0.00
      0.000 0.000 0.000 0.000 0.000 0.000 0.000
      0.00 0.00 0.00 0.00 0.00 0.00 0.00
Mn2 MMN3 1 0 0.00000 0.50000 0.00000 0.33771 1.000 0.000 -0.537 0.000
      0.00 0.00 0.00 191.00 0.00 0.00 341.00 0.00
      0.000 0.000 0.000 0.000 0.000 0.000 0.000
      0.00 0.00 0.00 0.00 0.00 0.00 0.00
Mn3 MMN3 1 0 0.50000 0.00000 0.50000 0.33771 1.000 0.000 0.537 0.000
      0.00 0.00 0.00 191.00 0.00 0.00 -341.00 0.0
      0.000 0.000 0.000 0.000 0.000 0.000 0.000
      0.00 0.00 0.00 0.00 0.00 0.00 0.00
Mn4 MMN3 1 0 0.50000 0.50000 0.00000 0.33771 1.000 0.000 0.537 0.000
      0.00 0.00 0.00 191.00 0.00 0.00 -341.00 0.00

```

```

0.000 0.000 0.000 0.000 0.000 0.000 0.000
0.00 0.00 0.00 0.00 0.00 0.00 0.00
!-----> Profile Parameters for Pattern # 1
! Scale      Shape1      Bov      Str1      Str2      Str3      Strain-Model
1.6528      0.04889    0.00000  0.00000  0.00000  0.00000    0
11.00000   241.000    0.000    0.000    0.000    0.000
! U          V          W          X          Y          GauSiz    LorSiz Size-Model
0.126511   -0.104837  0.115123  0.004581  0.000000  0.000000  0.000000  0
261.000    251.000    231.000    271.000    0.000      0.000      0.000
! a          b          c          alpha      beta       gamma      #Cell Info
7.786890   5.532544   5.516849  90.000000  90.026382  90.000000
31.00000   41.00000   51.00000  0.00000    61.0000    0.00000
! Pref1     Pref2     Asy1      Asy2      Asy3      Asy4
0.00000   0.00000   0.49040  0.09271  -0.68207  -0.09821
0.00      0.00      281.00   291.00   301.00   311.00

```

C Transformation of the orthorhombic *Pbnm* and *Pnma* symmetries

Space-group No: 62		Setting: 1		Space group: <i>Pnma</i>	
a (Å)	b (Å)	c (Å)	α (°)	β (°)	γ (°)
a ₀	b ₀	c ₀	90	90	90
Ion	Z	Wyck	x	y	z
La	57	4c	x ₀	0.25	z ₀
Sr	38	4c	x ₀	0.25	z ₀
Mn	25	4b	0.00	0.00	0.50
O1	8	4c	x ₁	0.25	z ₁
O2	8	8d	x ₂	y ₂	z ₂

Space-group No: 62		Setting: 3		Space group: <i>Pbnm</i>	
a (Å)	b (Å)	c (Å)	α (°)	β (°)	γ (°)
c ₀	a ₀	b ₀	90	90	90
Ion	Z	Wyck	x	y	z
La	57	4c	z ₀	x ₀	0.25
Sr	38	4c	z ₀	x ₀	0.25
Mn	25	4b	0.50	0.00	0.00
O1	8	4c	z ₁	x ₁	0.25
O2	8	8d	z ₂	x ₂	y ₂

Bibliography

- [1] H. Kawano, R. Kajimoto, M. Kubota, and H. Yoshizawa, Phys. Rev. B **53**, R14709 (1996).
- [2] H. Kawano, R. Kajimoto, M. Kubota, and H. Yoshizawa, Phys. Rev. B **53**, 2202 (1996).
- [3] D. N. Argyriou, J. F. Mitchell, C. D. Potter, D. G. Hinks, J. D. Jorgensen, and S. D. Bader, Phys. Rev. Lett. **76**, 3826 (1996).
- [4] J. H. Jung, K. H. Kim, H. J. Lee, J. S. Ahn, N. J. Hur, T. W. Noh, M. S. Kim, and J.-G. Park, Phys. Rev. B **59**, 3793 (1999).
- [5] M. Paraskevopoulos, F. Mayr, C. Hartinger, A. Pimenov, J. Hemberger, P. Lunkenheimer, A. Loidl, A. A. Mukhin, V. Yu. Ivanov, and A. M. Balbashov, J. Magn. Mater. **211**, 118 (2000).
- [6] G.-L. Liu, J.-S. Zhou, and J. B. Goodenough, Phys. Rev. B **64**, 144414 (2001).
- [7] J. Hemberger, A. Krimmel, T. Kurz, H.-A. Krug von Nidda, V. Yu. Ivanov, A. A. Mukhin, A. M. Balbashov, and A. Loidl, Phys. Rev. B **66**, 094410 (2002).
- [8] Anulekha Dutta, N. Gayathri, and R. Ranganathan, Phys. Rev. B **68**, 054432 (2003).
- [9] J. Geck, P. Wochner, S. Kiele, R. Klingeler, A. Revcolevschi, M. v. Zimmermann, B. Büchner, and P. Reutler, New J. Phys. **6**, 152 (2004).
- [10] H. F. Li, Y. Su, J. Persson, P. Meuffels, J. M. Walter, R. Skowronek, and Th. Brückel, J. Phys.: Condens. Matter **19**, 016003 (2007).
- [11] H. F. Li, Y. Su, J. Persson, P. Meuffels, J. M. Walter, R. Skowronek, and Th. Brückel, J. Phys.: Condens. Matter **19**, 176226 (2007).
- [12] J. Orenstein and A. J. Millis, Science **288**, 468 (2000).
- [13] W. Prellier, M. P. Singh, and P. Murugavel, J. Phys.: Condens. Matter **17**, R803 (2005).
- [14] Thomas Brückel, in *Atomic and Magnetic Structures in Crystalline Materials: Neutron and X-ray Scattering*, Vol. **34** of *Matter and Materials*, edited by K. Urban, C. M. Schneider, Th. Brückel, S. Blügel, K. Tillmann, W. Schweika, M. Lentzen, and L. Baumgarten (Eds.) (Schriften des Forschungszentrum Jülich, Germany, 2007).

- [15] M. Imada, A. Fujimori, and Y. Tokura, *Rev. Mod. Phys.* **70**, 1039 (1998).
- [16] A. Daoud-Aladine, J. Rodríguez-Carvajal, L. Pinsard-Gaudart, M. T. Fernández-Díaz, and A. Revcolevschi, *Phys. Rev. Lett.* **89**, 097205 (2002).
- [17] C. T. Chen, F. Sette, Y. Ma, M. S. Hybertsen, E. B. Stechel, W. M. C. Foulkes, M. Schuller, S-W. Cheong, A. S. Cooper, L. W. Rupp, Jr., B. Batlogg, Y. L. Soo, Z. H. Ming, A. Krol, and Y. H. Kao, *Phys. Rev. Lett.* **66**, 104 (1991).
- [18] M. Abbate, F. M. F. de Groot, J. C. Fuggle, A. Fujimori, O. Strelbel, F. Lopez, M. Domke, G. Kaindl, G. A. Sawatzky, M. Takano, Y. Takeda, H. Eisaki, and S. Uchida, *Phys. Rev. B* **46**, 4511 (1992).
- [19] V. Ferrari, M. Towler, and P. B. Littlewood, *Phys. Rev. Lett.* **91**, 227202 (2003).
- [20] P. Abbamonte, G. Blumberg, A. Rusydi, A. Gozar, P. G. Evans, T. Siegrist, L. Venema, H. Eisaki, E. D. Isaacs, and G. A. Sawatzky, *Nature* **431**, 1078 (2004).
- [21] C. Schüßler-Langeheine, J. Schlappa, A. Tanaka, Z. Hu, C. F. Chang, E. Schierle, M. Benomar, H. Ott, E. Weschke, G. Kaindl, O. Friedt, G. A. Sawatzky, H.-J. Lin, C. T. Chen, M. Braden, and L. H. Tjeng, *Phys. Rev. Lett.* **95**, 156402 (2005).
- [22] A. P. Ramirez, *J. Phys.: Condens. Matter* **9**, 8171 (1997).
- [23] C. N. R. Rao and B. Raveau, *Colossal Magnetoresistance, Charge Ordering, and related Properties of Manganese Oxides* (World Scientific, Singapore, 1998).
- [24] T. A. Kaplan and S. D. Mahanti, *Physics of Manganites* (Kluwer Academic/Plenum Publishers, New York, 1999).
- [25] J. M. D. Coey, M. Viret, and S. von Molnár, *Adv. Phys.* **48**, 167 (1999).
- [26] Y. Tokura, *Contribution to Colossal Magnetoresistance Oxides* (Gordon & Breach, Monographs in Condensed Matter Science, London, 1999).
- [27] Y. Tokura and Y. Tomioka, *J. Magn. Magn. Mater.* **200**, 1 (1999).
- [28] Y. Tokura, *Colossal Magnetoresistance Oxides* (Gordon & Breach, London, 1999).
- [29] Y. Okimoto and Y. Tokura, *J. Supercond.* **13**, 271 (2000).
- [30] S. L. Cooper, in *Optical Spectroscopic Studies of Metal-Insulator Transitions in Perovskite-Related Oxides*, Vol. **98** of *Structure and Bonding* (Springer-Verlag, Berlin, 2001).
- [31] E. Dagotto, T. Hotta, and A. Moreo, *Phys. Rep.* **344**, 1 (2001).
- [32] T. Chatterji, *Colossal Magnetoresistive Manganites* (Kluwer Academic Publishers,

- Dordrecht, Boston, London, 2004).
- [33] R. Simon and A. Smith, *Superconductor: Conquering Technology's New Frontier* (Plenum, New York, 1988).
- [34] J. G. Bednorz and K. A. Müller, *Z. Phys. B* **64**, 189 (1986).
- [35] L. Gao, Y. Y. Xue, F. Chen, Q. Xiong, R. L. Meng, D. Ramirez, C. W. Chu, J. H. Eggert, and H. K. Mao, *Phys. Rev. B* **50**, 4260 (1994).
- [36] Workshop on Basic Research Needs for Superconductivity, Washington, DC, May 8-11, 2006.
- [37] S. Tanaka, *Jpn. J. Appl. Phys.* **45**, 9011 (2006).
- [38] A. Urushibara, Y. Moritomo, T. Arima, A. Asamitsu, G. Kido, and Y. Tokura, *Phys. Rev. B* **51**, 14103 (1995).
- [39] J. Volger, *Physica (Amsterdam)* **20**, 49 (1954).
- [40] S. Jin, T. H. Tiefel, M. McCormack, R. A. Fastnacht, R. Ramesh, and L. H. Chen, *Science* **264**, 413 (1994).
- [41] C. Zener, *Phys. Rev.* **82**, 403 (1951).
- [42] P. W. Anderson and H. Hasegawa, *Phys. Rev.* **100**, 675 (1955).
- [43] P.-G. de Gennes, *Phys. Rev.* **118**, 141 (1960).
- [44] N. A. Spaldin and M. Fiebig, *Science* **309**, 391 (2005).
- [45] H. Schmid, *Ferroelectrics* **162**, 317 (1994).
- [46] C. N. Berglund and H. J. Guggenheim, *Phys. Rev.* **185**, 1022 (1969).
- [47] J. B. Clark, J. W. Hastie, L. H. E. Kihlberg, R. Metselaar, and M. M. Thackeray, *Pure Appl. Chem.* **66**, 577 (1974).
- [48] F. J. Morin, *Phys. Rev. Lett.* **3**, 34 (1959).
- [49] P. Schilbe, *Physica B* **316-317**, 600 (2002).
- [50] G. Andersson, *Acta. Chem. Scand.* **10**, 623 (1956).
- [51] A. Husmann, X. Yao, D. S. Jin, Y. V. Zastavker, T. F. Rosenbaum, and J. M. Honig, *Science* **274**, 1874 (1996).
- [52] M. Imada, A. Fujimori and Y. Tokura, *Rev. Mod. Phys.* **70**, 1039 (1998).

- [53] E. Abrahams and G. Kotliar, *Science* **274**, 1853 (1996).
- [54] R. V. Demin, L. I. Koroleva, A. Z. Muminov, and Ya. M. Mukovskii, *Phys. Solid State* **48**, 322 (2006).
- [55] M. R. Ibarra, P. A. Algarabel, C. Marquina, J. Blasco, and J. García, *Phys. Rev. Lett.* **75**, 3541 (1995).
- [56] A. I. Abramovich and A. V. Michurin, *Low Temp. Phys.* **27**, 278 (2001).
- [57] R. Demin, L. Koroleva, R. Szymczak, and H. Szymczak, *Phys. Lett. A* **296**, 139 (2002).
- [58] A. M. Kadomtseva, Yu. F. Popov, G. P. Vorob'ev, K. I. Kamilov, V. Yu. Ivanov, A. A. Mukhin, and A. M. Balbashov, *Phys. Solid State* **42**, 1110 (2000).
- [59] J. Hubbard, *Proc. R. Soc. A* **276**, 238 (1963); *ibid.* **277**, 237 (1964).
- [60] Martin C. Gutzwiller, *Phys. Rev. Lett.* **10**, 159 (1963).
- [61] F. H. L. Essler, H. Frahm, F. Göhmann, A. Klümper, and V. E. Korepin, *The One-Dimensional Hubbard Model* (Cambridge University Press, United Kingdom, 2005).
- [62] E. H. Lieb, F. Y. Wu, *Physica A* **321**, 1 (2003).
- [63] V. M. Goldschmidt, *Naturwissenschaften* **14**, 477 (1926).
- [64] L. D. Landau and E. M. Lifshitz, *Quantum Physics* (Pergamon Press, New York, 1965).
- [65] A. J. Millis, P. B. Littlewood, and B. I. Shraiman, *Phys. Rev. Lett.* **74**, 5144 (1995).
- [66] H. Röder, Jun Zang, and A. R. Bishop, *Phys. Rev. Lett.* **76**, 1356 (1996).
- [67] M. Gerloch and R. C. Slade, *Ligand-Field Parameters* (Cambridge, London, 1973).
- [68] K. Yoshida, *Theory of Magnetism* (Springer-Verlag, Berlin, 1996).
- [69] M. Quijada, J. Černe, J. R. Simpson, H. D. Drew, K. H. Ahn, A. J. Millis, R. Shreekala, R. Ramesh, M. Rajeswari, and T. Venkatesan, *Phys. Rev. B* **58**, 16093 (1998).
- [70] Y. Okimoto, T. Katsufuji, T. Ishikawa, A. Urushibara, T. Arima, and Y. Tokura, *Phys. Rev. Lett.* **75**, 109 (1995).
- [71] Y. Tokura and N. Nagaosa, *Science* **288**, 462 (2000).
- [72] J. B. Goodenough, *Magnetism and Chemical Bond* (Interscience Publisher, New York, London, 1963).
- [73] K. I. Kugel and D. I. Khomskii, *Sov. Phys. Usp.* **25**, 231 (1982).

- [74] H. A. Jahn and E. Teller, Proc. R. Soc. A **161**, 220 (1937).
- [75] G. A. Gehring and K. A. Gehring, Rep. Prog. Phys. **38**, 1 (1975).
- [76] Y. Su, in *Ordering phenomena in CTMO*, Vol. **26** of *Matter and Materials*, edited by S. Blügel, Th. Brückel, and C. M. Schneider (Eds.) (Schriften des Forschungszentrum Jülich, Germany, 2005).
- [77] J. B. Goodenough, Phys. Rev. **100**, 564 (1955).
- [78] J. Kanamori, Prog. Theor. Phys. **30**, 275 (1963).
- [79] P. W. Anderson, Phys. Rev. **115**, 2 (1959).
- [80] D. N. Argyriou and C. D. Ling, *Crystal and Magnetic Structure from Hole to Electron Doped Manganites*, in *Colossal Magnetoresistive Manganites*, edited by T. Chatterji (Kluwer Academic Publishers, Dordrecht, Boston, London, 2004).
- [81] J. W. Verwey, Nature **144**, 327 (1939).
- [82] X. H. Zhang, Z. Q. Li, W. Song, X. W. Du, P. Wu, H. L. Bai, and E. Y. Jiang, Solid State Commun. **135**, 356 (2005).
- [83] J. A. Alonso, M. J. Martínez-Lope, M. T. Casais, J. L. García-Muñoz, and M. T. Fernández-Díaz, Phys. Rev. B **61**, 1756 (2000).
- [84] H. Sawa, E. Ninomiya, T. Ohama, H. Nakao, K. Ohwada, Y. Murakami, Y. Fujii, Y. Noda, M. Isobe, and Y. Ueda, J. Phys. Soc. Jpn. **71**, 385 (2002).
- [85] E. Ninomiya, Ph. D. thesis, Chiba University (Japan), 2003.
- [86] K. Ohwada, Y. Fujii, Y. Katsuki, J. Muraoka, H. Nakao, Y. Murakami, H. Sawa, E. Ninomiya, M. Isobe, and Y. Ueda, Phys. Rev. Lett. **94**, 106401 (2005).
- [87] J. H. Martín, J. García, G. Subías, J. Blasco, and M. C. Sánchez, Phys. Rev. B **70**, 024408 (2004).
- [88] M. L. Medarde, J. Phys.: Condens. Matter **9**, 1679 (1997).
- [89] J. E. Lorenzo, J. L. Hodeau, L. Paolasini, S. Lefloch, J. A. Alonso, and G. Demazeau, Phys. Rev. B **71**, 045128 (2005).
- [90] J. B. Torrance, P. Lacorre, A. I. Nazzari, E. J. Ansaldo, and Ch. Niedermayer, Phys. Rev. B **45**, 8209 (1992).
- [91] T. Mizokawa, D. I. Khomskii, and G. A. Sawatzky, Phys. Rev. B **61**, 11263 (2000).
- [92] U. Staub, G. I. Meijer, F. Fauth, R. Allenspach, J. G. Bednorz, J. Karpinski, S. M.

- Kazakov, L. Paolasini, and F. d'Acapito, *Phys. Rev. Lett.* **88**, 126402 (2002).
- [93] M. V. Mostovoy and D. I. Khomskii, *Phys. Rev. Lett.* **92**, 167201 (2004).
- [94] H. Kuwahara, Y. Tomioka, A. Asamitsu, Y. Moritomo, and Y. Tokura, *Science* **270**, 961 (1995).
- [95] Y. Moritomo, H. Kuwahara, Y. Tomioka, and Y. Tokura, *Phys. Rev. B* **55**, 7549 (1997).
- [96] V. Kiryukhin, D. Casa, J. P. Hill, B. Keimer, A. Vigliante, Y. Tomioka, and Y. Tokura, *Nature* **386**, 813 (1997).
- [97] J. F. Mitchell, D. N. Argyriou, and J. D. Jorgensen, *Structural Response to Orbital, Spin, and Charge Ordering in Colossal Magnetoresistive Materials*, in *Colossal Magnetoresistive Oxides*, edited by Y. Tokura (Gordon and Breach Science Publishers, Australia, Canada, France, Germany, India, Japan, Luxembourg, Malaysia, The Netherlands, Russia, Singapore, Switzerland, 2000).
- [98] I. D. Brown and D. Altermatt, *Acta Cryst.* **B41**, 244 (1985).
- [99] I. D. Brown, *J. Appl. Cryst.* **29**, 479 (1996).
- [100] M. Zaghrioui, A. Bulou, P. Lacorre, and P. Laffez, *Phys. Rev. B* **64**, 081102(R) (2001).
- [101] S. Grenier, J. P. Hill, Doon Gibbs, K. J. Thomas, M. v. Zimmermann, C. S. Nelson, V. Kiryukhin, Y. Tokura, Y. Tomioka, D. Casa, T. Gog, and C. Venkataraman, *Phys. Rev. B* **69**, 134419 (2004).
- [102] G. Zheng and C. H. Patterson, *Phys. Rev. B* **67**, 220404(R) (2003).
- [103] M. Coey, *Nature* **430**, 155 (2004).
- [104] S. Margadonna and G. Karotsis, *J. Am. Chem. Soc.*, **128** (51), 16436 (2006).
- [105] <http://www.fkf.mpg.de/keimer/>.
- [106] M. W. Lufaso and P. M. Woodward, *Acta Cryst.* **B60**, 10 (2004).
- [107] M. v. Zimmermann, J. P. Hill, Doon Gibbs, M. Blume, D. Casa, B. Keimer, Y. Murakami, Y. Tomioka, and Y. Tokura, *Phys. Rev. Lett.* **83**, 4872 (1999).
- [108] G. R. Blake, T. T. M. Palstra, Y. Ren, A. A. Nugroho, and A. A. Menovsky, *Phys. Rev. B* **65**, 174112 (2002).
- [109] R. Kajimoto, H. Yoshizawa, H. Kawano, H. Kuwahara, Y. Tokura, K. Ohoyama, and M. Ohashi, *Phys. Rev. B* **60**, 9506 (1999).
- [110] V. B. Shenoy, D. D. Sarma, and C. N. R. Rao, *Chem. Phys. Chem.* **7**, 2053 (2006).

- [111] P. M. Woodward, D. E. Cox, T. Vogt, C. N. R. Rao, and A. K. Cheetham, *Chem. Mater.* **11**, 3528 (1999).
- [112] C. Ritter, R. Mahendiran, M. R. Ibarra, L. Morellon, A. Maignan, B. Raveau, C. N. R. Rao, *Phys. Rev. B* **61**, R9229 (2000).
- [113] L. Sudheendra, C. N. R. Rao, *J. Phys.: Condens. Matter* **15**, 3029 (2003).
- [114] J. Als-Nielsen and D. McMorrow, *Elements of modern X-ray physics* (John Wiley & Sons, New York, 2001).
- [115] B. L. Henke, E. M. Gullikson and J. C. Davis, "X-ray interactions: photoabsorption, scattering, transmission, and reflection at $E = 50\text{-}30000$ eV, $Z = 1\text{-}92$ ", *Atomic Data and Nuclear Data Tables* **54**, 181-342 (1993). (http://www-cxro.lbl.gov/optical_constants/)
- [116] J. Stempfer, Th. Brückel, G. J. McIntyre, F. Tasset, Th. Zeiske, K. Burger, and W. Prandl, *Physica B* **267-268**, 56 (1999).
- [117] J. Stempfer, Th. Brückel, W. Caliebe, A. Vernes, H. Ebert, W. Prandl, and J. R. Schneider, *Eur. Phys. J. B* **14**, 63 (2000).
- [118] V. K. Pecharsky and P. Y. Zavalij, *Fundamentals of Powder Diffraction and Structural Characterization of Materials* (Springer Science+Business Media, United states of America, 2005).
- [119] Gernot Heger, in *Structure determination*, Vol. **5** of *Matter and Materials*, edited by Thomas Brückel, Gernot Heger and Dieter Richter (Eds.) (Schriften des Forschungszentrum Jülich, Germany, 2000).
- [120] R. A. Young, *The Rietveld Method* (Oxford University Press, United States, 1993).
- [121] IUCr: <http://www.iucr.org>; CCP-14: <http://www.ccp14.ac.uk>.
- [122] David T. Attwood, *Soft X-Rays and Extreme Ultraviolet Radiation: Principles and Applications* (Cambridge University Press, New York, 1999).
- [123] Yixi Su, in *Charge and Orbital Ordering: Resonant X-ray scattering*, Vol. **34** of *Matter and Materials*, edited by K. Urban, C. M. Schneider, Th. Brückel, S. Blügel, K. Tillmann, W. Schweika, M. Lentzen, and L. Baumgarten (Eds.) (Schriften des Forschungszentrum Jülich, Germany, 2007).
- [124] R. M. Taylor and K. Norrish, *Clay Minerals* **6**, 127 (1966).
- [125] D. L. Bish and R. C. Reynolds, in *Sample preparation for X-ray diffraction*, Vol. **20** of *Modern Powder Diffraction*, edited by D. L. Bish and J. E. Post (Washington, 1989).
- [126] http://www.bruker-axs.com/d8_advance.html.

- [127] W. Schäfer, E. Jansen, R. Skowronek, and A. Kirfel, *Physica B* **234-236**, 1146 (1997).
- [128] <http://www.frm2.tum.de/en/index.html>.
- [129] R. Gilles, B. Krimmer, H. Boysen, and H. Fuess, *Appl. Phys. A* **74** [Suppl.], S148 (2002).
- [130] M. R. Weiss, R. Follath, K. J. S. Sawhney, F. Senf, J. Bahrtdt, W. Frentrup, A. Gaupp, S. Sasaki, M. Scheer, H.-C. Mertins, D. Abramssohn, F. Schäfers, W. Kuch, and W. Mahler, *Nucl. Instr. and Meth. A* **467-468**, 449 (2001).
- [131] J. Grabis, Ph.D. thesis, Ruhr-Universität Bochum (Germany), 2005.
- [132] J. Grabis, A. Nefedov, and H. Zabel, *Rev. Sci. Instr.* **74**, 4048 (2003).
- [133] U. Schubert and N. Hüsing, *Synthesis of inorganic materials* (Wiley-VCH, Germany, 2005).
- [134] R. Valenzuela, *Magnetic ceramics* (Cambridge University Press, New York, 1994).
- [135] K. Nakamura, *J. Solid State Chem.* **173**, 299 (2003).
- [136] M. Wolcyrz, R. Horyń, F. Bourée, and E. Bukowska, *J. Alloys Compd.* **353**, 170 (2003).
- [137] D. Cannell and P. Trigg, in *Processing of electronic ceramics*, Vol. **1** of *Advanced ceramic processing and technology*, edited by Jon G. P. Binner (Noyes Publications, U.S.A., 1990).
- [138] J. Rivas, L. E. Hueso, A. Fondado, F. Rivadulla, and M. A. López-Quintela, *J. Magn. Magn. Mater.* **221**, 57 (2000).
- [139] P. N. Lisboa-Filho, A. W. Mombrú, H. Pardo, E. R. Leite, and W. A. Ortiz, *Solid State Commun.* **130**, 31 (2004).
- [140] J. F. Mitchell, C. D. Ling, J. E. Millburn, D. N. Argyriou, A. Berger, and M. Medarde, *J. Appl. Phys.* **89**, 6618 (2001).
- [141] B. A. Smith and I. G. Austin, *J. Crystal Growth* **1**, 79 (1967).
- [142] D. Shulyatev, S. Karabashev, A. Arsenov, and Ya. Mukovskii, *J. Crystal Growth* **198/199**, 511 (1999).
- [143] D. Prabhakaran, A. I. Coldea, A. T. Boothroyd, and S. J. Blundell, *J. Crystal Growth* **237-239**, 806 (2002).
- [144] H. J. Scheel, *J. Crystal Growth* **211**, 1 (2000).
- [145] K. A. Jackson, *J. Crystal Growth* **198/199**, 1 (1999).

- [146] M. Velázquez, C. Haut, B. Hennion, and A. Revcolevschi, *J. Crystal Growth* **220**, 480 (2000).
- [147] <http://neutrons.phy.bnl.gov/crystal.shtm>.
- [148] Y. A. Tatarchenko, *Shaped crystal growth* (Kluwer, Dordrecht, Boston, London, 1993).
- [149] J. S. Shah, in *Zone refining and its applications*, Vol. **16** of *Crystal growth*, edited by B. R. Pamplin (Pergamon Press, Oxford, New York, Toronto, Sydney, Paris, Frankfurt, 1980).
- [150] D. B. Gadkari, P. Shashidharan, K. B. Lal, and B. M. Arora, *Bull. Mater. Sci.* **24**, 475 (2001).
- [151] Ch. Kloc, S.-W. Cheong, and P. Matl, *J. Crystal Growth* **191**, 294 (1998).
- [152] C. T. Lin, A. Maljuk, and B. Liang, *Supercond. Sci. Technol.* **15**, 1736 (2002).
- [153] http://www.fz-juelich.de/iff/e_ism_recent/.
- [154] Y. Su, K. Istomin, D. Wermeille, A. Fattah, P. Foucart, P. Meuffels, D. Hupfeld, and Th. Brückel, *J. Magn. Magn. Mater.* **272-276**, e291 (2004).
- [155] Y. Yamada, J. Suzuki, K. Oikawa, S. Katano, and J. A. Fernandez-Baca, *Phys. Rev. B* **62**, 11600 (2000).
- [156] Y. Yamada, O. Hino, S. Nohdo, R. Kanao, T. Inami, and S. Katano, *Phys. Rev. Lett.* **77**, 904 (1996).
- [157] L. Pinsard, J. Rodríguez-Carvajal, A. H. Moudden, A. Anane, A. Revcolevschi, and C. Dupas, *Physica B* **234-236**, 856 (1997).
- [158] X. Xiong, B. Dabrowski, O. Chmaissem, Z. Bukowski, S. Kolesnik, R. Dybziński, C. W. Kimball, and J. D. Jorgensen, *Phys. Rev. B* **60**, 10186 (1999).
- [159] J. Rodríguez-Carvajal, M. Hennion, F. Moussa, A. H. Moudden, L. Pinsard, and A. Revcolevschi, *Phys. Rev. B* **57**, R3189 (1998).
- [160] T. Chatterji, B. Ouladdiaf, P. Mandal, B. Bandyopadhyay, and B. Ghosh, *Phys. Rev. B* **66**, 054403 (2002).
- [161] A. Asamitsu, Y. Moritomo, Y. Tomioka, T. Arima, and Y. Tokura, *Nature* **373**, 407 (1995).
- [162] T. Ersez, *Materials Letters* **54**, 211 (2002).
- [163] Y. Endoh, K. Hirota, S. Ishihara, S. Okamoto, Y. Murakami, A. Nishizawa, T. Fukuda, H. Kimura, H. Nojiri, K. Kaneko, and S. Maekawa, *Phys. Rev. Lett.* **82**, 4328 (1999).

- [164] J. Rodríguez-Carvajal, *Physica B* **192**, 55 (1993).
- [165] J. F. Mitchell, D. N. Argyriou, C. D. Potter, D. G. Hinks, J. D. Jorgensen, and S. D. Bader, *Phys. Rev. B* **54**, 6172 (1996).
- [166] M. Medarde, J. Mesot, P. Lacorre, S. Rosenkranz, P. Fischer, and K. Gobrecht, *Phys. Rev. B* **52**, 9248 (1995).
- [167] S. Xu, Y. Moritomo, K. Ohoyama, and A. Nakamura, *J. Phys. Soc. Jpn.* **72**, 709 (2003).
- [168] J. Mizusaki, H. Tagawa, K. Naraya, and T. Sasamoto, *Solid State Ionics* **49**, 111 (1991).
- [169] J. A. M. Van Roosmalen, E. H. P. Cordfunke, R. B. Helmholtz, and H. W. Zandbergen, *J. Solid State Chem.* **110**, 100 (1994).
- [170] L. Malavasi, C. Ritter, M. C. Mozzati, C. Tealdi, M. S. Islam, C. B. Azzoni, and G. Flor, *J. Solid State Chem.* **178**, 2042 (2005).
- [171] M. Itoh, K. Nishi, J. D. Yu, and Y. Inaguma, *Phys. Rev. B* **55**, 14408 (1997).
- [172] D. E. Cox, T. Iglesias, E. Moshopoulou, K. Hirota, K. Takahashi, and Y. Endoh, *Phys. Rev. B* **64**, 024431 (2001).
- [173] J. Geck, P. Wochner, D. Bruns, B. Büchner, U. Gebhardt, S. Kiele, P. Reutler, and A. Revcolevschi, *Phys. Rev. B* **69**, 104413 (2004).
- [174] B. Dabrowski, X. Xiong, Z. Bukowski, R. Dybziński, P. W. Klamut, J. E. Siewenie, O. Chmaissem, J. Shaffer, C. W. Kimball, J. D. Jorgensen, and S. Short, *Phys. Rev. B* **60**, 7006 (1999).
- [175] T. Maitra, P. Thalmeier, and T. Chatterji, *Phys. Rev. B* **69**, 132417 (2004).
- [176] L. Pinsard, J. Rodríguez-Carvajal, and A. Revcolevschi, *J. Alloys Compd.* **262-263**, 152 (1997).
- [177] J. B. Goodenough, A. Wold, R. J. Arnett, and N. Menyuk, *Phys. Rev.* **124**, 373 (1961).
- [178] G. H. Jonker and J. H. van Santen, *Physica* **16**, 337 (1950).
- [179] M. Korotin, T. Fujiwara, and V. Anisimov, *Phys. Rev. B* **62**, 5696 (2000).
- [180] G. Papavassiliou, M. Pissas, G. Diamantopoulos, M. Belesi, M. Fardis, D. Stamopoulos, A. G. Kontos, M. Hennion, J. Dolinsek, J.-Ph. Ansermet, and C. Dimitropoulos, *Phys. Rev. Lett.* **96**, 097201 (2006).
- [181] K. Tsuda, M. Tanaka, K. Hirota, and Y. Endoh, *J. Phys. Soc. Jpn.* **70**, 1010 (2001).
- [182] M. Pissas, I. Margiolaki, G. Papavassiliou, D. Stamopoulos, and D. Argyriou, *Phys. Rev. B* **72**, 064425 (2005).

- [183] R. Ranjan, A. Agrawal, A. Senyshyn, and H. Boysen, *J. Phys.: Condens. Matter* **18**, L515 (2006).
- [184] <http://abulafia.mt.ic.ac.uk/shannon/ptable.php>.
- [185] J. M. De Teresa, M. R. Ibarra, P. A. Algarabel, C. Ritter, C. Marquina, J. Blasco, J. García, A. del Moral, and Z. Arnold, *Nature* **386**, 256 (1997).
- [186] J. Nogués, Vassil Skumryev, J. S. Muñoz, B. Martínez, J. Fontcuberta, L. Pinsard, and A. Revcolevschi, *Phys. Rev. B* **64**, 024434 (2001).
- [187] R. P. Borges, F. Ott, R. M. Thomas, V. Skumryev, J. M. D. Coey, J. I. Arnaud, and L. Ranno, *Phys. Rev. B* **60**, 12847 (1999).
- [188] S. Uhlenbruck, R. Teipen, R. Klingeler, B. Büchner, O. Friedt, M. Hücker, H. Kierspel, T. Niemöller, L. Pinsard, A. Revcolevschi, and R. Gross, *Phys. Rev. Lett.* **82**, 185 (1999).
- [189] J. P. Wright, J. P. Attfield, and P. G. Radaelli, *Phys. Rev. Lett.* **87**, 266401 (2001).
- [190] S. Ishihara and S. Maekawa, *Rep. Prog. Phys.* **65**, 561 (2002).
- [191] S. B. Wilkins, P. D. Hatton, M. D. Roper, D. Prabhakaran, and A. T. Boothroyd, *Phys. Rev. Lett.* **90**, 187201 (2003).
- [192] S. B. Wilkins, P. D. Spencer, P. D. Hatton, S. P. Collins, M. D. Roper, D. Prabhakaran, and A. T. Boothroyd, *Phys. Rev. Lett.* **91**, 167205 (2003).
- [193] K. J. Thomas, J. P. Hill, S. Grenier, Y.-J. Kim, P. Abbamonte, L. Venema, A. Rusydi, Y. Tomioka, Y. Tokura, D. F. McMorrow, G. Sawatzky, and M. van Veenendaal, *Phys. Rev. Lett.* **92**, 237204 (2004).
- [194] J. H. Martín, J. García, G. Subías, J. Blasco, M. C. Sánchez, and S. Stanescu, *Phys. Rev. B* **73**, 224407 (2006).
- [195] S. B. Wilkins, N. Stojić, T. A. W. Beale, N. Binggeli, C. W. M. Castleton, P. Bencok, D. Prabhakaran, A. T. Boothroyd, P. D. Hatton, and M. Altarelli, *Phys. Rev. B* **71**, 245102 (2005).
- [196] U. Staub, V. Scagnoli, A. M. Mulders, M. Janousch, Z. Honda, and J. M. Tonnerre, *Europhys. Lett.*, **76**, 926 (2006).
- [197] R. Suryanarayanan, G. Dhalenne, A. Revcolevschi, W. Prellier, J.-P. Renard, C. Dupas, W. Caliebe, and T. Chatterji, *Solid State Commun.* **113**, 267 (2000).
- [198] M. Kubota, H. Fujioka, K. Hirota, K. Ohoyama, Y. Moritomo, H. Yoshizawa, and Y. Endoh, *J. Phys. Soc. Jpn.* **69**, 1606 (2000).
- [199] T. Chatterji, G. J. McIntyre, W. Caliebe, R. Suryanarayanan, G. Dhalenne, and A.

- Revcolevschi, Phys. Rev. B **61**, 570 (2000).
- [200] M. Kubota, H. Yoshizawa, Y. Moritomo, H. Fujioka, K. Hirota, and Y. Endoh, J. Phys. Soc. Jpn. **68**, 2202 (1999).
- [201] S. B. Wilkins, P. D. Spencer, T. A. W. Beale, P. D. Hatton, M. v. Zimmermann, S. D. Brown, D. Prabhakaran, and A. T. Boothroyd, Phys. Rev. B **67**, 205110 (2003).
- [202] S. Di. Matteo, T. Chatterji, Y. Joly, A. Stunault, J. A. Paixao, R. Suryanarayanan, G. Dhalle, and A. Revcolevschi, Phys. Rev. B **68**, 024414 (2003).
- [203] S. B. Wilkins, N. Stojić, T. A. W. Beale, N. Binggeli, P. D. Hatton, P. Bencok, S. Stanescu, J. F. Mitchell, P. Abbamonte, and M. Altarelli, J. Phys.: Condens. Matter **18**, L323 (2006).
- [204] T. Kimura, R. Kumai, Y. Tokura, J. Q. Li, and Y. Matsui, Phys. Rev. B **58**, 11081 (1998).
- [205] D. Sébilleau, R. Gunnella, Z-Y. Wu, S. Di. Matteo, and C. R. Natoli, J. Phys.: Condens. Matter **18**, R175 (2006).
- [206] M. v. Zimmermann, C. S. Nelson, Y.-J. Kim, J. P. Hill, Doon Gibbs, H. Nakao, Y. Wakabayashi, Y. Murakami, Y. Tokura, Y. Tomioka, T. Arima, C.-C. Kao, D. Casa, C. Venkataraman, and Th. Gog, Phys. Rev. B **64**, 064411 (2001).
- [207] C. D. Ling, J. E. Millburn, J. F. Mitchell, D. N. Argyriou, J. Linton, and H. N. Bordallo, Phys. Rev. B **62**, 15096 (2000).
- [208] D. N. Argyriou, H. N. Bordallo, B. J. Campbell, A. K. Cheetham, D. E. Cox, J. S. Gardner, K. Hanif, A. dos Santos, G. F. Strouse, Phys. Rev. B **61**, 15269 (2000).
- [209] K. Yamamoto, T. Kimura, T. Ishikawa, T. Katsufuji, and Y. Tokura, Phys. Rev. B **61**, 14706 (2000).

Acknowledgements

First and foremost, I would like to give a million thanks to my supervisor, **Prof. Dr. Thomas Brückel**, for this optimum educational opportunity in an international and nice atmosphere of his group and for his continuous interest and sustained support in my work. He has a high sense of responsibility and unweariedly imparts his wisdom to his students. His insightful and judgematic suggestions on my experiments and manuscripts lie embedded in my mind. His every encouragement makes me gain more confidences. Love will creep where it cannot go. His kindness certainly merits my greatest respect. I am greatly indebted to him more than he knows. The accumulation of these three years is not only the knowledge but also more exact a key to my scientific career.

I would particularly like to thank Dr. Yixi Su, from whom I have learned a lot about the experimental skills, synchrotron radiation x-ray resonant scattering, correlated electrons, etc. It was the greatest opportunity and pleasure for me to share all the beamtimes with him. His skillful technical knowledge and extraordinary experience are astounding. Every beamtime and every discussion with him were valuable and fruitful. His great insight into the science is amazing. His idea was always the key idea to advance my projects. I especially respect his courage of advance despite difficulties. I am grateful to him for everything and hope that we can continue to collaborate in the future.

I really appreciate DP. Jörg Perßon for being a highly motivating and helpful colleague and for growing of the $\text{La}_{0.875}\text{Sr}_{0.125}\text{MnO}_3$, and thank Dr. Volker Kaiser (RWTH, Aachen) for the using of mirror furnace at the Institute for Crystallography, RWTH.

My special thanks go to Dr. Paul Meuffels. All my powder preparation work has been accomplished at his laboratory for the preparation of electroceramic materials. He imparted me a lot of experimental skills with regard to materials preparation. He is a very conscientious laboratory conservator and a selfless man.

I appreciate the efforts of Mr. Schmitz Berthold, DI. Hiller Peter and Mr. Bergs Wolfgang for the development of our new portable UHV goniometer for resonant soft x-ray scattering experiments. Furthermore, I greatly appreciate Mr. Schmitz Berthold for his driving and timely help in BESSY experiments. I admire DI. Hiller Peter for his fine sense of humour. I have received much pleasure to work with them.

Many thanks to Dr. Ulrich Rucker and DI. Hiller Peter for keeping the high performances of our BRUKER AXS D8 ADVANCE system.

I am grateful to Dr. Alexei Nefedov, Dr. Florin Radu and Mr. Numan Akdogan from the Bochum University, Germany, for their skillful technical assistance with the soft x-ray scattering measurements on the ALICE chamber.

It is a pleasure to acknowledge Mr. Rolf Skowronek and Dr. Jens M. Walter for the warmhearted help in the neutron powder diffraction measurements on the powder diffractometer SV7-a at the FRJ-2 research reactor in Jülich, Germany. I would like to thank Dr. Markus Hölzel and Dr. Anatoliy Senyshyn for the kindly assistance in the neutron powder diffraction measurements on the SPODI diffractometer at the Forschungsneutronenquelle Heinz Maier-Leibnitz (FRM II) research reactor in Garching, Germany.

I would like to thank Dr. Tapan Chatterji for his sample support of $\text{La}_1\text{Sr}_2\text{Mn}_2\text{O}_7$.

I would like to thank BESSY technical and scientific staffs for providing excellent conditions of the storage ring and the corresponding beamline. The work at BESSY was supported in part by the BMBF under contract No O3ZA6BC2.

I would like to thank Dr. Heiko Braak for his kindly help in SQUID measurements and Dipl. Ing. Friedrich Jochen for the TGA measurements. I acknowledge ZCH (Central Division of Analytical Chemistry) of Research Center Jülich GmbH, Germany, for the composition measurement.

I would like to thank the other three examiners Prof. Dr. Gernot Heger, Prof. Dr. Matthias Wuttig and Prof. Dr. Stefan Blügel.

I wish to convey my gratitude to all my colleagues for being so cooperative. The group of scattering methods of Prof. Dr. Thomas Brückel at Forschungszentrum Jülich GmbH employs the enthusiastic staff with a high work efficiency motivated by the aspiring team spirit in an international atmosphere.

Special thanks to my wife, Songrui Hou, my parents and parents-in-law are beyond words. Without their remarkable patience, inexhaustible support and considerable encouragement, this thesis would not have been finished. I owe them a lot. All my promises will be definitely carried out after this Ph.D. thesis.

As students so far from home, my wife and I have learned to appreciate those of life's pleasures and displeasures in Germany. Gratitude is the sign of noble souls. A supreme happiness in life is the conviction that you have the gratitude.

Curriculum Vitae

Personal

- Male
- Born: November, 1977
- Married
- Chinese by birth

Education

- Feb. 2004 — present:
Ph.D.
Institut für Festkörperforschung, Forschungszentrum Jülich GmbH, Germany
Present dissertation RWTH Aachen
Supervisor: **Prof. Dr. Thomas Brückel**
- May. 2003 — Aug. 2003:
Visiting scientist as a Ph.D. candidate for Forschungszentrum Jülich GmbH, Germany
- Sept. 2000 — Apr. 2003:
Master
Materials Physics and Chemistry, University of Science and Technology Beijing, China
Thesis: *Investigation on high magnetoresistance $Ni_{0.81}Fe_{0.19}$ films grown on $(Ni_{0.81}Fe_{0.19})_{1-x}Cr_x$ seed layers*
Supervisor: **Prof. Dr. Fengwu Zhu**
- Sept. 1996 — Jul. 2000:
Bachelor
Materials Physics and Chemistry, University of Science and Technology Beijing, China
Thesis: *Investigation on the tendency of austenite grain growth in the new generation '956' steel for naval ships*
Supervisor: **Prof. Dr. Xinlai He**

Publications

As the first author:

- [1] *Neutron-diffraction study of structural transition and magnetic order in orthorhombic and rhombohedral $\text{La}_{7/8}\text{Sr}_{1/8}\text{Mn}_{1-\gamma}\text{O}_{3+\delta}$*
H. F. Li, Y. Su, J. Persson, P. Meuffels, J. M. Walter, R. Skowronek, Th. Brückel
J. Phys.: Condens. Matter **19**, 176226-1 - 176226-12 (2007)
- [2] *Correlation between structural and magnetic properties of $\text{La}_{7/8}\text{Sr}_{1/8}\text{Mn}_{1-\gamma}\text{O}_{3+\delta}$ with controlled nonstoichiometry*
H. F. Li, Y. Su, J. Persson, P. Meuffels, J. M. Walter, R. Skowronek, Th. Brückel
J. Phys.: Condens. Matter **19**, 016003-1 - 016003-12 (2007)
- [3] *Ultrathin high anisotropic magnetoresistance $\text{Ni}_{0.81}\text{Fe}_{0.19}$ films*
H. F. Li, G. H. Yu, J. Teng, F. W. Zhu
J. Phys. D Appl. Phys. **39**, 4915-4919 (2006)
- [4] *Effects of composition and thickness of $(\text{Ni}_{0.81}\text{Fe}_{0.19})_{1-x}\text{Cr}_x$ seed layers on magnetism and microstructure of $\text{Ni}_{0.81}\text{Fe}_{0.19}$ films*
H. F. Li, J. D. Ma, H. Zhang, G. H. Yu, F. W. Zhu
Acta Metall. Sin. **39**, 1043-1046 (2003) (in Chinese)
- [5] *Investigation on high magnetoresistance $\text{Ni}_{0.81}\text{Fe}_{0.19}$ Films grown on $(\text{Ni}_{0.81}\text{Fe}_{0.19})_{1-x}\text{Cr}_x$ underlayers*
H. F. Li, J. D. Ma, G. H. Yu, S. B. Long, H. C. Zhao, F. W. Zhu
Chin. Sci. Bull. **48**, 1087-1089 (2003)
- [6] *Crystal and magnetic structure of powdered single-crystalline $\text{La}_{1-x}\text{Sr}_x\text{MnO}_3$ ($x \approx 1/8$)*
H. F. Li, Y. Su, J. Persson, P. Meuffels, Th. Brückel
To be published
- [7] *Resonant soft x-ray scattering studies of double-layered $\text{La}_1\text{Sr}_2\text{Mn}_2\text{O}_7$*
H. F. Li, Y. Su, A. Nefedov, Tapan Chatterji, J. Persson, P. Meuffels, Th. Brückel
To be published
- [8] *Soft x-ray resonant scattering studies of 2D $\text{BaNi}_2\text{V}_2\text{O}_8$*
H. F. Li, Y. Su, Th. Wolf, F. Radu, J. Persson, P. Meuffels, Th. Brückel
To be published